Development of Far-Red / Near-Infrared Luminescent Chromophores and Nanoparticles for in vivo Biphotonic Applications

Zheng Zheng

Numéro National de Thèse : 2016LYSEN024

THESE de DOCTORAT DE L'UNIVERSITE DE LYON
opérée par
l'Ecole Normale Supérieure de Lyon

Discipline : Chimie

Laboratoire de Chimie de l'ENS de Lyon

École Doctorale de Chimie de Lyon

Présentée et soutenue publiquement le 26 septembre 2016, par :

Zheng ZHENG

Development of Far-Red / Near-Infrared Luminescent Chromophores and Nanoparticles for *in vivo* Biphotonic Applications

---

Développement de chromophores émettant dans le rouge lointain et le proche infra-rouge et leur formulation en nanoparticules pour une application en imagerie *in vivo* par microscopie bi-photon

---

Directrice de thèse : Mme Chantal ANDRAUD
Co-encadrant de thèse : M. Yann BRETONNIERE

Devant le jury composé de :

Mme Isabelle LERAY, ENS Cachan	Rapporteure
M. Anthony ROMIEU, Université de Bourgogne	Rapporteur
Mme Christine PAUL-ROTH, INSA de Rennes	Examinatrice
M. Jens HASSERODT, ENS de Lyon	Examinateur
M. Boudewin VAN DER SANDEN, INSERM (Grenoble)	Membre Invité
Mme Chantal ANDRAUD, ENS de Lyon	Directrice de thèse
M. Yann BRETONNIERE, ENS de Lyon	Co-encadrant de thèse

Acknowledgements

This dissertation was funded by the China Scholarship Council (CSC) and École Normale Supérieure de Lyon (ENS-Lyon). I would like first of all to extend my gratitude to CSC and ENS-Lyon for giving me the opportunity to work on this project and for funding the research.

This thesis was completed with the supervision of Dr. Chantal Andraud and Dr. Yann Bretonnière. I would like to express my sincere thanks to Dr. Chantal Andraud, the director of Laboratoire de Chimie de l'Ecole Normale Supérieure de Lyon, for giving me an opportunity to work in her lab under her guidance. I deeply appreciate her for providing care, support and help, both in my life and study, in the last three years. I also want to show my great thanks to Dr. Yann Bretonnière, who taught me how to do the research and enjoy life. In my PhD study, he always encouraged and motivated me to do what I interested in, and also gave me a lot of professional ideas and suggestions. I benefit a lot from his scientific attitude and profound knowledge on his field of research.

I would like to take this opportunity to also thank the following people for their support and help:

- Dr. Patrice Baldeck, Dr. Yuanyuan Liao from Laboratoire de Chimie de l'ENS-Lyon, for two-photon absorption measurement.
- Dr. Boudewijn van der Sanden from Clinatec Lab Campus Minatec in Grenoble, for two-photon excited bio-imaging.
- Dr. Nathalie Calin from Laboratoire de Chimie de l'ENS-Lyon, for X-ray single crystal analysis.
- Prof. Hongping Zhou from Anhui University, for theoretical calculation and cellular bio-imaging.
- All our group members (current and former) and all staff members of Laboratoire de Chimie de l'ENS-Lyon.
- All my friends. I cherished all the wonderful moments that we spent together.

Finally, I would like to thank my family for their never ending support and motivation throughout the course of my education. You offered me every ounce of love and opportunity throughout my life and that will be forever treasured.

This Thesis is dedicated to my grandfather, Junyang Zheng, who brought me up and I miss him every day.

Table of Contents

Abbreviations

Δv	Stokes shift
μ_e	Dipole moment of the emissive state
μ_g	Dipole moment of the ground states
2D	Two-dimensional
2PA	Two-photon absorption
3D	Three-dimensional
3PA	Three-photon absorption
a	Onsager radius
A	Electron acceptor
ACQ	Aggregation caused quenching
AIE	Aggregation-induced emission
CH_2Cl_2	Dichloromethane
D	Electron donor
DCM	Dichloromethane
DEDMS	Diethoxydimethylsilane
DFT	Density functional theory
DLS	Dynamic light scattering
DMF	Dimethylformamide
DMSO	Dimethyl sulfoxide
ET	Electron transfer
eV	Electron volt
F127	Pluronic F127
FR	Far red
FRET	Förster resonance energy transfer
f_w	Water fraction
GM	Goeppert-Mayer 1 GM = 10^{-50} cm^4 s
h	Hour
HOMO	Highest occupied molecular orbital
Hz	Hertz
IC	Internal conversion
ICT	Intramolecular charge transfer
ISC	Intersystem crossing
J	Coupling constant
LUMO	Lowest unoccupied molecular orbital
MPIF	Multi-photon-induced fluorescence

NIR	Near-infrared
NMR	Nuclear magnetic resonance
NPs	Nanoparticles
OD	Optical density
ppm	Parts per million (NMR data)
RIM	Restriction of Intramolecular Motions
RIR	Restriction of Intramolecular Rotations
RIV	Restriction of Intramolecular Vibrations
SEM	Scanning electron microscopy
TBAC	Tetrabutylammonium Chloride
TEM	Transmission electron microscopy
TEOS	Tetraethyl orthosilicate
THF	Tetrahydrofuran
TICT	Twisted intramolecular charge-transfer
TLC	Thin-layer chromatography
TPA	Triphenylamine
TPE	Tetraphenylethene
TPEF	Two-photon-excited fluorescence
UV	Ultraviolet
ε	Molar absorption coefficient
λ_{em}	Maximum emission
λ_{max}	Maximum absorption
μM	Micromolar
ν_{abs}	Frequency of absorption maximum
ν_{em}	Frequency of emission maximum
σ	Two-photon absorption cross-section
τ	Fluorescence lifetime
Φ_f	Fluorescence quantum yield

General Introduction

Far red (FR) and near-infrared (NIR) luminescent dyes are very attractive candidates for biological applications, because they allow for imaging with low background auto-fluorescence from biological samples, reduced light scattering and high tissue penetration. Two-photon fluorescence microscopy offers the possibility to shift the excitation of dyes to the near-infrared region, using wavelength ranges corresponding to the optical transparency window of tissues, but also provides three dimensional image of specimen. Therefore, the development of chromophores with efficient two-photon absorption properties and emission of fluorescence in the FR/NIR is important, especially for in depth *in vivo* optical imaging.

In this thesis, we aim at developing new FR/NIR emitting fluorophores for *in vivo* two-photon microscopy targeting two practical applications of paramount importance in biology. As such, the first topic deals with the development of new two-photon phosphorescent probes for *in vivo* monitoring of oxygen pressure. The second part is devoted to the molecular engineering of a new family of far red emitting push-pull fluorophores displaying interesting solvatochromic properties, aggregation-induced emission (AIE), along with high two-photon absorption (2PA) cross-sections and to the practical use in two-photon imaging of the vascular system in living animal.

Since the main topic of this thesis is the development of NIR luminescent chromophores for two-photon microscopy, the importance of NIR light and of two-photon microscopy in biological imaging will be presented in detail in **Chapter 1**. Emphasis will then be put on the main NIR luminescent probes that have been already developed for two-photon luminescence imaging. Each chapter afterward will start with a brief specific introduction for a better understanding of the work presented in the chapter.

Chapter 2 will describe our work on oxygen sensitive two-photon phosphorescent probes. Molecular oxygen concentration is of paramount importance for many vital physiological processes and is a key factor for cell and organ survival. Two new phosphorescent palladium porphyrin complexes (**P-1** and **P-2**) were designed and synthesized in which efficient two-photon absorbers acting as antennae were covalently grafted. Properties of these compounds are based on a Förster Resonance Energy Transfer (FRET) process between the antennae and the phosphorescent core. Different antennae were studied first and the best suited chosen for the final molecules. Finally, the energy transfer as well as the two-photon properties and the sensitivity towards oxygen were studied.

Chapter 3 deals with the design, synthesis and study of a new series of eleven asymmetrical fluorene-based push-pull fluorophores (**a1**-**a11**). Most fluorophores exhibit good 2PA properties and AIE behaviours in the NIR region. New NIR emissive co-precipitation nanoparticles were prepared based on an AIE fluorophore and a non-AIE active fluorophore. The NIR fluorescent AIE aggregate and co-precipitation nanoparticles were studied and applied to *in vivo* imaging vasculature in mice ear using two-photon microscopy. In **Chapter 4**, a micelle/silica coprotection strategy was proposed to prepare

original nanoparticles incorporating the newly designed fluorophores. The resulting far red emissive nanoparticles were then successfully used for two-photon fluorescence imaging of blood vessels in tumour inside mouse ear skin.

In addition, all the experiment details are provided in **Chapter 5** and **Annexes**. Literature references are listed separately afterwards.

Chapter 1. Introduction to Near-Infrared Luminescent Probes for Two-Photon Luminescence Imaging

1. Near-Infrared Luminescence in Biological Applications

1.1. Absorption and Luminescence Principles

Absorption of light is known as a process which consists of the promotion of one electron from an occupied orbital of one molecule to its unoccupied orbital. Generally, the molecule is initially in its electronic ground state and light absorption brings it to an excited state. It is a very fast process (10^{-17}-10^{-15} s) with respect to all the other processes presented in **Figure 1-1**, so that there is no concomitant displacement of the nuclei according to Franck-Condon principle. Experimentally, the efficiency of light absorption at a wavelength (λ) by an absorbing medium is characterized by the absorbance $A(\lambda)$ or the transmittance $T(\lambda)$. In general case, the absorbance of a sample follows the Beer-Lambert law:

$$A(\lambda) = \log(\frac{I_\lambda^0}{I_\lambda}) = -\log[T(\lambda)] = \varepsilon(\lambda) l c \qquad (1\text{-}1)$$

$$T(\lambda) = \frac{I_\lambda}{I_\lambda^0} \qquad (1\text{-}2)$$

in which I_λ^0 and I_λ are the light intensities of the beam entering and leaving the absorbing medium, respectively; $\varepsilon(\lambda)$ is the molar absorption coefficient (usually expressed in $L.mol^{-1}.cm^{-1}$), c is the concentration (in $mol.L^{-1}$) of compound and l is the path length through the absorbing medium (in cm).

The excited molecules lose their energy excess by different chemical and physical processes. The Perrin-Jablonski diagram (**Figure 1-1**) is often used to describe the physical processes of excitation and deactivation: photon absorption, internal conversion (IC), intersystem crossing (ISC) and luminescence (phosphorescence and fluorescence). Generation of luminescence through relaxation of an excited molecule is a phenomenon termed photoluminescence, which can be divided into fluorescence and phosphorescence, depending on the nature of the excited state.

Characteristic times (τ):

Absorption: 10^{-17}-10^{-15} s

Fluorescence: 10^{-10}-10^{-7} s

Phosphorescence: 10^{-6}-1 s

Internal conversion (IC): 10^{-15}-10^{-10} s

Vibrational relaxation: 10^{-15}-10^{-10} s

Intersystem crossing (ISC): 10^{-10}-10^{-8} s

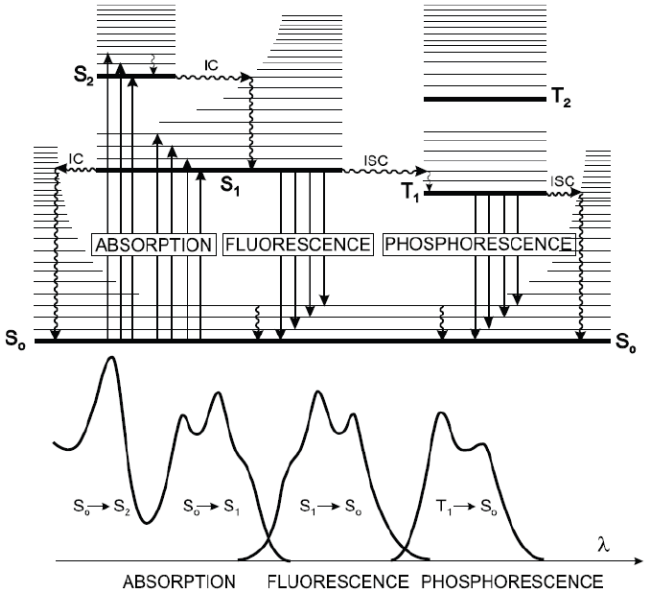

Figure 1-1. Perrin-Jablonski diagram scheme for the photophysical processes in the molecules.[1-2]

Fluorescence is defined as radiative transition from an excited electronic state (usually the first singlet excited state, S_1) to a lower lying state of the same spin multiplicity (usually the singlet ground state of the molecule, S_0).[3] Normally the fluorescence emission spectrum does not depend on the excitation wavelength. The fluorescence spectrum is located at higher wavelengths (lower energy) than the absorption spectrum because of energy loss in the excited state due to the vibrational relaxation (**Figure 1-1**). The gap between the maximum of the first absorption band and the maximum of the corresponding fluorescence band is called the Stokes shift. These radiative deactivations are quantified by two important values: quantum yield (Φ), defined as the ratio of the number of photons emitted to the number of photons absorbed and lifetime (τ), referring to the average time the molecule stays in its excited state before emitting a photon.

The process of phosphorescence occurs in a manner similar to fluorescence. Phosphorescence is the radiative de-excitation through $T_1 \rightarrow S_0$ emission (**Figure 1-1**). In general, the transition $T_1 \rightarrow S_0$ is spin forbidden and the corresponding radiative rate constant is very low. Since phosphorescence involves the intersystem crossing between S_1 and T_1, lifetime (τ, 10^{-6}–1 s) and Stokes' shift of phosphorescence are typically longer and larger than that of fluorescence (τ: 10^{-10}–10^{-7} s).[2]

1.2. Advantages of Near-Infrared Luminescence for Biological Imaging

Ultraviolet light excitation of chromophores in biological systems can damage tissues. As shown in **Figure 1-2**, blue or green irradiations are more suitable for surface imaging

applications, such as superficial structures or small-animal imaging, associated with their poor tissue penetration. It is because many biological chromophores, in particular hemoglobin (Hb) and related molecules, can be excited at lower wavelength (*eg* blue, green, yellow) range, thereby limiting depth penetration to a few millimeters and leading to excessive autofluorescence. Besides, the infrared light with longer wavelength can be absorbed by some other biological components such as water and lipids, which show less absorption (optically transparent) in the visible to the NIR range. So the optimal excitation wavelength of a chromophore is in the far red to NIR range (650-900 nm), which is called biological transparency window (**Figure 1-2**). In this region, the absorption coefficient of tissues and the autofluorescence are at their minimum, leading to maximal light penetration. For this same reason, both excitation and emission wavelengths of a chromophore in this range are ideal for biological applications.

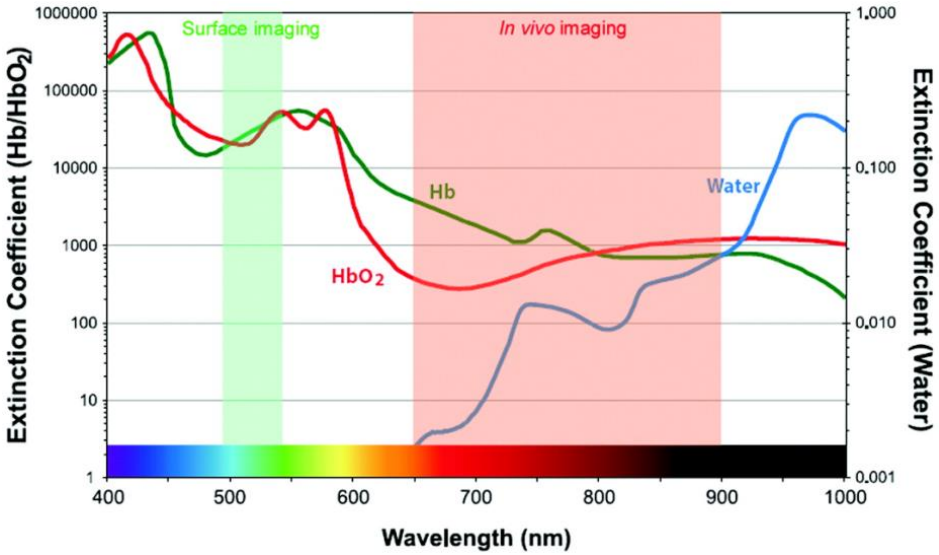

Figure 1-2. The NIR window is ideally suited for *in vivo* imaging because of minimal light absorption by hemoglobin (<650 nm) and water (>900 nm).[4]

Fluorescence-based imaging in this NIR region has outstanding signal-to-noise ratios (SNR) due to minimum interference from tissue autofluorescence. This is illustrated in **Figure 1-3**, which shows the relationship between excitation and emission wavelengths, and tissue autofluorescence in mice body.[5] As we can see, 'green' autofluorescence of the skin and viscera (especially gallbladder, small intestine and bladder), is astoundingly high when excited with blue light. Even a small amount of urine leaking from the urethra (overlying the tail) is easily seen. However, autofluorescence from gallbladder and bladder is markedly reduced using a 'red' filter set (that include green light excitation). Still intestinal autofluorescence remains significant. On the other hand, use of a NIR filter set essentially eliminates autofluorescence. Hence, high tissue autofluorescence precludes the use of visible light for most *in vivo* imaging applications, and NIR light solves this problem by reducing fluorescence background. Furthermore, NIR optical imaging can prospectively be used to resolve molecular events through deep tissue volumes at high depths.[6] Realization of the full

potential for fluorescence-based *in vivo* imaging will be dependent upon the design of contrast agents that both absorb and emit in NIR.[7-10]

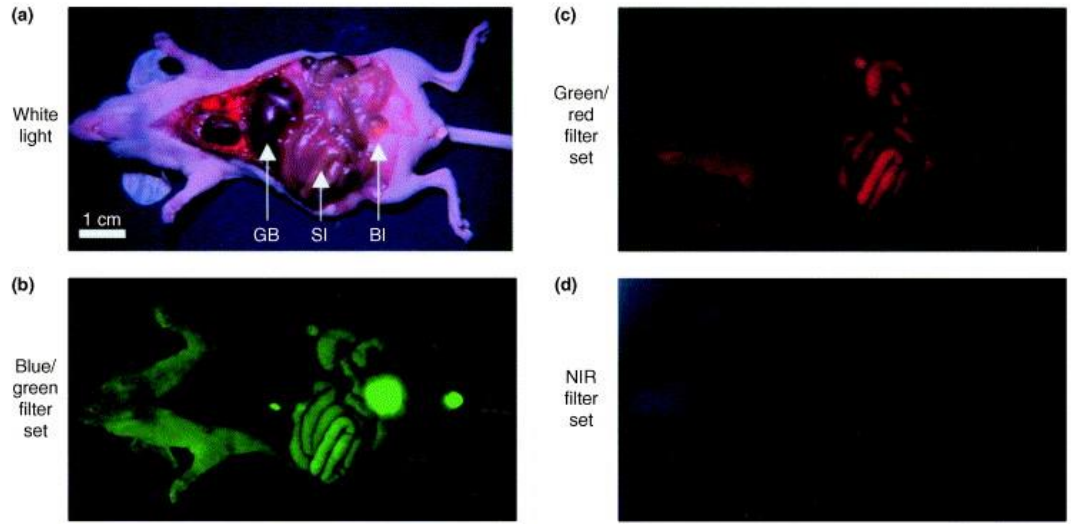

Figure 1-3. Wavelength-dependent autofluorescence of vital organs and bodily fluids. (a) Immediately after sacrifice, the viscera of a hairless, athymic *nu/nu* mouse were exposed. Tissue autofluorescence was then imaged using three different excitation/emission filter sets: (b) blue/green (460–500 nm/505–560 nm); (c) green/red (525–555 nm/590–650 nm); and (d) NIR (725–775 nm/790–830 nm). The fluence rate provided by each filter set was adjusted to 2 mW/cm^2. To compensate for differences in emission filter wavelength width and camera sensitivity, exposure times were adjusted accordingly. For orientation, the white light color image of the animal is shown in (a). Arrows mark the location of the gallbladder (GB), small intestine (SI) and bladder (Bl). Pictures taken from reference [5].

2. Two-Photon Excitation Microscopy

2.1. Nonlinear Optical Effects

Non-linear optical effects occur when the response of a material system to an applied optical field depends in a nonlinear manner upon the strength of the optical field. The field of nonlinear optics has developed rapidly since the advent of the laser in the beginning of 1960s.[11]

Once a medium is subjected to an electric field the electrons in the medium are polarized. In the case of conventional (*i.e.*, linear) optics, the induced polarization (P) depends linearly upon the electric field strength (E) in a manner that can often be described as:

$$P = \chi^{(1)} E \tag{1-3}$$

where the constant of proportionality $\chi^{(1)}$ is known as the linear susceptibility.

In nonlinear optics, the optical response can often be described by generalizing Eq. (1-4) by expressing the polarization *P* as a power series in the field strength *E* as:[12]

$$P = \chi^{(1)}E + \chi^{(2)}E^2 + \chi^{(3)}E^3 + \chi^{(5)}E^5 \cdots\cdots \quad (1\text{-}4)$$

where $\chi^{(2)}$ is called the second-order nonlinear susceptibility, $\chi^{(3)}$ is called the third-order nonlinear susceptibility, and so on. A number of interesting optical phenomena arise from the second- and third-order susceptibilities. For example, $\chi^{(2)}$ gives rise to second harmonic generation, the linear electro-optic effect or Pockels effect, parametric oscillation and three-frequency processes. The third-order susceptibility $\chi^{(3)}$ is responsible for third harmonic generation, the quadratic electro-optic effect or Kerr effect, two-photon absorption (2PA), and Raman, Brillouin, and Rayleigh scattering. Similarly, $\chi^{(5)}$ is the fifth-order nonlinear susceptibility, which can be utilized to phenomenologically describe the three-photon absorption (3PA).

2.2. Two-Photon Absorption

2PA is a third-order nonlinear optical phenomenon, which was originally predicted by Maria Göppert-Mayer in 1931 in her doctoral dissertation.[13] Until 1961, only one year after the invention of the first laser device, 2PA-induced frequency-upconversion fluorescence was first observed from a CaF_2:Eu^{2+} crystal by Kaiser and Garrett.[14] The same authors later further demonstrated that two-photon excitation also can excite the fluorescence of organic dyes. Since then, many materials with two-photon properties have been developed and reported.[15-17] 2PA process corresponds to the simultaneous absorption of two photons of identical or different frequencies by the same molecule, which was then excited to a higher energy level through a 'virtual state'. The transition energy for this process is equal to the sum of the energies of the two photons absorbed. Generally, the two photons have the same energy, and then the probability that a molecule undergoes two-photon absorption depends on the square of the intensity of the incident light.

Figure 1-4 depicts the one- or two-photon excitation and emission processes. By the way, 3PA processes were first observed in napthalene crystals by Singh & Bradley in 1964 [18] and then others further demonstrated 3P excitation processes.[19-20]

2PA in a material can be quantified by the 2PA cross-section (σ) with the unit of GM (1 GM = 10^{-50} cm^4 s $photon^{-1}$). Theoretical derivation indicates that the value of the σ is proportional to the imaginary part of the third susceptibility ($\chi^{(3)}$):[21]

$$\sigma = \frac{8\pi^2 h \nu^2}{n^2 c^2 N} \mathrm{Im}(\chi^{(3)}) \quad (1\text{-}5)$$

where $\mathrm{Im}(\chi^{(3)})$ is the imaginary part of the third susceptibility ($\chi^{(3)}$), *h* is the Planck's constant, *v* is the frequency of an incident laser beam, *n* is the refractive index of the medium and *c* is the speed of light.

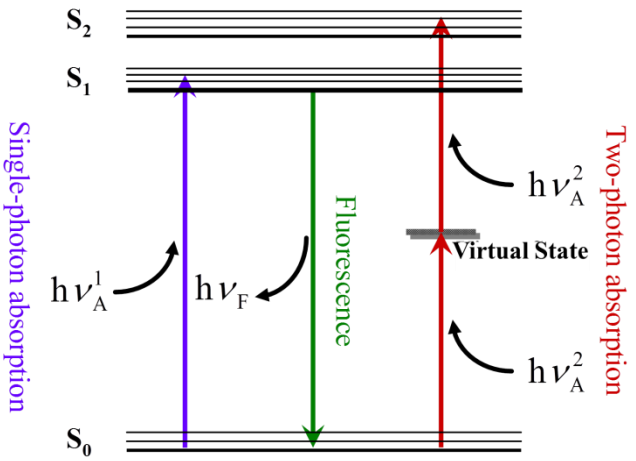

Figure 1-4. Schematic description of one- or two-photon excitation and emission processes.

2PA cross-section, which reflects the capability of absorbing two-photon by molecules, is a relevant parameter of the two-photon excitation process. The measurement of 2PA cross section requires high power, which is now easily available from pulsed lasers. Up to now, there is no commonly used standard method and instrument for measuring σ, which can be strongly influenced by the measurement technique because of a variety of artifacts. The main techniques for measuring 2PA cross section are nonlinear transmission (NLT), two-photon-excited fluorescence (2PEF), transient absorption, four-wave mixing and Z-scan.[22] Among them, 2PEF and Z-scan are widely used to determine the σ values of molecules.

2.3. Measure of Two-Photon Cross-Section

2.3.1. Two-Photon-Excited Fluorescence

With the use of a pulsed laser, the 2PEF intensity provides direct information on the efficiency of 2PA. The relationship between the intensity of the incident light and the 2PEF intensity can give rise to the information about the order of the nonlinear process in the sample upon excitation. For example, second order process corresponding to two-photon absorption, third order process corresponding to three-photon absorption, and so on.

By using 2PEF method, when a suitable reference compound with a known 2PA spectrum is chosen, the 2PA cross-section σ of the sample can be calculated by comparing 2PEF excitation spectra of the sample and of the reference under identical conditions. Thus, σ of the sample was determined by the following equation:[23-24]

$$\sigma = \sigma_{ref} \frac{\Phi_{ref}}{\Phi_s} \frac{c_{ref}}{c_s} \frac{n_{ref}}{n_s} \frac{F_s}{F_{ref}} \tag{1-6}$$

where the subscripts *ref* and *S* stand for reference and sample respectively, σ is the 2PA cross-section value, c is the concentration of the sample, n is the refractive index of the

solution, F is the 2PEF integral intensity of the light emitted at the excitation wavelength, and Φ is the fluorescence quantum yield. The value of σ_{ref} could be taken from the literature. The main drawback of this method is the requirement of luminescent materials.

2.3.2. z-scan technique

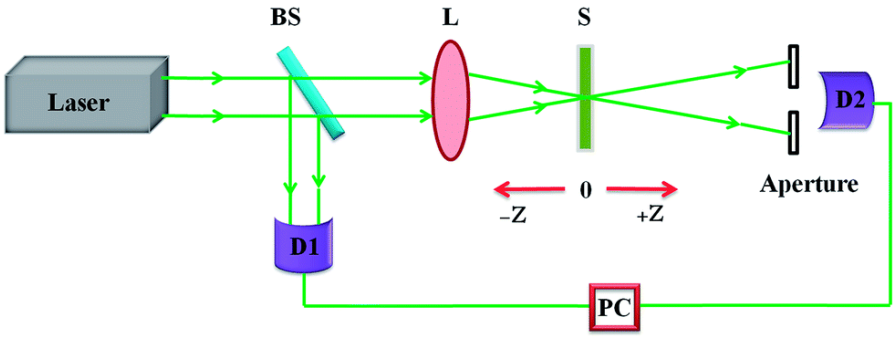

Figure 1-5. Setup for the *z*-scan measurements. BS-beam splitter, L-lens, S-sample, D1 and D2 – detectors, PC-computer. The left detector is used for monitoring the incident pulse energy.

As seen in **Figure 1-5**, the *z*-scan method involves moving a sample along the path of a focused laser beam and measuring the light intensity at the detector as a function of its position along this *z*-axis.[25] If the detector has a narrow aperture (as in the so called "closed-aperture" setup), then the output is sensitive to intensity-dependent changes in the refractive index (as a result of third-order nonlinear polarizability or thermal effects) which lead to self-focusing or defocusing of the beam. Alternatively, if the detector collects all the light from the sample ("open-aperture" setup), then the output only reflects the intensity-dependent transmission, and can be used to measure 2PA cross-sections.

The open aperture *Z*-scan data can be fitted by using the following equations:[26-27]

$$T(z, s=1) = \sum_{m=0}^{\infty} \frac{[-q_0(z)]^m}{(m+1)^{3/2}} \tag{1-7}$$

$$q_0(z) = \frac{\beta I_0 L_{eff}}{1+x^2} \tag{1-8}$$

where $x = z/z_0$, z is the distance of the sample and beam focus, $z_0 = \pi\omega_0^2/\lambda$ is the diffraction length of the beam with ω_0 the spotsize at focus, λ is the wavelength of the beam, β was the 2PA coefficient, I_0 is the input intensity at the focus (z = 0) calculated by the input energy divided by $\pi\omega_0^2$, $L_{eff} = (1\text{-}e^{-\alpha L})/\alpha$ is the effective length with α the linear absorption coefficient and L the sample length. Furthermore, the molecular 2PA cross-section (σ) could be determined by using the following relationship:

$$\sigma = h\gamma\beta / N_A d \times 10^{-3} \tag{1-9}$$

in which h is the Planck's constant, γ is the frequency of input intensity, N_A is the Avogadro constant, and d is the concentration of the sample. Unlike 2PEF, z-scan is not restricted to fluorescent materials. However, in practice, 2PA cross-sections obtained from z-scan measurements (even using femtosecond pulses) often appear to be over-estimated, when compared with the values obtained from 2PEF method.[16]

2.4. Two-Photon Fluorescence Microscopy

The conventional optical microscopy is an important tool in life science as well as material science, but its ability to resolve microscopic structures in optically thick specimens is limited because the image at the focal plane is blurred by out-of-focus noise. The invention of confocal microscopy in the 1960s [28] has started to address three-dimensional imaging needs with improved optical resolution and contrast of a micrograph. Confocal microscopy achieves three-dimensional resolution using a set of conjugate apertures, one for illumination and one for detection of the scattered or fluorescent light. These conjugate pinholes, functioning as spatial filters, ensure that the microscope will illuminate and detect light from the same volume within the specimen. Based on the discovery of non-linear optical effects of molecules, two-photon fluorescence microscopy (2PFM) was subsequently invented by Winfried Denk in Watt W. Webb laboratory at Cornell University in 1990.[29] 2PFM is a technique very similar to confocal microscopy. Differently, 2PFM does not require a pinhole to obtain three-dimensional resolution, allowing flexibility in detection geometry. This technique combines the idea of two-photon excitation with the use of an ultrafast pulsed laser scanner.

2.4.1. Advantages of Two-Photon Fluorescence Microscopy

2PFM is considered a revolutionary development in biological imaging because of its unique advantages compared with conventional optical microscopy and confocal microscopy.

Firstly, a key feature of 2PFM is the limitation of fluorescence excitation to within a femtoliter size focal volume. According to the definition of two-photon process,[30] the excitation probability is linearly dependent on the squared intensity of the laser beam. The nonlinear feature of excitation implies that two-photon-induced absorption occurs most strongly within a spatially confined volume at the focal plane where the laser light is most concentrated (**Figure 1-6b**).[31] In contrast, the total two-photon fluorescence falls off rapidly away from the focal plane (**Figure 1-6c**),[16] demonstrating that most of the fluorescence generated is limited to the focal region. This localized excitation volume results in greatly improved axial depth discrimination and improvement in image contrast compared with conventional optical microscopy. By acquiring images at equally spaced positions across the vertical axis of the specimen, a three dimensional volume image can be obtained. Furthermore, this localization leads to less tissue damage to the regions above and below the focal plane that are not being imaged.

Secondly, like traditional one-photon microscopy, two-photon microscopy requires high

power laser to excite the chromophore within a sample with detectors to collect the emitted light. However, unlike the lasers used for one-photon microscopy, lasers used in two-photon microscopy excite the chromophore through a simultaneous absorption of two long wavelength photons. From the point of view of chromophore, the most commonly used chromophores have one-photon excitation spectra in the range of 350–500 nm, whereas the corresponding laser used to excite the two-photon fluorescence lies in the ~700–1000 nm region, which is located in biological transparency window. Thus, within two-photon microscopy, many two-photon active chromophores used for bio-imaging can be excited with the NIR light, which provides several distinct benefits such as improved depth penetration in scattering media and reduced phototoxicity.

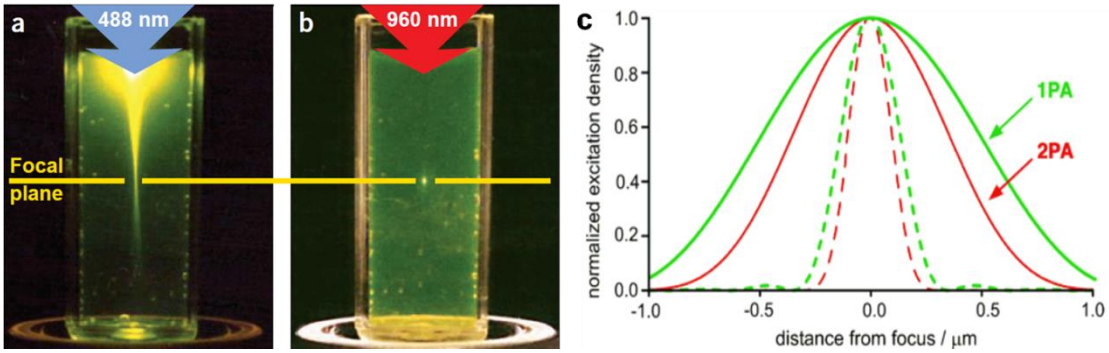

Figure 1-6. Localization of the excitation of fluorescein: a) single-photon excitation by focused light (488 nm; 0.16 NA); b) two-photon excitation using focused (0.16 NA) femtosecond pulses of 960 nm light; c) Excitation density as a function of axial and radial distance from the focal point (green: 1PA; red: 2PA; solid line: axial, dashed line: radial; NA = 1.4, λ = 800 nm).

Thirdly, for chromophores used in traditional one-photon microscopy, the excitation wavelength is usually spectrally close to their fluorescence emission band. To eliminate the leakage of the excitation light into the detection channel, the optical filter often cuts off a part of the emission band, resulting in a reduction in microscope sensitivity. For two-photon microscopy, the two-photon excitation wavelength is much farther removed from the emission band, which makes it easier to reject excitation light by using highly efficient filters, with minimal loss of emission photons.

2.4.2. Two-Photon Fluorescence Microscope

Figure 1-7 shows a typical two-photon microscope setup, which features three basic components including an excitation light source, a high-throughput scanning fluorescence microscope, and a high-sensitivity detection system. The critical component in a two-photon microscope is its light source. Different from conventional confocal microscopy, two-photon fluorescence microscopy requires a higher (kW to MW) beam power from a NIR pulsed laser to obtain simultaneous absorption of two photons and to produce significant fluorescence for imaging. High repetition rate (100 MHz), ultrafast (femtosecond or picosecond pulse widths) lasers, such as Ti: sapphire and Nd:YLF lasers, are the most widely used light sources, which

are considered to be optimal for two-photon microscopy.

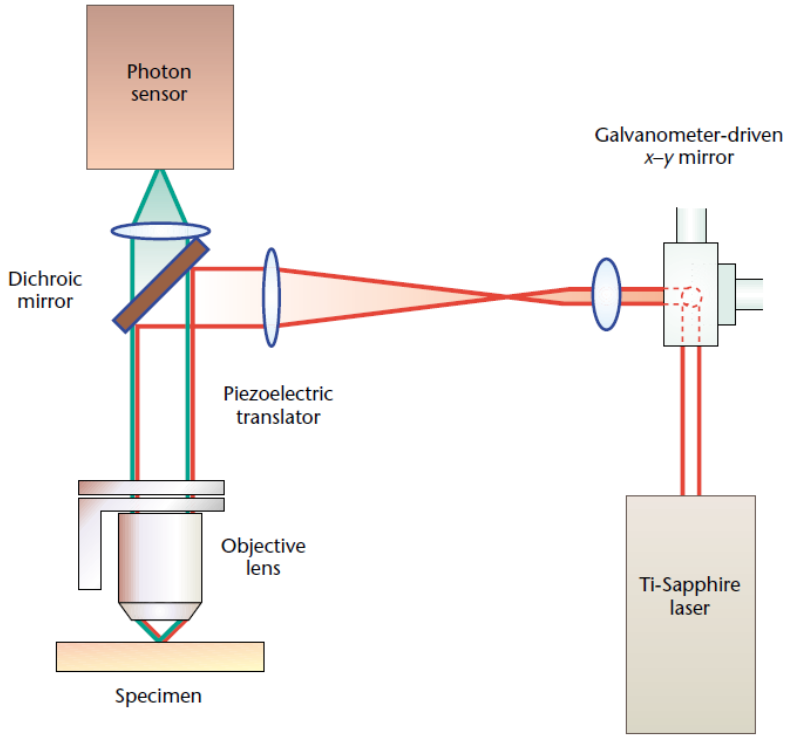

Figure 1-7. A schematic drawing of typical components in a two-photon microscope.[30] This system typically consists of a high-peak-power pulsed laser, a high-throughput scanning microscope and high-sensitivity detection circuitry.

Figure 1-7 shows laser excitation directed into the microscope *via* an epiluminescence light path. The excitation light is reflected by a dichroic mirror to the microscope objective and is focused in the specimen. Two-photon induced fluorescence is generated at the diffraction-limited volume. Images are constructed by raster scanning the fluorescent volume in three dimensions using a galvanometer- driven *x*–*y* scanner and a piezo-objective *z*-driver. The emission signal is collected by the same objective and transmitted through the dichroic mirror along the emission path. An additional barrier filter is needed to further attenuate the scattered excitation light. High-sensitivity detection electronics, such as single-photon counting circuitry, are used to ensure maximal detection efficiency and signal dynamic range.

As an example for typical two-photon imaging, two-dimensional (2D) and three-dimensional (3D) reconstruction of HCT 116 cells stained with compound **I** is shown in **Figure 1-8**, revealed a punctuate staining pattern with a predominantly endosomal localization.[32] The possibility of using two-photon microscope to simultaneously excite different colour fluorophores for multiple cellular label imaging has been explored (**Figure 1-9**). Xu *et al.* imaged rat basophilic leukemia cells simultaneously labelled with four two-photon absorbing probes with different functionalities.[33] This study demonstrates that the simultaneous imaging of four cellular structural components and the potential for studies in which the interaction of various cellular organelles can be monitored over time in 3D. In

addition to this, 2PFM has been successfully applied to a variety of imaging tasks on molecular level, cellular level, vascular level and tissue level.[12, 16-17, 30-31, 34-42]

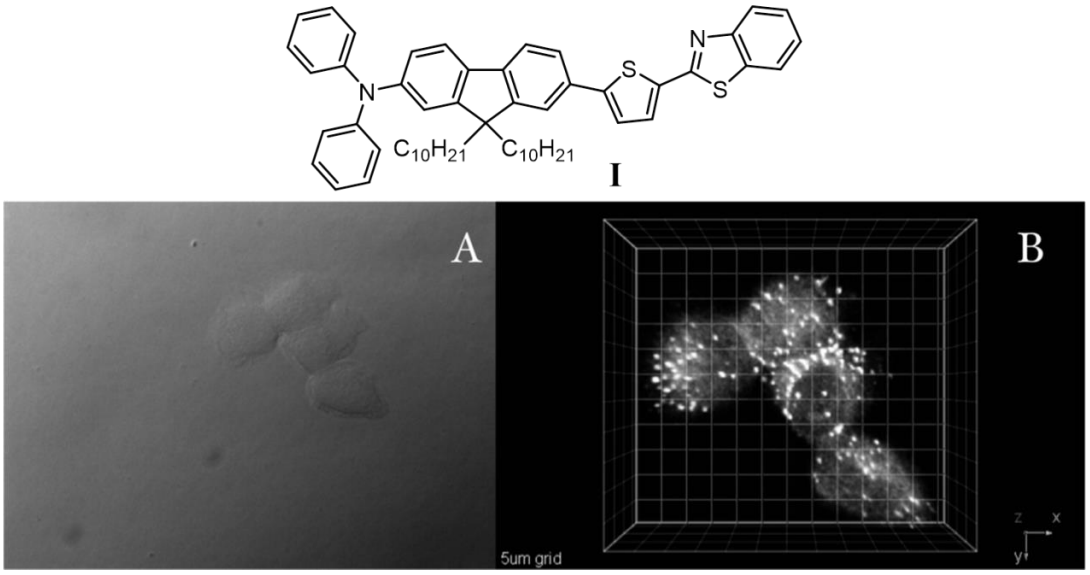

Figure 1-8. Two-photon fluorescence micrograph of HCT 116 cells incubated with probe **I** (20 μM, 1 h 50 min). (A) DIC and (B) 3D reconstruction from overlaid 2PFM images obtained from a modified laser scanning confocal microscopy system equipped with a broadband, tuneable Ti:sapphire laser (220 fs pulse width, 76 MHz repetition rate), pumped by a 10 W frequency doubled Nd:YAG laser. (60x objective, NA = 1.35). Scale: 5 μm grid. Pictures taken from reference [32].

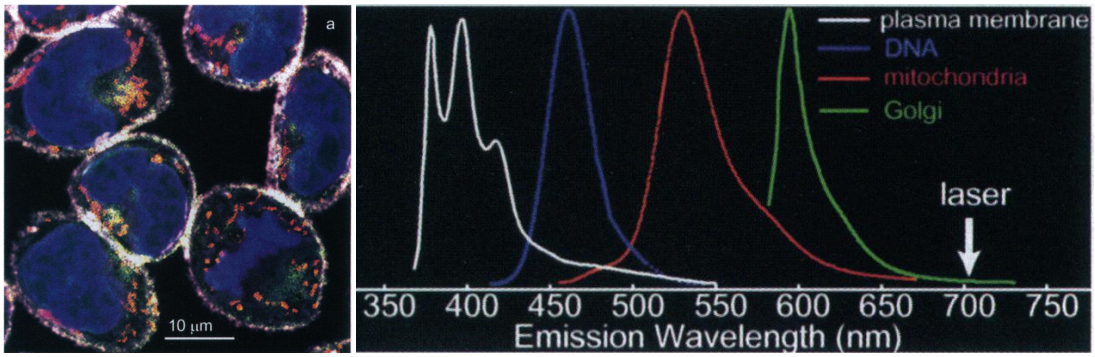

Figure 1-9. (Left) Four-color staining of plasma membrane, nuclei, Golgi complex, and mitochondria in rat basophilic leukemia (RBL) cells visualized with two-photon illumination. RBL cells were incubated with four different stains: a plasma membrane label (pyrene lysophosphatidylcholine), a nuclear stain (DAPI), a Golgi label (Bodipy sphingomyelin), and a mitochondrial stain (rhodamine 123). Epifluorescence was collected by using nondescanned external detection into four channels: 400 nm, 30 nm full width at half maximum (FWHM) (pyrene fluorescence, white); 440 nm, 50 nm FWHM (DAPI fluorescence, blue); 530 nm, 30 nm FWHM (rhodamine 123 fluorescence, red/orange) and 580 nm, 30 nm FWHM (Bodipy fluorescence, green); (Right) Approximate emission spectra of the dyes used (colour coded as in the image) and the excitation laser wavelength. Taken from reference [33].

3. Near-Infrared Luminescent Probes for Two-Photon Luminescence Imaging

3.1. General Design of Two-Photon Chromophores

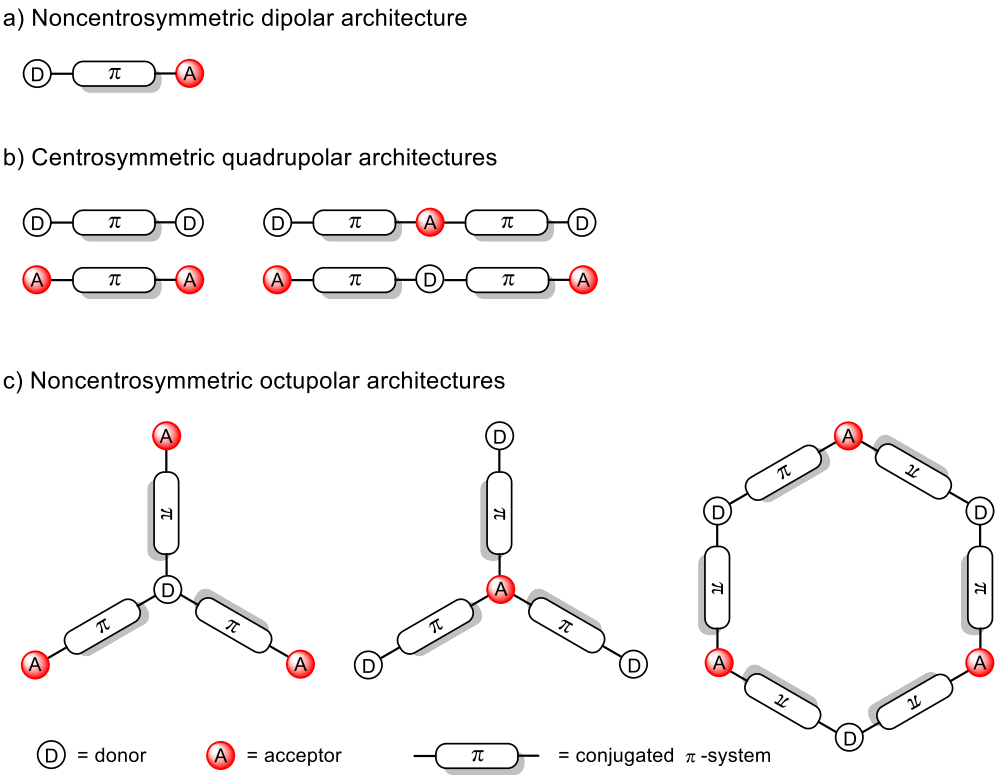

Figure 1-10. Typical molecular architectures for the design of fluorophores with large two-photon absorption cross-sections.[17]

Since the first observation of 2PA by organic compounds in 1963,[43] the structure–property relationships in the two-photon absorbing chromophores have been well studied.[12] To meet the increasing demand in the practical applications, a number of important molecular features have been identified for designing ideal chromophores with large 2PA cross-sections.[12, 16] Generally, the value of 2PA cross-section is associated with intramolecular charge-transfer (ICT) process in the chromophore. The presence of an electron-donor moiety, an electron-acceptor moiety, or both of them connected by a conjugated path, can effectively increase the dipole strength in molecules. In addition, the length of conjugation has been demonstrated as particularly important to the 2PA cross-section, as it leads to states with extended charge separation. Coplanarity is also critical in enhancing the efficiency of an intramolecular charge transfer. Besides, increasing the number of conjugation paths, or connecting several linear paths to form a 2D or a 3D configuration has also been shown theoretically and experimentally to be able to greatly increase 2PA responses.[12] For example,

as shown in **Figure 1-10**, several typical design strategies have been put forward to enhance the 2PA cross-section of molecules, in which π-conjugation has been employed to connect an electron donor group (D) and an electron acceptor group (A) to form non-centrosymmetric dipolar (a), centrosymmetrical quadrupolar (b), or more complex non-centrosymmetric octupolar structures (c). Based on these molecular architectures, a huge number of 2PA chromophores with large 2PA cross-sections have been reported for various applications such as microscopy, microfabrication, three-dimensional data storage, optical power limiting and up-converted lasing.[12, 16-17] It is not the purpose of this chapter to provide an extensive describe of such systems and we invite the reader to refer to recent reviews.[12, 16-17] We will mainly describe here some NIR luminescent organic materials for two-photon microscopy in two aspects: organic molecules and organic nanoparticles.

3.2. Organic Molecules

One-photon excited fluorescence in the NIR region has been commonly observed in organic molecules such as cyanine derivatives, BODIPY derivatives, squaraine derivatives, phthalocyanines/porphyrin derivatives and diketopyrrolopyrrole (DPP) derivatives,[44-49] which have attracted ongoing attention in biomedical applications.

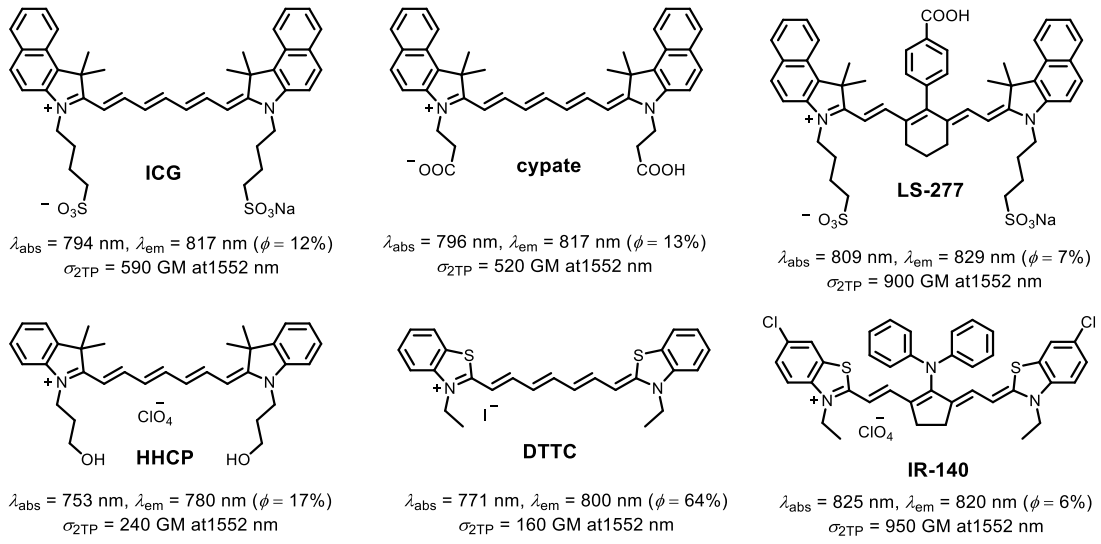

Figure 1-11. Examples of two-photon active cyanine-based fluorophores.

Typically, Indocyanine Green (**ICG**) is the only NIR fluorescent contrast agent which has been approved by the FDA (Food and Drug Administration) for direct administration in medical diagnostics. **ICG** is also the earliest NIR imaging agent used for the non-invasive detection of tumours in both animals and patients.[7] Despite its low toxicity and current clinical use as a contrast agent for visualizing blood and clearance, studying liver function and guiding biopsies,[50-61] **ICG** displays numerous drawbacks severely limiting its usage: rapid clearance (about 2-4 min), tendency to aggregate in aqueous solutions resulting in strong fluorescence quenching, binding to proteins (in particular albumin) leading to rapid

agglomeration, instability in aqueous solution and photobleaching under light exposure, rapid oxidation or dimerization resulting in decreased absorption/emission and variability in the maximum absorption wavelength.[62-63] Few other dye derivatives such as **IR-820** (λ_{exc} = 710 nm, λ_{em} = 820 nm)[64] or **Crimson carrier** (λ_{exc} = 745 nm and λ_{em} = 820 nm)[65] were reported as better alternative than **ICG**, when stability of the dye solution over time is concerned, or when a consistent peak emission wavelength is desired.

Recently, a number of cyanine-based near infrared fluorescent fluorophores for 2PFM have been reported by Berezin and coworkers.[66] Interestingly, good two-photon optical properties of **ICG** (σ_{2TP} = 590 GM and λ_{em} = 817 nm) and its derivatives (**Figure 1-11**) have been demonstrated using a two-photon fluorescence spectrophotometer under 1552 nm excitation.[66] Although cyanines represent interesting candidates to serve as NIR probes for two-photon imaging applications, their one-photon absorption is often too far in the visible resulting in NIR 2PA response out of the biological window, where water exhibit main absorption.[67-68]

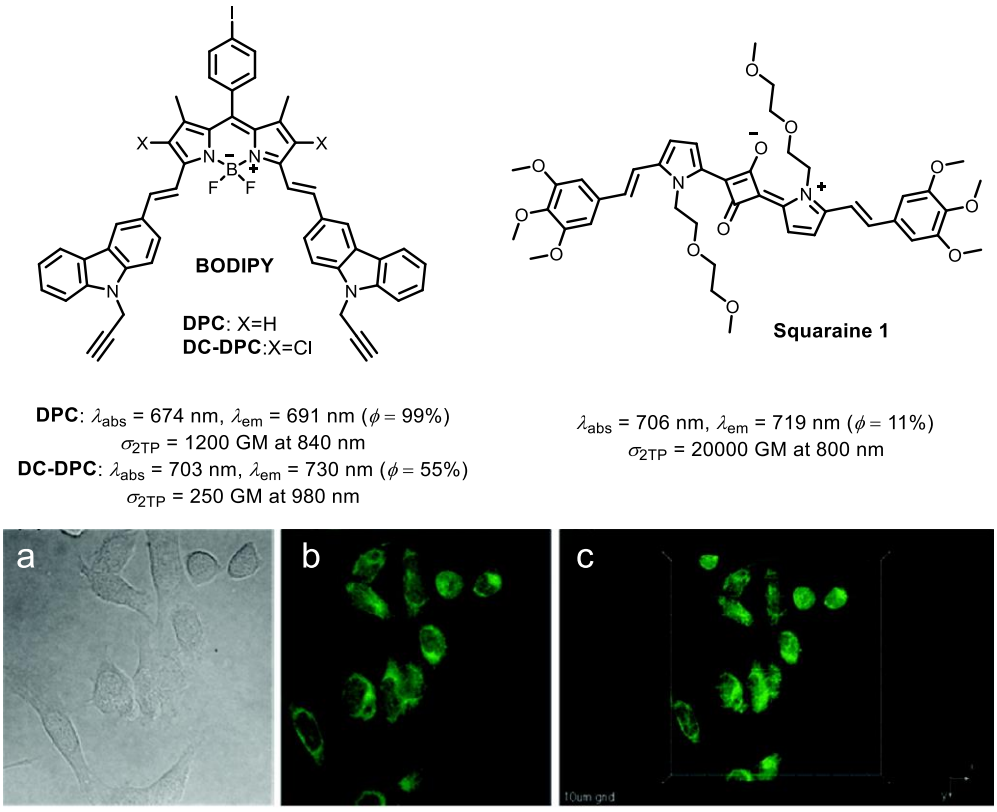

Figure 1-12. (Top) Chemical structures of near-infrared dyes **DPC**, **DC-DPC** and **Squaraine 1**; (Bottom) Images of HCT 116 incubated with **Squaraine 1** (a) DIC, (b) 2PFM (2D single X-Y optical section), and (c) 2PFM 3D reconstruction. Pictures taken from reference [69].

BODIPY (borondipyrromethane) fluorophores usually have sharp fluorescence with high quantum yield and excellent thermal and photochemical stability.[70-71] However, most BODIPY dyes emit from yellow to deep-red emission with relatively short fluorescence emission maxima (around 500 nm). Meanwhile, a number of NIR fluorescent BODIPY fluorophores have been developed through different synthetic approaches,[44] whereas the NIR

BODIPY applied to two-photon biological imaging are still rare. Belfield *et al.* reported two BODIPY derivatives **DPC** and **DC-DPC**, which show high fluorescence quantum yields (99% and 55%) in NIR region (**Figure 1-12**). [72] They were demonstrated much more efficient and photostable than common NIR dye **Cy5**. Both **DPC** and **DC-DPC** show good 2PA cross-sections in the range of 800–1000 nm, which is located in the biological window. These characteristics make them good candidate probes for two-photon imaging in NIR region.

Squaraine dyes are generally promising as NIR fluorescent probes.[73] There are a few squaraine dyes which were found to exhibit high two-photon absorption cross-sections,[74-76] whereas the potential of squaraine dyes as two-photon fluorescence probes has not been fully explored probably due to their poor water-solubility. An efficient two-photon absorbing squaraine fluorophore was developed by Belfield and coworkers (**Figure 1-12**).[69] **Squaraine 1** exhibits a high two-photon absorption cross-section (σ_{2PA} = ~20000 GM in DMSO determined by Z-scan) at 800 nm and high photostability. To improve water-solubility, an amphiphilic copolymer was employed to facilitate micelle encapsulation of **Squaraine 1**. The potential utility of the obtained probes for two-photon fluorescence-based *ex vivo* and *in vivo* bioimaging has been demonstrated in **Figure 1-12-bottom**.

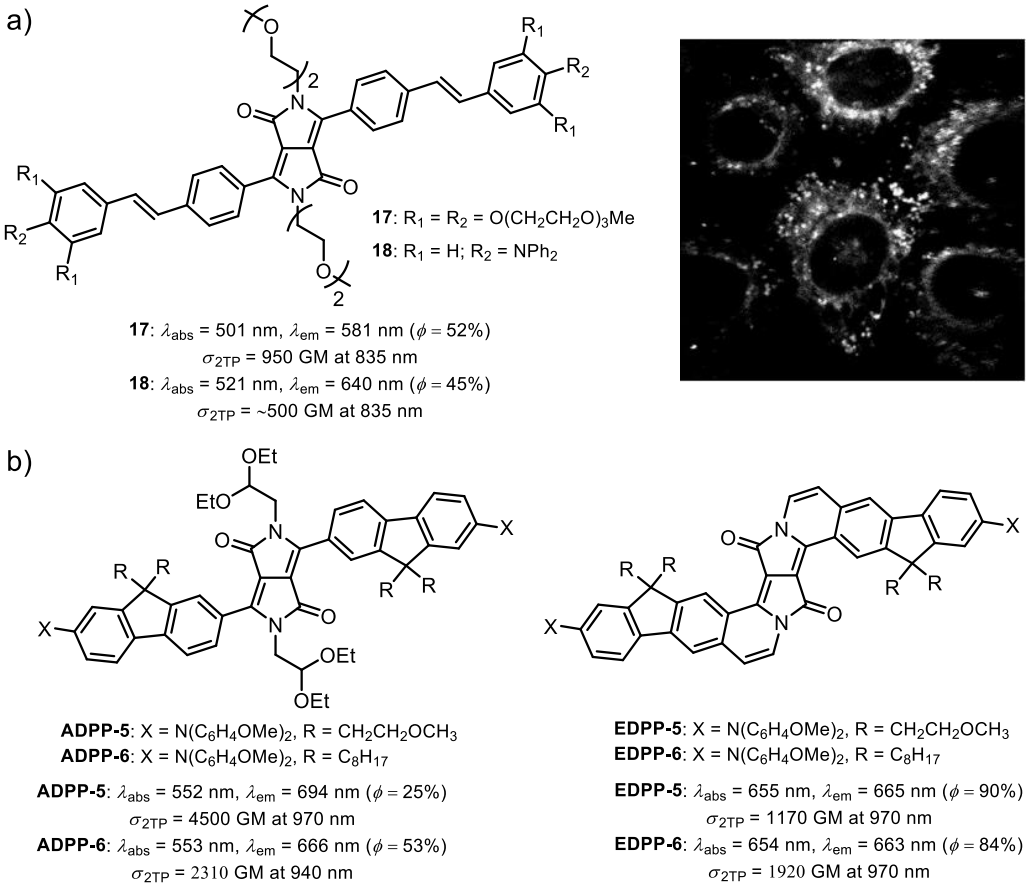

Figure 1-13. a) Left: Chemical structures of NIR diketopyrrolopyrrole (DPP) derivatives; Right: Two-photon imaging of HeLa cells stained with dye **18**; b) Chemical structures of π-expanded diketopyrrolopyrroles.

Diketopyrrolopyrrole (DPP) derivatives have been known for a long time in the pigment industry due to their bright reddish color, high stability, but also insolubility, which makes them excellent pigments.[77] Owing to their interesting fluorescence properties, a number of DPP-based probes have been developed for fluorescence imaging in the last few years.[78] In 2013, Bolze and co-workers reported several water-soluble probes based on a diketopyrrolopyrole (DPP) core for two-photon microscopy (**Figure 1-13a**).[47] These dyes showed good water solubility, efficient two-photon induced fluorescence even in water, and remarkable photostability. The two-photon optimized fluorophore can be further bioconjugated to HIV-I Tat (44-61), and their cellular localization was demonstrated by two-photon microscopy.[79] In 2014, Gryko and co-workers reported a new series of π-expanded diketopyrrolopyrroles with large intrinsic 2PA in the NIR range, showing very high brightness and red-shifted fluorescence (**Figure 1-13b**).[49] These characteristics make these new π-expanded DPP molecules of major promise as two-photon dyes for bioimaging applications.

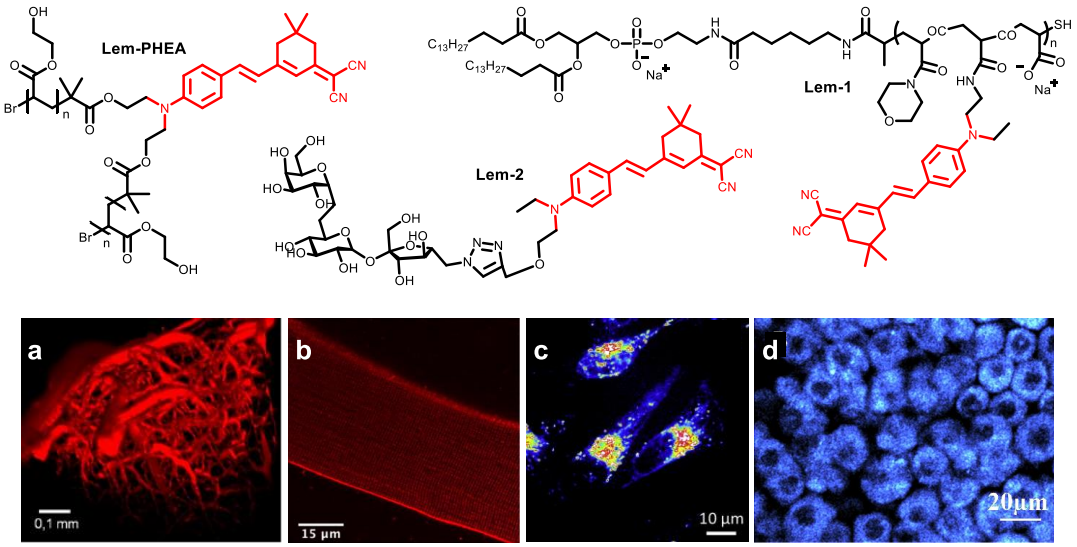

Figure 1-14. Chemical structures and bio-imaging of isophorone derivatives. a) two-photon cerebral vascular imaging with **Lem-PHEA**; b) membrane optical imaging with **Lem-2**; c) HeLa cells imaging with **Lem-1**; d) two-photon imaging of zebrafish live embryos with **Lem-1**. Picture taken from references [80-82].

In 2011, our group synthesized new push-pull NIR fluorophores based on isophorone, showing positive solvatochromism along with negative solvatokinetic effect.[83] Indeed, these red fluorophores are almost not emissive in low-polarity solvents such as toluene, but interestingly, the fluorescence quantum yield as well as the emission wavelength gradually increased upon increasing the polarity of solvent. As a result, they show very good far red/NIR fluorescence in polar environment such as aqueous media. This particular feature provides a possibility of molecular modification with water soluble group for NIR bioimaging applications, which require the probes to work in physiological media (**Lem-PHEA**). In addition, its two-photon properties have been demonstrated in the range 800–1000 nm with

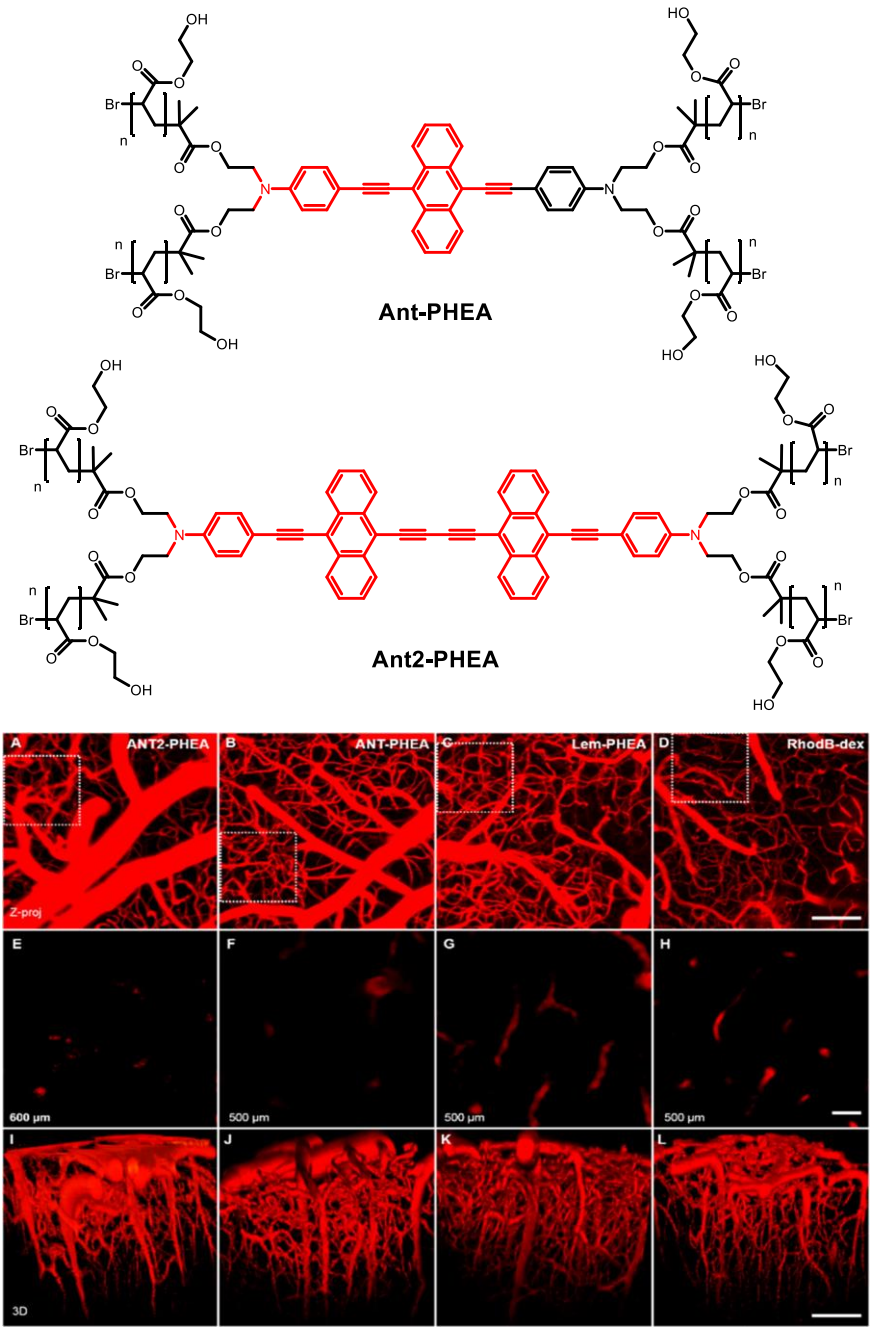

Figure 1-15. 2PLSM z-stacks projection images (standard deviation) of the cortical vasculature after **Ant2-PHEA** intra-veinous injection (A), **Ant-PHEA** (B), **Lem-PHEA** (C), and **rhodamine B–dextran** (D) after a craniotomy (scale bar: 100 µm). The white dotted square on each image indicates the area of the image that has been expanded in the corresponding zooms: A zoom at 550 µm depth for **ANT2-PHEA** (E), and at 500 µm depth for **Ant-PHEA** (F), **Lem-PHEA** (G), and **rhodamine B–dextran** (H) (scale bar: 20 µm). A 3D reconstruction of the cerebral vasculature with **Ant2-PHEA** staining (I), **Ant-PHEA** (J), **Lem-PHEA** (K), and **rhodamine B–dextran** (L) staining (scale bar: 100 µm). Picture taken from reference [84].

reasonable 2PA cross-sections (maximum: 440 GM). As shown in **Figure 1-14**, three different FR/NIR water-soluble probes (λ_{em} = 670–690 nm) have been developed based on this scaffold for two-photon fluorescence imaging (cerebral vascular, membrane, living cell and zebrafish embryo).[80-82]

Very recently, another approach based on ground state symmetry breaking of quadrupolar dyes was also used to shift both 2PA and emission to the NIR range. Introduction of a diyne bridge in the middle of the conjugated backbone of bis-anthracenene derivative **Ant2-PHEA** induces a significant distortion of the ground-state conformation of the symmetrical molecule leading to dramatic alteration of the spectroscopic properties, in particular the emission wavelength and the 2PA cross-sections. This molecule was functionalized with water-solubilizing poly(2-hydroxyethyl)acrylate polymer chains like previously and deep two-photon imaging in living animal was achieved (**Figure 1-15**).[84]

3.3. Organic Nanoparticles

Fluorescent nanoparticles offer an interesting alternative to soluble organic-based fluorophores and have emerged as powerful tools in medicine and *in vivo* imaging.[85-86] Formulation in nanoparticles offers considerable advantages including easy dispersion in water, the possibility for bioconjugation to active targeting or for multimoding by surface modification, and enhanced cell permeability. More importantly, nanoparticles tend to preferentially accumulate at sites of increased vascular permeability, an effect called enhanced permeability and retention effect (EPR) that is considered a major breakthrough in cancer-targeting drug design.[87-88]

Organic nanoparticles combine the pros of inorganic nanoparticles (quantum dots, phosphorescent upconversion nanoparticles or organic modified silica nanoparticles): size, high brightness due to high dye loading, photostability; but without the main drawbacks traditionally associated with inorganic nanoparticles: complicated surface chemistry, concerns about their toxicity or their *in vivo* biodistribution, bio-degradability and clearance.[89-95] In contrast, organic nanoparticles offer all the advantages of soluble organic dyes including low cytotoxicity, synthetic versatility and facile functionalization for specific targeting of soluble organic fluorophores. Many different organic nanoparticles of various sizes can be found associated with diverse preparation methods. Encapsulation in liposomes, peptosomes, polymeric nano-micelles obtained either by direct polymerization of polymerizable organic dyes and reprecipitation, emulsion polymerization techniques or direct grafting of a functionalized fluorophore on the polymer backbone, are the most commonly used techniques enabling the preparation of very bright objects of very small size (from 4-10 nm up to 100 nm in diameters).[96-107]

Owing to the merits of organic nanoparticles, lots of efforts have been dedicated worldwide to obtain organic nanoparticles for *in vivo* imaging, but mostly with fluorescent dyes emitting in the visible, not in the NIR range.[96-102, 104-107] Examples of probes featuring both NIR 2PA and NIR emission are even scarcer. Only a few cases are described. For example, very

recently, a new kind of hybrid fluorescent nanoparticles capable of NIR emission light (λ_{em} = ~730 nm) upon excitation with 800 nm laser light were designed by Huang *et al*. (**Figure 1-16**).[108] In the nanoparticles, a new type of conjugated polymer **P-F8-DPSB** was used as the two-photon light harvesting component and the energy donor while a NIR fluorescent dye, **DPA-PR-PDI**, was used as the energy acceptor and the NIR-light emitting component. The practicability of the hybrid nanoparticles for fluorescence imaging in Hela cells was validated.

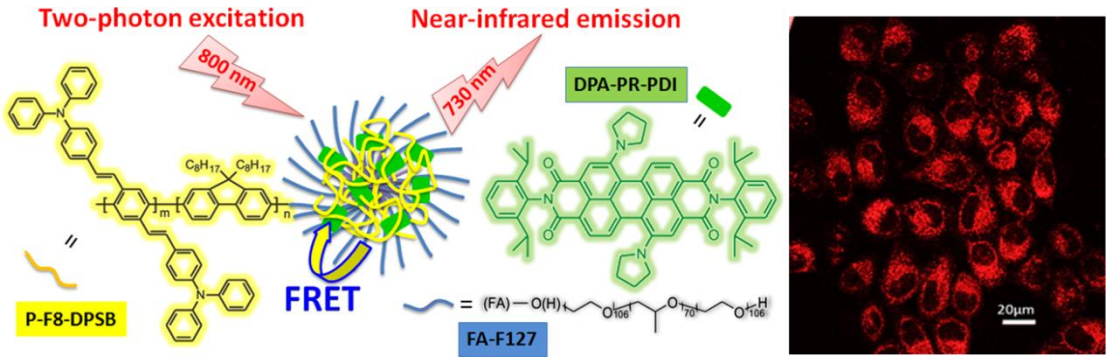

Figure 1-16. (Left) Chemical structures of the conjugated polymer **P-F8-DPSB**, near-infrared fluorescent dye **DPA-PRPDI**, the amphiphilic tri-block polymer with grafted folate moiety FA-F127 used for the construction of the hybrid nanoparticles, and illustration showing the near-infrared fluorescence emission of the nanoparticles upon two-photon excitation using 800 nm pulse laser; (Right) 2PEF image of Hela cells after incubation with hybrid nanoparticles. Pictures taken from reference [109].

The preparation of nanoparticles with conventional dyes often suffers from the aggregation-caused fluorescence quenching (ACQ) effect of dyes. For instance in the case of **ICG**, **IR-820** and other NIR cyanines dyes, aggregation is detrimental to the fluorescence. 80 to 150 nm size serum albumin or hyaluronic acid nanoparticles loaded with **ICG** show enhanced permeability and retention (EPR) effect and selectively stain tumours but are not fluorescent due to quenching. It is only the dissociation of the nanoparticle and the release of the free fluorophore in the tumour that generate back the fluorescence.[110] Only recently several strategies of dye design were proposed to overcome ACQ in nanoparticles: aggregation-induced emission (AIE).[109, 111] The phenomenon and mechanism of AIE effect as well as preparation of nanoparticles with AIE dyes will be described in details in **Chapter 3**.

4. Objectives of This Thesis

As reviewed above, 2PEM enables excitation of chromophores in the NIR region and shows obvious advantages over conventional one-photon excited fluorescence imaging techniques, such as deeper penetration depth, high spatial resolution, reduced photoinduced damage and lower autofluorescence, making it particularly useful for biological imaging. Additionally, chromophores displaying far-red and NIR emission could also minimize background interference, improve tissue depth penetration, image sensitively and

noninvasively. Among present probes, however, examples of probes combining both NIR 2PA and NIR 2PEF applied to bio-imaging are still rare. In this regards, the objective of this thesis was to develop NIR luminescent chromophores and nanoparticles for two-photon luminescence bio-imaging.

The first part of this dissertation is to fabricate two-photon absorbing Pd-porphyrin probes for the *in vivo* monitoring of oxygen pressure by two-photon microscopy. Palladium (Pd) porphyrin complexes are known as popular oxygen sensors. Their characteristic NIR phosphorescence was shown to be highly sensitive to the concentration of dissolved oxygen but not upon the nature of the environment. However, they are hard to be used for two-photon microscopy because of the extremely low 2PA cross-sections. To solve this problem, we intend to first synthesize a series of new two-photon absorbing chromophores (antennae), and then study their optical properties. The optimum antenna will be grafted to the Pd-porphyrin to enhance their two-photon activity through FRET effect.

The main research direction in our laboratory is to design and synthesize small push-pull chromophores for solid-state emitters and bio-imaging probes. In the second part of my work, on the basis of previous work, a new series of linear, asymmetrical fluorene-based chromophores with various strong π-electron donors and acceptors were designed. The fluorenyl ring is mainly used to increase 2PA properties of chromophores, and also to enrich their other optical properties in solution. In these chromophores, electron-donor groups and electron-acceptor groups with different strengths were proposed to tune their two-photon excitation and emission wavelengths to the NIR region. By using the synthesized chromophores, several different kinds of far red/NIR fluorescent nanoparticles will be constructed for two-photon fluorescence bio-imaging.

Chapter 2. Design of Two-Photon Absorbing Probes for the *in vivo* Monitoring of Oxygen Pressure

In this chapter, two new two-photon absorbing (2PA) oxygen sensors will be designed based on Förster Resonance Energy Transfer (FRET) strategy by grafting the two-photon chromophores to a palladium porphyrin complex core. To find a suitable 2PA chromophore for our system, a series of fluorene-based 2PA chromophores will be designed and synthesized. Then the optimum chromophore will be grafted to the palladium porphyrin complex through an efficient Cu(I) catalyzed click reaction. The optical properties of 2PA chromophores and 2PA oxygen sensors will be studied. The oxygen sensing property will be also evaluated for the synthesized 2PA oxygen sensors.

1. Introduction

1.1. Oxygen Sensing *in vivo*

Molecular oxygen concentration is of paramount importance for many vital physiological processes and is a key factor for cell and organ survival. In mammals, oxygen is transported by circulating red blood cells in a well-organized vasculature. In normal condition, partial oxygen pressure pO_2, also called *physioxia*, results from the balance between oxygen delivery and its consumption by the organ. O_2 levels in different tissues and cells of our body normally range 0.5–10%, but the partial oxygen pressure varies widely depending on the metabolic requirements or the functional status of each organ or tissue. For instance O_2 level is at highest in the lungs from which O_2 is supplied to other tissues. Normal homeostatic conditions *in vivo* are called *normoxia*. Any variation in the oxygen pressure and in particular decrease of oxygen pressure can be sign of pathological states and alteration of tissue environment. *Hyperoxia* describe high level of oxygen (above 21%), whereas *Hypoxia*, on the contrary, designs a condition of low oxygen tension, typically in the range 1–5% O_2.[112] Hypoxic conditions have been observed in many different pathological situations where it is considered to underlie the inflammatory response, like obesity,[113] coronary heart disease and stroke,[114-115] brain abnormality,[116] or transcient ischemia,[117] etc... Above all, hypoxia is one of a characteristic pathophysiological property of advanced solid tumours (**Figure 2-1**).[118-119] A gradient decrease in oxygen concentration with increasing distance from tumour blood vessels can be observed, and due to the poor vascularisation, the median oxygen (O_2) concentration in some solid tumours is around 4% and may even decrease to 0% locally.[120] As a consequence, assessing tissue oxygenation in real-time is fundamental as it can not only lead to accurate

diagnosis of cancer, but can also be used to evaluate specific therapeutic effects. In particular, in order to better understand the biochemical mechanisms of hypoxia tolerance, methods for low oxygen concentration measurements in tumour in real time are required.[112, 121]

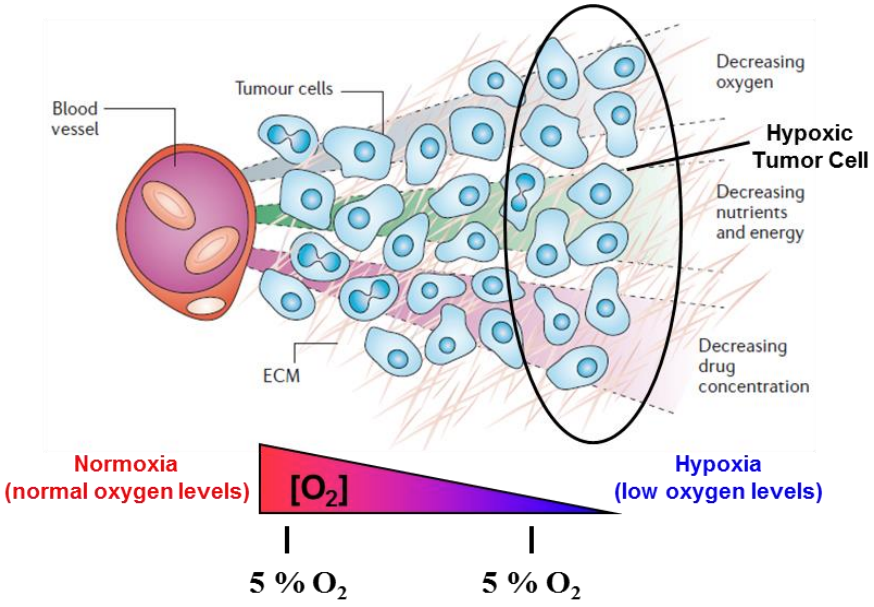

Figure 2-1. Diagrammatical representation of part of a tumour showing a gradient decrease in oxygen level with increasing distance from blood vessels.

To date, many methods have been proposed for mapping *in vivo* oxygen concentration. Indirect methods include immunohistochemical or mass spectrometric detection of hypoxia markers associated with histology. Direct imaging mapping techniques embrace positron emission tomography (PET) or positron emission tomography–computed tomography (PET/CT) with hypoxia-targeted radioactive agent **^{18}F-fluoroisonidazole** or **Copper(II)-diacetyl-bis(N4-methylthiosemicarbazone)**; near-infrared spectroscopy (range 700–1000 nm) applies to changes in the amount of oxygen bound to hemoglobin in blood; ^{19}F MRI after intravenous injection of perfluorocarbon (PFC) probes; or blood oxygen level-dependent MRI reflecting the changes in the amount of oxygen bound to hemoglobin and the blood content of paramagnetic deoxyhemoglobin compared to diamagnetic oxyhemoglobin.[112, 122-125] These techniques are especially described in cancer studies, given the importance of hypoxia. They give valuable information on overall oxygen consumption, changes in blood oxygenation, vascular oxygenation and show hypoxic area, but are very limited as far as direct pO_2 evaluation is concerned and they do not provide absolute oxygen concentration in tissue, nor comprehensive picture of oxygen status.

1.2. Oxygen Sensing Based on Phosphorescence Quenching

In that prospect, optical techniques based on sensors whose optical response is modulated by the presence of oxygen seem very promising. Unlike polarographic sensing that used

oxygen electrodes, optical processes do not consume oxygen but solely relies on the amount of oxygen present. Use of fluorescence is not adapted to determine oxygen concentrations because of the low sensitivity to oxygen. In addition, experiment based on fluorescence intensity variation is prone to artefact due to probes concentration or changes in the environment (adsorption to protein, aggregation, changes in turbidity…).

Quenched-phosphorescence oxygen detection, on the other hand, relies on the ability of molecular oxygen to efficiently quench the emission of excited triplet state molecules *via* a direct process of collisional quenching. The overall process is described by the Jablonski-Perrin diagram in **Figure 2-2**. Absorption of photons populates the fluorophore excited states that quickly relaxed to the excited triplet state T_1 through internal conversion (IC) and intersystem crossing (ISC) processes. The generated triplet state T_1 releases energy by either emitting phosphorescence or by passing it onto a quencher molecule such as oxygen through collisional interaction. The latter is consequently promoted to its' excited state $^1\Delta_g$ O_2. As a result, phosphorescence from the excited triplet state T_1 undergoes quenching in the presence of oxygen molecules, which reduce the yield and lifetime of the phosphorescence in a concentration-dependent manner. In biological systems phosphorescence quenching is highly specific to oxygen, since oxygen is the only small-molecule dynamic quencher present in sufficiently high concentration.

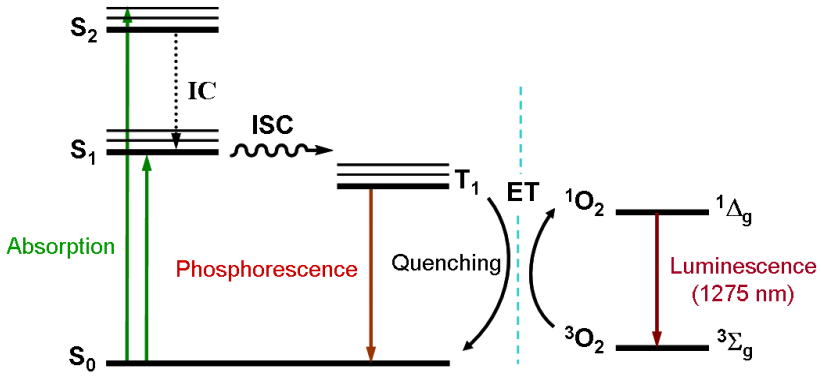

Figure 2-2. Jablonski diagram showing the main energy transitions during the process of phosphorescence quenching by O_2. [S_0, S_1, S_2–ground state, first and second excited singlet states of the indicator, and T_1 – its excited triplet state. IC–internal conversion; ISC–intersystem crossing; ET–energy transfer.]

The relation between quenched intensity or lifetime and the oxygen concentration is described by the classical Stern-Volmer equations:

$$\frac{I_0}{I} = \frac{\tau_0}{\tau} = 1 + K_{SV}[O_2] = 1 + \mathrm{k}_q \tau_0 [O_2] \qquad (2\text{-}1)$$

in which I and τ are the phosphorescence intensity and lifetime at a specified oxygen concentration [O_2], I_0 and τ_0 are the phosphorescence intensity and lifetime in the absence of oxygen, K_{SV} is the Stern-Volmer quenching constant, k_q is the bimolecular quenching constant.[126-128] Alternative equations can also be found that expressed lifetime and intensity

as a function of pressure of dissolved oxygen pO_2.

Since O_2 phosphorescence imaging can be performed either through intensity- or lifetime-based measurements, this technique is very sensitive. One of the first *in vivo* measurement of oxygen distribution in perfused tissue using intensity-based phosphorescence imaging (palladium coproporphrin) was reported in 1988 by the groups of Wilson.[129] Lifetime imaging techniques were set up in the early 1990s using either time-domain (pulsed)[130] or frequency-domain (phase-resolved) phosphorescene lifetime measurement.[131] Lifetime imaging presents the major advantage of not depending on intensity variation that can derive from photobleaching or variable probe concentrations.[132] As presented in the previous chapter, measurements in animal tissue and highly scattering media call for indicators that are excitable and are emitting in the red and very-near infrared spectral region (600–900 nm). As succinctly described in **Chapter 1**, various oxygen sensitive photoluminescent chromophores have been developed these last 30 years or so as oxygen sensors giving rise to substantial literature. The next section will provide a survey of the literature, with emphasis on compounds that have found direct application in *in vivo* oxygen sensing.

1.3. Oxygen sensitive phosphorescent probes

1.3.1. Organic Compounds and Ruthenium(II) Complexes

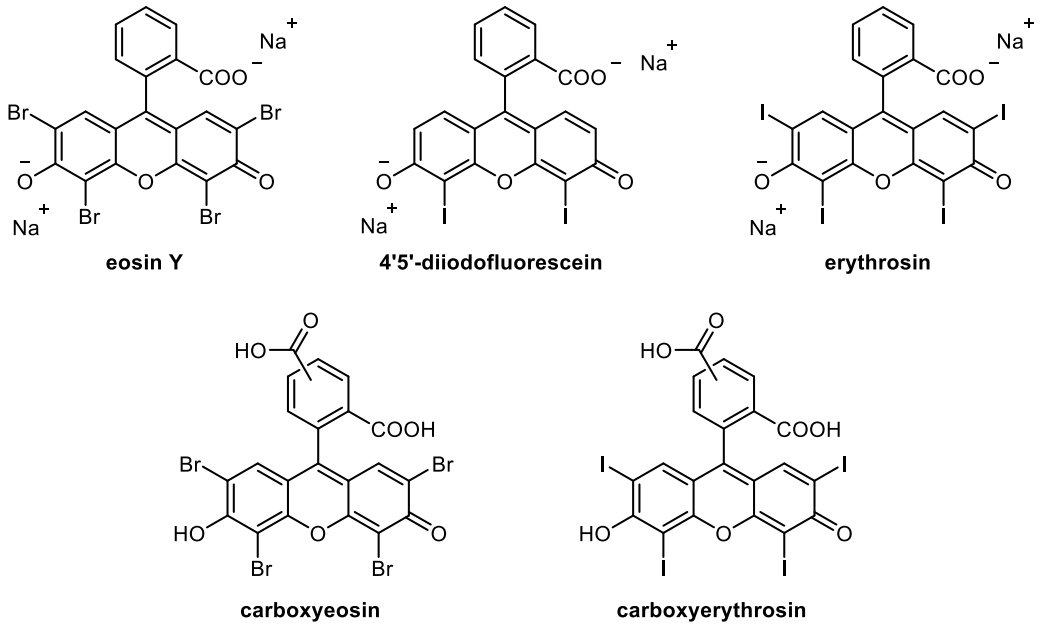

Figure 2-3. Type II photosensitizers: **eosin Y**, **4'5'-diiodofluorescein**, **erythrosin**, **carboxyeosin**, and **carboxyerythrosin**.

Organic phosphorescent compound such as **eosin Y**, **4'5'-diiodofluorescein**, **erythrosin**, **carboxyeosin**, and **carboxyerythrosin** (**Figure 2-3**) can be employed,[128] but phosphorescent

metal complexes with a long-lived triplet excited state have attracted the most interest in this field. Phosphorescence intensity and lifetime of these complexes are reversibly dependent on the change in O_2 concentration enabling fully reversible real-time monitoring of O_2 levels *in-vitro* and *in vivo* with high-resolution.

Ru(II) complexes with diimine ligands such as **2,2'-bipyridine**, **1,10-phenanthroline** and **4,7-diphenyl-1,10-phenanthroline** ligands [126, 133] (**Figure 2-4**) emit red phosphorescence at room temperature following excitation in the MLCT band. However, with absorption maxima in the range 440-480 nm, they can only be excited by halogen lamps or blue LEDs. Expanding the π-conjugating system of the ligand using 2,2'-bisquinoline for instance, red-shift the excitation (570 nm).[134] The phosphorescence lifetimes are rather short (0.1−5 µs) resulting in a much lower O_2 sensitivity than other metallic compounds. As a consequence, they have seldom been used for direct *in vivo* oxygen imaging, but rather in the development of oxygen-sensitive materials and solid-state optical sensors and devices.[135-136]

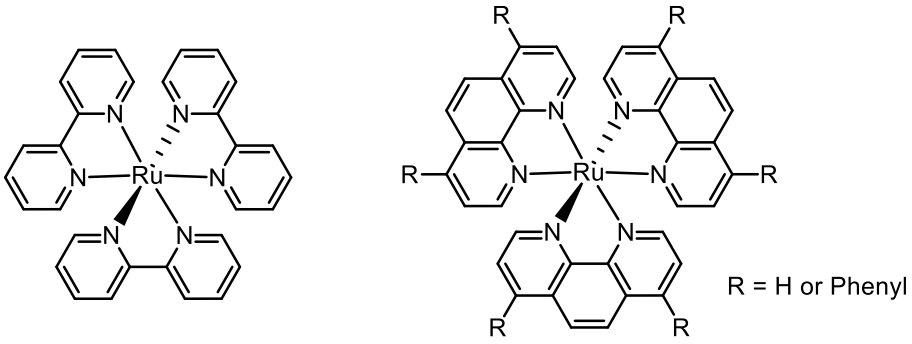

Figure 2-4. Chemical structures of representative Ru(II) complexes for use in oxygen sensing.

Same can be said about Os(II) complexes such as **Os(Ph$_2$phen)$_2^{2+}$** or **Os(2,2',2"-terpyridine)$_2^{2+}$**. Although, unlike their Ru(II) analogues, Os(II) complexes can be excited by readily available, high-intensity, low-cost, red diode lasers at 635, 650 and 670 nm, they display much poorer sensitivity.[137] Fluorescence lifetime measurement using phase fluorimetry in transcutaneous oxygen sensing was nevertheless reported.[138]

1.3.2. Iridium(III) Complexes

Ir(III) complexes and in particular cyclometalated Ir(III) complexes display ultrafast (faster than 100 fs) intersystem crossing from the singlet MLCT state to the triplet MLCT state (^{3}MLCT) facilitated by the electronic contribution of the Iridium atom. Consequently, high quantum yield room-temperature phosphorescence with moderately long lifetimes (1−15 µs) is produced.[139] The phosphorescence of iridium can easily be tuned and extended to the near-infrared region by modification of the ligand.[140] The large Stokes shifts associated with the phosphorescence and the exceptional photochemical and physicochemical stabilities are additional advantages of these complexes, that why they gained ever increasing interests in the field of oxygen sensors (for *in vivo* application in particular) these last years.[141-142]

The first example of use of Ir(III) complexes for intracellular and *in vivo* oxygen sensing was reported by Takeuchi and Tobita in 2010. Deep-red (λ_{em} = 616 nm, τ = 5.8 µs in absence of oxygen) **Ir(btp)$_2$(acac)** or **BTP** (for [bis(2-(2′-benzothienyl)-pyridinato-N,C$^{3'}$]iridium(III), **Figure 2-5**) was used for the determination of hypoxia in the margin of tumours. Extension of the π-electronic system (in **BTPH** or **BTPHSA**, **Figure 2-5**) shifts the phosphorescence maximum to 720 nm without decreasing the quantum yield too much (0.24 against 0.30 for **BTP**) or changing the oxygen sensing properties. Brighter phosphorescence was observed under hypoxic conditions (5% O_2) than under normoxic conditions (20% O_2) in cells and in mice bearing tumour.[143] **Ir(btp)$_2$(acac)** is turn-on probe only. Ratiometric version was reported by the same authors (**C343-Pro$_4$-BTP**, **Figure 2-5**) consisting of a blue fluorescent coumarin and a red phosphorescent cationic iridium complex connected polyproline linker together with successful oxygen levels in living cells.[144] Despite some energy transfer from the coumarin343 moiety to the Ir(III) core, remaining fluorescence was observable and served as a reference signal. Modifying the auxiliary acetylacetonato ligand enables different bio-distribution. For instance, introduction of cationic dimethylamino group (compound **BTPDM1**, **Figure 2-5**) resulted in an almost 20-fold increase in cellular uptake efficiency by HeLa cells compared with **BTP** [145] and enable quantification of oxygen tension in mice kidneys.[146]

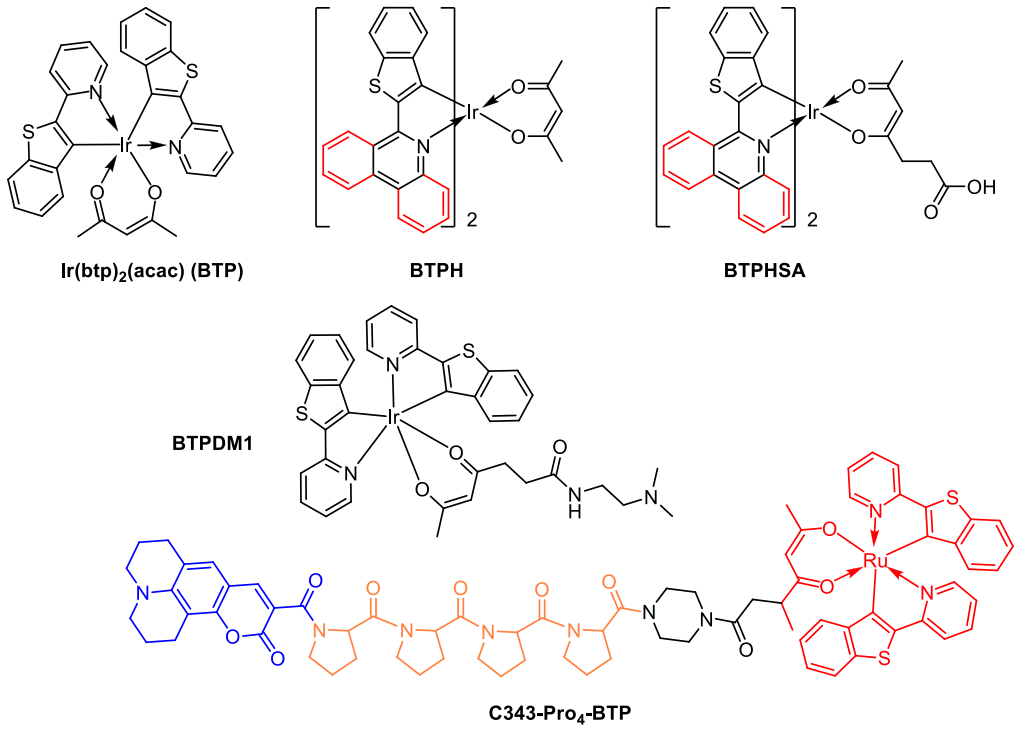

Figure 2-5. Oxygen sensitive phosphorescent Ir(III) complexes based on 2-(2′-benzothienyl)-pyridine (btp).

To improve water solubility of **BTP** and prolong the *in vivo* circulation time, polymeric derivatives (poly(*n*-butyl cyanoacrylate, (**(btp)$_2$Ir(PBCA)**, **Figure 2-6**) were synthesized and coated with chitosan. The core-shell nanoparticles produced (size 93 nm) significantly

reduced the toxicity of **BTP**. Hypoxia imaging in mice were performed revealing enhanced emission as compared to the isolated fluorophore.[147]

Very recently, another water-soluble macromolecular probe was reported based on **BTPHSA** analogue conjugated to poly-*N*-vinylpyrrolidone (PVP), **Ir-PVP** fluorophore on **Figure 2-6**. NIR *in vivo* O_2-sensing (λ_{em} = 720 nm, quantum yield 0.15) was performed showing ultrasensive detection. Continuous imaging in mice, in which small number of cancer cells was subcutaneously implanted, revealed that the probe can detect small amount of cancer cells at a very early stage of tumour development.[148] Incorporation of a rhodamine or cyanine fluorophore also enable ratiometric measurement with phosphorescence intensity ratio of in oxygen-free to oxygen-saturated as high as 62. Furthermore, the same authors reported the formation of co-micelles based on **Ir-PVP** and poly(ε-caprolactone)-*b*-poly(*N*-vinylpyrrolidone) polymer (**PCL-PVP**, **Figure 2-6**) to obtain O_2 sensitive probe that could not only detect primary tumours, but was also sufficiently sensitive to detect lymph node (important organs for the proper functioning of the immune system) metastasis after systemic injection into mice.[149]

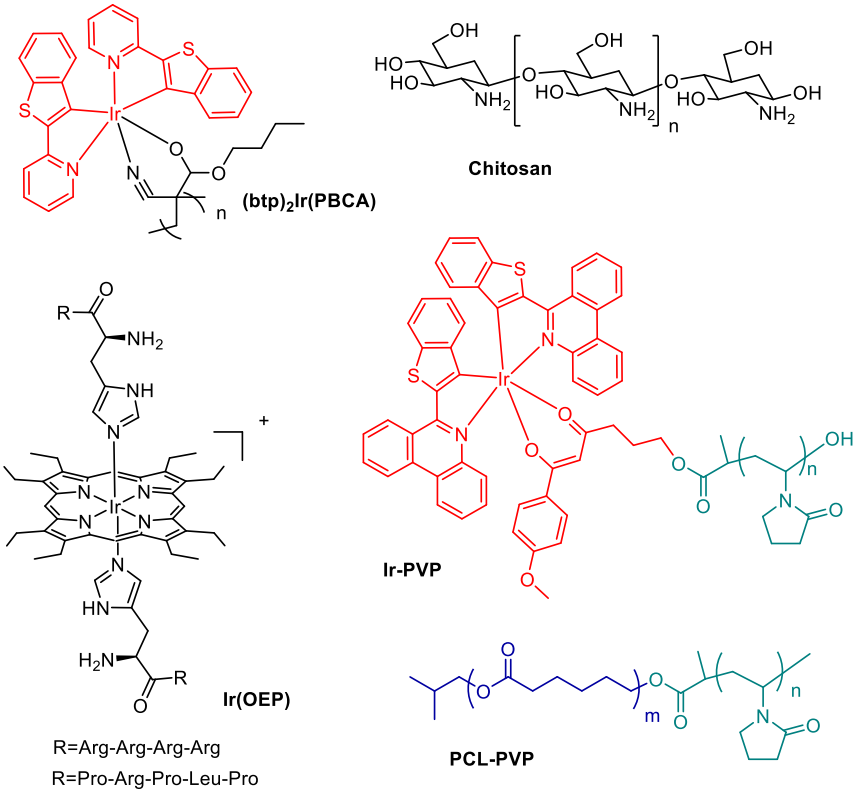

Figure 2-6. The water-soluble macromolecular oxygen sensitive probes.

All the previous examples illustrate the limited design in this field as all the structures are turning around the same basic skeleton **BTP**. Further expansion will be much needed in order to further shift the emission to higher wavelength or use two-photon absorption microscopy (see next paragraph) for which these compounds have not been designed. One of the very few

examples of non **BTP** based Ir(III) probe is **Ir(OEP)** (**OEP** designing **octaethylporphyrin**, **Figure 2-6**) that was coupled to peptide for enhanced cellular uptake. The high quantum yield of phosphorescence and the deep-red emission (λ_{em} = 655 nm, quantum yield 0.13-0.16) enable efficient intracellular O_2 sensing.[150]

Very recently, Chao and co-workers reported a new series of reductase-reactive phosphorescent ("off-on") oxygen probes for hypoxia detection in three-dimensional multicellular spheroid models[151] or for mitochondria imaging and tracking under hypoxia.[152] The iridium(III) complexes incorporate an azo or anthraquinone group as an reductase reactive moiety to detect hypoxia (**Figure 2-7**). Reduction of non-phosphorescent probes by reductases under hypoxic conditions resulted in the generation of highly phosphorescent corresponding molecules for detection of hypoxic regions. Moreover, these probes can penetrate into 3D multicellular spheroids over 100 μm and image the hypoxic regions. Most importantly, these probes display a high selectivity for the detection of hypoxia in 2D cells and 3D multicellular spheroids.

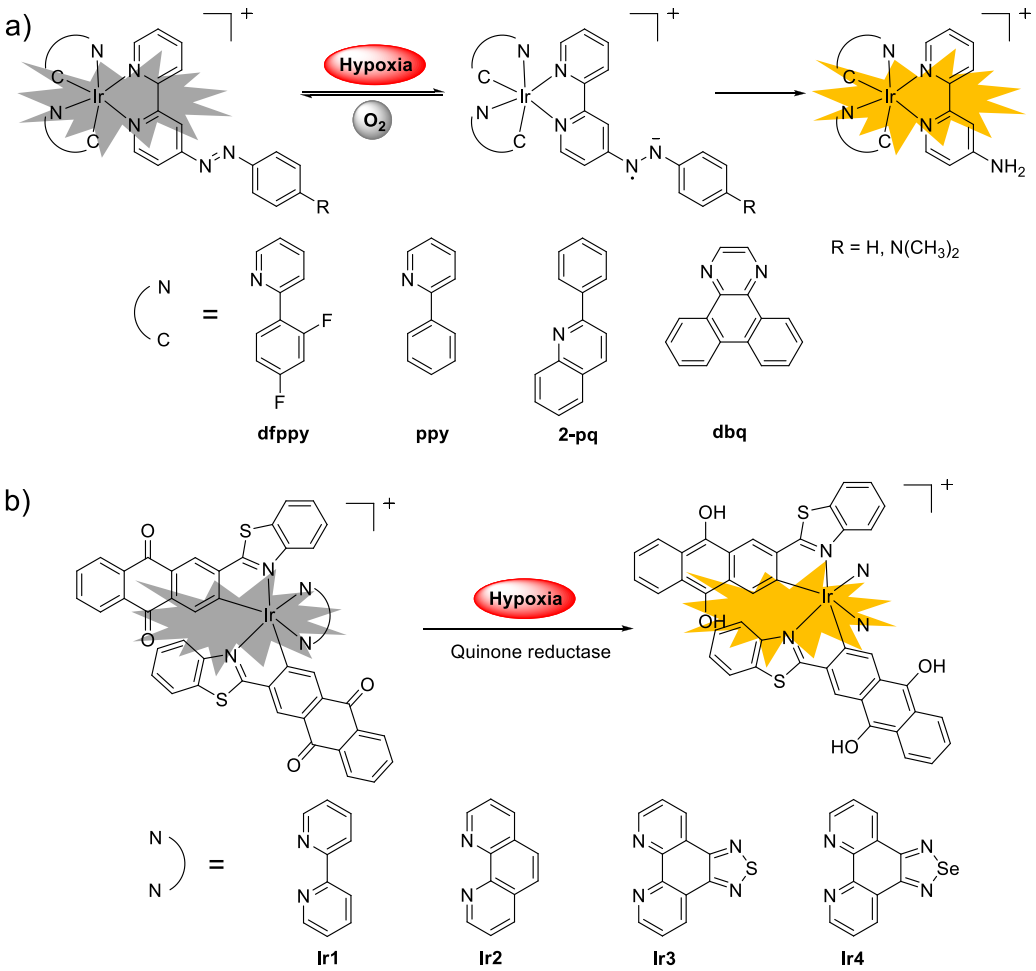

Figure 2-7. Reductase-reactive phosphorescent oxygen probes based on Ir(III) complexes and detection mechanism.

1.3.3. Porphyrin Complexes (Palladium and Platinum)

Relatively long phosphorescence lifetimes (10−1000 µs), intense deep-red phosphorescence (platinum *meso*-tetra(4-methoxycarbonylphenyl)porphyrin, **Pt(TMCPP)** in **Figure 2-8** displays phosphorescence with λ_{em} = 668 nm and quantum yield Φ_p = 7.5%) and favourable photostability make Pt(II)- and Pd(II)-porphyrin derivatives particularly attractive for O_2 sensing. These compounds are probably the most suited for *in vivo* oxygen imaging as they permit measurements of very low O_2 concentrations and of small O_2 level variation such as those encountered in biological systems. As a consequence, they have been the most studied for the design of O_2 sensing devices and for O_2 imaging.[153-155]

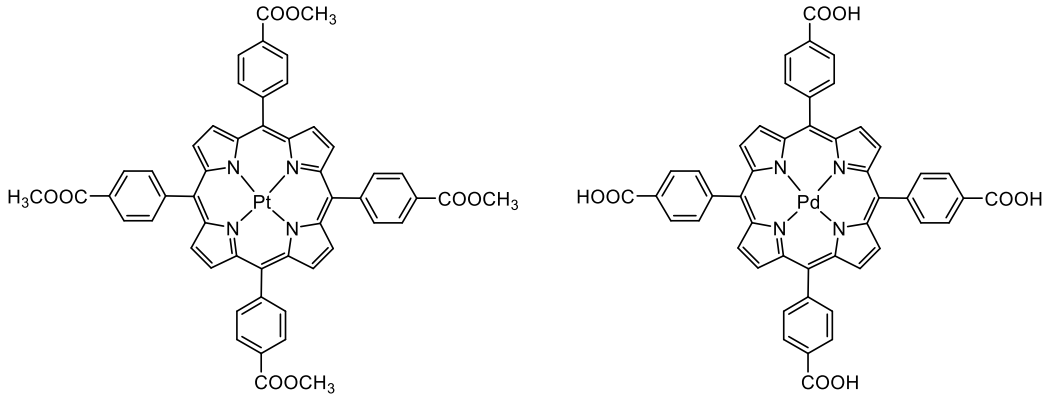

Figure 2-8. Molecular structures of **Pt(TMCPP)** and **Pd(TCPP)**.

However, simple water soluble derivatives of tetraphenylporphyrine, such as Pd-*meso*-tetra-(4-carboxyphenyl)-porphine (**Pd(TCPP)**) (**Figure 2-8**), showed limited interest for *in vivo* application as it is necessary to bind the dye to albumin in order to limit its diffusion out of the vascular system, to restrict the dye to the circulation and to prevent aggregation. Foreign albumin is a potential source of toxicity and immunogenic responses. Nevertheless, oxygen sensitive albumin-bound **Pd(TCPP)** was successfully used in high-resolution two-dimensional mapping of the oxygen pressure in the cortex of cat brain,[156] to measure interstitial pO_2 [157] or to continuously monitor the pO_2 in the blood of the cerebral cortex of newborn pigs.[158]

Modifications of the phosphorescent core allow tuning the spectral characteristics and introducing variable degrees of quenching leading to higher selectivity for oxygen. In particular, π-extension of the core macrocycle, for instance by annealing of their pyrrole residues with external aromatic rings (**Figure 2-9**) induces considerable red-shift of the absorption and emission (up to 1022 nm for **Pt-Ar$_4$TAP**). Introduction of fluorine atoms enhances the photostabilty and the phosphorescence quantum yield, all parameters that are important to meet the requirements for particular imaging application.[159-165] **Pt(PFPP)** (Mesotetrakis(pentafluorophenyl)porphyrinato]platinum(II), **Figure 2-10**) is probably the most commonly used oxygen sensitive phosphor. However, due to accrued hydrophobicity, aggregation in aqueous solutions cannot be avoided.[166] Click-modification of perfluorinated

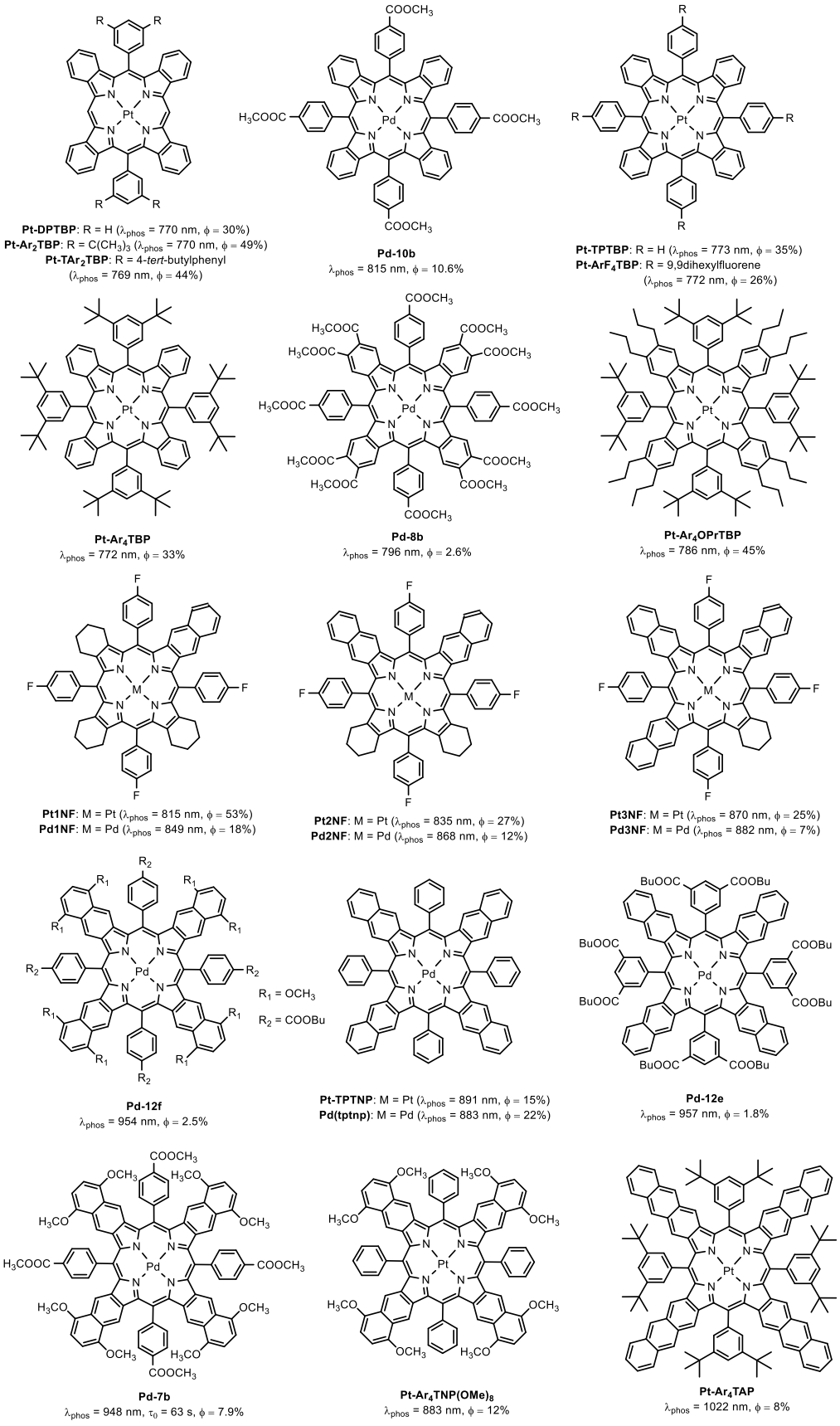

Figure 2-9. Extended porphyrins for red-shifting the phosphorescence.

porphyrins enables substitution of up to four *para*-fluorine atoms with thiols. Thio-sugar or thio-peptide modified **Pt(PFPP)** dyes were recently reported, together with their evaluation in high-resolution phosphorescence lifetime based O_2 imaging in multi-cellular spheroids of cancer cells (3D tissue models), primary neural cells and slices of brain tissue. Their performances strongly depend on their structure.[167]

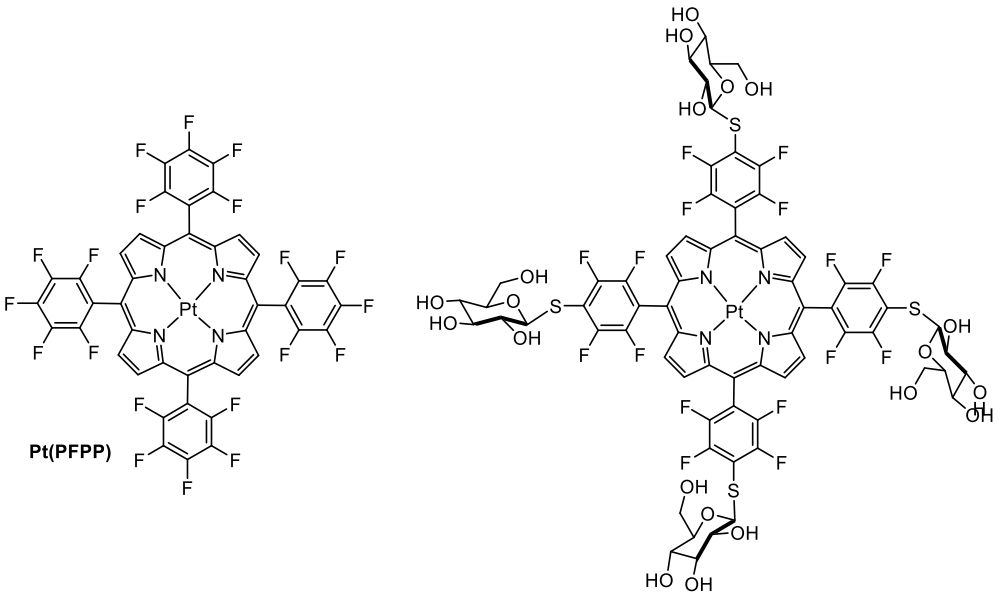

Figure 2-10. Commonly used oxygen sensors based on **Pt(PFPP)**.

1.3.4. Dendritic and Ratiometric Oxygen Probes

Incorporation of the phosphorescent porphyrin core into a dendritic shell, especially polyglutamic dendrimers composed of L-glutamate moieties represented a major breakthrough in the design of O_2 phosphorescent probes (**Oxyphor™ R2**, **Oxyphor™ G2**, **Figure 2-11**). The polyglutamic dendritic structure not only provides intrinsic aqueous solubility, eliminating the necessity of prebinding porphyrins to albumin, but also create diffusion barrier for oxygen,[168-169] making it possible to regulate the sensitivity and the dynamic range of the method.[170-171] However, when in the blood, theses dendrimeric structures further complexe with endogeneous albumin, limiting their use to to albumin-rich environments, such as blood plasma. Encapsulation in hydrophobic dendrimer, such as arylglycine, combined with PEGylation of the periphery to restore the water solubility circumvent this issue (**Oxyphor G3**, **Oxyphor R4** and **Oxyphor G4**, **Figure 2-11**).[172-173] Phosphorescent O_2 sensitive **Oxyphor™ R2** and **Oxyphor™ G2** are commercialized by OxygenEnterprise, Ltd. They were used for intravital oxygen imaging to study cerebral vasculature, neuronal activity,[174] tumour oxygenation,[175] microcirculation,[176] muscle physiology [177] and so on.[155]

For intensity-based experiments, probes offering a ratiometric response (*i.e.*, ratio of emission intensity at different wavelength) may sometime be advantageous especially as the ratio will not depend on the concentration of the probes. Ratiometric responses also eliminate

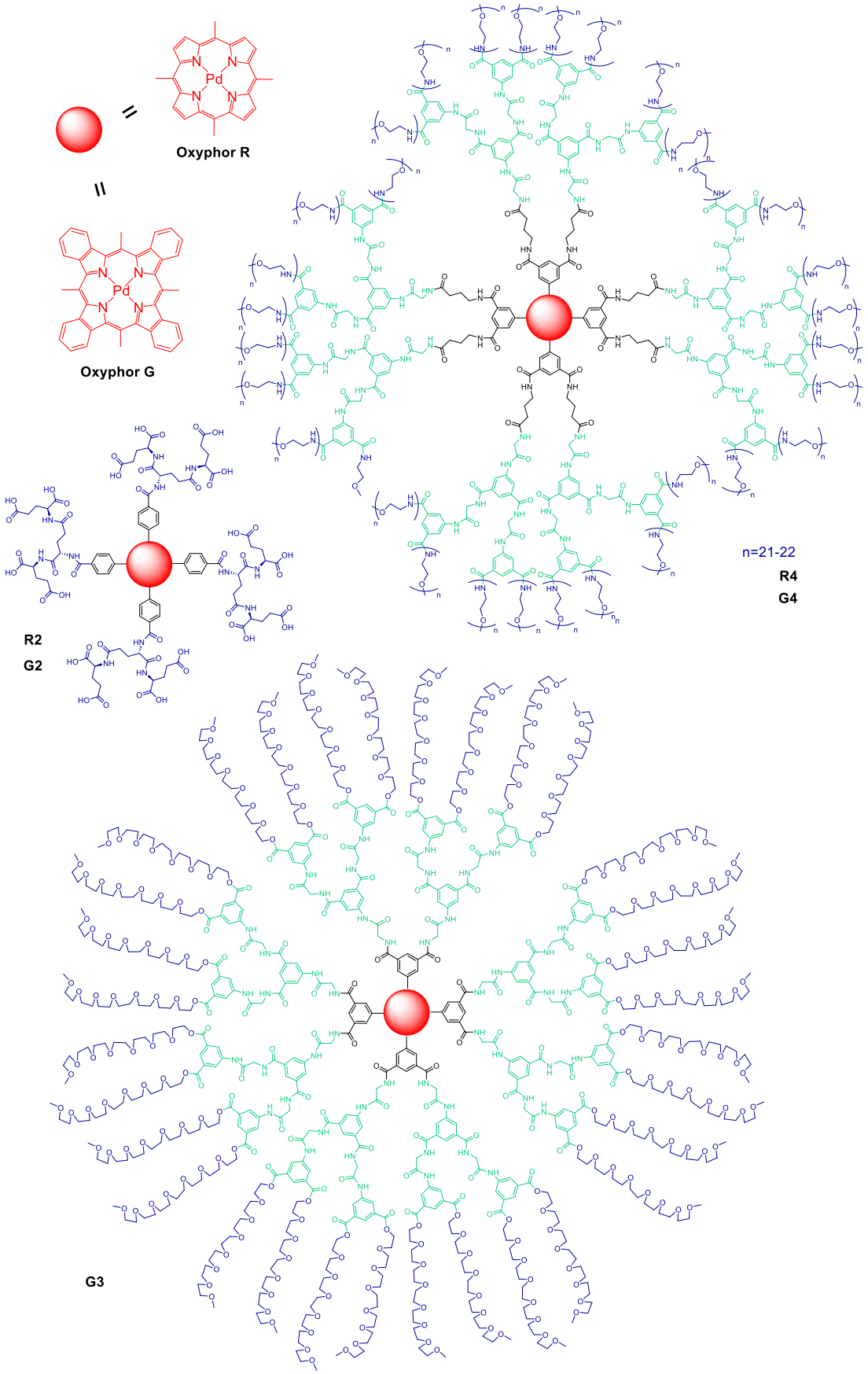

Figure 2-11. Some dendritic oxygen sensors.

troubleshooting due to photobleaching or excitation power fluctuation. Small size polymer-based nanoparticles (P-dots) have been proposed, in which a phosphorescent O_2 sensitive core (usually one of the previous transition-metal complex) and a fluorescent part are added to a polymer. Relative intensities of fluorescence and phosphorescence are tuned by modifying the composition of the phosphorescent core and fluorescent part (**Figure 2-12**). The fluorescent part can be the polymer itself as it is the case for polyfluorenes (**PFO**).

Oxygen sensitive P-dots were thus used for *in vitro* O_2 sensing in adherent cells and neurospheres representing 2D and 3D respiring objects, to monitor the metabolic responses of mouse embryonic fibroblast cells under ambient and hypoxic macroenvironment, and *in vivo* for imaging of tumour hypoxia in nude mice (**Figure 2-12**).[178-183] Polyfluorene displaying remarkable two-photon absorption properties, P-dots show very promising for two-photon microscopy. Finally, ultra-small silica-pluronic nanoparticles as the one developed in **Chapter 4** were reported by Wolfbes and Wang, in which oxygen-sensitive phosphorescent **Pt(TBTBP)** was encapsulated together with **TFPP** as the fluorescent part. **Fluorescein isothiocyanate** was further grafted on the periphery of the particle. As the fluorescen of fluorescein is pH sensitive, this creates a dual pH/Oxygen. The small molecule of oxygen can freely diffuse in and out of the particles that are then truly oxygen sensitive. Unfortunately, only cellular measures were reported, but this system is particularly interesting and worth more consideration (see **Chapter 4**).[184]

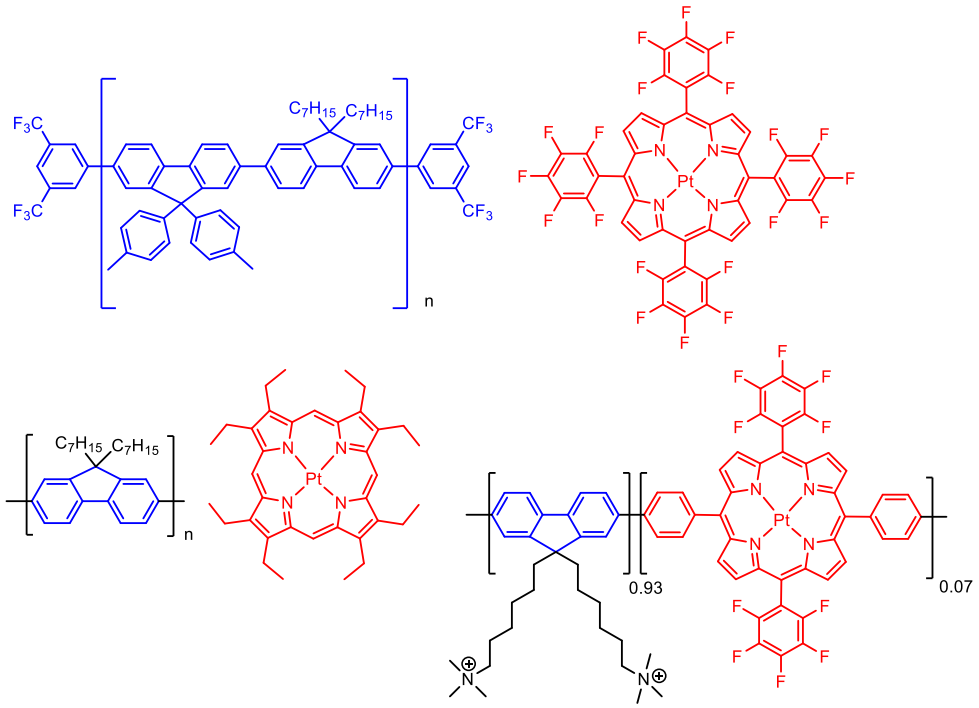

Figure 2-12. Chemical structures of some polyfluorenes (**PFO**)-based nanoparticles (P-dots) for *in vivo* oxygen sensing.

1.4. Two-photon absorbing oxygen probes

We have exposed in **Chapter 1** the advantages provided by two-photon microscopy combined to NIR emission over linear methods, especially for high resolution in depth 3D imaging. In this regard, the coupling of phosphorescence quenching with two-photon microscopy is favored because two-photon excitation, which is characterized by a high degree of spatial confinement and a reduced risk of photodamage, should allow pO_2 measurements deeper in the tumour with high resolution. However, classical phosphorescent probes, typically those based on simple Pt- or Pd-porphyrins, are characterized by extremely low two-photon absorption cross-section (in the order of just a few GM units),[185-186] making them unsuited for practical application given the exceedingly high excitation powers it would require. To give an idea, Ince *et al.* indicate that producing detectable phosphorescence signals with **Pd(TCPP)** is only possible with high excitation powers (0.1–1.0 W) and high probe concentration (0.5 mM) using 10 ns pulses at 1064 nm and at a 10 Hz repetition rate.[187] It is therefore necessary to improve the two-photon absorption cross-section of oxygen-sensitive phosphorescent probes and two approaches were proposed for that.

The most obvious one consists in extending the conjugation of the porphyrin macrocycle as described (**Figure 2-13**) or appropriately substituting by strong electron withdrawing groups. The 2PA cross-section of porphyrin can be improved to some extent, but little information is available on the influence of the phosphorescence properties.[185, 188] Also, as the electronic system is considerably modified, this leads to a dramatic red-shift of not only the emission but also the excitation maximum and the two-photon absorption range out of the window of interest for microscopy (range 800-1000 nm corresponding to the optimum of the first transparency window). Porphryine compounds with extensive π-extended system are also much less photostable and prone to oxidation [159, 165] and still cannot meet the requirement for its practical applications.

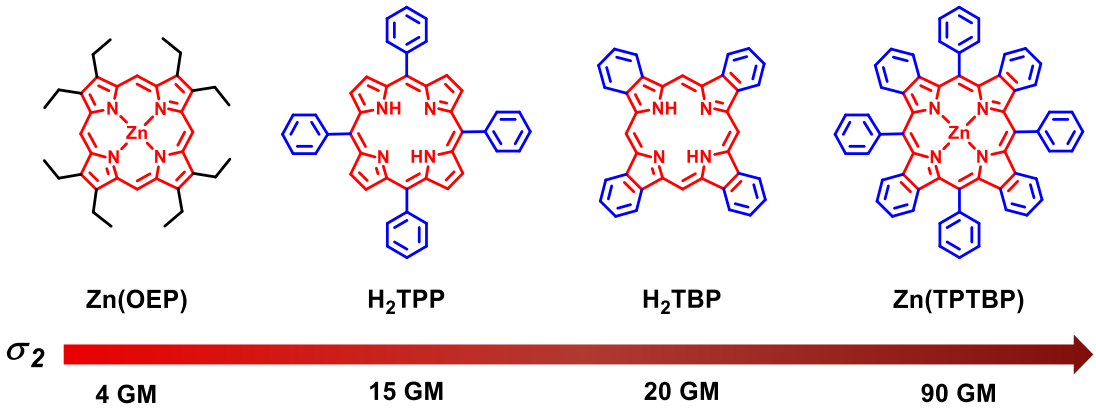

Figure 2-13. Optimization of 2PA cross-section of porphyrin by modification.

The second approach to amplify the two-photon absorption cross sections of the system, while leaving porphyrins electronic systems intact, is to couple them to suitable two-photon absorbers that act as light harvesting antennae and energy donor through nonradiative

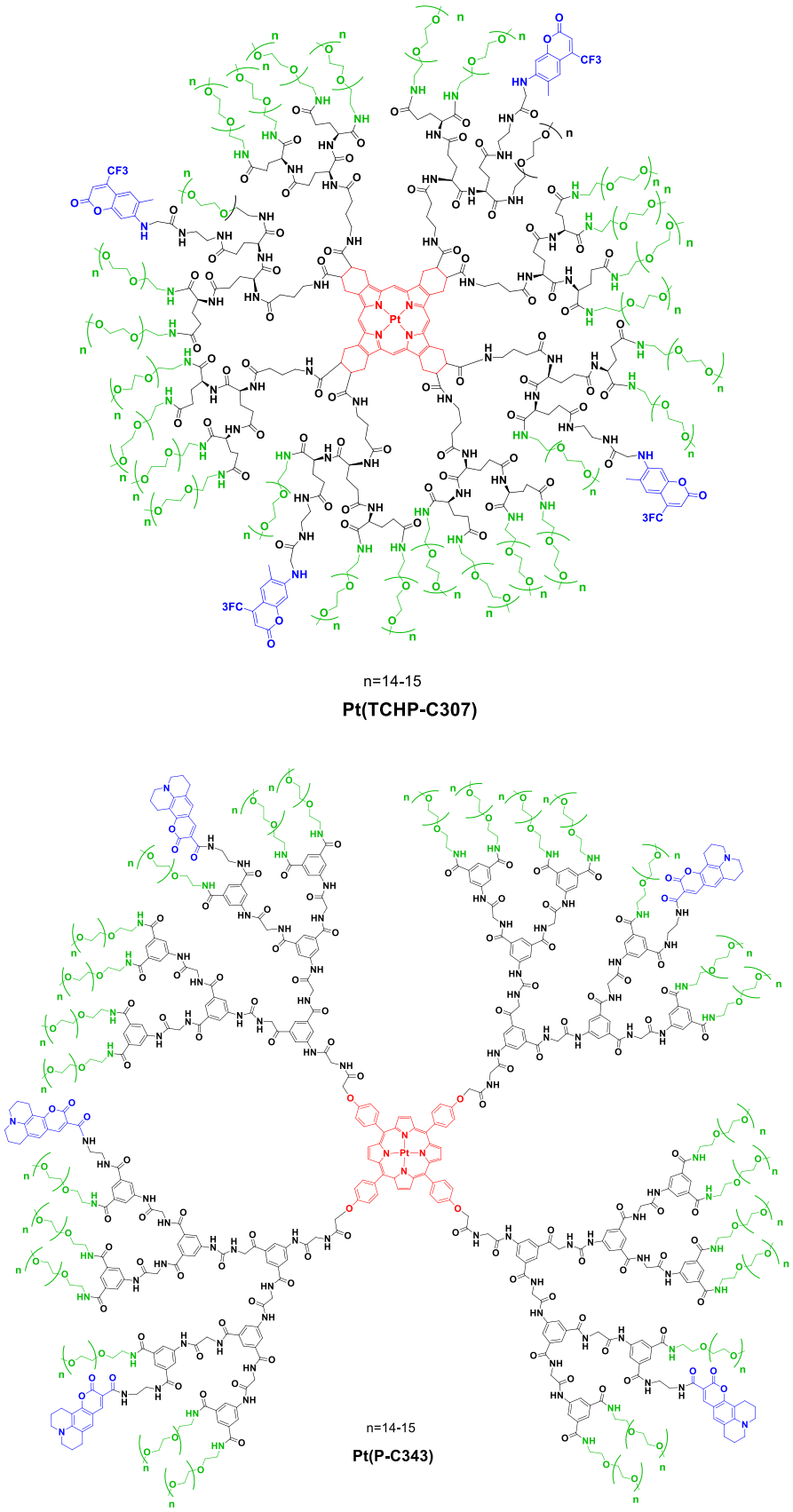

Figure 2-14. Two-photon FRET systems based on porphyrin.

dipole–dipole coupling in a Förster Resonance Energy Transfer process (FRET). After two-photon absorption of donor chromophores, energy transfer from the donor excited state to the acceptor porphyrin or Pd- or Pt-porphyrin (**Figure 2-14** and **Figure 2-15**) leads to intersystem crossing and interaction with oxygen. The phenomenon is also sometimes called "antenna effect".

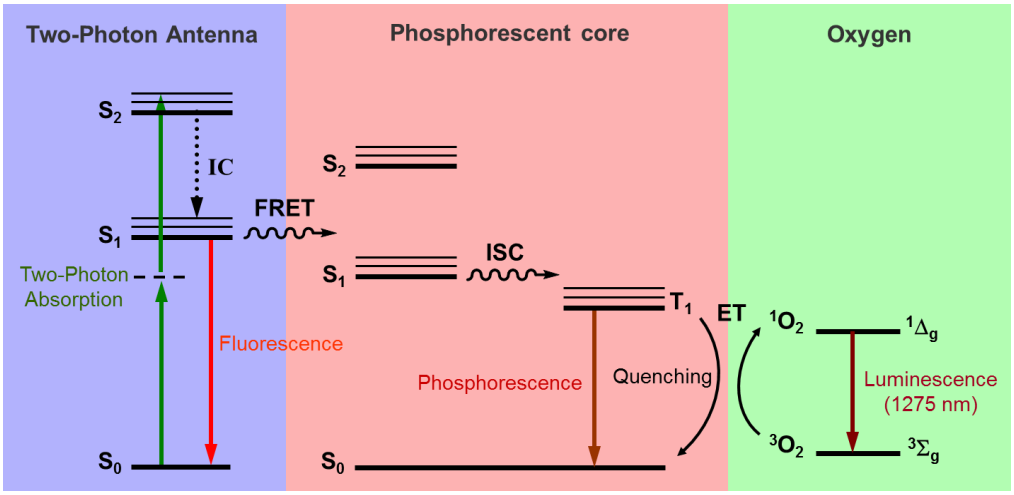

Figure 2-15. The photophysical processes in FRET-based two-photon absorbing oxygen probes.

Increasing the number of antenna enhances the light harvesting properties and the final two-photon absorption cross-section of the system. Fréchet and Prasad were the first to report such a system, in the frame of the development of singlet oxygen generation dyes, but not oxygen-sensors.[189] Eight two-photon absorbers (AF-343) were grafted to a central porphyrin core (free base).[189-190] Vinogradov took over and extended this concept for oxygen-sensor by adding specific two-photon absorber (Coumarin 343) in the dendritic systems of Oxyphor dyes (**Figure 2-14**).[191] Experimental results demonstrate that this approach has the potential to enhance the two-photon absorption cross-section of the molecule well beyond what is available by direct modification of porphyrin.

In the case of the construction of two-photon absorbing FRET system based on metal-porphyrin acceptors, as with all systems based on this process, the choice of the donor part is crucial and dictated in part by the choice of the acceptor. So, beside strong and NIR shifted 2PA, the following characteristics should be considered to optimize FRET, when selecting 2PA antenna:

(1) High fluorescence quantum yield of the antenna;

(2) Substantial spectral overlap between the donor fluorescence and the acceptor absorption (Pd-porphyrin or Pt-porphyrin) for efficient FRET (**Figure 2-16**).

(3) Suitable donor-acceptor distances, typically less than 10 nm. The efficiency of the energy transfer is inversely proportional to the sixth power of the distance between the donor and the acceptor due to the dipole-dipole coupling mechanism.

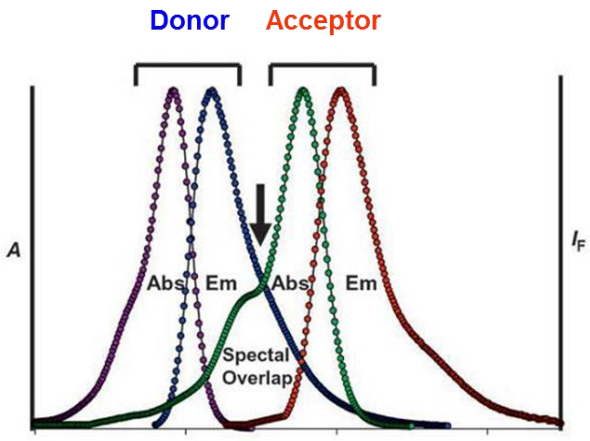

Figure 2-16. Spectral overlap between the emission of donor and the absorption of acceptor necessary for efficient FRET.

Finally, the relative redox potentials of the donor and the acceptor counterpart must be carefully tuned in order to prevent intramolecular quenching of phosphorescence *via* electron transfer (ET). Several 2PA dyes capable of FRET onto Pt-porphyrins have been studied by Vinogradov et al., including some dyes specifically designed for 2P applications. They all induce strong reductive quenching of the porphyrin triplet states by electron transfer, reducing the phosphorescence quantum yield and decreasing the probe's performance. The authors concluded that electron rich porphyrin core must be privileged as acceptors, whereas strong electron donating groups in the donor may be problematic.[192-193] The choices of Coumarin 307 or Coumarin 343 (having moderate cross-section, not more than 28 GM at 840 nm for C-343) as the two-photon absorption antennae in the last generation of Oxyphor™ dyes (**Pt(P–C343)** and **Pt(TCHP-C307)**, **Figure 2-14**) were driven by the overall efficiency of the phosphorescence, two-photon absorption and FRET resulting from these studies.[192, 194] Several studies report the use of **PtP–C343** in *in vivo* two-photon microsecond life-time imaging; for instance measurement of vasculature oxygenation in live animal brain,[195] local oxygen tension in the bone narrow of live mice,[196] simultaneous imaging of blood flow and oxygenation in rat cerebellum with penetration depth of up to 300 µm and spatial resolution of roughly 1 µm,[197] measure of pO_2 in brain vasculature revealing local O_2 gradients around individual erythrocytes in blood microvessels.[198]

1.5. Objectives

As we have seen, the two-photon absorption chromophores used in the design of oxygen sensors are mainly focused on simple commercial coumarins (coumarin 343 and coumarin 307) showing rather low two-photon absorption cross-sections (tens of GM units). Therefore, the development of appropriately functionalized two-photon absorption chromophores with high two-photon absorption cross-sections is of great significance for construction of optimized two-photon oxygen sensors. The aim of this project is to optimize the two-photon absorption cross-sections of Pd-porphyrin complexes through FRET effect for practical

biological applications (**Figure 2-14**). In this chapter, we propose to first study four different antennae with high two-photon absorption cross-sections in the range of 800-900 nm in solution. Then the optimal antenna will be grafted to the Pd-porphyrin core using efficient chemical strategies and in particular copper catalyzed alkyne–azide cycloaddition (click chemistry).[199-200] The energy transfer process as well as oxygen sensing behaviour will be evaluated after one- or two-photon excitation of the antennae.

2. Design, Synthesis and Optical Properties of Palladium (II) Porphyrin Acceptor

2.1. Design and Synthesis

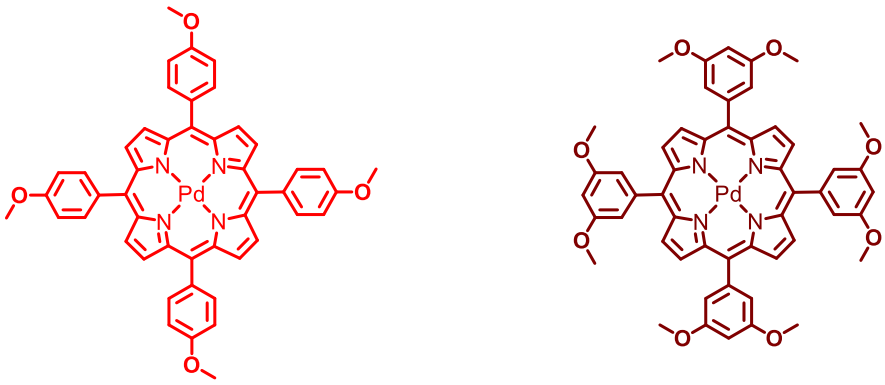

Figure 2-17. Chemical structures of the model complexes **Pd-por-1** and **Pd-por-2**.

In this section, as seen in **Figure 2-17**, two palladium porphyrin complexes **Pd-por-1** and **Pd-por-2** will be employed as two model compounds (acceptor) for designing and optimizing energy donors (2PA chromophores). **Pd-por-1** and **Pd-por-2** bearing methoxyl groups show electron rich feature, which make them a good acceptor in FRET system for preventing phosphorescence quenching *via* electron transfer (ET). On the other hand, methoxy group provide a possibility of modification on pophyrin in order to introduce the other groups. By changing methyl group for propargyl group, the antennae molecules can be introduced by click reaction. As the newly introduced antennae won't be conjugated to the porphyrin core, this shouldn't change the optical properties of porphyrin. These merits make them good candidates for our FRET system.

As shown in **Figure 2-18**, **Pd-por-1** and **Pd-por-2** are obtained from free-base porphyrin ligands **2** and **4** by complexation with $PdCl_2$ in refluxing benzonitrile. Free-base porphyrin **2** and **4** are prepared by the classical Adler-Longo method from pyrrole and the corresponding benzaldehyde (*para*-methoxybenzaldehyde **1** or 3,5-dimethoxybenzaldehyde **3**) in refluxing

propionic acid. All compounds were characterized by NMR (^{1}H and ^{13}C) spectroscopy. The ^{1}H NMR spectra of free porphyrin **2** and **4** show a characteristic NH signal at -2.76 or -2.84 ppm as a result of the shielding effect of porphyrin ring. Disappearing of the NH signals occurs after the complexation with palladium (II) salts. The increase of symmetry resulting from the metallation was manifested by the occurrence of sharp signals for both C_{α} and C_{β} at around 131 and 142 ppm, whereas these signals were absent in the free base ligand.

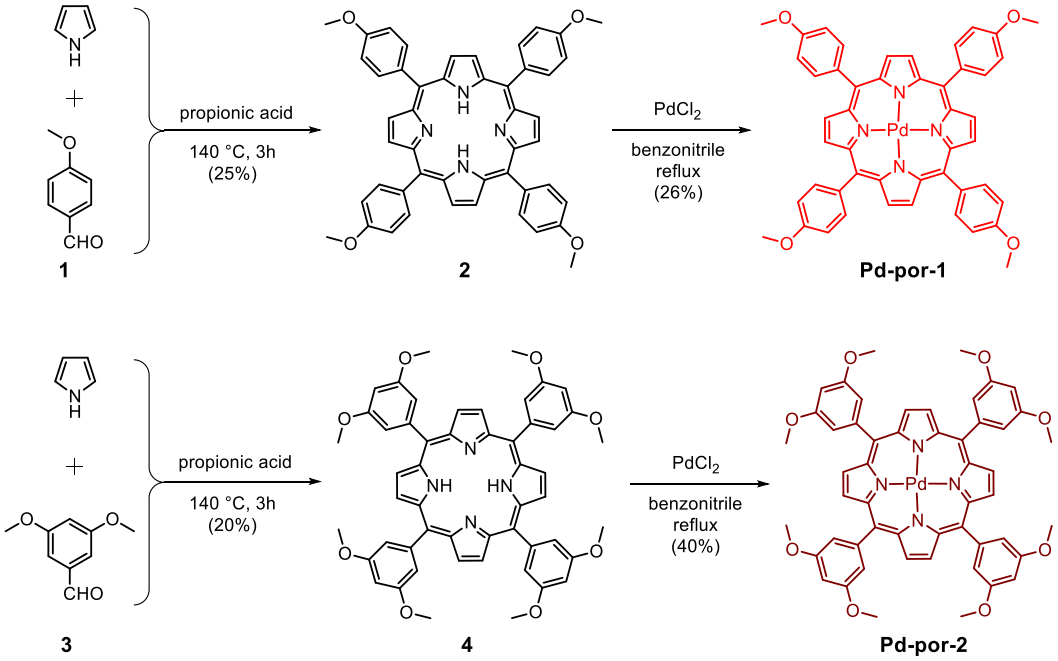

Figure 2-18. Synthesis of model Pd-complexes **Pd-por-1** and **Pd-por-2**.

2.2. Optical Properties of Pd-por-1 and Pd-por-2

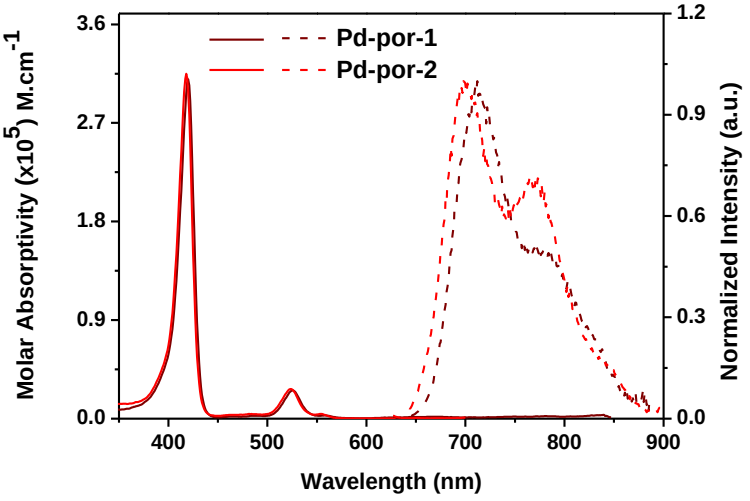

Figure 2-19. Absorption (solid) and emission (dash) spectra of **Pd-por-1** and **Pd-por-2** in $CHCl_3$. Excitation: 420 nm.

Figure 2-19 presents the absorption and phosphorescence spectra of model complexes **Pd-por-1** and **Pd-por-2**. As we can see the two model complexes have almost identical absorption spectra displaying the two characteristic Soret (or B) and Q bands of porphyrin complexes. The very intense Soret band ($S_0 \rightarrow S_2$) appears at 420 nm and a less intense Q-band at 526 nm for **Pd-por-1** whereas the weaker Q band ($S_0 \rightarrow S_1$) is split into two components Q(0,0) and Q(1,0), consequence of the increase in the symmetry of the ring-system compared to the free bases (which show four distinct bands). **Pd-por-2** shows slightly blue-shifted (2 nm) Soret and Q-band at 418 nm and 524 nm compared to those of **Pd-por-1** (**Table 2-1**).

Table 2-1. Photophysical data of **Pd-por-1** and **Pd-por-2**.

	Absorption	**Emission**
	λ_{em} / nm ($\varepsilon \times 10^4$/M^{-1}cm^{-1})	λ_{max} / nm
Pd-por-1	420 (31.0)	720, ~778
	526 (2.51)	
Pd-por-2	418 (31.5)	700, ~769
	524 (2.68)	

In air, no obvious fluorescence is observed after excitation in the Q band. This is expected for palladium porphyrin complexes, as the $S_1(\pi, \pi^*) \rightarrow T_1(\pi, \pi^*)$ inter-system crossing rate is favoured by the presence of the heavy atom providing spin-orbit coupling. Thus, the triplet state is formed quantitatively and almost all absorbed photons are relaxed *via* the triplet state quenching mechanisms, where spin-transfer to oxygen dominates.[201] In degassed solution, on the other hand, intense phosphorescence is observed. When the complex is planar, as it is the case for the palladium complexes of *meso*-tetraphenylporphyrin derivatives, the (d, d) transitions of the Pd^{2+} ion are higher in energy than the $T_1(\pi, \pi^*)$ state, resulting in a strong phosphorescence from the $T_1 \rightarrow S_0$ path of the latter, even at room temperature.[202] Two distinct vibrationally split bands, T(0,0) and T(1,0), could be observed in each case, with main

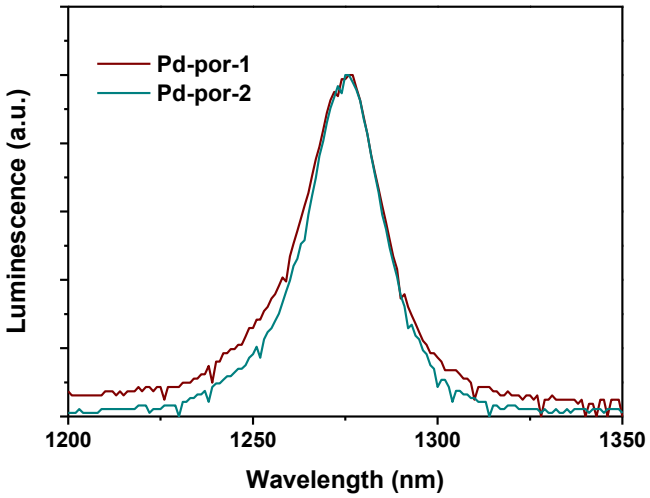

Figure 2-20. Normalized oxygen luminescence spectra obtained from air-saturated $CHCl_3$ solutions (2×10^{-7} mol L^{-1}) of **Pd-por-1** and **Pd-por-2**.

maxima at 720 and ~778 for **Pd-por-1**, and 700 and ~769 for **Pd-por-2**. It is worth noting that the different substituents (number and position) in **Pd-por-1** and **Pd-por-2** cause a difference in their phosphorescence spectra. As listed in **Table 2-1**, λ_{em} of **Pd-por-1** is 720 nm, showing a 20 nm red shift relative to that of **Pd-por-2** due to the electron donating effects of the methoxy groups on the *meso*-phenyl rings.[203]

The ability to generate singlet oxygen ($^1O_2$) through the triplet state was assessed by recording the luminescence of singlet oxygen at 1275 nm. Following excitation in either the Soret (420 nm) or the Q band (520 nm), the characteristic signal of $^1O_2$ phosphorescence was observed (**Figure 2-20**).

3. Design, Synthesis and Optical Properties of Two-Photon Antennae

3.1. Molecular Design

Förster-type energy transfer onto the B-band (Soret) of a porphyrin would be advantageous, given the much higher extinction coefficient of this transition compared to the Q-band ($\lambda_{max}^{(B)}$ = 420 nm, $\varepsilon^{(B)}$ = 310000 $M^{-1}cm^{-1}$ to be compared to $\lambda_{max}^{(Q)}$ = 526 nm, $\varepsilon^{(Q)}$ = 25100 $M^{-1}cm^{-1}$ for **Pd-por-1**). According to our previous study,[204] energy transfer to oxygen is favoured by excitation through the Q band. So we were looking for two-photon absorbers characterized by high cross-section values (σ_{2PA}) in the range 700-900 nm and possessing emission bands overlapping with Pd-porphyrin absorptions (Q-band or ideally both B- and Q- bands). Consequently, we turned our attention to the most recent and thorough literature review listing synthetic two-absorption dyes designed up-to-date.[12] Based on the above definition of a suitable two-photon absorbing antenna (particularly high two-photon cross-section at 800 nm combined with emission maxima overlapping with the absorption of the model Pd-complexes, *i.e* λ_{em} ~500 nm), chromophore **PH** [205] presented in **Figure 2-21** was initially chosen.

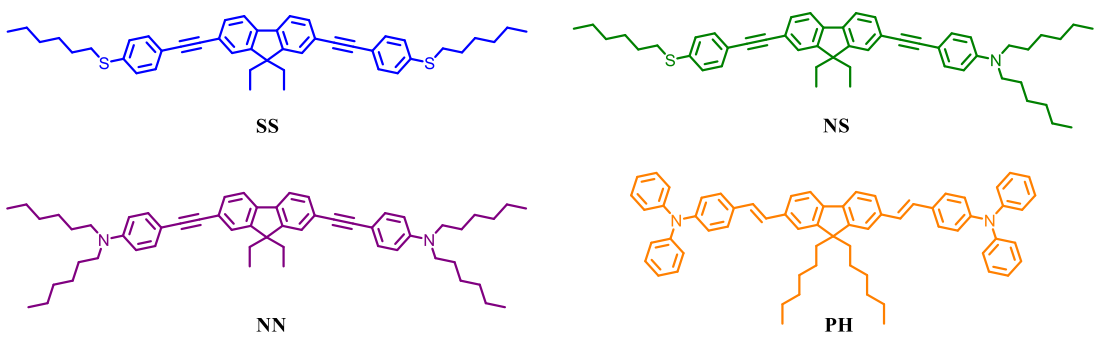

Figure 2-21. Chemical structures of the chromophores **SS**, **NS**, **NN** and **PH**.

To further improve the photostability of chromophores, triple bonds were used instead of double bonds to connect aryl amino-containing donors with a fluorene bridge.[206] Then the chromophores **SS**, **NS** and **NN** with different electron-donating group were designed and synthesized for the optimization of emission wavelength and two-photon properties. These four molecules are charge transfer systems with a quadrupolar structure.

3.2. Synthesis

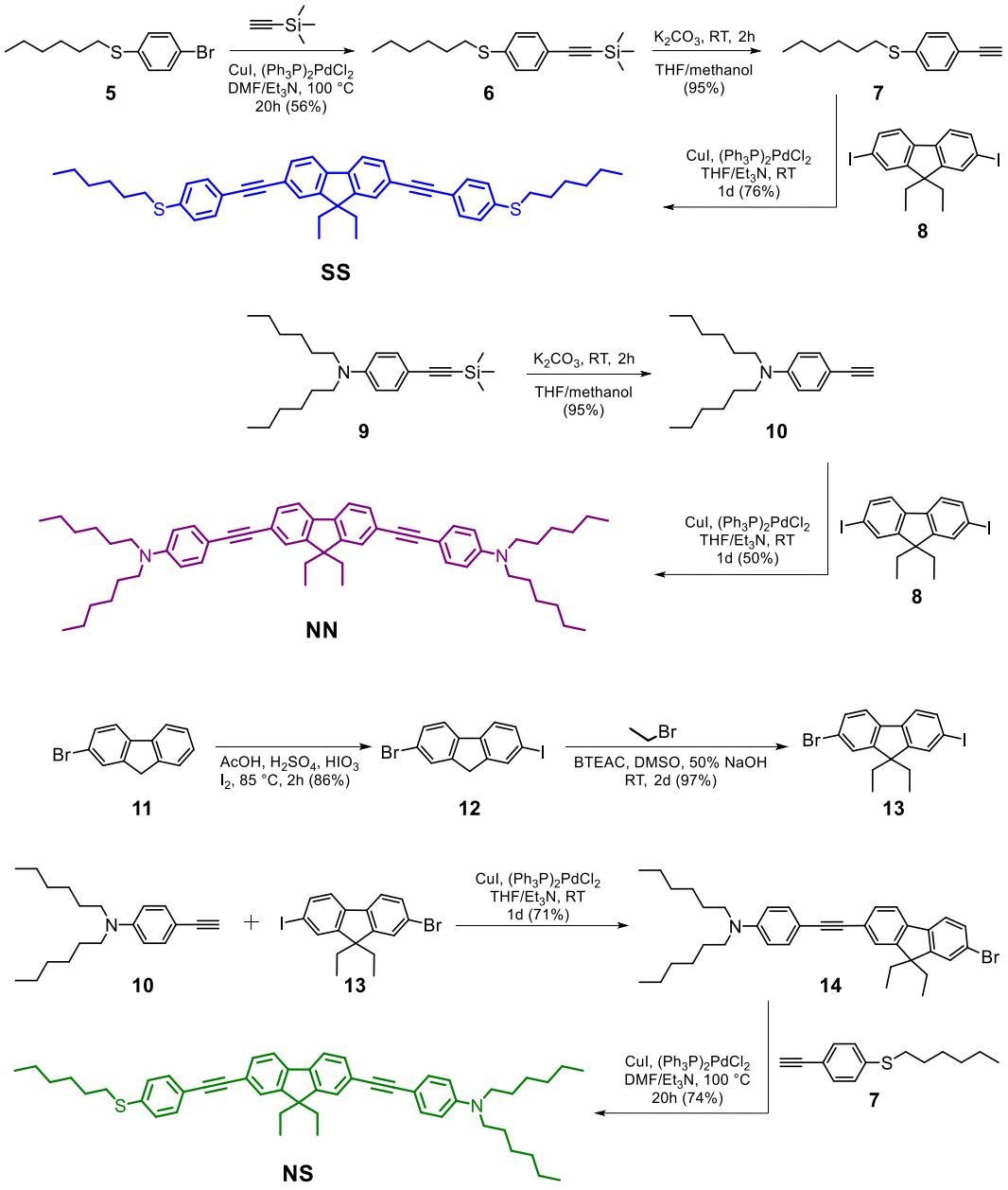

Figure 2-22. Synthesis of fluorophores **SS**, **NS** and **NN**.

The synthesis of **PH** was carried out by Heck coupling reaction between 9,9-dihexyl-2,7-

divinylfluorene with *N*,*N*-diphenyl-4-bromoaniline according to the literature.[207] Synthetic routes for the chromophores **SS**, **NS** and **NN** and their intermediates are depicted in **Figure 2-22**. Target chromophores **SS**, **NS** and **NN** were constructed by palladium-catalyzed Sonogashira cross-coupling reactions between iodo- or bromo-fluorene and corresponding alkyne intermediates.

The symmetrical compounds **SS** and **NN** were synthesized by similar synthetic procedures. At first, (4-bromophenyl)(hexyl)sulfane **5** was converted into protected alkyne **6** through a Pd-catalyzed Sonogashira coupling with ethynyltrimethylsilane. The alkyne intermediate **7** or **10** was obtained after hydrolysis of the TMS group of **6** and **9** in methanol with K_2CO_3. Then the two alkynes **7** or **10** were further coupled through a Sonogashira reaction with 9,9-diethyl-2,7-diiodo-9*H*-fluorene **8**, yielding symmetrical D-π-D fluorenyl chromophore **SS** or **NN** in good yield.

The unsymmetrical compound **NS** was synthesized through two Sonogashira coupling reactions on 2-bromo-7-iodo-9,9-diethylfluorene **13** taking advantage of the halo-selectivity of the reaction. The precursor **13** was obtained in two steps starting from 2-bromo-9*H*-fluorene **11**. Iodination of **11** with iodic acid as the oxidant generated 2-bromo-7-iodo-9*H*-fluorene (**12**) in 86% yield, which after alkylation with bromoethane gave 2-bromo-7-iodo-9,9-diethylfluorene **13** in 97% yield.[208] The first Sonogashira coupling reaction between 4-ethynyl-*N*,*N*-dihexylaniline **10** and **13** occurred at room temperature and gave rise to the intermediate **14**. The unsymmetrical D-π-D chromophore **NS** was then obtained through the second Sonogashira reaction between **14** and (4-ethynylphenyl)-(hexyl)sulfane **7** at 100 ℃.

3.3. Crystal Structures

Single crystals of the chromophores **SS** and **PH** were obtained by slow evaporation from methanol/$CHCl_3$ mixture solution. The crystal structures were satisfactorily determined by

Table 2-2. Selected bond lengths [Å] for **SS** and **PH**.

SS			
S1-C5	1.755(6)	C27-C36	1.437(2)
C13≡C36	1.198(2)	C6-C13	1.437(2)
S2-C40	1.748(6)	C31-C39	1.427(2)
C12≡C31	1.203(2)	C8-C12	1.430(2)
PH			
C38-N2	1.395(5)	C39-N2	1.422(5)
C27-N2	1.429(4)	C11-C9	1.468(5)
C12=C11	1.329(5)	C12-C4	1.466(5)
C13-C8	1.465(5)	C19=C13	1.325(5)
C19-C10	1.463(5)	C3-N1	1.411(4)
C36-N1	1.413(5)	C29-N1	1.432(5)

single crystal X-ray diffraction analysis. Crystal data and collection parameters are summarized in **Annexes**. Selected bond lengths are listed in **Table 2-2**. The ORTEP diagrams with atom numbering scheme and some of the interactions in the crystal are presented.

As shown in **Figure 2-23** for **SS**, the two acetylenic bonds and the fluorene framework in the structure of the chromophore are almost co-planar. The dihedral angles between the fluorene ring and two neighbouring benzene-ring planes are 29.1 °and 29.4 °. These values of the dihedral angles can be attributed to the free rotation of acetylenic bond. The selected bond lengths were listed in **Table 2-2**.

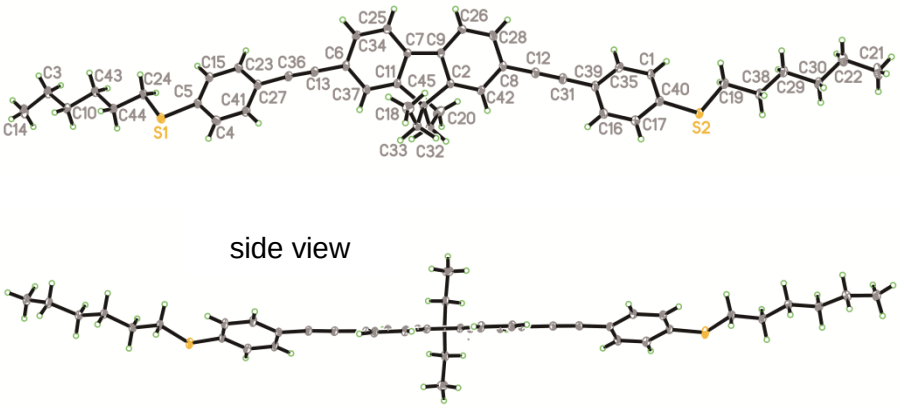

Figure 2-23. ORTEP drawing of **SS** with the ellipsoids drawn at the 30% probability level.

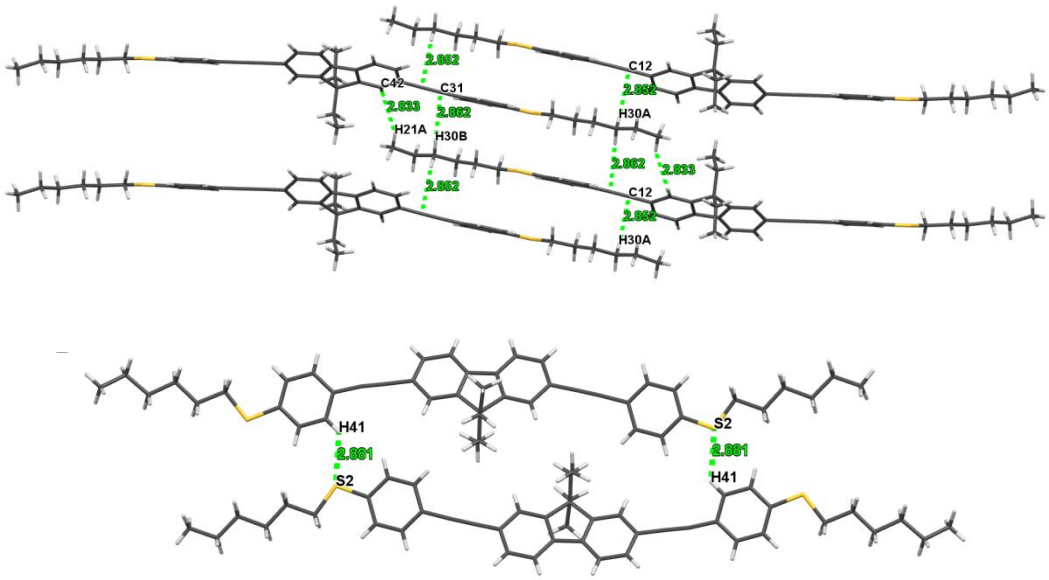

Figure 2-24. (Top) Illustration of the C−H···π stacking and (Bottom) C−H···S hydrogen bond in **SS**. Dotted lines represent the weak interactions.

Figure 2-24-top shows all the C−H···π stacking in the crystal of **SS**, including three different C−H···π hydrogen bonds with distances of 2.833−2.862 Å. In addition, C−H···S

hydrogen bonds with distance of 2.881 Å are formed between adjacent molecules (**Figure 2-24-bottom**). These various intermolecular interactions help the construction of the final three-dimensional crystal structure.

For the crystal structure of **PH** shown in **Figure 2-25**, the dihedral angles between two benzene rings (I and II) and fluorene ring are 7.1 °and 19.7 °, respectively. The selected bond lengths were listed in **Table 2-2**. Moreover, in the crystal parking of **PH** depicted in **Figure 2-26**, each molecule is surrounded by six other molecules through various C−H···π interactions.

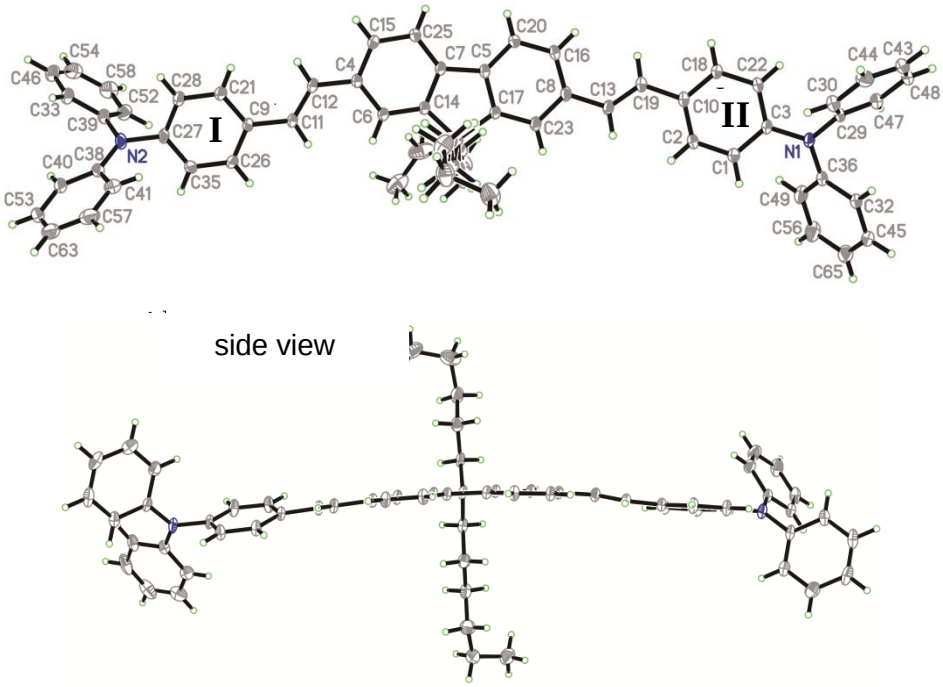

Figure 2-25. ORTEP drawing of **PH** with the ellipsoids drawn at the 30% probability level.

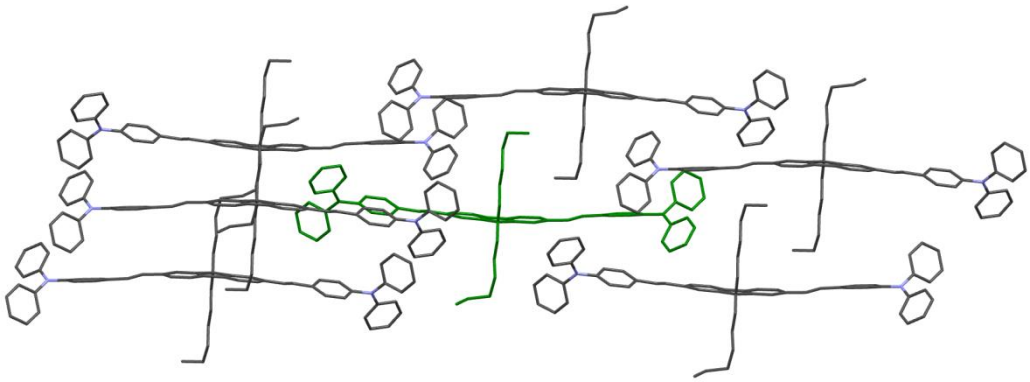

Figure 2-26. Illustration of the packing structure around one **PH** molecule.

3.4. Optical Properties of the Antennae

3.4.1. One-Photon Properties and Solvatochromism

The optical properties of antennae **SS**, **NS**, **NN** and **PH** were recorded at room temperature in different solvents of various polarities to take into account eventual solvatochromic effects

Table 2-3. Photophysical properties of dyes **SS**, **NS**, **NN** and **PH**.

	solvents	λ_{max} [a]	ε_{max} [b]	λ_{max} [c]	$\Delta\nu$ [d]	Φ [e]	τ [f]
SS	benzene	366	8.6	415	3226	0.41	0.57
	chloroform	365	9.3	415	3300	0.40	0.60
	ethyl acetate	362	9.9	411	3293	0.32	0.56
	THF	364	9.7	414	3317	0.37	0.57
	ethanol	361	8.1	412	3428	0.36	0.66
	acetonitrile	362	9.7	412	3352	0.37	0.72
	DMF	365	9.5	417	3416	0.46	0.72
NS	benzene	375	7.3	426	3192	0.63	0.88
	chloroform	375	7.0	460	4927	0.62	1.17
	ethyl acetate	372	7.8	474	5784	0.64	1.41
	THF	375	7.4	481	5876	0.68	1.46
	ethanol	372	7.7	501	6921	0.65	1.81
	acetonitrile	374	7.7	544	8355	0.62	2.32
	DMF	378	7.0	542	8004	0.66	2.39
NN	benzene	388	7.9	421	2020	0.47	0.70
	chloroform	387	7.0	434	2798	0.38	0.85
	ethyl acetate	384	8.4	445	3569	0.39	0.99
	THF	387	8.1	454	3813	0.42	1.02
	ethanol	383	8.6	469	4787	0.39	1.20
	acetonitrile	387	8.7	507	6115	0.44	1.72
	DMF	391	8.0	505	5773	0.49	1.72
PH	benzene	411	8.7	454	2304	0.47	0.91
	chloroform	411	8.0	463	2732	0.49	1.04
	ethyl acetate	405	8.9	481	3901	0.44	1.07
	THF	408	8.8	483	3805	0.48	1.09
	ethanol	405	9.0	481	3901	0.45	1.20
	acetonitrile	405	8.8	502	4771	0.49	1.52
	DMF	410	8.5	500	4390	0.56	1.50

[a] Absorption peak position in nm (1×10^{-6} mol L^{-1}). [b] Maximum molar absorbance in 10^4 mol^{-1} L cm^{-1}. [c] Peak position of emission in nm (1.0×10^{-6} mol L^{-1}), excited at 370 nm (**SS**, **NS**) and 390 nm (**NN**, **PH**). [d] Stokes shift in cm^{-1}. [e] Quantun yields determined by using coumarin 307 in ethanol, (Φ = 0.56) (1.0×10^{-6} mol L^{-1}) as the standard. [f] The fitted fluorescence lifetime in ns.

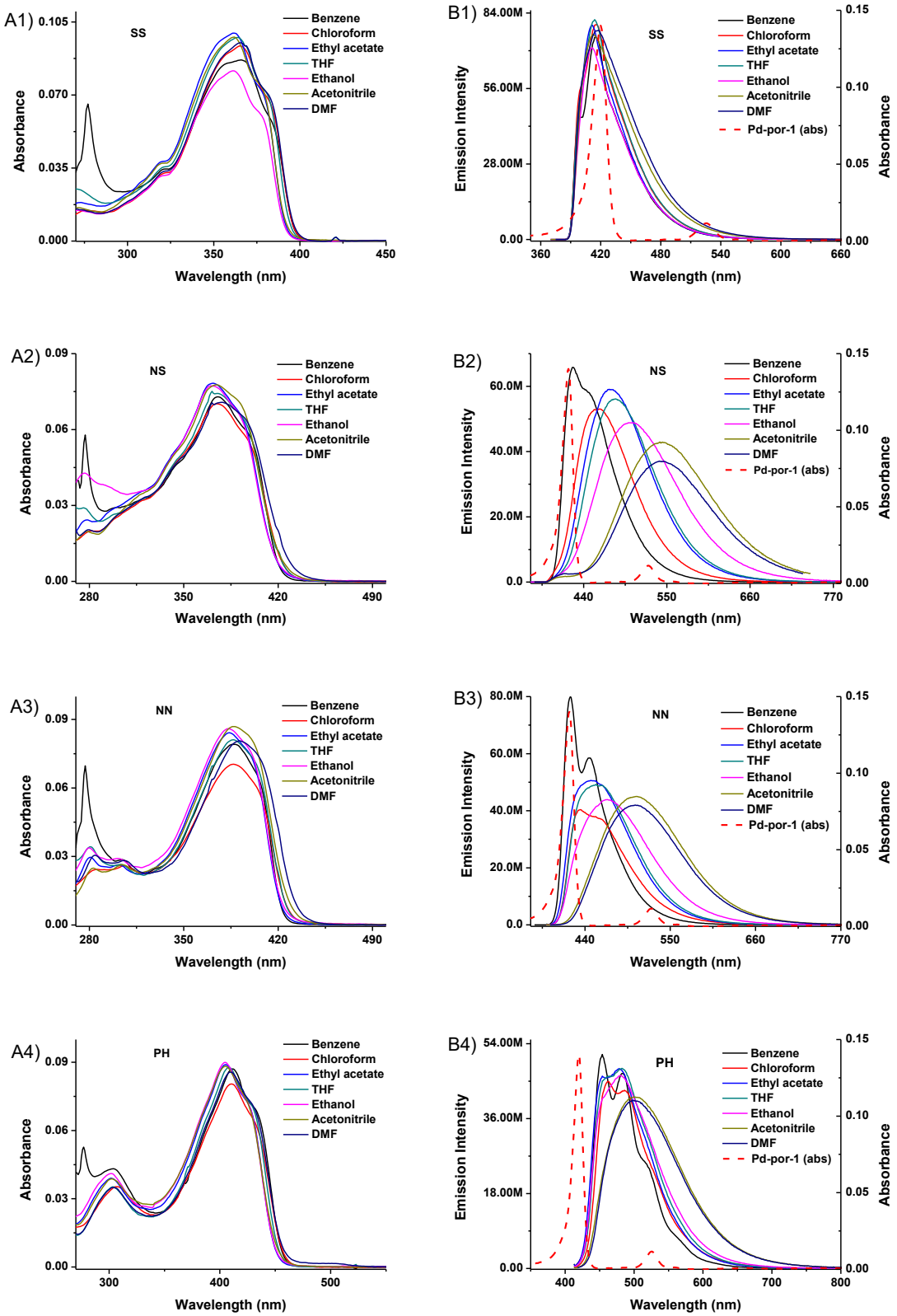

Figure 2-27. A) One-photon absorption and B) fluorescence spectra of fluorophores **SS**, **NS**, **NN** and **PH** in seven organic solvents of different polarities with a concentration of 1×10^{-6} mol L^{-1}.

in the energy transfer to the core and check that the transfer would be feasible whatever the environment of the final oxygen probe. So, the photophysical data (one-photon absorption and one-photon excited fluorescence) of compounds **SS**, **NS**, **NN** and **PH** in seven solvents are collected in **Table 2-3**, including the fluorescence quantum yields and lifetimes.

As can be seen in **Figure 2-27**, the linear absorption spectra of **SS**, **NS**, **NN** and **PH** in various solvents exhibit main peaks between 361 and 411 nm with molar absorption coefficient of 7.0-9.9 $\times 10^4$ mol^{-1} L cm^{-1}. For each compound **SS**, **NS**, **NN** and **PH**, the absorption spectra in different solvents exhibit almost no difference, suggesting negligible solvatochromic behaviour. Within the same solvent, the absorption wavelength of **SS**, **NS**, **NN** and **PH** follow the order of λ_{abs}(**PH**) > λ_{abs}(**NN**) > λ_{abs}(**NS**) > λ_{abs}(**SS**). It is because that the dihexylamine group is a stronger electron-donating group than hexylthio group. The extended conjugation length of **PH** makes its absorption wavelength larger than that of **NN**.

However, with increasing the polarity of the solvent, as shown in **Figure 2-27**, the fluorescence spectra of dyes **NS**, **NN** and **PH** show obvious bathochromic shifts. The Stokes shifts also show a tendency to increase, especially for **NS**. For example, λ_{em} of **NS** is located at 426 nm in benzene and red-shift to 542 nm in DMF. A significant increase in the Stokes shift was observed from 3192 cm^{-1} in benzene to 8004 cm^{-1} in DMF. Furthermore, upon increasing the solvent polarity, the fluorescent lifetimes of the chromophores **NS**, **NN** and **PH** are also increased. The above results indicate that the excited state of the molecules should possess a higher polarity than the ground state. An increased dipole-dipole interaction between the solute and polar solvent leads to a lowering of the energy level. The quantum yields (Φ) of the four compounds in different solvents are determined by using coumarin 307 as a standard. For each compound of **SS**, **NS**, **NN** and **PH**, their fluorescence quantum yields exhibit no obvious change in different solvents, which is a promising characteristic for application in bio-imaging. Among the four compounds, **NS** shows higher fluorescence quantum yield (Φ = 62-68% in various solvent) compared with those of others (32-46% for **SS**, 38-49% for **NS**, 44-56% for **PH**).

As described above, the fluorescence spectra of dyes **NS**, **NN** and **PH** show an obvious solvatochromism in various solvents with different polarity, suggesting a large change in dipole moment between the ground and emissive excited states. The Lippert–Mataga equation is the most typically used equation to evaluate the dipole moment changes (μ_e-μ_g) of the dyes with photoexcitation:

$$\Delta\nu = \frac{2\Delta f}{4\pi\varepsilon_0 \hbar c a^3}(\mu_e - \mu_g)^2 + b \qquad (2\text{-}2)$$

$$\Delta f = \frac{\varepsilon - 1}{2\varepsilon + 1} - \frac{n^2 - 1}{2n^2 + 1} \qquad (2\text{-}3)$$

in which $\Delta\nu$ = ν_{abs} - ν_{em} stands for Stokes shift, ν_{abs} and ν_{em} are the frequencies of the absorption and emission maxima, $\hbar$ is the Planck's constant, c is the velocity of light in

vacuum, a is the Onsager radius and b is a constant. Δf is the orientation polarizability, μ_e and μ_g are the dipole moments of the emissive and ground states, respectively and ε_0 is the permittivity of the vacuum. $(\mu_e-\mu_g)^2$ is proportional to the slope of the Lippert -Mataga plot.

Plots of the Stokes shifts as a function of the solvent polarity factor Δf are shown in **Figure 2-28**. As shown, the slope of the best-fit line is related to the dipole moment change between the ground and excited states ($\mu_e-\mu_g$). The slopes of all four lines are calculated as: 601, 23706, 22924 and 11828 cm^{-1} for **SS**, **NS**, **NN** and **PH**, respectively, which implies larger dipole moment changes for **NS**, **NN** and **PH** upon photoexcitation, in the order **SS** > **PH** > **NN** ≈ **NS**, of we assume the Onsager radius a constant for all these chromophores. This reveals a significant non-centrosymmetry for **PH**, **NN** and **NS** molecules, which will lead to some unexpected 2PA properties as discussed below.

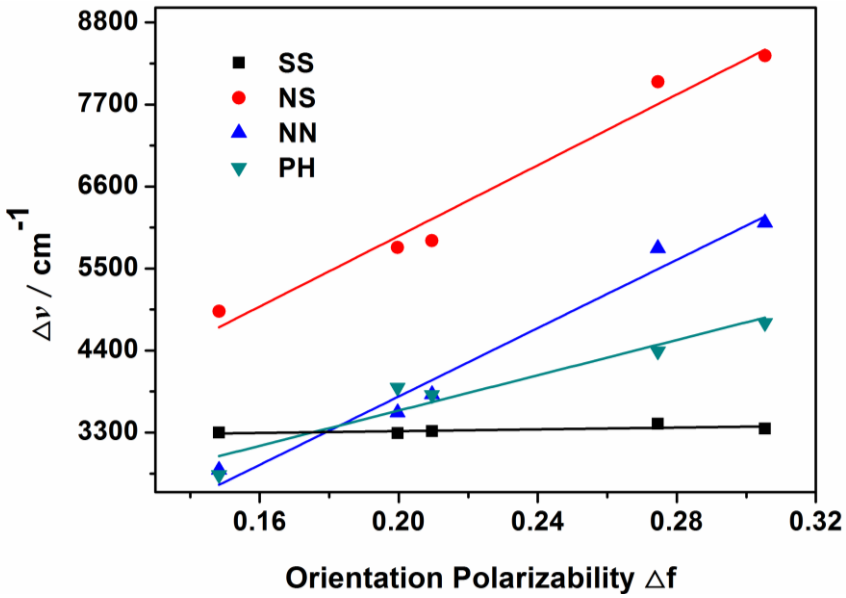

Figure 2-28. Lippert-Mataga plots for **SS**, **NS**, **NN** and **PH**.

3.4.2. Spectral Overlap of Donor Emission with Pd-por-1 and Pd-por-2 Absorption

To investigate the spectrla overlap between the absorption of model complexes (**Pd-por-1**, **Pd-por-2**) and the emission of antennae compounds (**SS**, **NS**, **NN** and **PH**), all the absorption and the emission spectra are studied in chloroform, solvent of intermediate polarity, in which the energy transfer will be studied.

Figure 2-29A shows the absorption spectra for the individual chromophores **SS**, **NS**, **NN**, **PH** and for **Pd-por-1** and **Pd-por-2** in chloroform. The absorption spectra of **Pd-por-1** and **Pd-por-2** have very weak absorption intensity in the range of 340-380 nm, in which antennae compounds **SS**, **NS**, **NN** and **PH** show intense absorption. This field (340-380 nm) in their absorption spectra allow for excitation of the donor chromophores for examination of energy transfer processes in our new systems.

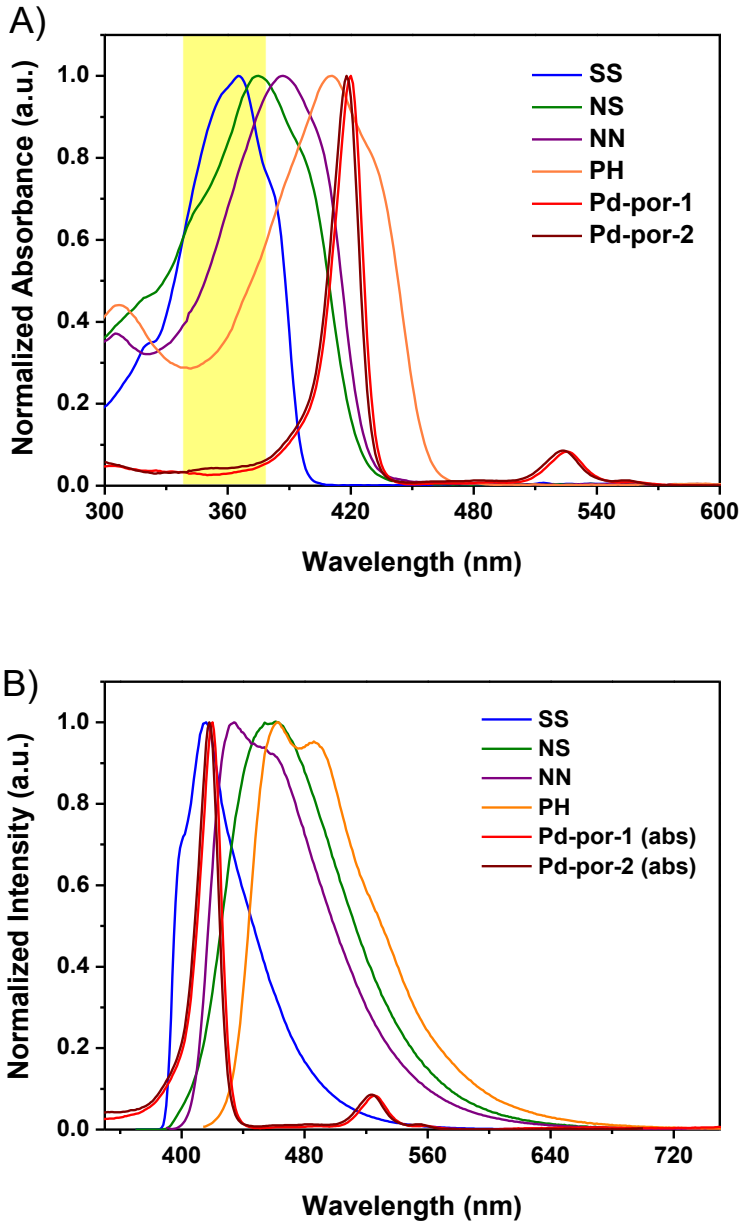

Figure 2-29. One-photon absorption (A) and fluorescence (B) spectra of **SS**, **NS**, **NN**, **PH**, **Pd-por-1** and **Pd-por-2** in chloroform.

The emission spectra of the antennae compounds **SS**, **NS**, **NN** and **PH** along with the absorption spectra (signified by the shaded region) of the model complexes **Pd-por-1** and **Pd-por-2** are shown in **Figure 2-29B**. For an efficient energy transfer toward the palladium porphyrin core, the emission of the antenna must overlap with the absorption of the Pd-porphyrin complex and in particular with the Q-band from which the transfer to oxygen is favoured. In this regard, as shown in **Figure 2-29B**, the emission of antennae compounds **SS**, **NS**, **NN** and **PH** all have good overlap with both the B-band and Q-band of **Pd-por-1** and **Pd-por-2**, in particular Q-band, which set up a favourable situation for efficient FRET between chromophores.

3.4.3. Two-Photon Properties of the Antennae

To further evaluate the two-photon activity of compounds **SS**, **NS**, **NN** and **PH**, their two-photon excited fluorescence spectra were recorded in chloroform (c = 1×10^{-4} mol L^{-1}) in the range of 700–890 nm using a femtosecond Ti-Sapphire laser. Since there is no linear absorption in the wavelength range 700–890 nm for the four chromophores, any frequency up-converted fluorescence appearing upon excitation in this range should be safely attributed to multi-photon absorption excited fluorescence. **Figure 2-30(A1-A2)** and **Figure 2-31(A3-A4)** show the two-photon excited fluorescence spectra of **SS**, **NS**, **NN** and **PH** under different input laser power. **Figure 2-30(B1-B2)** and **Figure 2-31(B3-B4)** show the logarithmic plots of the fluorescence integral *versus* input power. The logarithmic plots have slopes of 2.20 (**SS**), 2.11 (**NS**), 1.97 (**NN**) and 2.06 (**PH**) as the input laser power is increased, suggesting a two-photon excitation mechanism. The experiments reveal that, from 700 to 890 nm, the peak positions of the two-photon excited fluorescence spectra for these chromophores are independent of the excitation wavelengths, but the two-photon absorption cross-sections are dependent over this range. By tuning the pump wavelengths incrementally from 700 to 890 nm while keeping the input power fixed and then recording the 2PEF intensity, the two-photon absorption spectra were obtained. The two-photon absorption spectra of chromophores **SS**, **NS**, **NN** and **PH** are shown in **Figure 2-32**.

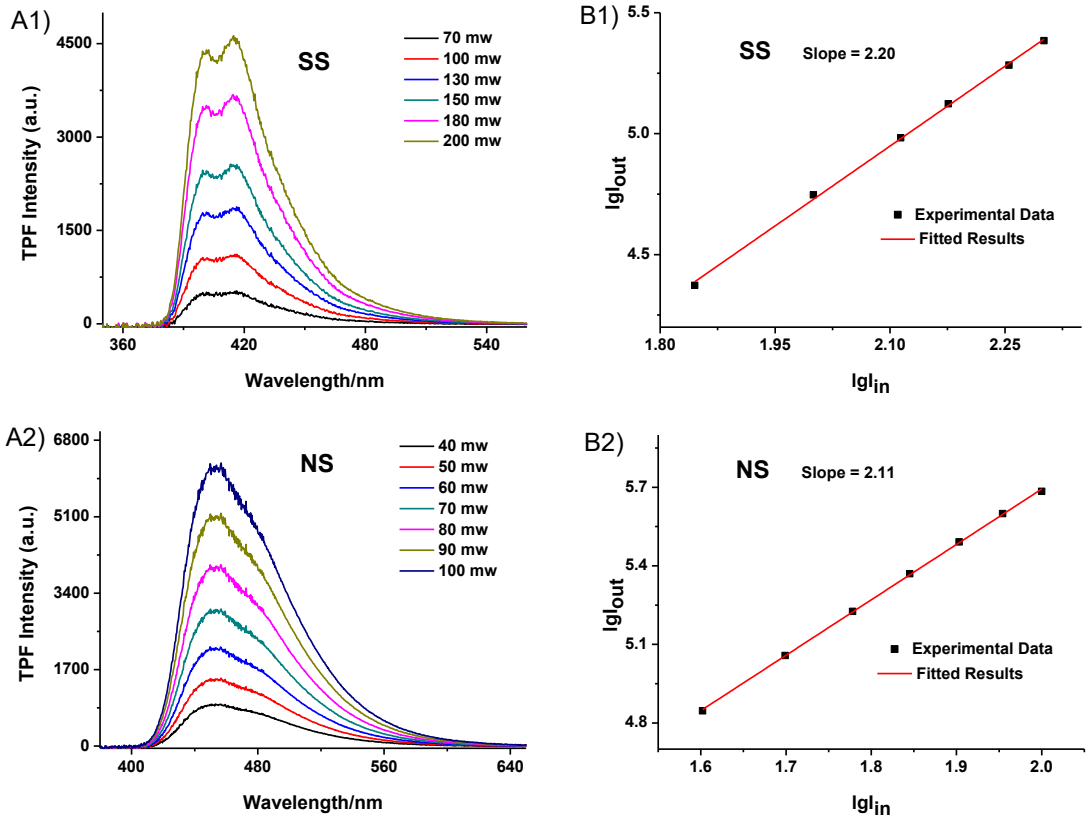

Figure 2-30. A) 2PEF spectra of **SS** and **NS** under different pumped powers at 730 nm (**SS**) and 780 nm (**NS**), with c = 1.0 ×10^{-4} mol L^{-1} in $CHCl_3$; B) The logarithmic plots of the output fluorescence (I_{out}) versus input laser power (I_{in}).

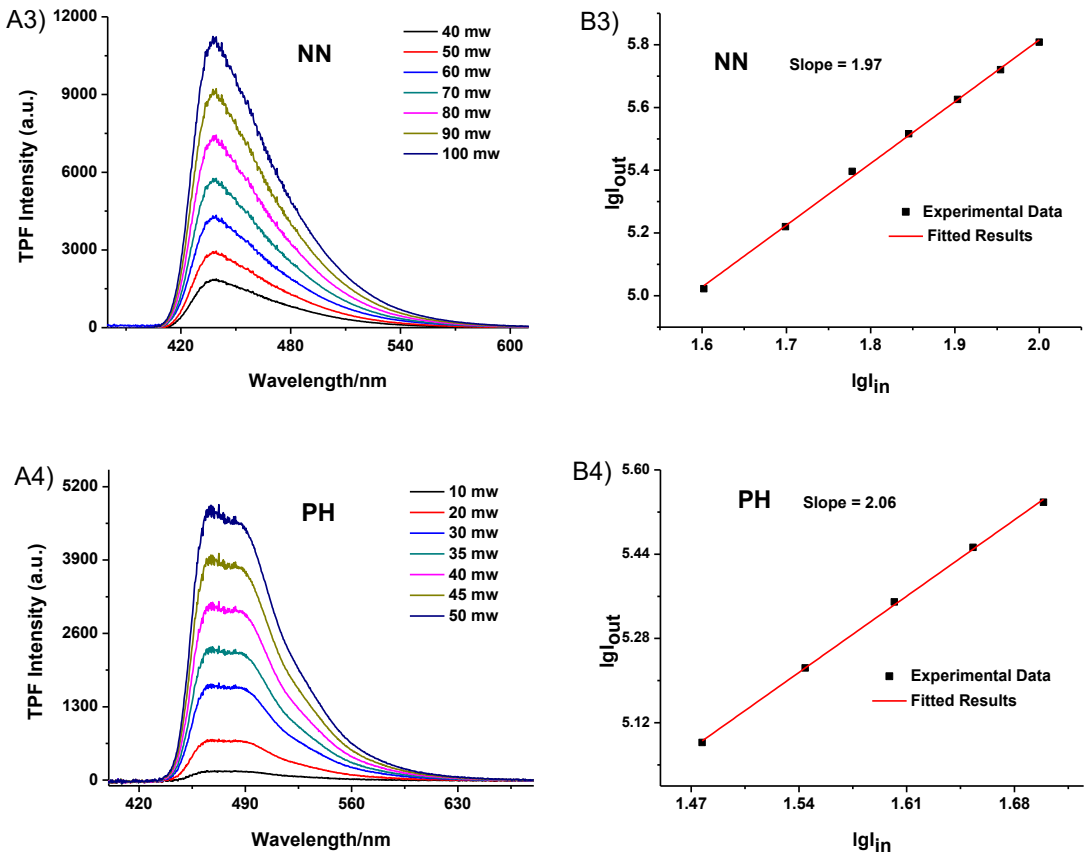

Figure 2-31. A) 2PEF spectra of **NN** and **PH** under different pumped powers at 740 nm (**NN**) and 750 nm (**PH**), with $c = 1.0 \times 10^{-4}$ mol L^{-1} in $CHCl_3$; B) The logarithmic plots of the output fluorescence (I_{out}) versus input laser power (I_{in}).

As shown in **Figure 2-32**, the experimental results indicate that **NS**, **NN** and **PH** display good 2PA activities in the range of 700-690 nm. 2PA cross-section of **NN** at 705 nm (2000 GM) is slightly bigger than the value of 1200 GM at 705 nm for the same conjugation structure in the literature.[209] **Figure 2-32** also shows that, for all molecules, the two-photon excitation spectra present two contributions: (1) a transition that overlaps with the 1PA band; and (2) a second one at higher energy and not observed in the case of **SS** since located out of the available wavelength range. The first transition is theoretically forbidden by 2PA in centrosymmetric molecules. Its observation is nevertheless in good agreement with the above solvatochromism results and allows assuming a centrosymmetry breaking, leading to a significant change in the dipole moment of the molecule between the ground and the first excited state [210] in the order **SS** < **PH** < **NN** ~ **NS**. The 2PA cross-section as defined in eq. (1-5) (see **Chapter 1**), is directly related to the change of dipole moment according to the following expression eq. (2-4) that connect the susceptibility related to 2PA and the spectroscopic parameters, based on three-level model (*i.e.*, ground state S_0, lowest excited state S_1 and a higher excited state S_2).[211]

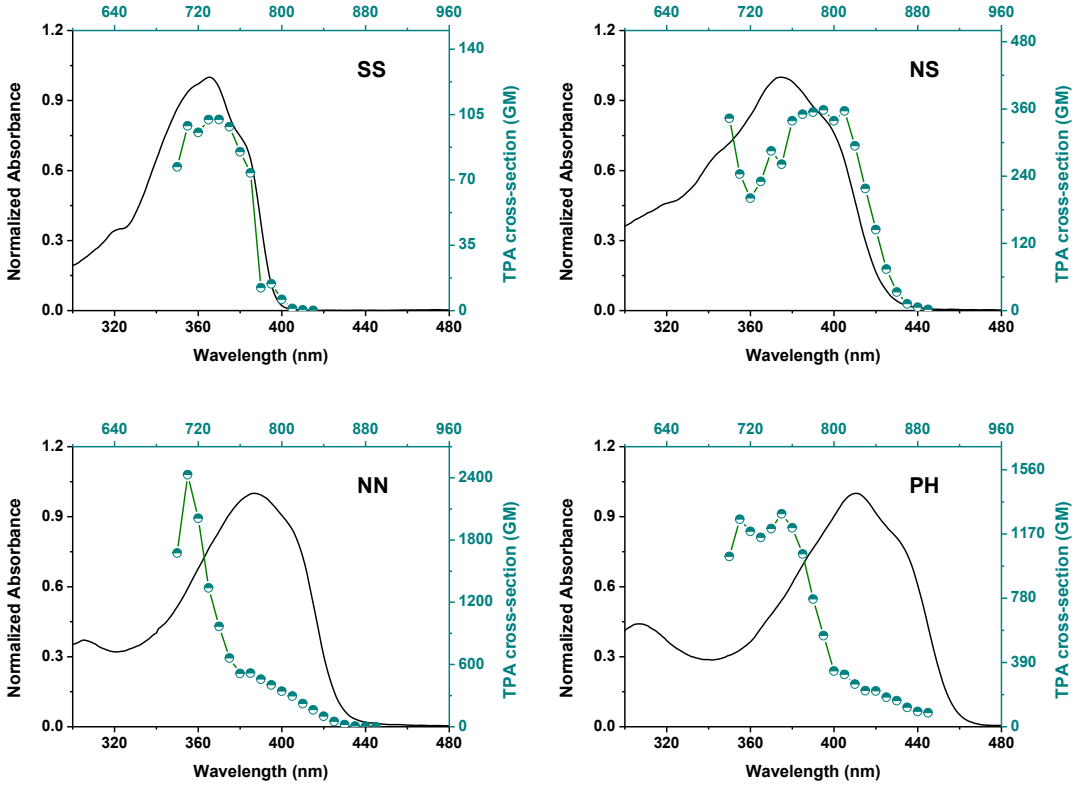

Figure 2-32. Absorption spectra and two-photon absorption cross-sections of **SS**, **NS**, **NN** and **PH** in 700-890 nm regions (c = 10^{-4} mol L^{-1} in $CHCl_3$).

$$\chi_{xxxx} \propto \left[\begin{array}{l} -\frac{\mu_{01}^4}{(E_{01}-\hbar\omega-i\Gamma)^2(E_{01}+\hbar\omega-i\Gamma)}\Big\}N \\ +\frac{\mu_{01}^2\Delta\mu_{01}^2}{(E_{01}-\hbar\omega-i\Gamma)^2(E_{01}-2\hbar\omega-i\Gamma)}\Big\}D \\ +\frac{\mu_{01}^2\mu_{12}^2}{(E_{01}-\hbar\omega-i\Gamma)^2(E_{02}-2\hbar\omega-i\Gamma)}\Big\}T \end{array} \right] \qquad (2\text{-}4)$$

In this relationship, μ_{01} and μ_{12} are the dipole moments transition between S_0 and S_1, and S_0 and S_2 respectively; $\Delta\mu_{01} = \mu_e - \mu_g$ is the dipole moment difference between S_0 and S_1; E_{01} and E_{02} are the transition energies from S_0 and S_2 respectively.

The relation of eq. (2-4) consists in 3 terms:

-the negative term N, which depends mainly on μ_{01} and E_{01}; this term only becomes significant for one-photon resonance and can be neglected in the case of 2PA

- the dipolar term D, which depends on μ_{01}, E_{01} and $\Delta\mu_{01}$ and cancels for centrosymmetric systems.

- the two-photon contribution T, which reflects the contribution of two-photon excited state S_2 and depends on E_{02} and μ_{121} the dipole moment transition between S_1 and S_2.

According to this relationship, the first two-photon transition corresponds to the D term,

while the higher energy one would correspond to the *T* term. **Figure 2-32** shows a reasonable 2PA cross-section from this dipolar part of 100, 200 and 400 GM for respectively **SS**, **PH** and **NN** or **NS**, in line with μ_e-μ_g variations reported above. This leads to significant 2PA efficiency at 800 nm, the wavelength used for bio-imaging applications, for the three last molecules.

3.4.4. Influence of the Antennae on the Phospohorescence of Pd-por-1 and Pd-por-2

One inherent problem in the design of FRET-based two-photon absorbing phosphorescent probes is the possible quenching of the triplet states of the metalloporphyrin by photoinduced electron transfer (PET) from the two-photon antennae. So, in order to evaluate the effect on the triplet states phosphorescence of **Pd-por-1** and **Pd-por-2** in the presence of the designed two-photon antennae, phosphorescence intensities were recorded as a function of the antennae concentration.

The general procedure in our experiments involved titration of dilute solutions of Pd-porphyrins (**Pd-por-1** and **Pd-por-2**, with a constant concentration of c = 3.7~4.0 × 10^{-6} mol L^{-1}) with two-photon antennae in dimethylformamide in the absence of oxygen. Phosphorescence intensities were measured as a function of the concentration of the antennae (**SS**, **NS**, **NN** or **PH**) under excitation in the Pd-porphyrins.

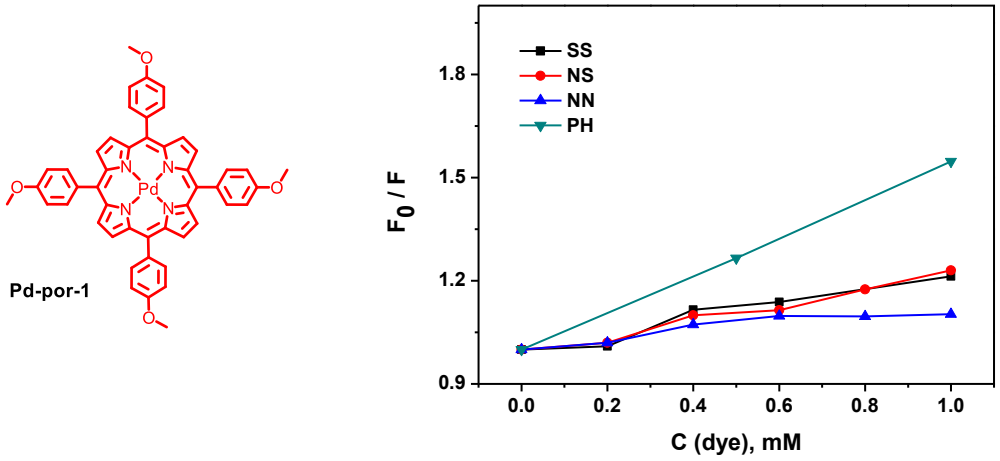

Figure 2-33. Plot of the phosphorescence intensity of **Pd-por-1** (optical density = 0.1 at 525 nm) with different concentration of dyes **SS**, **NS**, **NN** and **PH**. Excitation: 420 nm.

Figure 2-33 and **Figure 2-34** illustrate the study of the effect of the antennae **SS**, **NS**, **NN** and **PH** on the phosphorescence of model complexes **Pd-por-1** and **Pd-por-2**. The quenching effect of antennae **SS**, **NS** and **NN** to the phosphorescence of **Pd-por-1** and **Pd-por-2** is slightly increased with increasing the concentration of antennae up to 10^{-3} mol L^{-1}. Among these antennae molecules, **PH** is the strongest quencher especially for **Pd-por-2** compared with other antennae compounds **SS**, **NS** and **NN**. The results indicate that, at concentration below 2.0 × 10^{-4} mol L^{-1}, antennae **SS**, **NS**, **NN** practically show negligible quenching effect

for the phosphorescence of **Pd-por-1** and **Pd-por-2**. Since the quenching effect is normally associated with the relative redox potentials of the donor and the acceptor counterpart, the electrochemistry will be carried out to understand the above experiment results.

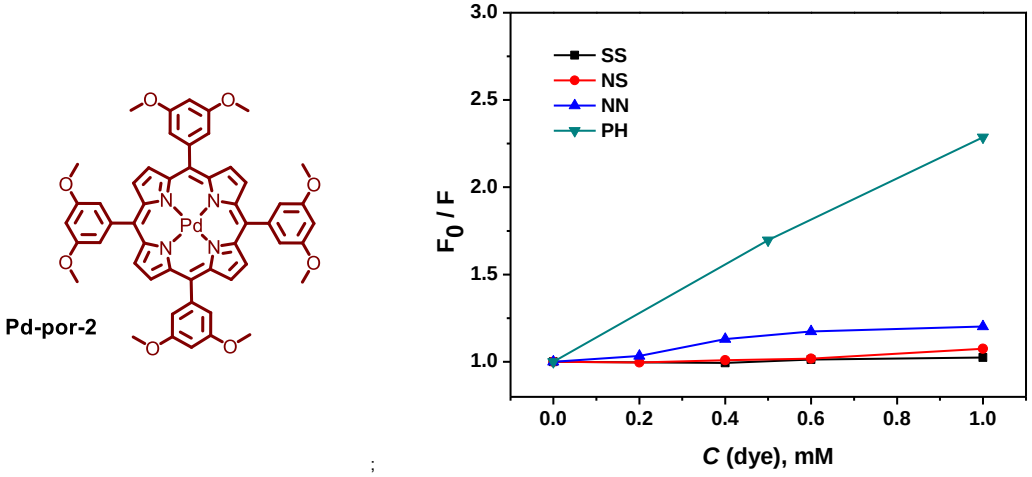

;

Figure 2-34. Quenching of phosphorescence of **Pd-por-2** (optical density = 0.1 at 525 nm) by dyes **SS**, **NS**, **NN** and **PH**.

3.4.5. Choice of the Antenna for Oxygen Probe

As described before, for the design of FRET-based two-photon absorption oxygen sensors, the choice of the antenna was mainly based on the overall efficiency of three aspects, including (1) the two-photon absorption activity of antenna, (2) FRET efficiency from antenna to Pd-porphyrin, and phosphorescence yield of Pd-porphyrin.

For this purpose, four two-photon absorbing chromophores **SS**, **NS**, **NN** and **PH** have been specifically designed and their linear optical properties were studied in details. The fluorescence quantum yield of the chromophores **SS**, **NS**, **NN** and **PH** in chloroform were determined to be 40%, 62%, 38% and 49% respectively. Among them, **NS** shows the highest value. The emissions of chromophores all show substantial spectral overlap with the absorption of the two model complexes **Pd-por-1** and **Pd-por-2**. Moreover, except **SS**, the two-photon cross-sections of **NS**, **NN** and **PH** are around 340 GM at 800 nm, where usually be used as 2P excitation wavelength in bio-applications. Finally, the phosphorescence quenching experiments reveal that **PH** leads to an obvious quenching effect to the phosphorescence of **Pd-por-1** and **Pd-por-2**, while almost no quenching effect was observed for **SS**, **NS** and **NN** at low concentration. Considering all the factors described above, chromophore **NS** with high fluorescence quantum yield, large spectral overlap, good two-photon activity and negligible quenching effect was finally chosen as 2PA antenna candidate.

4. Design and Synthesis of Two-Photon Absorbing Oxygen Probes

4.1. Synthetic Design

Based on the comparison among the four synthesized antennae chromophores, the optimum **NS** was selected for constructing the designed FRET-based donor-acceptor systems (**Figure 2-35**). After the choice of suitable two-photon absorbing antenna, another issue existing in the construction of the target system is synthetic strategy. In short, how to combine this two counterparts (antennae donor and Pd-porphyrin acceptor) by chemical synthesis? In fact, the synthesis of peripheral tetra-substituted porphyrins has always been challenging for the synthetic chemists because of the low yield of multiple peripheral functionalization of porphyrin, and it is even worse for octa-substituted porphyrins. To date, many tetra- or octa-substituted porphyrin dendrimers possessing different peripheral functionalities have been successfully constructed using three efficient synthetic strategies, including the formation of aryl-alkyl ether,[189, 212] the formation of amide or ester [169, 190-191, 194, 196, 213-215] and the formation of 1,2,3-triazole by Cu(I)-catalyzed click reaction.[216-221] Among these synthetic methods, Cu(I)-catalyzed click reaction between a terminal alkyne and an azide presents an attractive strategy for assembling molecular donor−acceptor systems due to its high synthetic yield, mild reaction conditions, and tolerance of other functional groups. Additionally, the 1,4-substituted 1,2,3-triazole obtained from click reaction provides a stable linker between adjacent chromophores in physiological environment.

In this regard, as illustrated in **Figure 2-35**, the compounds **P-1** and **P-2** were designed, which contain four or eight 2PA antennae molecules connected to the central Pd-porphyrin acceptor *via* 1,2,3-triazole linkages. These two molecules were synthesized using the click reaction from azide-functionalized antenna and propargyl-functionalized Pd-porphyrin.

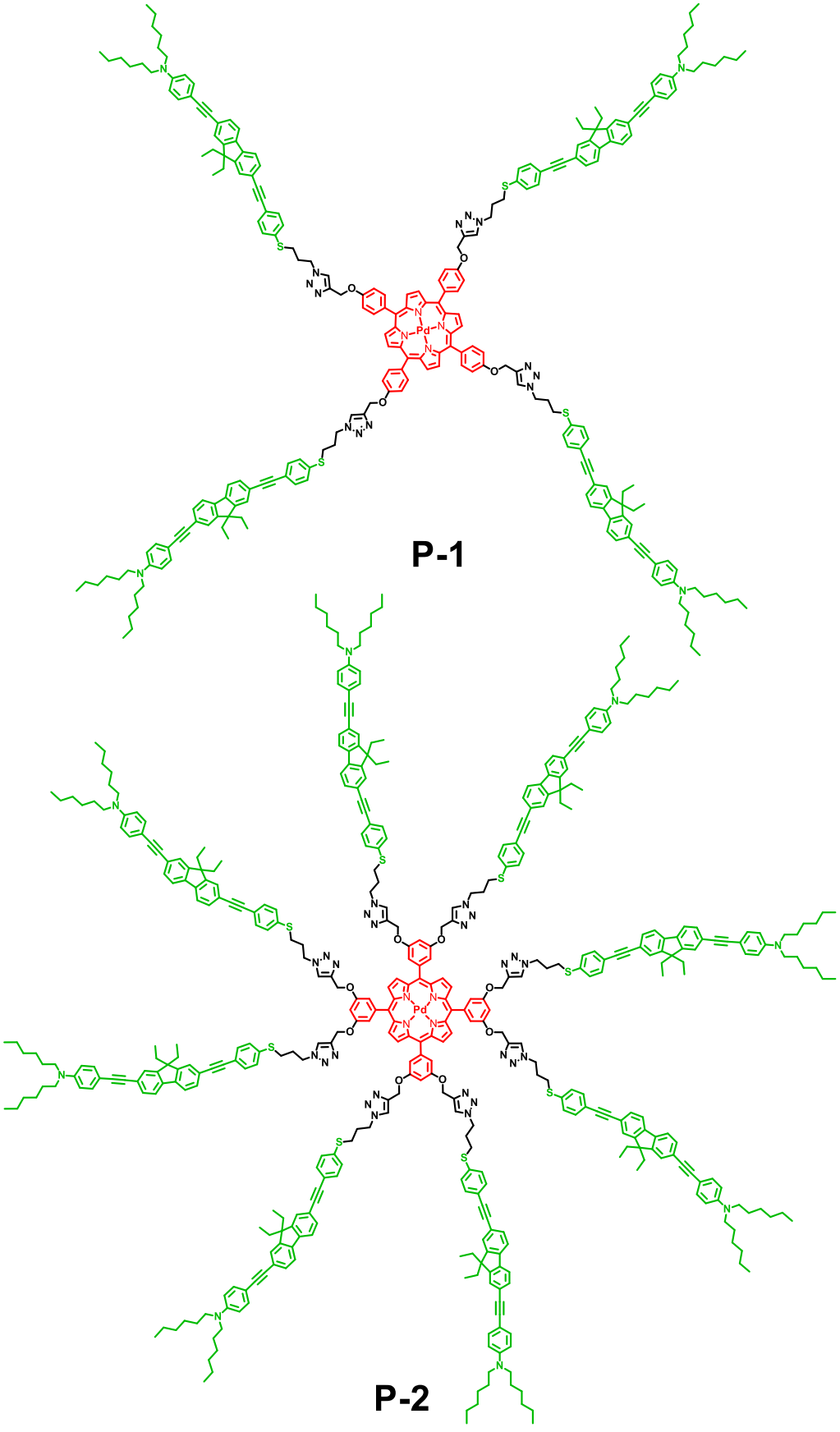

Figure 2-35. The target molecules **P-1** and **P-2**.

4.2. Synthesis of P-1 and P-2

4.2.1. Synthesis of Azide-Functionalized Antenna

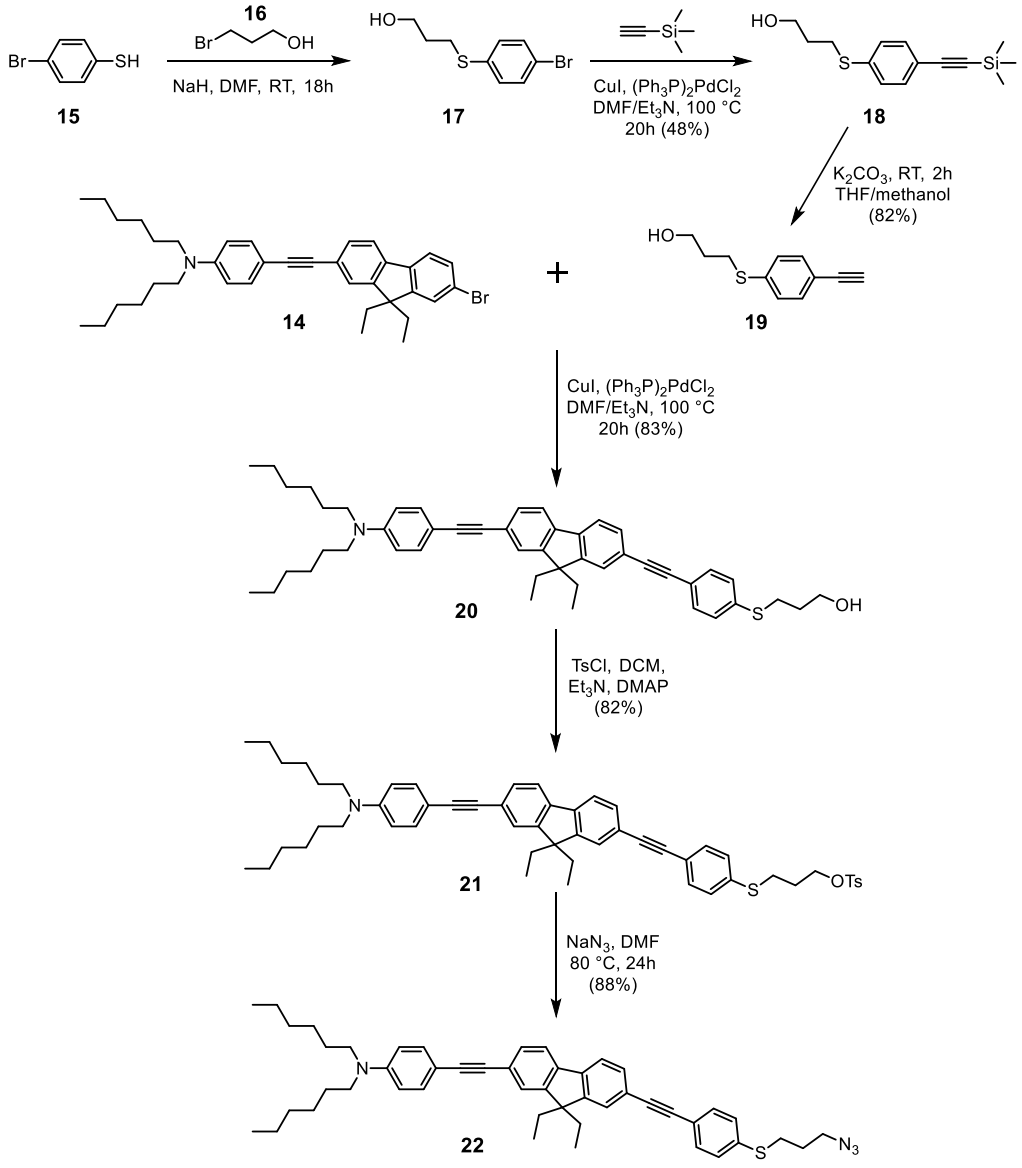

Figure 2-36. Synthesis of azid-functionalized antenna **22**.

As shown in **Figure 2-36**, the synthesis of azide-functionalized antenna **22** began with the alkylation of *para*-bromothiophenol **15** with 3-bromopropan-1-ol **16** to afford **17**, which was converted into protected alkyne **18** by Pd-catalyzed Sonogashira coupling reaction. After hydrolysis of **18** in toluene with K_2CO_3, alkyne **19** was obtained. The second Sonogashira coupling between the alkyne **19** and the intermediate **14**, which was synthesized in **3.2** section, yielded hydroxyl derivative **20**. The alcohol functionality of **20** was then functionalized with 4-toluenesulfonyl group, affording the derivative **21** in high yield. Finally, the azidation of **21**

with sodium azide in DMF was accomplished to produce azide-functionalized antenna **22** in 88% yield.

4.2.2. Synthesis of Propargyl-Functionalized Pd-porphyrin

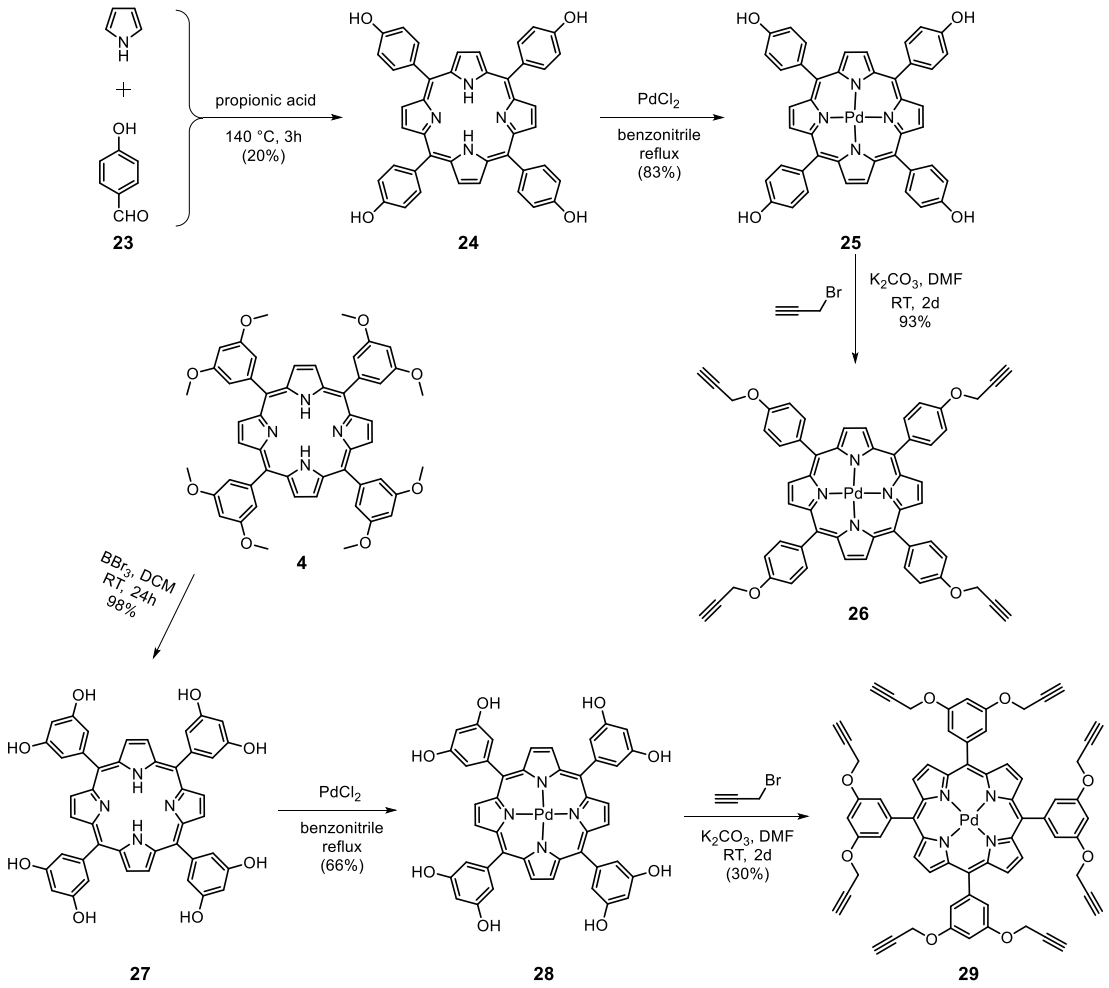

Figure 2-37. Synthesis of propargyl functionalized Pd-porphyrin.

As illustrated in **Figure 2-37**, the synthesis of propargyl functionalized Pd-porphyrin **26** started with the condensation of *para*-hydroxybenzaldehyde with pyrrole in refluxing propionic acid, followed by complexation with $PdCl_2$ in refluxing benzonitrile and alkylation with propargyl bromide in the presence of K_2CO_3.

Propargyl functionalized Pd-porphyrin **29** was synthesized from 5,10,15,20-tetra-(3,5-dimethoxyphenyl)porphyrin **4**, which was described in **2.1** section. Demethylation of the methyl ethers of **4** was accomplished using boron tribromide in dichloromethane at room temperature to produce 5,10,15,20-tetra(3,5-dihydroxyphenyl)porphyrin **27** in 98% yield. Then, the complexation of **27** with $PdCl_2$ generates Pd-5,10,15,20-tetra(3,5-dihydroxyphenyl) porphyrin **28**, which were further propargylated with propargyl bromide under basic condition to obtain **29**.

The synthesis result indicates that the propargylation of Pd-5,10,15,20-tetra(3,5-dihydroxyphenyl)porphyrin **28** shows a much lower yield (30%) than 93% of Pd (II)-5,10,15,20-tetra(4-hydroxyphenyl)porphyrin **25**. This is probably due to the double increase in the number of reaction centres (hydroxy functionality). It is also important to note that the complexation of porphyrin **24** and **27** with $PdCl_2$ should be performed before the step of alkylation with propargyl bromide. Since the complexation of the propargyl functionalized porphyrin (the free base structure same to **29**) with $Zn(OAc)_2$ has been reported,[217] we tried to do the complexation of the same porphyrin with $PdCl_2$ at the beginning. However, an insoluble dark solid was obtained in refluxing benzonitrile. It is because that Pd(II) has the ability to catalyze the dimerization of terminal alkynes.[222] We also found that it is difficult to synthesize **25** and **28** from the model compounds (**Pd-por-1** and **Pd-por-2**) through demethylation with BBr_3.

4.2.3. Synthesis of Oxygen Probes P-1 and P-2

After synthesizing the azide-functionalized antenna **22** and propargyl-functionalized Pd-porphyrins (**26** and **29**) we next attempted the synthesis of target oxygen probes **P-1** and **P-2**. As shown in **Figure 2-38**, the azide-functionalized antenna **22** was clicked with propargyl-functionalized Pd-porphyrin **26** or **29** to afford the respective probe **P-1** or **P-2** in

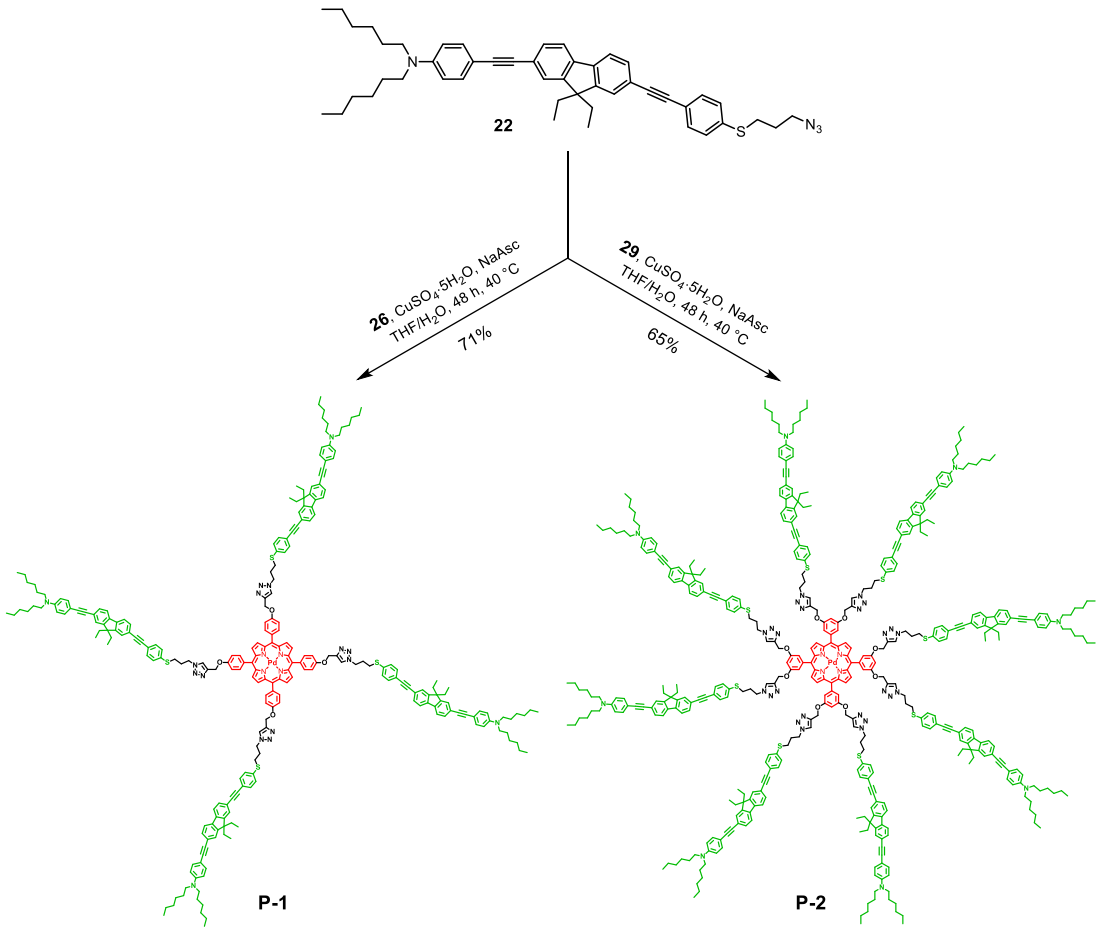

Figure 2-38. Synthesis of **P-1** and **P-2**.

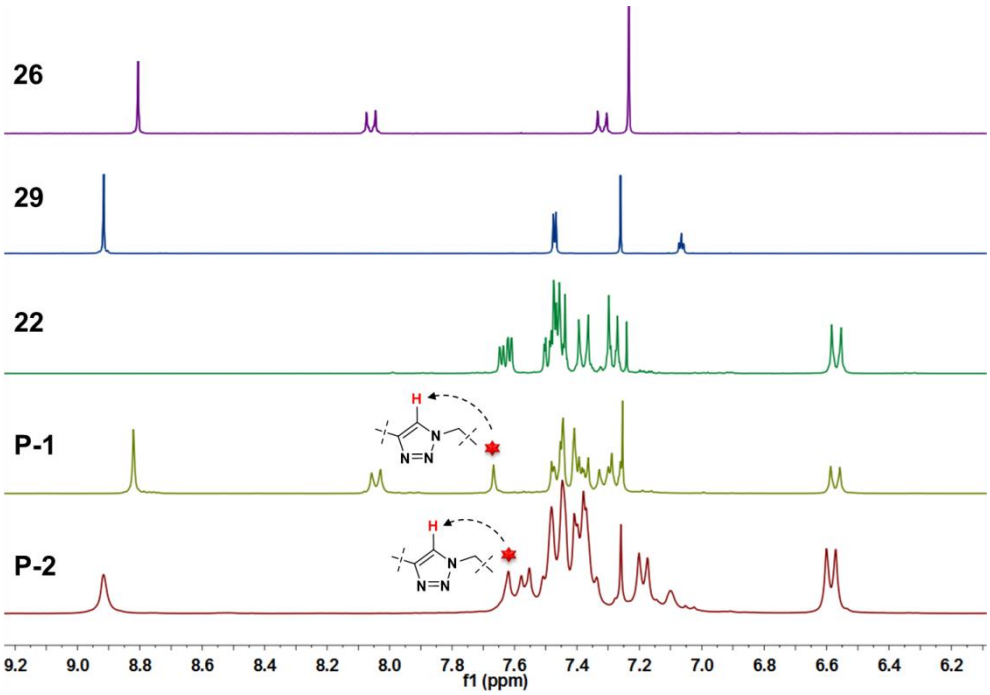

Figure 2-39. ^{1}H NMR spectra of **26**, **29**, **22**, **P-1** and **P-2** at high field.

high yields of 71% (**P-1**) and 65% (**P-2**). The resulting 1,2,3-triazole linked products are easily purified using silica gel column chromatography with chloroform/methanol (50:1, v:v) as the eluent.

As can be seen in **Figure 2-39**, the formation of **P-1** and **P-2** were confirmed by ^{1}H NMR. The spectra of **P-1** show a singlet at δ 7.67 ppm with integral corresponding to four protons, characteristic of the triazole proton. In term, a slightly up-field shifted signal was observed at δ 7.62 ppm for **P-2** with integral corresponding to eight protons. ^{1}H NMR spectra of the intermediates (**26**, **29** and **22**) and the final compounds (**P-1** and **P-2**) also show a clear combination of the Pd-porphyrin and antennae in a 1:4 ratio for **P-1** and a 1:8 ratio for **P-2**. Additionally, they were further characterized by UV−vis absorption spectra, ^{13}C NMR and MALDI-TOF mass spectra.

5. Optical Properties of P-1 and P-2

5.1. One-Photon Properties of P-1 and P-2

5.1.1. Absorption

In the study of the optical properties of target probes **P-1** and **P-2**, precursor azide-functionalized antenna (antenna-N_3) **22** can serve as model donor chromophore, and complexes **Pd-por-1** and **Pd-por-2** serve as model acceptor chromophores. **Figure 2-40**

shows the fluorescence photographs of antenna-N_3 (**22**), **29**, **P-1** and **P-2** in chloroform under UV lamp irradiation (365 nm). We can see that antenna-N_3 (**22**) exhibits strong fluorescence in chloroform, while this emission is almost completely quenched in molecules **P-1** and **P-2**. This phenomenon is consistent with FRET from antenna moieties to the palladium porphyrin complex core. Also, compound **29** was presented for comparison.

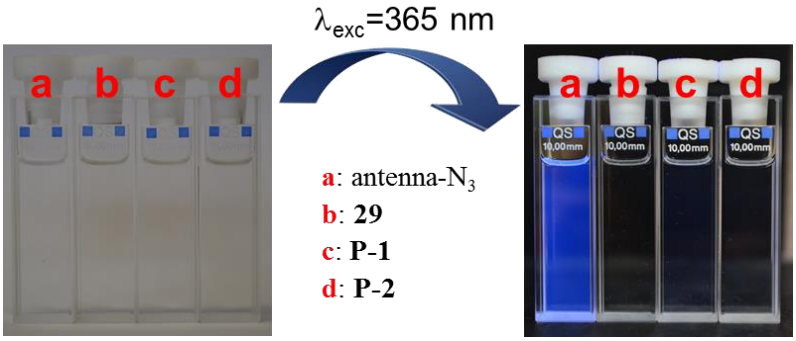

Figure 2-40. The photographs of antenna-N_3 25, 29, P-1 and P-2 in $CHCl_3$ under UV lamp.

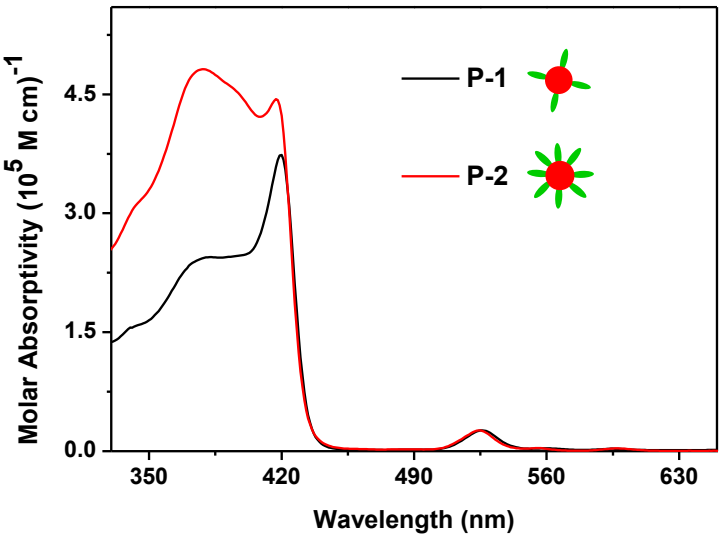

Figure 2-41. Absorption spectra of **P-1** and **P-2** (solid black and solid red lines) in $CHCl_3$.

Figure 2-41 shows the absorption spectra of **P-1** and **P-2** in chloroform. **P-1** displays the expected Soret and Q-band at 420 and 526 nm of **Pd-por-1**, in addition to the antennae π–π* transition at around 375 nm. The absorption spectrum of **P-2** is very similar to that of **P-1**, besides the typical Soret band (418 nm) and less intense Q-band (524 nm) of **Pd-por-2**, the spectrum shows an expected double increase in the antennae π–π* transition relative to that of **P-1**.

As seen in **Figure 2-42**, the absorption spectra of **P-1** and **P-2** are the summation of the absorption spectra of the component chromophores (four antennae and one Pd-porphyrin in **P-1**, eight antennae and one Pd-porphyrin in **P-2**), indicating the presence of all of the chromophores and the absence of any significant ground-state interactions.[190]

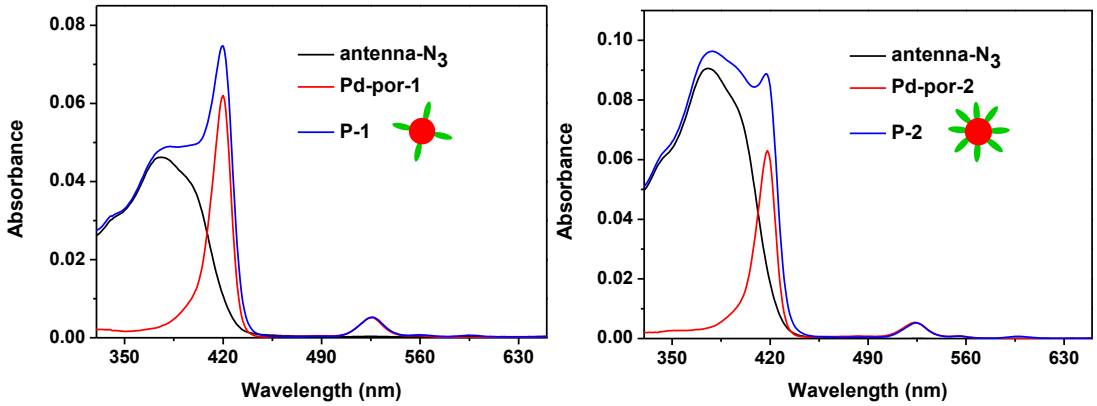

Figure 2-42. Left: Absorption spectra of antenna-N_3 (**22**) ($c = 8\times10^{-7}$ mol L^{-1}), **Pd-por-1** ($c = 2\times10^{-7}$ mol L^{-1}) and **P-1** ($c = 2\times10^{-7}$ mol L^{-1}) in chloroform. Right: Absorption spectra of antenna-N_3 (**22**) ($c = 1.6\times10^{-6}$ mol L^{-1}), **Pd-por-2** ($c = 2\times10^{-7}$ mol L^{-1}) and **P-2** ($c = 2\times10^{-7}$ mol L^{-1}) in chloroform.

5.1.2. Emission

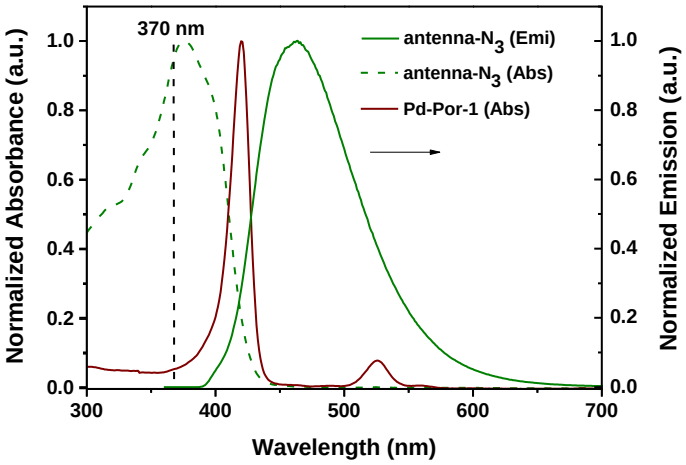

Figure 2-43. Absorption spectra of antenna-N_3 (**22**) and **Pd-por-1** (olive and wine lines), and the emission spectrum of **22** (dashed olive line) in $CHCl_3$ (excitation at 370 nm)

The absorption spectra of **Pd-por-1** and antenna-N_3, as well as the emission spectrum of antenna-N_3 were shown **Figure 2-43**. As expected, the emission spectrum of antenna-N_3 has the same profile with **NS**. Both Soret band and Q band of porphyrin have a good overlap with the emission of antenna-N_3, which is necessary for efficient FRET.

Figure 2-44 shows the emission spectra recorded in deoxygenated chloroform following an excitation at 370 nm close to the maximum absorption of the antennae, for compounds **Pd-por-1**, **P-1** and **P-2**. For model compound **Pd-por-1**, no obvious emission could be observed upon excitation at 370 nm. On the other hand, both **P-1** and **P-2** show greatly enhanced phosphorescence from Pd-porphyrin core with the main peaks at 716 nm for **P-1** and 697 nm for **P-2**. The phosphorescence intensities of **P-1** and **P-2** are 57 and 89 times

more intense relative to the emission from **Pd-por-1**. Besides that, the fluorescence of antennae in **P-1** and **P-2** is greatly quenched, but they still show some remaining fluorescence in the region from 390 to 650 nm with the fluorescence quantum yields (Φ_f) of 1% for both **P-1** and **P-2** (λ_{ex} = 370 nm).

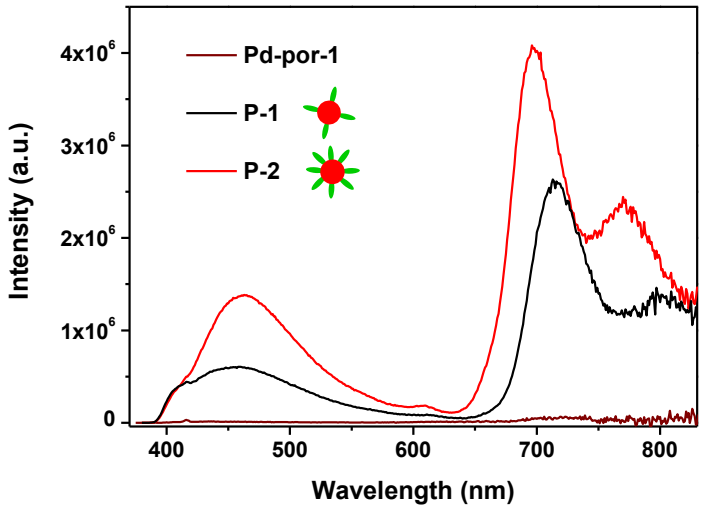

Figure 2-44. Luminescence spectra of **Pd-por-1**, **P-1** and **P-2** in deoxygenated $CHCl_3$ (2×10^{-7} mol L^{-1}) upon the excitation at 370 nm.

Moreover, with increasing the number of grafted antennae from four to eight, the residual fluorescence and the enhanced phosphorescence of **P-2** increase by 2.3 fold and 1.6 fold separately than those of **P-1** as a result of the local concentration increase of antennae (**Figure 2-44**). The above results indicate that, in the designed FRET system, the increase of the number of grafted donor molecules can facilitate the phosphorescence enhancement.

To analyze the efficiency of energy transfer (EnT) in molecules **P-1** and **P-2**, we compared the fluorescence spectra of the antenna chromophore (same concentration as in **P-1** and **P-2**) to that of **P-1** and **P-2**. We found out that the emission from antennae is quenched almost 88-fold in **P-1** and 51-fold in **P-2** as compared to the free antennae. Thus, the efficiency of EnT in **P-1** and **P-2** can be calculated by quenching of the antennae emission according to the following equation:

$$FRET(\%) = (1 - \frac{I_{DA}}{I_D}) \times 100\% \qquad (2\text{-}5)$$

I_{DA} and I_D are the fluorescence intensity of the donor in the presence and absence of the acceptor, respectively. FRET efficiencies (%) of 99% and 98% were obtained for **P-1** and **P-2** respectively. These large values demonstrate an efficient energy transfer in the synthesized molecules **P-1** and **P-2**.

As we know that the Pd-porphyrin is capable of generating singlet oxygen, the ability of **Pd-por-1**, **Pd-por-2**, **P-1** and **P-2** to generate singlet oxygen upon excitation at 370 nm was

evaluated by observing the characteristic luminescence of singlet oxygen at 1270 nm using a Horiba Jobin-Yvon Fluorolog-3® spectrofluorimeter equipped with InGaAs photodetector (Electro-optical Systems). As seen in **Figure 2-45**, air-saturated solution of **Pd-por-1** and **Pd-por-2** show a negligible oxygen luminescence signal upon excitation with the 370 nm light. Under the same conditions, compared with bare Pd-porphyrin, 12-fold increase in the oxygen luminescence was observed from a solution of **P-1**, and 19-fold increase was observed for **P-2** with the same concentration. This enhancement in oxygen luminescence confirms that the presence of the grafted antennae chromophores dramatically enhances the ability of the Pd-porphyrin to generate singlet oxygen through FRET effect.

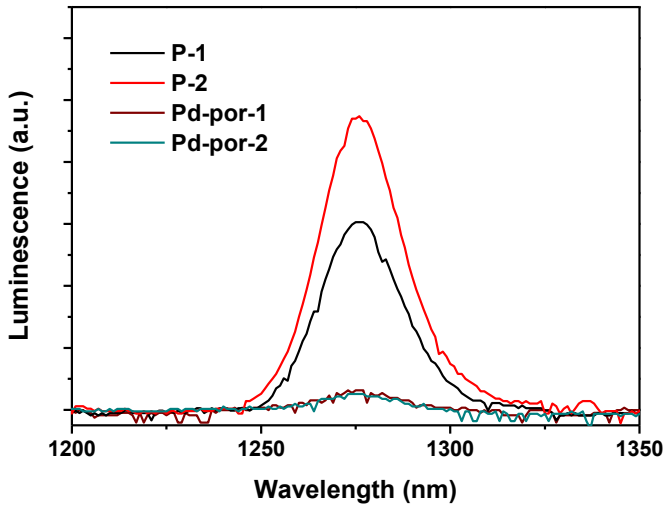

Figure 2-45. Oxygen luminescence spectra obtained from air-saturated $CHCl_3$ solutions (2×10^{-7} mol L^{-1}) of **Pd-por-1**, **Pd-por-2**, **P-1** and **P-2** with the excitation at 370 nm.

5.2. Two-Photon Properties

Upon confirmation that the antennae chromophores are capable of efficient energy transfer to the central Pd-porphyrin under one-photon conditions, two-photon excited emission spectra of **P-1** and **P-2** were recorded in deoxygenated chloroform (2×10^{-5} mol L^{-1}) using a femtosecond Ti-Sapphire laser as the excitation source. **Figure 2-46** presents the two-photon fluorescence spectra of **Pd-por-1**, **P-1** and **P-2** in chloroform pumped by femtosecond laser pulses at 220 mW at 800 nm. Compared with spectra under one-photon excitation (**Figure 2-44**), the deformation of the spectra in red part is because of using filter cut at 800 nm, which is used to cut the laser beam. All the solutions of **P-1** and **P-2** were degassed by argon before experiments. Under these conditions, the phosphorescence intensities of **P-1** and **P-2** show 12 and 28 times increase respectively relative to the emission from **Pd-por-1**. This result affirms the design of molecules **P-1** and **P-2**, in which the 2PA of the donor chromophores using near-infrared irradiation can be utilized to efficiently generate porphyrin excited states through FRET process.

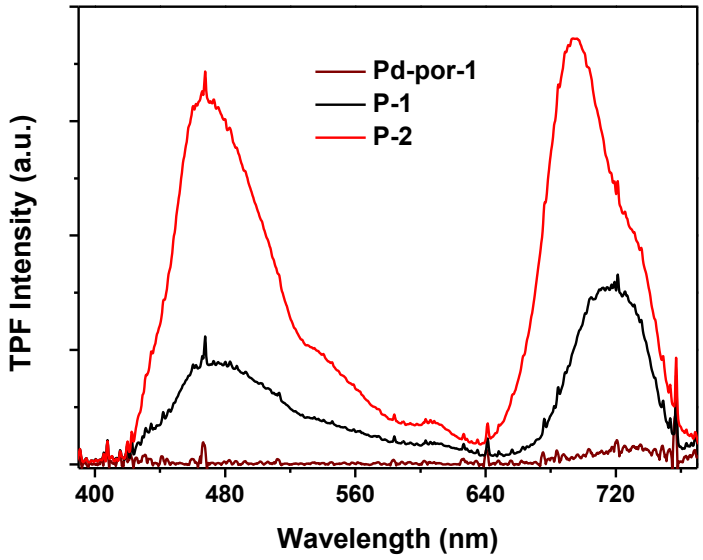

Figure 2-46. Emission spectra of **Pd-por-1**, **P-1** and **P-2** in deoxygenated $CHCl_3$ (2×10^{-5} mol L^{-1}) upon two-photon excitation (800 nm, Ti:Sa 140 fs, 220 mW). Emission spectra were recorded with filter cut at 800 nm.

To confirm that the emission observed from **P-1** and **P-2** under 800 nm laser irradiation was indeed arising from a two-photon absorption process, the two-photon excited emission spectra of **P-1** and **P-2** under different excitation powers were recorded (**Figure 2-47**, **Figure 2-48**). Then both the relative emission intensities of **P-1** and **P-2** were plotted over a range of laser powers. The quadratic dependence of emission intensity on laser power was observed

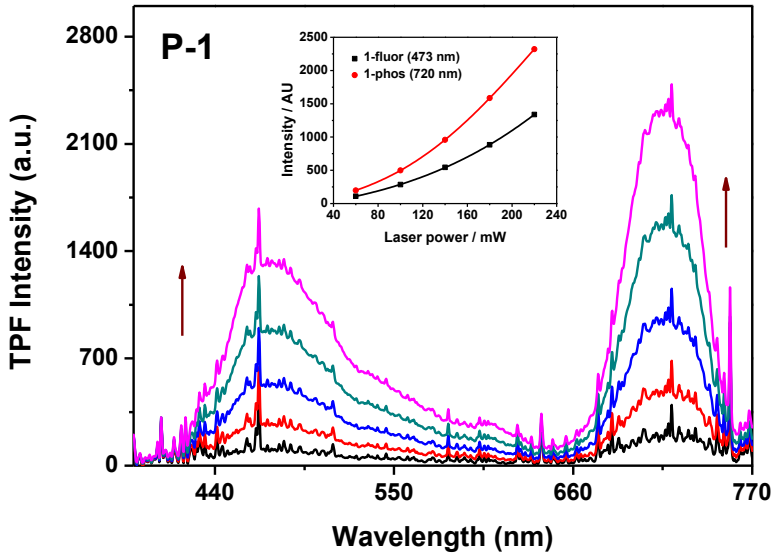

Figure 2-47. Emission spectra of **P-1** upon two-photon excitation (800 nm) at different excitation powers. Emission spectra were recorded with filter cut at 800 nm. Inset: Power dependence for residual fluorescence (red) and phosphorescence (black) of **P-1**.

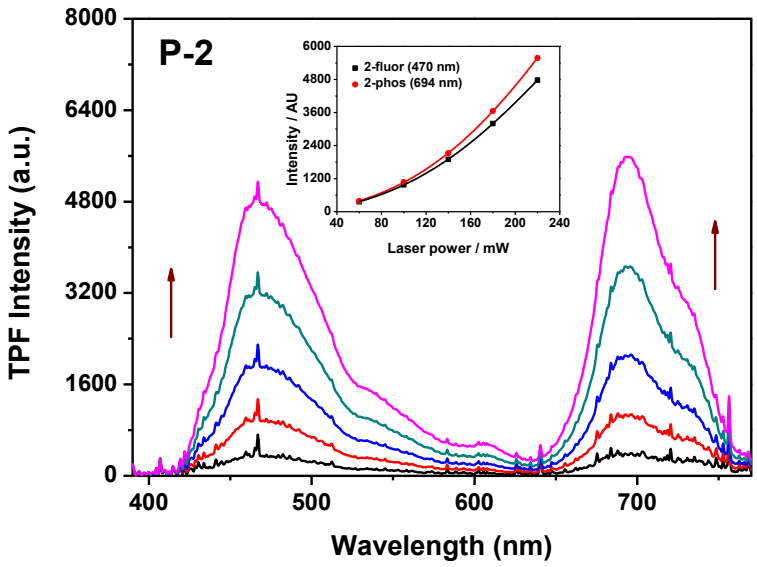

Figure 2-48. Emission spectra of **P-2** upon two-photon excitation (800 nm) at different excitation powers. Emission spectra were recorded with filter cut at 800 nm. Inset: Power dependence for residual fluorescence (red) and phosphorescence (black) of **P-2**.

for both residual fluorescence and enhanced phosphorescence in each compound of **P-1** and **P-2**. This characteristic for **P-1** and **P-2** prove their origin in the two-photon process, and also supports the fact that the oxygen sensitive Pd-porphyrin excited states arise from two-photon absorption of the peripheral donor chromophores, followed by efficient FRET to Pd-porphyrin core.

6. How to Improve the Water Solubility of P-1

After confirming the design of the two-photon absorbing oxygen sensitive probes **P-1** and **P-2**, the improvement of their water-solubility were considered to facilitate their utility in biological applications. We first tried to modify the molecule structure by introducing two hydroxyl groups on the periphery of antennae. These two hydroxyl functionalities in each antenna molecule can be further functionalized with water-soluble components (such as sulfate, PEG, glucose…), which can impart water-solubility to the entire molecular assembly. The hydroxyl groups of the antennae were protected by acetyl groups before click reaction with propargyl-Pd-porphyrin **26**. After click reaction, the obtained dendrimer could be deprotected to generate hydroxyl-functionalized compound, which have the potential to be modified with water-soluble framework. Keeping these in mind, we first proposed a new synthetic route to the hydroxyl-protected oxygen probe **P-1-OAc**, which is slightly different from that of **P-1**. The synthesis of azide-antenna **38** was achieved starting from **13**, **19** and **30** in eight steps. Briefly, as seen in **Figure 2-49**, the acetyl-protected intermediate **31** was prepared through a protection of dihydroxyl derivative **30**. Sonogashira cross-coupling between **31** and ethynyltrimethylsilane yielded the protected alkyne derivative **32**. Subsequent

deprotection was performed in the presence of dry K_2CO_3 in anhydrous methanol, generating compound **33** in excellent yield (90%). We notice that both hydroxyl and alkyne were deprotected in this step, which was not expected. The intermediate **34** was obtained from a

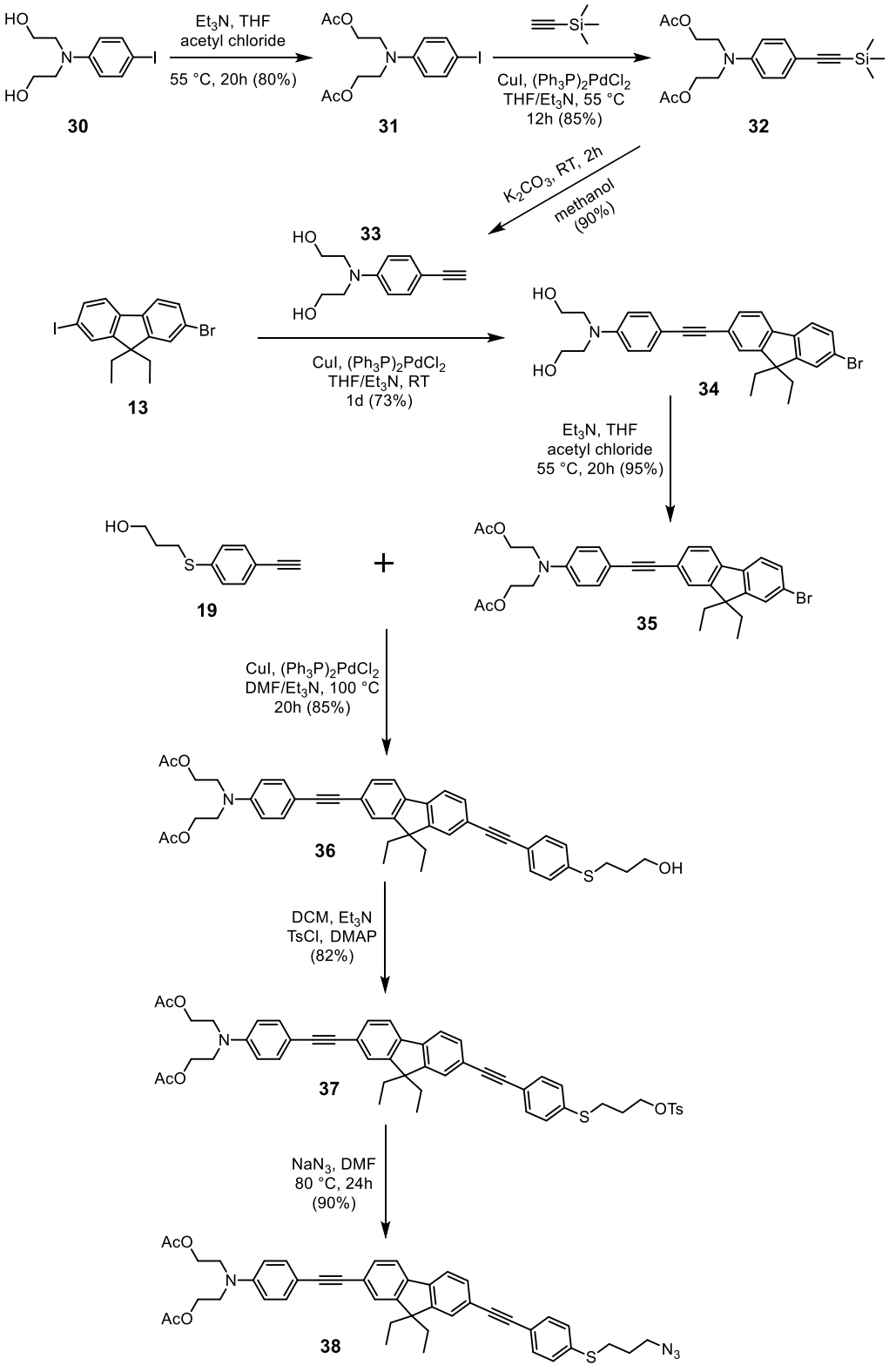

Figure 2-49. Synthesis of modified azid-antenna **38**.

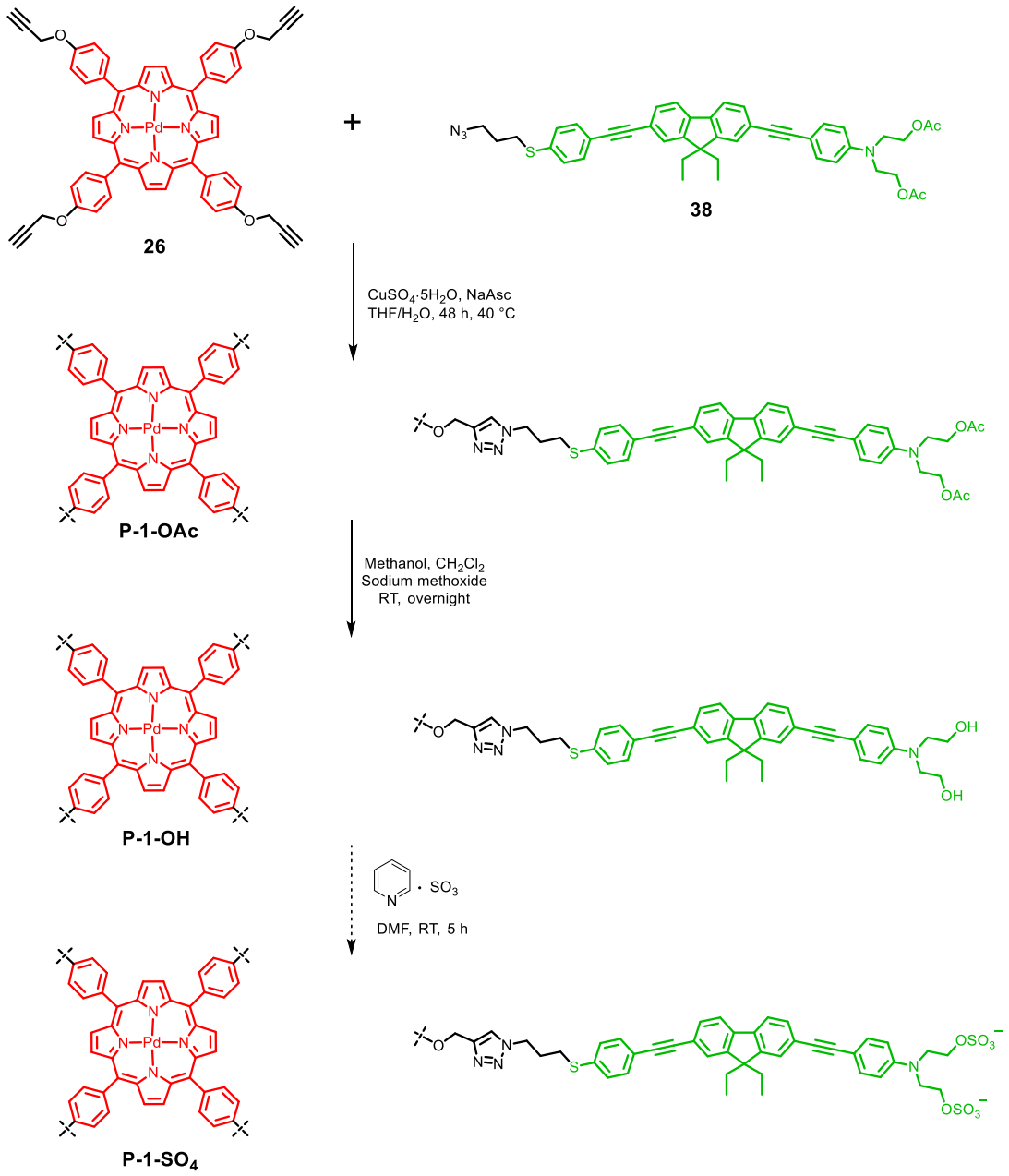

Figure 2-50. Synthesis of **P-1-OH** and **P-1-SO$_4$**.

selectively Sonogashira cross-coupling between **33** and 2-bromo-9,9-diethyl-7-iodofluorene **13**. After a new protection of hydroxyl intermediate **34** with acetyl chloride, the result **35** was converted to the derivative **36** through a third Sonogashira cross-coupling with 3-((4-ethynylphenyl)thio)propan-1-ol **19**, which was synthesized before. The reaction of **36** with tosyl chloride in the presence of triethylamine afforded hydroxyl-activated intermediate **37**. Finally, azidation of **37** with NaN_3 generated azide-functionalized antenna **38**.

After obtaining the azide-functionalized antenna **38**, highly efficient click reaction was accomplished between **38** and propargyl functionalized Pd-porphyrin **26**, yielding dendrimer **P-1-OAc** in an excellent 78% yield (**Figure 2-50**). Compounds **P-1-OAc** was well

characterized by NMR spectra. As shown in **Figure 2-50**, further deprotection of **P-1-OAc** in the presence of sodium methoxide in methanol gave the hydroxyl free molecules **P-1-OH**. It is well known that the sulfate can greatly improve the water-solubility of the hydrophobic molecule. So we tried first to do the sulfatation for the molecule **P-1-OH** with sulphur-trioxide pyridine complex in DMF.[223] Disappointedly, it didn't work so far. Considering the difficulties in the modification of molecule **P-1-OH**, new strategy will be considered.

7. Conclusion

In this chapter, two new FRET-based oxygen probes were designed and fabricated for *in vivo* two-photon microscopy. Two oxygen sensitive model complexes (**Pd-por-1** and **Pd-por-2)** were selected and studied for optimizing the two-photon absorbing chromophore, which will be finally grafted to the model complexes. First of all, four new fluorene-based two-photon absorbing chromophores (**SS**, **NS**, **NN** and **PH**) have been designed and synthesized. Their one- and two-photon photophysical properties have been investigated in details. Among these four two-photon absorbing chromophores, compound **NS** shows a higher fluorescence quantum yield (Φ = 62-68% in various solvents) compared with that of others. Two-photon excited fluorescence experiments indicate that chromophores **NS**, **NN** and **PH** display obvious two-photon absorption activity in the range of 700-690 nm. Besides, the emission spectra of **NS**, **NN** and **PH** show sufficient spectral overlap with both the B- and the Q-band of **Pd-por-1** and **Pd-por-2**, particularly in polar solvents. Moreover, phosphorescence quenching experiment demonstrate that compounds **SS**, **NS**, **NN** practically show negligible quenching effect to the phosphorescence of **Pd-por-1** and **Pd-por-2**.

The chromophore **NS** (antenna) with the highest fluorescence quantum yield, the largest two-photon cross-section at 800 nm and the largest spectral overlap with Pd-porphyrin was successfully attached covalently to a model complexes by efficient Cu(I)-catalyzed click reaction. The new probes (**P-1** and **P-2**) contain four or eight two-photon absorbing chromophore donors connected to a Pd-porphyrin acceptor *via* 1, 2, 3-triazole linkages, in which two-photon chromophores singlet excited state emission is significantly quenched. Compounds **P-1** and **P-2** demonstrate that the incorporation of a suitable donor chromophore can enhance the effective 2PA cross section of the system, allowing efficient sensitivity towards oxygen at 800 nm. At last, we tried to improve the water solubility of the designed oxygen probes by structural modification and the work is still going on.

Chapter 3. Biocompatible Nanoparticles with Aggregation-Induced Near-Infrared Emission for Biphotonic *in vivo* Vascular Imaging

1. Aggregation-Induced Emission Fluorophores Based Near-Infrared Nanoparticles for Bio-imaging

The recent years have seen the development of intense researches on organic nanoparticles based on fluorophores showing Aggregation-Induced Emission (AIE) [109, 111] for optical sensing and imaging motivated by the unique properties of such dyes. AIE molecule-based nanoprobes show several advantages over inorganic quantum dots or small soluble fluorescent molecules, such as large absorptivity, high luminosity, excellent biocompatibility, free of random blinking, and strong photobleaching resistance.[224] In this chapter, we will present the AIE phenomenon, including the proposed working mechanisms, and we will show the different NIR fluorescent AIE systems described in the literature. Then, the development of original NIR nanoprobes based on new AIE active compounds, followed by their practical application in *in vivo* two-photon imaging, will be described.

1.1. Aggregation-Induced Emission (AIE)

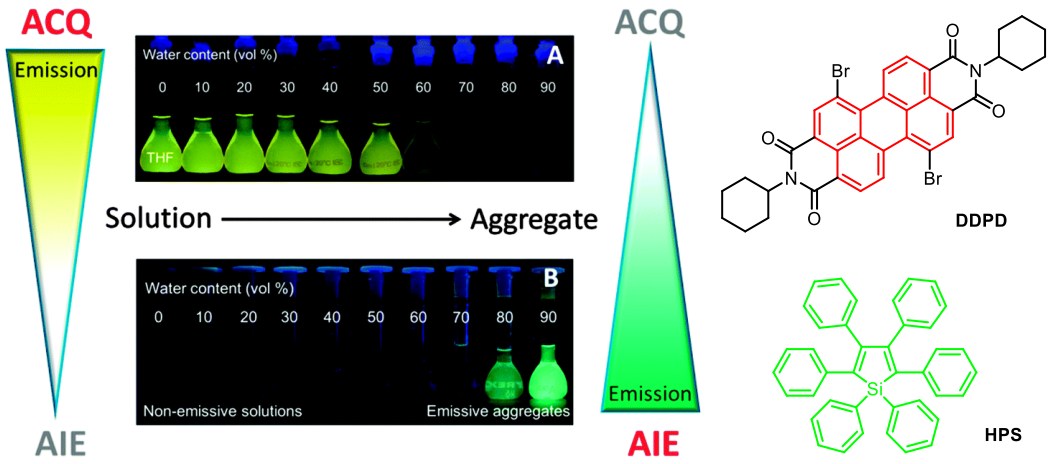

Figure 3-1. Fluorescence photographs of solutions/suspensions of DDPD and HPS in THF/water mixtures with different water contents. Taken from reference [225].

Generally, compared with the free fluorophores in dilute solution, fluorophores may show reduced, rarely enhanced emission in the aggregate form. Indeed, the emission of most

conventional fluorophores is quenched at high concentrations or in the aggregate state. This phenomenon is sometimes called concentration quenching or aggregation caused quenching (ACQ).[226] Typical example of ACQ effect is illustrated in **Figure 3-1**.[224, 227-228] The very strong emission of dilute solution (less than 10 mM) of *N*,*N*-dicyclohexyl-1,7-dibromo-3,4,9,10-perylenetetra-carboxylicdiimide (**DDPD**) can be seen in THF. When water, in which the compound is not soluble, is added to THF solution of the fluorophore (increase fraction of water f_w), the fluorescence steadily decreases until complete quenching. This is caused by precipitation, because the immiscibility of **DDPD** with water increases the local fluorophore concentration and causes **DDPD** molecules to aggregate. The **DDPD** molecule contains a planar perylene core prone to form π–π stacking interaction in the aggregate state. This prompts the formation of detrimental species as excimers, leading to the observed ACQ effect. This ACQ effect has shown great limitations in practical applications.[2]

AIE is the reverse effect about light emission associated with fluorophore aggregation.[109, 111] In this process, the fluorophores are non-luminescent when in solution and emission is induced when aggregation occurs. **Figure 3-1** shows the historical example of hexaphenylsilole (**HPS**). **HPS** is not emissive when well dissolved in a good organic solvent such as THF. With gradual addition of water into its THF solution, aggregates are formed and fluorescence is turned on when f_w reaches to 80 vol %. This concept of AIE was firstly proposed by Ben Zhong Tang as early as 2001, and has rapidly grown in importance these last ten years as proved by the huge literature associated.[229] This unique AIE phenomenon offers a straightforward solution to the ACQ problem. The main structural difference between ACQ and AIE systems is that the former usually involve large conjugated coplanar molecular structures which result in strong intermolecular interactions such as π–π stacking interactions, while the latter is generally encountered for free rotatable molecular structures. In the aggregate state, ACQ dyes normally experience red-shifted and weakened emission, while emission intensity of the AIE dyes is greatly increased without significantly shifted emission.[230]

1.2. Working mechanisms

Great efforts have been made to reveal the working mechanisms of the AIE effect since the discovery of this phenomenon. To date, three main mechanisms associated with motions were proposed supported by a great number of experimental and theoretical works. They are: Restriction of Intramolecular Rotations (RIR), Restriction of Intramolecular Vibrations (RIV), and Restriction of Intramolecular Motions (RIM).[109] Three representative AIE samples are depicted in **Figure 3-2** in order to facilitate the understanding and the difference between these different mechanisms.

The RIR mechanism has been proposed on the basis of systematic study of **HPS** (**Figure 3-2A**) and was suggested as the main cause for most of the reported AIE systems. In the **HPS** molecule, the silole core is surrounded by six phenyl rings through single bonds, which makes the molecule conformationally flexible. Thus, in solution, excited molecules lose their energy mainly by nonradiative relaxation process involving rotational motions of the phenyl rings. In

aggregate or crystal, on the other hand, the mutiple inter- and intramolecular interactions synergistically constrain the **HPS** molecules and suppress the rotations of the phenyl rings. So emission is turned on in the solid state.

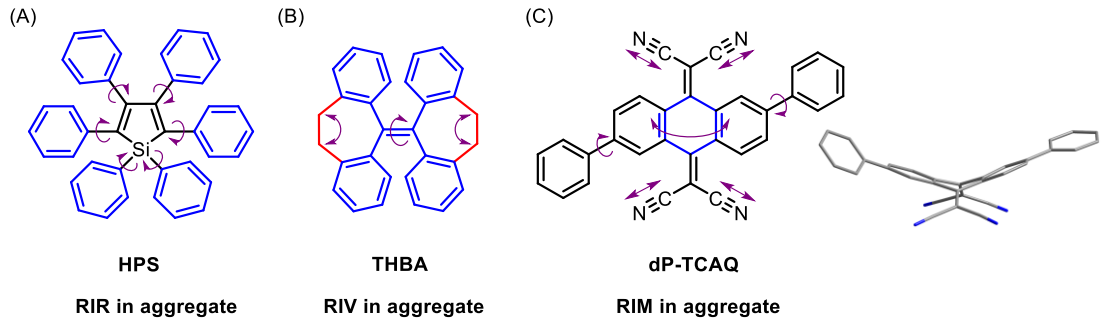

Figure 3-2. Examples of molecules whose AIE activities are ascribed to the process of (A) RIR, (B) RIV and (C) RIM.

Besides fluorophores containing rotatable units, some other compounds without rotatable moieties also show obvious AIE activity. Another mechanism was proposed to explain the AIE, that is, RIR. Typical example is **THBA** (**Figure 3-2B**), in which because the phenyl rings are locked by a pair of ethylene tethers, there are no rotatable units. For **THBA** in solution, vibrational motions play the same role as rotational motions for **HPS**, resulting in the exciton energy consumption. In the aggregate, a decrease in the vibrational motions enables **THBA** to relax radiatively, leading to the observed AIE effect.

If an AIE system containing both RIR and RIV processes, we call the working mechanism of this AIE system as Restriction of Intramolecular Motions (RIM), in which includes M (motion), R (rotation) and V (vibration). An example of **dP-TCAQ** is shown in **Figure 3-2C**.

1.3. Aggregation-Induced Emission Fluorophore Based Nanoparticles for Bio-imaging

With the ever-growing research interest in AIE materials, a huge number of AIE compounds have been developed by various research groups. Typical structures include tetraphenylethene (**TPE**), siloles, distyrylanthracene (**DSA**) and so on (**Figure 3-3**).[109, 183, 225, 230-232] The impressive advances in the construction of AIE materials were well documented in the literature and were recently reviewed in detail by B. Z. Tang *et al.*[109, 111]

Although some studies reported the use of bare aggregates of fluorophore for cellular imaging,[233-235] their poor colloidal stability in physiological medium or more complex *in vivo* media precluded their use directly as prepared. Stabilizing the aggregate is necessary. Thus various modified fluorescent nanoparticles based on AIE molecules were developed for fluorescence bio-imaging which take advantage of solid-state emission, in particular increasing the concentration of fluorophores, enhancing the emission and the photobleaching

resistance.[224]

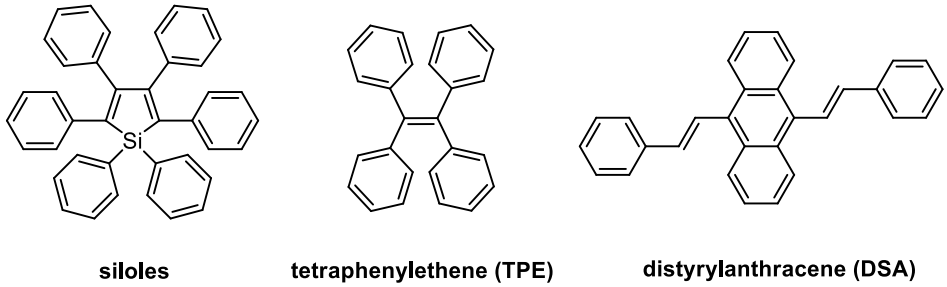

Figure 3-3. Molecular structures of siloles and tetraphenylethene (**TPE**) distyrylanthracene (**DSA**).

The typical way used to construct nanoparticles is to embed the AIE compounds into a stabilizing polymer matrix. **Figure 3-4** shows some popular encapsulation matrices. Among them, 1,2-distearoyl-*sn*-glycero-3-phosphoethanolamine-N-(polyethylene glycol) (**DSPE-PEG$_{2000}$**) and **DSPE-PEG$_{5000}$-folate** were widely used due to their good biocompatibility. To expand the functionality of nanoparticles in biology and medicine, the surface of the fluorescent nanoparticles can be functionalized with various functional groups, such as targeting biomolecules, drugs, and genes, which make them useful for imaging of complex biological structures and processes, the targeted imaging and treatment of various cancers.[227, 236-237]

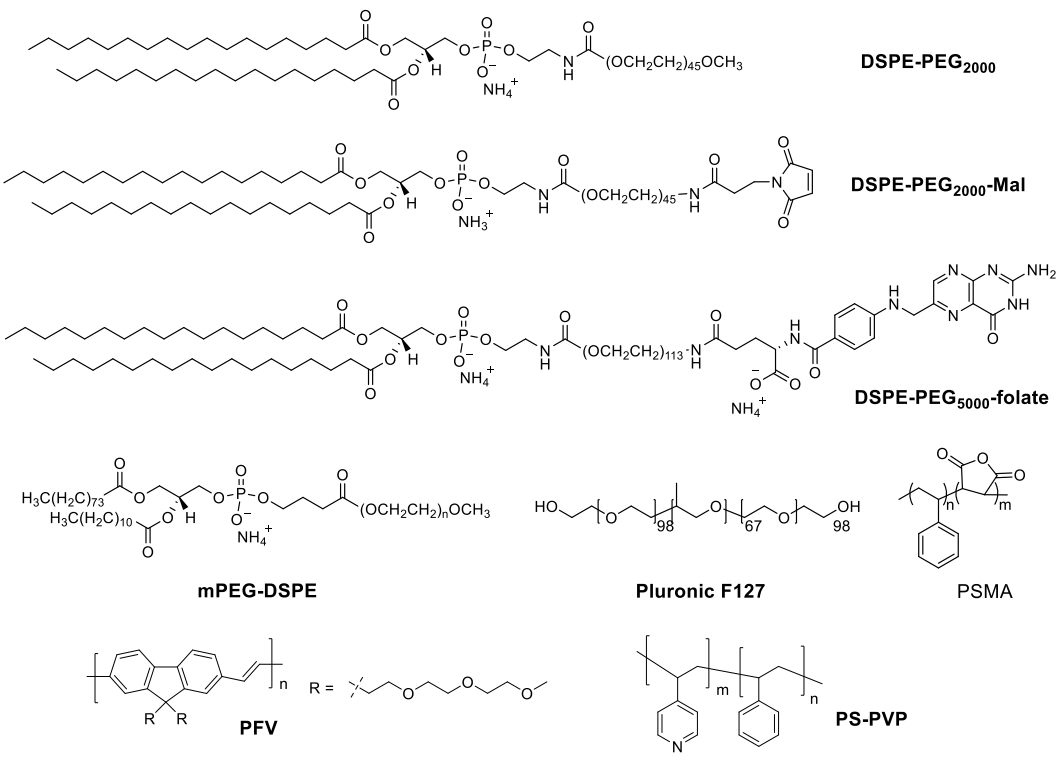

Figure 3-4. Chemical structures of **DSPE-PEG$_{2000}$**, **DSPE-PEG$_{2000}$-Mal**, **DSPE-PEG$_{5000}$- folate**, **mPEG-DSPE**, **Pluronic F127**, **PSMA**, **PFV** and **PS-PVP**.

Figure 3-5 shows the example of **TTD** nanoparticles prepared by a nano-precipitation method using maleimide functionalized DSPE-PEG polymer (**DSPE-PEG-Mal**) as the encapsulation matrix. **TTD** is a typical AIE fluorophore emitting at 660 nm in the FR. The hydrophobic DSPE segment could intertwine **TTD** to form the core, while hydrophilic PEG chains render outside towards the water phase and provide the surface maleimide group for further conjugation. The obtained TTD-NPs were further conjugated with targeting biomolecule **cRGD-SH** using click chemistry between the surface maleimide and -SH to yield **T-TTD** NPs which can specifically recognize cancer cells with overexpressed $\alpha_v\beta_3$ integrin.[238]

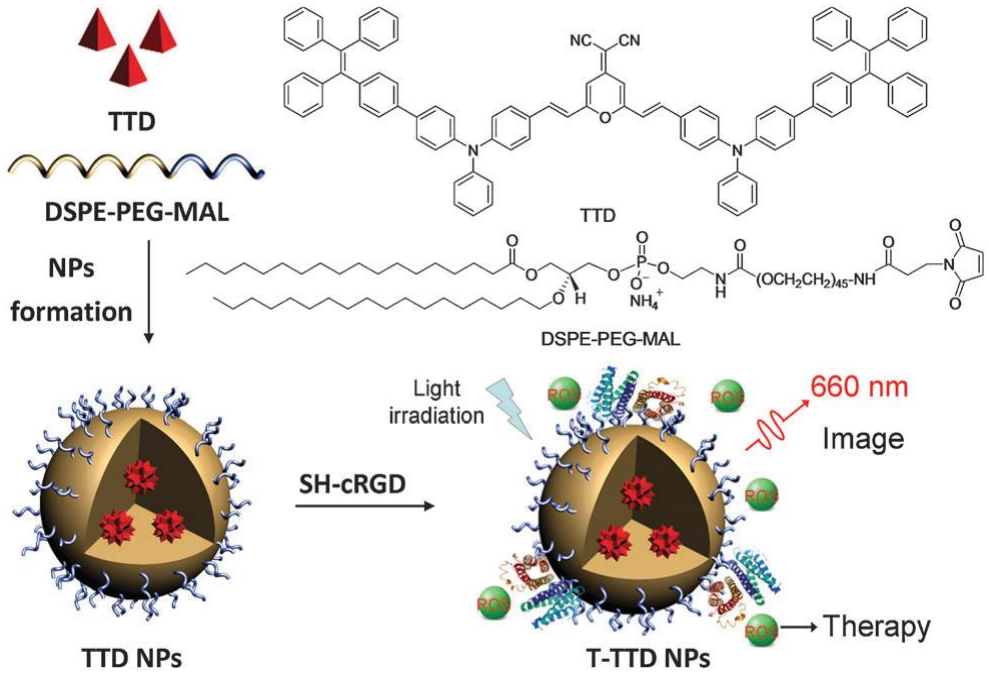

Figure 3-5. Schematic illustration of T-TTD NP formation and surface modification with the target moiety of cRGD. Taken from reference [238]

1.4. Far-Red/Near-Infrared Aggregation-Induced Emission Fluorophore and Their Nanoparticles for Bio-imaging

To date, great efforts have been made to exploit the applications of AIE active nanoparticles in bio-imaging. However, the AIE compounds that have been developed so far are mostly blue and green emitters,[109] which are not ideal for *in vivo* imaging. Owing to the benefits of FR/NIR emission in bio-applications, a number of FR/NIR AIE-active compounds were synthesized for the fabrication of nanoparticles.[237] Here, we classified FR/NIR AIE-active fluorophores into two types. The first type of fluorophores was decorated with tetraphenylethene (TPE), which covers the most widely studied FR/NIR AIE-active fluorophores. The second type of fluorophores was decorated with triphenylamine (TPA). As mentioned before, most of conventional fluorophores are usually coplanar molecules that

always show obvious ACQ effect in the aggregate state due to the strong π–π stacking interactions. In general, this ACQ effect is even worse for many FR/NIR emitting compounds, which usually possess large planar conjugated structures. Studies demonstrated that the covalent integration of TPE and TPA can efficiently improve this situation and even can transform conventional ACQ chromophores to AIE-active chromophores.

1.4.1. Far-Red/Near-Infrared Aggregation-Induced Emission Fluorophores Incorporating Tetraphenylethene Units

Tetraphenylethene (TPE) has been extensively and intensively investigated as an efficient AIE-active segment, in which the central ethylene is surrounded by four rotatable phenyl rings. The isolated TPE molecules in a dilute solution are not emissive, while they become fluorescent upon aggregate formation. The AIE activity of TPE molecules can be ascribed to the RIR process which was described above. Due to its excellent AIE behaviour, TPE moiety can be incorporated into the ACQ fluorophore structures to improve their AIE activity.

As shown in **Figure 3-6**, Tang and co-workers developed a FR/NIR emissive AIE fluorophore **TPEPBI** [228, 239] in 2012, which was constructed by conjugating TPE with 3,4,9,10-tetracarboxylic perylene bisimide (PBI). Encapsulation of **TPEPBI** with a mixture of **DSPE-PEG$_{2000}$** and **DSPE-PEG$_{5000}$-folate** led to folic acid functionalized NPs with red-NIR emission (680 nm). Studies on the staining of MCF-7 breast cancer cells and *in vivo* imaging of a tumour bearing mouse model with **BTPEPBI**-containing NPs reveal that they can serve as effective fluorescent probes for cancer cell and *in vivo* tumour diagnosis with high specificity, high photostability and good fluorescence contrast.

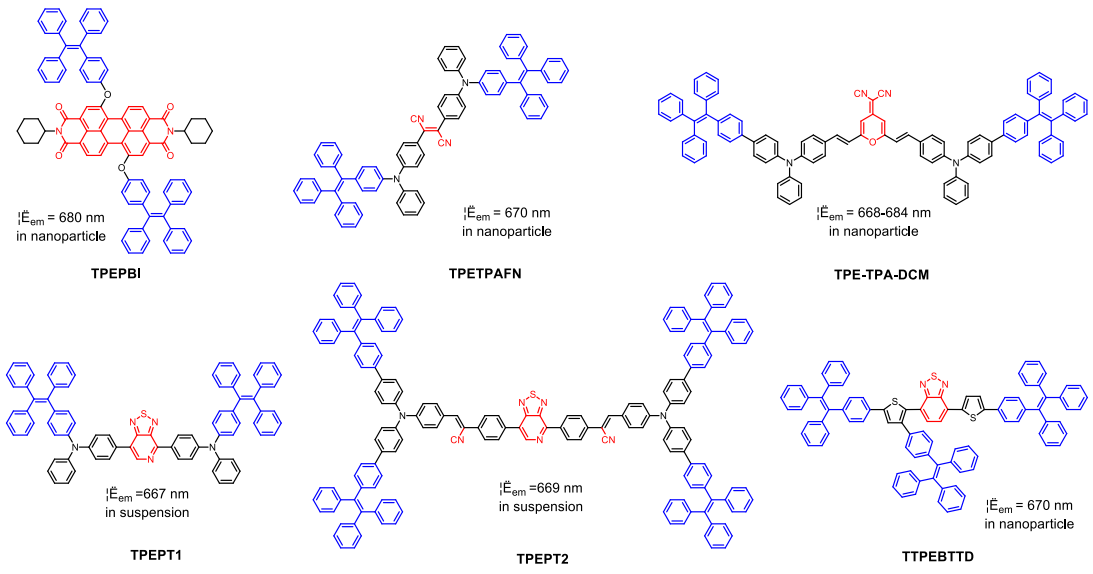

Figure 3-6. Chemical structures of FR/NIR AIE-active compounds decorated with TPE.

FR/NIR AIE-active fluorophore **TPETPAFN** was first synthesized and reported by Tang and co-workers (**Figure 3-6**).[240-241] It is an adduct of tetraphenylethene (TPE), triphenylamine (TPA) and fumaronitrile (FN). It has been widely used to construct the FR/NIR fluorescent

NPs systems for different biological research purpose. They first developed **TPETPAFN**-NPs functionalized by the cell-penetrating peptides derived from the transactivator of transcription proteins and used the resultant AIE dots as biotrackers for noninvasive long-term cell tracing.[240] Then another nanoparticles was fabricated by using poly(lactide-co-glycolide) as the encapsulation matrix and poly(vinyl alcohol) as the emulsifier through a solvent extraction/evaporation procedure.[242] The obtained polymer-encapsulated **TPETPAFN**-NPs can serve as bioprobes for *in vitro* cell imaging under one-photon excitation. Besides, they also developed many other similar **TPETPAFN**-NPs with different functionalities, which show widely applications in bio-imaging.[101, 241, 243-246]

In 2012, Tang and co-workers reported another interesting FR/NIR emissive AIE fluorophore **TPE-TPA-DCM** (**Figure 3-6**).[247] The **TPE-TPA-DCM**-NPs was synthesized using bovine serum albumin (BSA) as the polymer matrix result in uniformly sized protein nanoparticles with high brightness and low cytotoxicity. Studies on MCF-7 breast-cancer cells and murine-hepatoma-22(H_{22})-tumour bearing mouse model demonstrate that **TPE-TPA-DCM**-loaded BSA NPs show an excellent cancer cell uptake and prominent tumour-targeting ability *in vivo* due to the enhanced permeability and retention effect.[247] Moreover, **TPE-TPA-DCM**-based Lipid-PEG-Folate encapsulated NPs display excellent two-photon activity and FR/NIR emission, allowing two-photon fluorescence imaging of MCF-7 breast cancer cells and ensuring efficient penetration depth in tumour tissue (about 400 μm) upon intratumoural injection on a C6 glioma tumour-bearing nude mouse model.[244, 248] One year later, another work was carried out about **TPE-TPA-DCM** in their group, in which a fluorescence-amplified FR/NIR probe was prepared through co-encapsulation of a conjugated polymer donor (PFV) and an AIE **TPE-TPA-DCM** acceptor into biocompatible BSA NPs. The obtained **PFV/TPE-TPA-DCM** co-loaded BSA-RGD NPs show bright FR/NIR signals and specific targeting effect for both cancer cell and live animal imaging.[227]

In addition, TPE units were successfully introduced to the periphery of the 4,7-di(thiophen-2-yl)benzo-2,1,3-thiadiazole (**BTTD**) and [1,2,5]thiadiazolo[3,4-*c*] pyridine (**PT**) core to generate AIE active compounds **TTPEBTTD**,[228] **TPEPT1** and **TPEPT2**,[249] emitting FR/NIR light in the aggregate state (**Figure 3-6**). They are demonstrated to be potential FR/NIR materials for bio-imaging applications.

1.4.2. Far-Red/Near-Infrared Aggregation-Induced Emission Fluorophores Incorporating Triphenylamine Units

Besides TPE, triphenylamine (TPA) can also be incorporated into the construction of FR/NIR AIE compounds. The three phenyl rotors and the nonplanar structure of TPA make it an ideal building block for AIE fluorophore. The rotational motions of the phenyl rings in TPA aid in dissipating excited-state energy in the solution state and assist in RIR in the solid state. Furthermore, the addition of electron-rich TPA moiety can easily generate molecules with push-pull structure, shifting their emission to the NIR region, and also increasing their two-photon activity.

In 2014, as shown in **Figure 3-7**, **DPPAM** was obtained by conjugating TPA with

diketopyrrolopyrrole (**DPP**), followed by the functionalization with trimethylammonium groups. **DPPAM** is AIE-active and exhibits a distinct enhancement of the NIR emission around 703 nm owing to aggregate formation resulting of the complexation of the ammonium groups with BSA through electrostatic interactions. It was demonstrated to be a potential NIR biosensor for BSA detection and AIE-assisted bioimaging.[250] One year later, a new **DPP**-based compound **DPP-1** with large two-photon absorption cross-sections and AIE properties was reported by Liu and co-workers.[251] **DPP-1** is AIE-active in the FR/NIR range and show large Stokes shifts (3571 cm^{-1}). The nanoparticles based on this derivative have been used for cell imaging and two-photon imaging with clear visualization of blood vasculature inside mouse ear skin with a depth up to 80 μm. In 2011, a two-photon absorbing and aggregation enhanced FR/NIR emitting pyrane derivative **DFP** (**Figure 3-7**) was reported by Belfield and co-workers.[252] It was further encapsulated in silica nanoparticles (SiNPs) for two-photon bio-imaging. The new SiNPs exhibited aggregate-enhanced emission producing

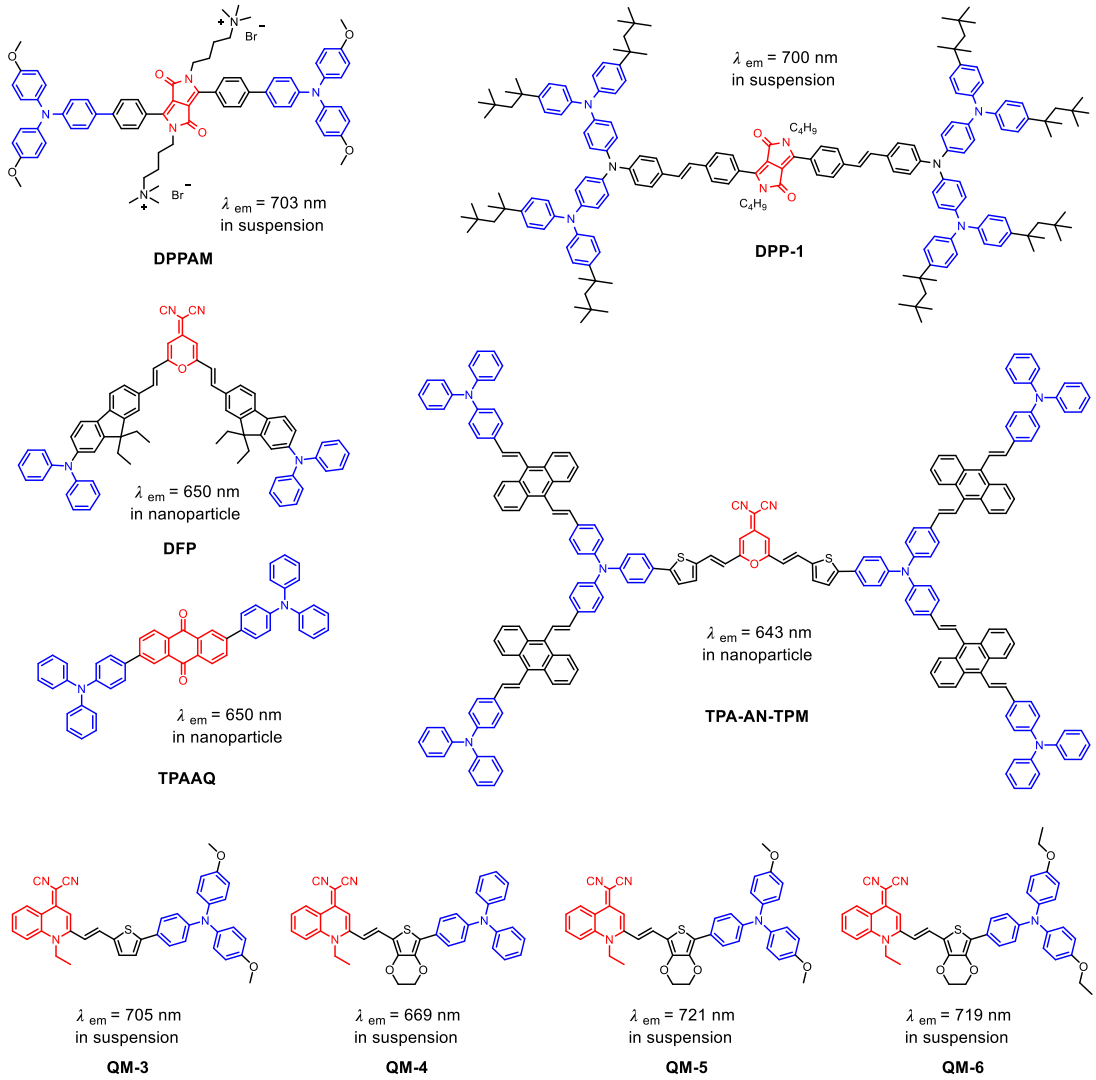

Figure 3-7. Chemical structures of FR/NIR AIE-active compounds decorated with TPA.

nearly twice as strong a signal as the isolated dye, a 3-fold increase in two-photon absorption relative to the **DFP** in solution, and approximately 4-fold increase in photostability. The surface of the nanoparticles was further modified with a folic acid derivative for targeting tumour. These **DFP**-encapsulated SiNPs were demonstrated as efficient probes for *in vivo* fluorescence bioimaging upon intravenous administration into mice bearing HeLa tumours. Two-photon fluorescence microscopy bioimaging provided three-dimensional (3D) cellular-level resolution imaging up to 350 μm deep in the HeLa tumour. In 2014, Tian and co-workers reported a new large conjugated pyran derivative,[246] which was fabricated by coating disc-like red emissive fluorophores with propeller-shaped AIE fluorophores. The AIE dots **TPA-AN-TPM**@PS-PVP was prepared from **TPA-AN-TPM** by using PS-PVPas the encapsulation matrix. The obtained AIE dots with high fluorescence quantum yield can be applied effectively in cytoplasm and nucleus imaging.

AIE compound **TPAAQ** is an adduct of anthraquinone (AQ) and TPA (**Figure 3-7**). Based on this compound, a highly stable NIR fluorescent organic nanoprobe (**NFO**-NPs) was fabricated *via* well-documented reprecipitation method.[235] **NFO**-NPs are demonstrated to be ideal fluorescent probes for noninvasive long-term cellular tracing and imaging applications. For example, the strong red fluorescence from the **NFO**-NPs can still be clearly observed in A549 human lung cancer cells after incubation for six generations over 15 days.

Very recently, a series of push-pull quinoline–malononitrile (**QM**) derivatives were designed and synthesized by Zhu and co-workers.[234] Among them, **QM-3** and **QM-6** show obvious AIE effect in FR/NIR field (**Figure 3-7**). Their nanoaggregates were prepared by precipitation. The result indicates that the morphology of organic nanoaggregates could be controlled by changing the electron donor groups and thiophene π-bridge. Impressively, the spherical shape of NIR **QM-5** nanoaggregates exhibits excellent tumour-targeted bioimaging performance after intravenously injection into mice, but not the rod-like aggregates of others.

2. Objectives

2.1. Previous Works in the Laboratory

Our group has been working on the development of different series of small push-pull dipolar compounds exhibiting intense fluorescence properties in the solid state, in the crystal, and also in self-aggregate due to AIE properties. In the last several years, we have developed two families of interesting dyes emitting in the red to NIR region in the solid state.[253-255] As shown in **Figure 3-8**, a first series of push-pull dipolar molecules based on dicyanoisophorone with various donor structures was developed and studied in 2011. They all show impressive NIR solid state fluorescence in the range 716–791 nm. X-ray crystallographic studies have correlated the solid state emission to specific molecular arrangements in the solid.

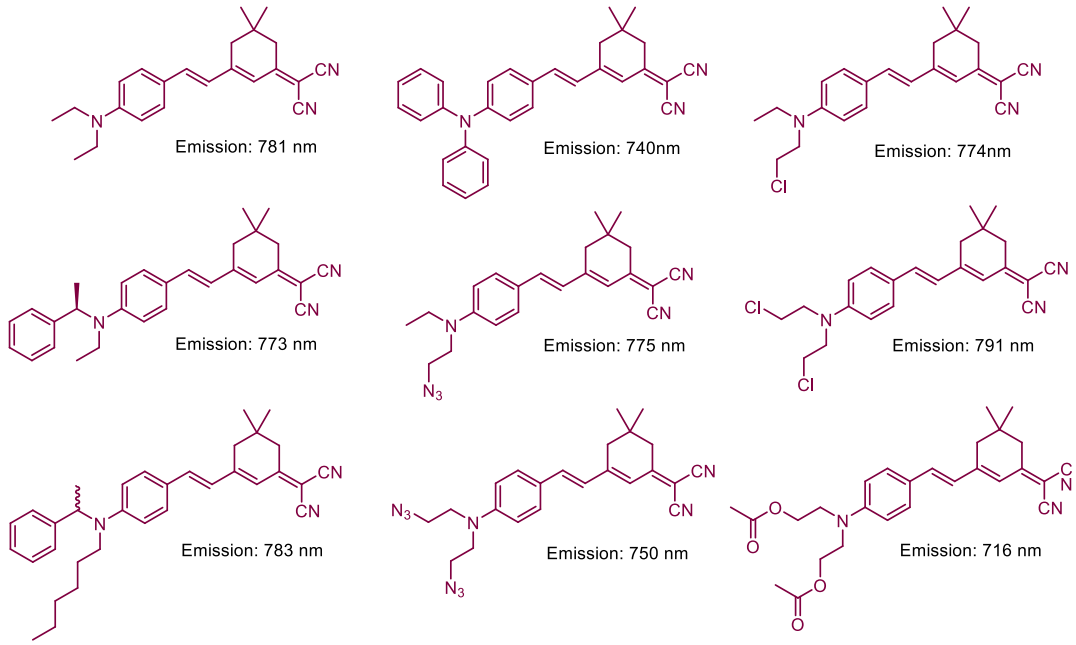

Figure 3-8. Solid-state NIR emitters based on dicyanoisophorone with variation of donor structure.[253]

Very recently, we developed another series of small push–pull dipolar fluorophores based on 2-dicyanomethylene-3-cyano-4,5,5-trimethyl-2,5-dihydrofurane (TCF) as electron accepting group (**Figure 3-9**). They exhibit interesting solid state emission and particularly AIE properties in the red–NIR range very different from one compound to another, highlighting the role of the number and of the position of the methoxy electron-donor groups. The result demonstrated that careful molecular engineering around the dipolar structure enables not only fine tuning in the emission wavelength but also considerable enhancement of the fluorescence quantum yield (**Figure 3-9**). However, almost all of these TCF-based compounds show solid emission in the FR below 660 nm except two compounds showing emission above 700 nm. Even blue-shifted emission (below 622 nm) was observed for their aggregation-induced emission. In addition, the straightforward syntheses we have developed give access to grams of fluorescent push-pull compounds, obtained in limited number of steps, high yield and with high purity. Preliminary studies performed on different cell lines showed the very limited toxicity of TCF-based probes.

We also show that optimization of the respective strength of the electron-donor and electron acceptor groups as well as modification of the peripheral groups allow identifying interesting small dipolar molecule based on carbazole as electron-donating group (**Figure 3-10**), which displays high solid state fluorescence (Φ = 11%) with emission wavelength at 740 nm. Interestingly, the result indicated that this new fluorophore display significant aggregation-induced emission when nano-precipitated in water with a 375 enhancement of fluorescence at 678 nm.[254]

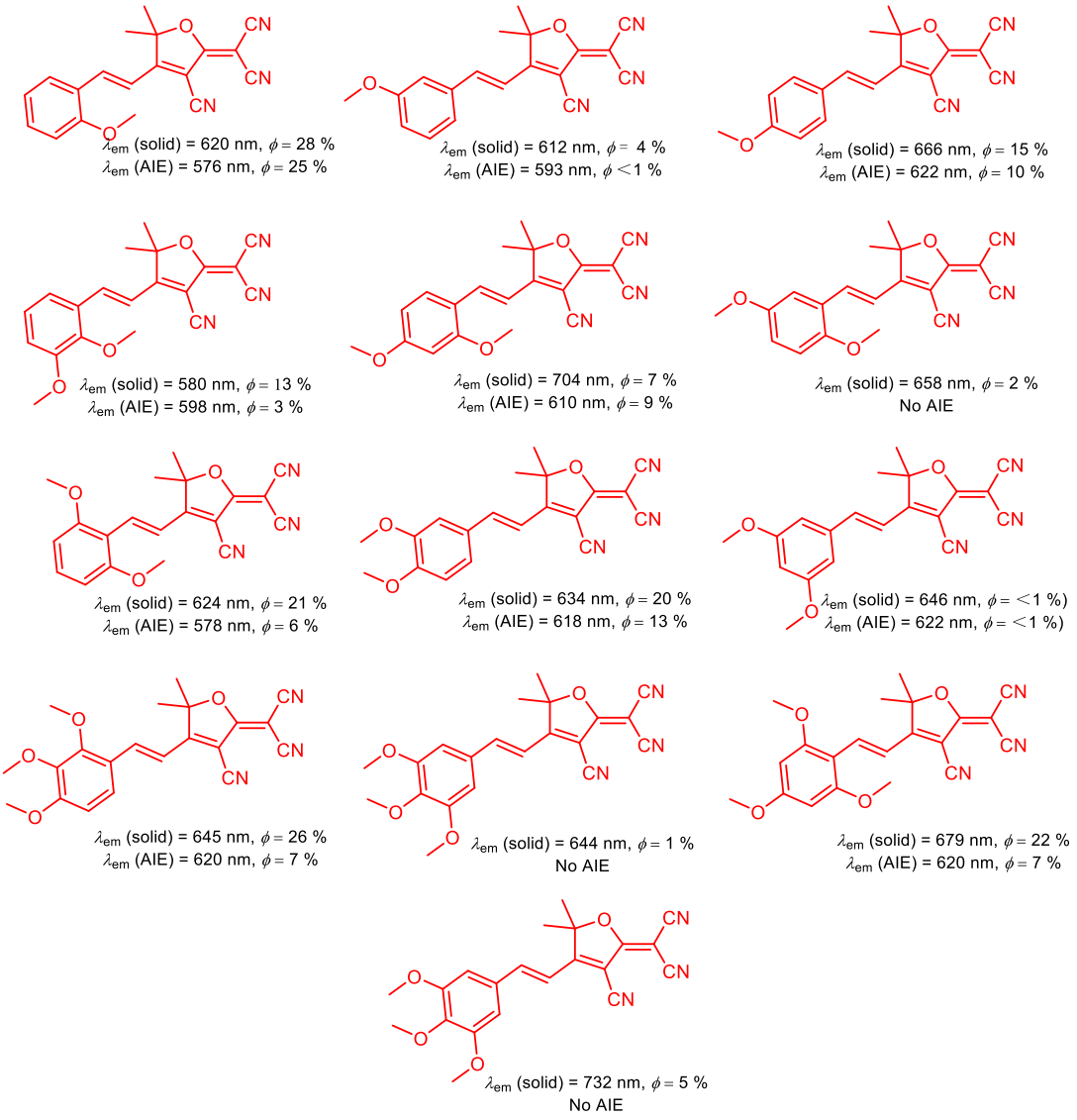

Figure 3-9. Small push-pull fluorophores based on TCF as acceptor showing AIE properties with variation of donor group.[254-255]

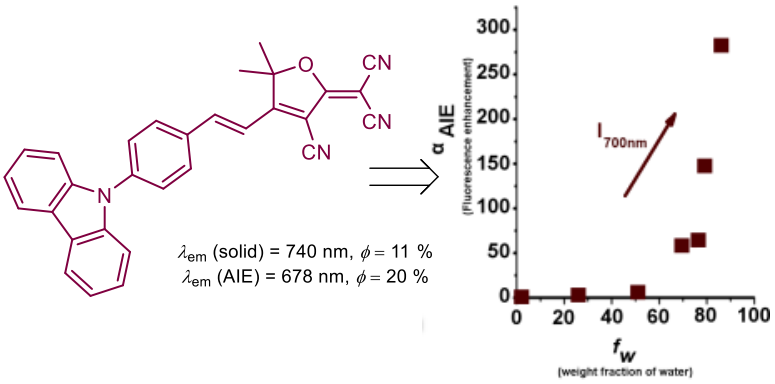

Figure 3-10. Small dipolar molecule based on carbazole as electron-donating group for AIE.[254]

2.2. Design of New Dipolar Compounds

As already noticed, excitation and emission spectra of the AIE fluorophores reported are usually limited to the visible region. Only a few of efficient NIR AIE fluorophores have been reported so far and they were reviewed above. As a continuing project in our group, we aim to develop new NIR AIE fluorophores for the fabrication of fluorescent organic nanoparticles for practical application in two-photon *in vivo* imaging. The main challenge here will be to further shift the emission of the AIE emitter's wavelength to the NIR by keeping AIE feature. Since the dipolar fluorophores developed previously in the laboratory are mainly short conjugated systems employing phenyl ring as the bridge, most of them exhibit weak two-photon absorption properties. So another challenge is to endow the AIE fluorophore with good two-photon absorption properties in the range 650–1000 nm by molecular engineering. The two-photon absorption property of AIE fluorophore not only can bring both the excitation and the emission in the biological transparency window but also can achieve three-dimensional (3D) imaging in biological objective.

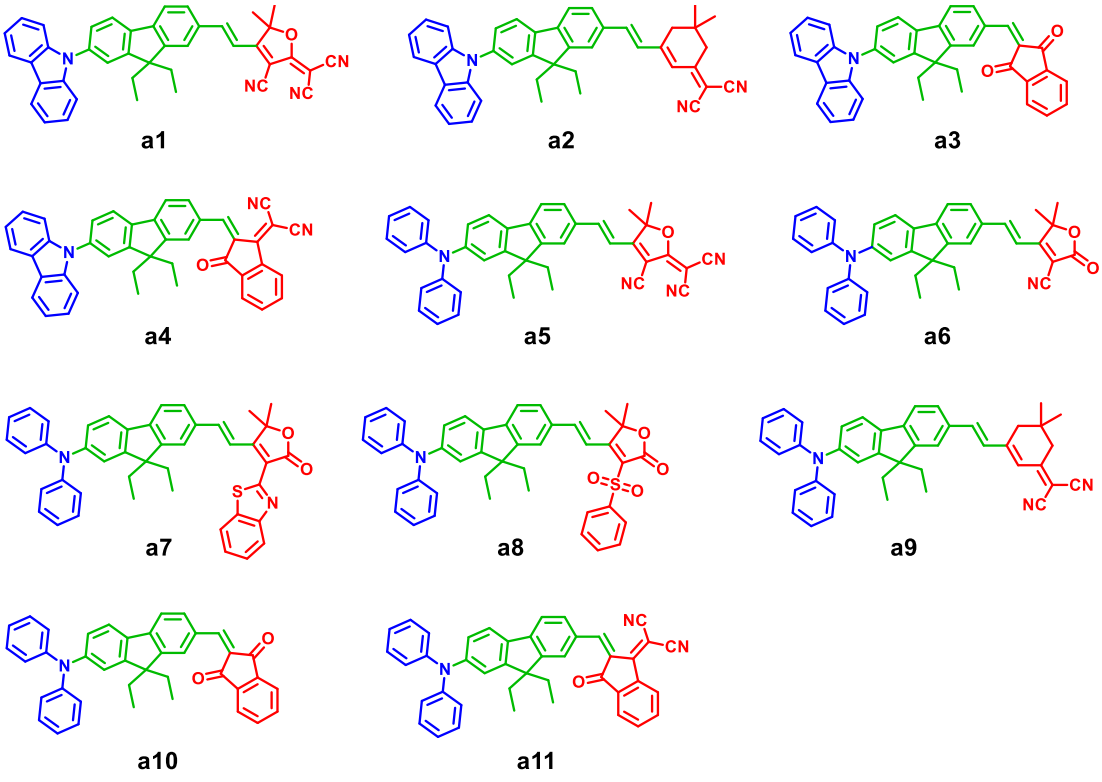

Figure 3-11. Molecular structures of **a1**−**a11**.

It is well known that the effective way to shift the emission wavelength is the increase of the push-pull strength of fluorophore. In addition to this, the emission can also be red-shifted by increasing the conjugation length, which can simultaneously improve the two-photon absorption properties of fluorophore. Based on the previous work in the laboratory, a new

series of fluorene-based push-pull fluorophores were designed (**Figure 3-11**). In the molecules, we perform a molecular engineering around the fluorophore structure by elongating the conjugated system, *i.e.*, replacing the initial phenyl ring by fluorenyl ring. Then change in the nature of the electron-donating moiety was performed employing group carbazole or diphenyl amino, known for enhancing AIE effect.[109, 254, 256-257] Systematic variation of the electron-accepting end was carried out including new original electron withdrawing groups derived from the cyano-furan cycle. The different pair of donor/acceptor in each compound will be optimized to obtain compound with both NIR aggregation-induced emission and good two-photon behaviour. In addition, introduction of two ethyl groups on fluorenyl ring will help to prevent the significant π–π stacking between the molecules in the solid state (powder, crystal and aggregate), and may favour the AIE phenomenon in the aggregates.

3. Synthesis and Spectroscopic Studies of Push–Pull Two-Photon Absorbing Chromophores

3.1. Synthesis of the Molecules

This section will present the employed strategies in the synthesis of the new designed dipolar molecules and their intermediates. Generally, the strategy in the construction of this kind of traditional dipolar molecules is the formation of C=C bond in the molecules, which was achieved by efficient one-pot Knoevenagel condensation between the corresponding aldehyde donor and active methylene or methyl acceptor. Aldehydes of carbazolylfluorenyl (**41**) and diphenylaminofluorenyl (**46**) were chosen as donor building blocks with different π-electron donating strengths. As the counterpart, seven acceptor building blocks (**47**-**53**) were selected among active methylene or methyl compounds that contain different electron-accepting substituents (cyano, carbonyl, benzothiazolyl and phenylsulfonyl).

For synthesizing molecules **a1**−**a11**, two aldehydes and seven acceptor moieties were required. The acceptor indane-1,3-dione **48** was obtained commercially and the other six acceptor groups were previously synthesized in our laboratory.[254] The synthesis of two aldehyde derivatives **41** and **46** will be described below.

The precursor carbaldehyde **41** was obtained in two steps starting from 2-bromo-7-iodo-9,9-diethylfluorene **39** (**Figure 3-12**). The *N*-arylation of carbazole was carried out by the Ullmann condensation of carbazole with 2-bromo-7-iodo-9,9-diethylfluorene **39** to give 9-(7-bromo-9,9- diethylfluoren-2-yl)carbazole **40** in 58% yield.[258] Lithiation of **40** with n-BuLi, followed by reaction with dimethylformamide (DMF) and subsequent acidic hydrolysis, provided aldehyde derivative **41** in 70% yield.

As shown in **Figure 3-13**, the aldehyde derivative **46** was synthesized in three steps starting

from **42**, as previously reported.[32] The starting material 2,7-dibromo-9*H*-fluorene **42** was first alkylated with bromoethane, giving 2,7-dibromo-9,9-diethylfluorene **45** in an excellent yield of 95%. Upon lithiation with a stoichiometric amount of n-BuLi, followed by reaction with DMF and hydrolysis, **43** generated 7-bromo-9,9-diethylfluorene-2-carbaldehyde **44** in 89% yield. Aryl amination of **44** was readily performed using Buchwald−Hartwig amination coupling in the presence of $Pd(OAc)_2$ and Cs_2CO_3, to afford aldehyde **46** in 85% yield.

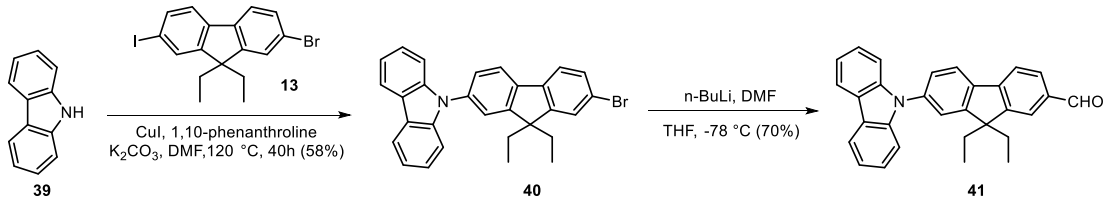

Figure 3-12. Synthesis of aldehyde derivative **41**.

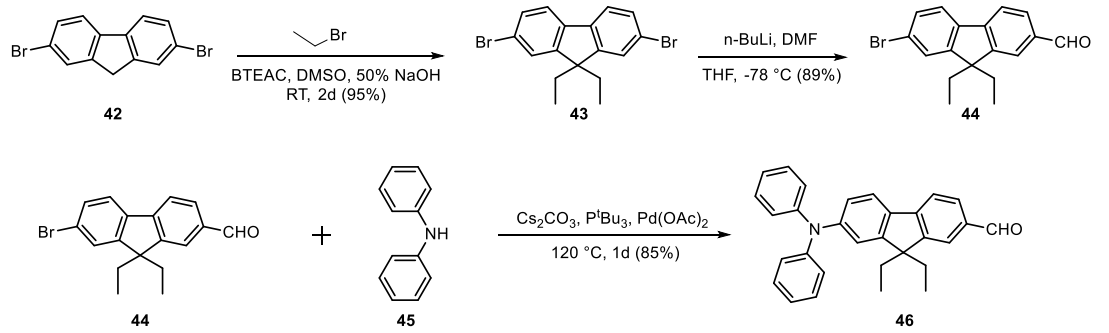

Figure 3-13. Synthesis of aldehyde derivative **46**.

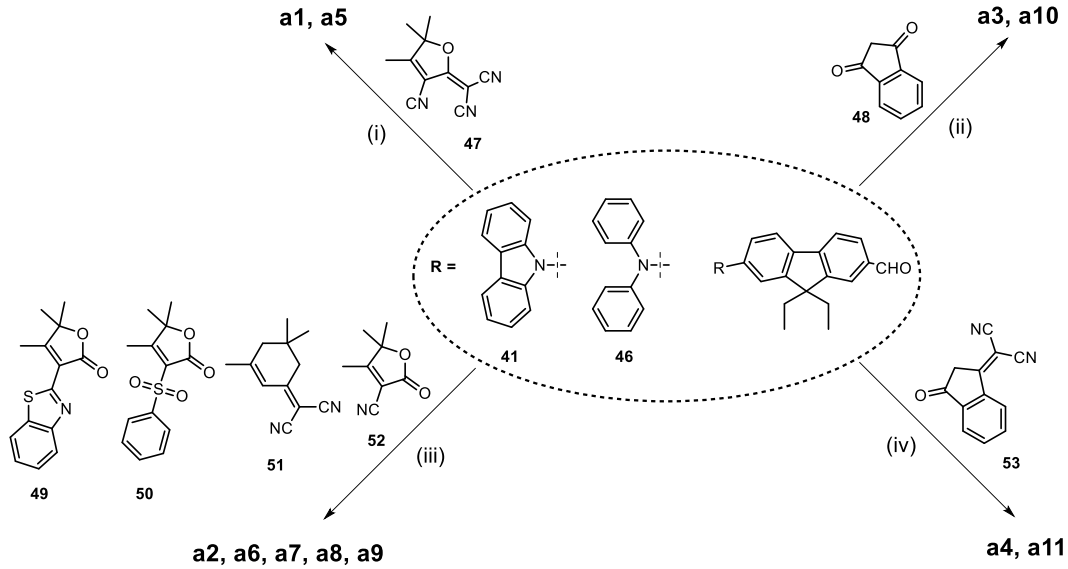

Figure 3-14. Synthetic pathway of push−pull chromophores **a1**−**a11**. (i) ethanol, piperidine, 80 ℃, overnight; (ii) ethanol, piperidine, 80 ℃, 3h; (iii) acetonitrile, piperidine, 80 ℃, overnight; (iv) ethanol, 60 ℃, 3h.

The synthesis of push−pull chromophores are presented in **Figure 3-14**. The key step in the synthesis of compounds **a1**−**a11** was the Knoevenagel condensation of aldehydes with acceptors. The reaction was performed in ethanol or acetonitrile in the presence of catalytic amounts of piperidine. All the compounds **a1**−**a11** were synthesized in good yields. They were carefully purified and fully characterized mass spectroscopies and by NMR. In particular, ^{1}H NMR spectra confirmed the expected molecular structures with only *E* configuration obtained as prove by the value of coupling constant between the two vinylic proton ^{3}J closing to 16 Hz, characteristic of a J_{trans} constant.

3.2. DFT Calculations

To better understand the relationship between the optical properties and electronic structure, density functional theory (DFT) calculations were carried out using the Gaussian 03 program. The nonlocal density function of B3LYP with 6-31G basis sets was used for the calculations.

Figure 3-15 shows the ground-state optimized geometries for molecules **a1**–**a11**. We can see that, for all molecules, the nitrogen atom in the carbazolyl or diphenylamino is essentially coplanar with the fluorene ring, resulting in a good delocalization of the electron from nitrogen to the whole π conjugation. In the optimized geometries of molecules, the nitrogen atom, the fluorene core and the acceptor group were located essentially in the same plane except for compounds **a4** and **a11**, which exhibit twisted geometries due to the big steric hindrance between dicyanovinyl group and the fluorene core with the dihedral angle between fluorene ring and indane ring of 34.9 °for **a4** and 34.8 °for **a11** (**Figure 3-15**).

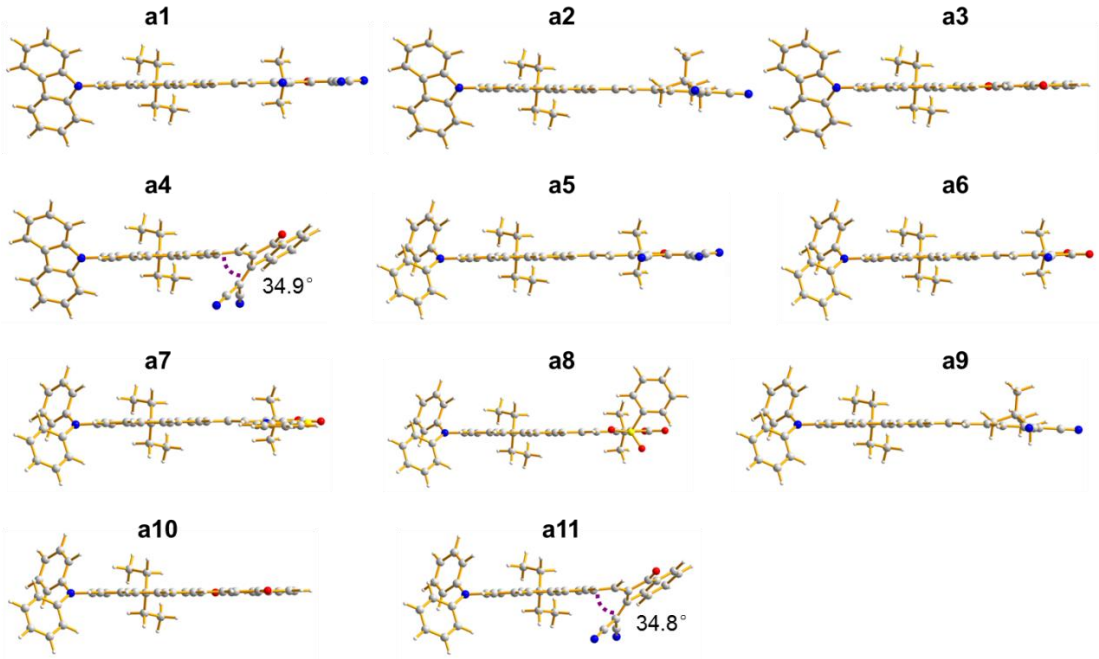

Figure 3-15. DFT optimized geometry of compounds **a1**–**a11**.

The optimal molecular orbitals of the ground state for the dyes **a1**–**a11** are shown in **Figure 3-16**. The HOMOs of all the compounds are mainly dominated by an electronic density mainly distributed on donor diphenylamino or carbazolyl units, while the LUMOs correspond mainly to a distribution on the acceptor groups. This allows expecting remarkable increase of the charge transfer between the ground and excited states. Upon excitation on the lowest excited state, the electron transition, which corresponds generally mainly to HOMO-LUMO transition, is accompanied by a charge transfer from the diphenylamine or carbazole to the acceptor moieties. The calculated band gaps of compounds are in the range of 2.12–2.68 eV, and the values of **a5** and **a11** are smaller than those of other compounds.

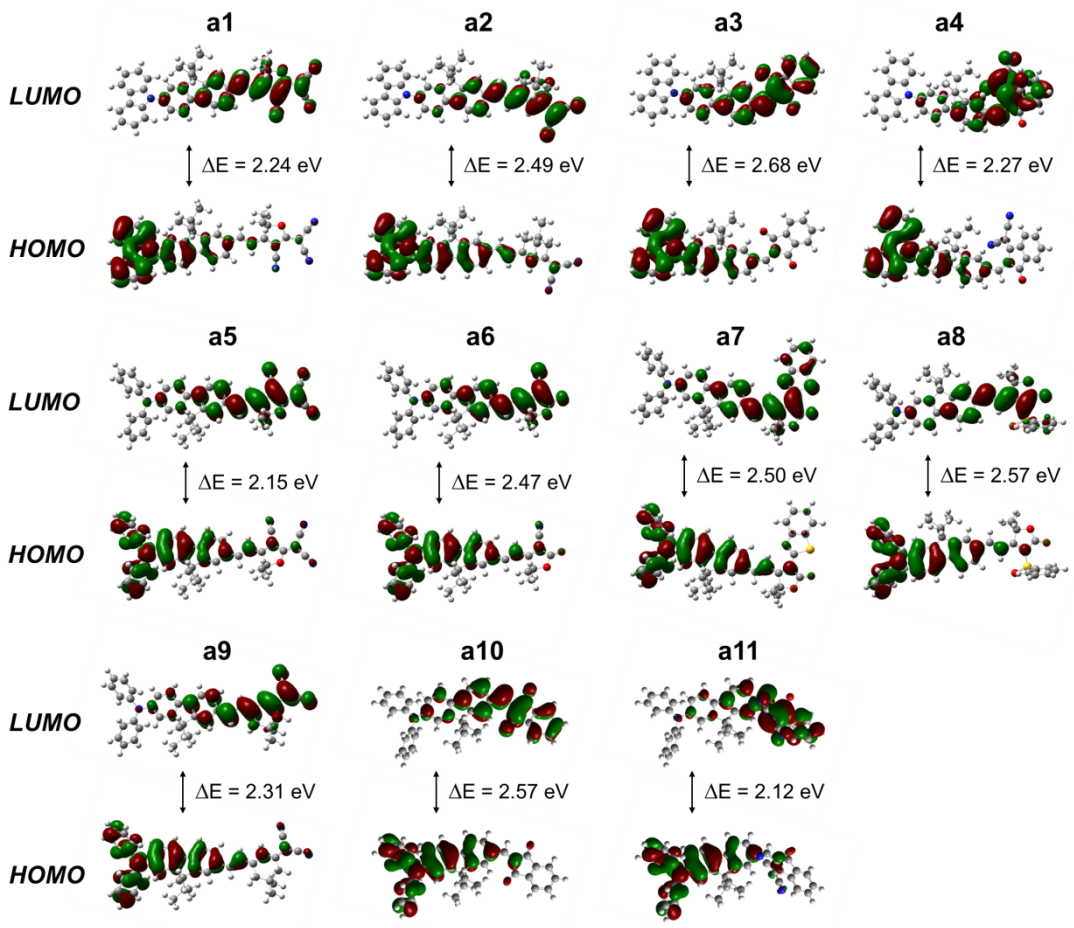

Figure 3-16. Molecular orbital diagram for compounds **a1**–**a11.**

3.3. Linear Optical Properties in Solution

3.3.1. Absorption and Emission Properties

The linear absorption and emission properties of dipolar compounds **a1**–**a11** were recorded in chloroform at a concentration of 1×10^{-6} mol L^{-1}. The relevant photophysical data are collected in **Table 3-1**, including the fluorescence quantum yields (Φ_f) and lifetimes (τ_{exp}).

Table 3-1. Photophysical data of compounds **a1**–**a11** in chloroform.

Sample	λ_{max} [a]	ε_{max} [b]	λ_{em} [c]	$\Delta\nu$ [d]	Φ_f [e]	τ_{exp} [f]
a1	485	2.41	689	6230	0.26	2.04
a2	443	3.48	623	6392	0.03	0.28
a3	439	3.08	590	5829	0.01	--
a4	495	2.53	--	--	--	--
a5	580	4.11	771	4865	0.13	1.09
a6	496	3.20	697	5997	0.55	2.96
a7	482	2.93	675	6019	0.39	2.76
a8	485	3.06	697	6474	0.55	3.00
a9	495	4.11	720	6596	0.40	2.21
a10	509	3.73	677	4897	0.58	2.78
a11	587	3.25	--	--	--	--

[a] Absorption in nm (1×10^{-6} mol.L^{-1}). [b] Molar absorption coefficient in 10^4 mol^{-1}.L.cm^{-1}. [c] Emission in nm (1×10^{-6} mol L^{-1}). [d] Stokes shift in cm^{-1}. [e] Quantum yields determined by using rubrene in methanol (Φ = 27 %) as the standard.. [f] Fluorescence lifetime (ns).

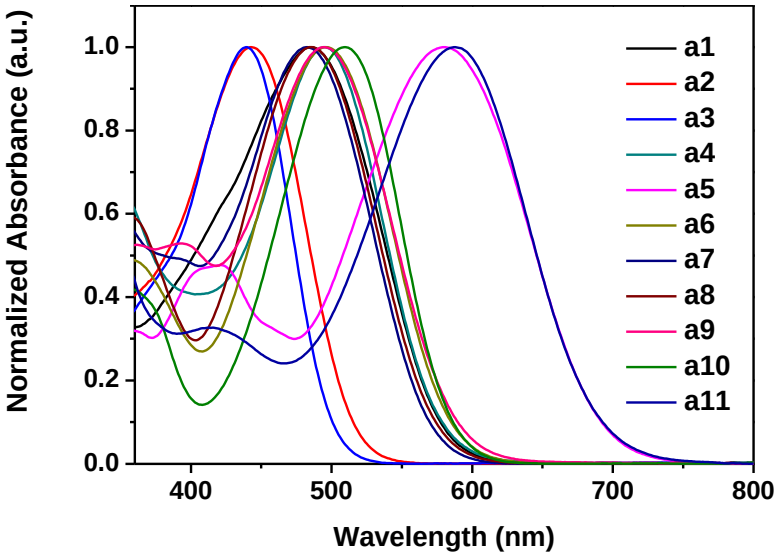

Figure 3-17. Normalized absorption spectra of compounds **a1**–**a11** in chloroform.

The absorption spectra of compounds **a1**–**a11** in chloroform are shown in **Figure 3-17**. All spectra are characterized by a strong and broad structureless absorption band in the visible range. These absorption bands originate from the intramolecular charge transfer (ICT) transitions in push-pull dipolar molecules. By changing the donor or acceptor moiety, the maximum absorption wavelengths range from 439 nm for **a3** up to 587 nm for **a11**. Obviously, compounds **a2** and **a3** bearing a weaker electron-donating group display a much blue-shifted absorption at around 440 nm, whereas compounds **a5** and **a11** bearing a stronger electron-accepting group show a largest red-shifted absorption at around 580 nm. The other compounds show the similar absorption in the range 482–509 nm. As shown in **Table 3-1**, the

molar absorption coefficients, ε, of compounds **a1**–**a11** are of the same order of magnitude with the values between 24100 and 41100 $mol^{-1}.L.cm^{-1}$.

Upon excitation at their maximum absorption wavelengths, broad emission spectra were observed in chloroform, changing from 590 nm for **a3** to 771 nm for **a5**, which are characteristic of ICT nature of the dipolar molecules. As shown in **Figure 3-18**, the emission colour of the dipolar series with various donor/acceptor groups covers a wide spectral range up to the NIR region (above 700 nm). Quantum yields of fluorescence (Φ_f) for all compounds were measured in dilute chloroform solution by using rubrene in methanol (Φ = 27 %) as the standard and the data are reported in **Table 3-1**.

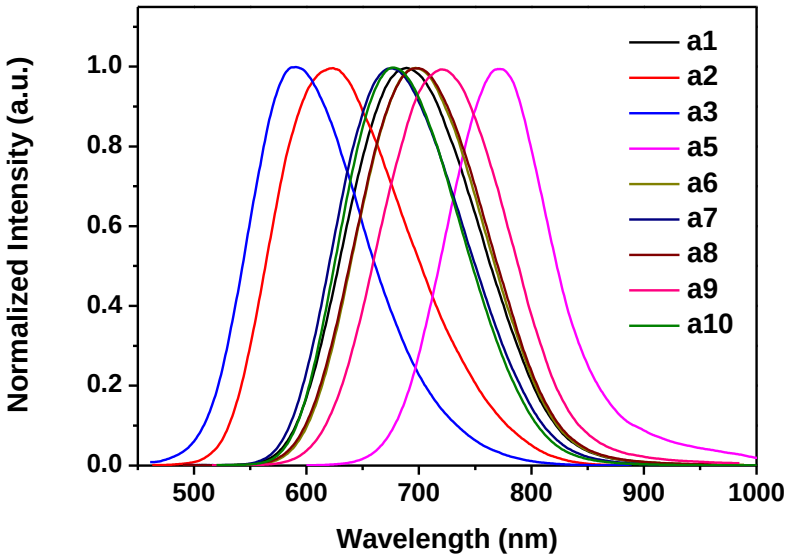

Figure 3-18. Normalized emission spectra of compounds **a1**–**a3** and **a1**–**a10** in chloroform.

The compound **a5** containing a diphenylamino donor group and a 2-dicyanomethylene-3-cyano-4,5,5-trimethyl-2,5-dihydrofurane (TCF) acceptor group is the most red-shifted molecule of the family, showing an interesting Φ_f of 13% at 771 nm. Moreover, as shown in **Table 3-1**, fluorophores **a1** and **a6**–**a10** possess excellent Φ_f values (26%-58%) in the FR/NIR region (675–720 nm). However, the carbazolyl substituted compounds **a2** and **a3** showed very low fluorescence quantum yields (3% for **a2**, 1% for **a3**), which are much weaker than their diphenylamino analogues (**a9** and **a10**). It was found that the compounds **a4** and **a11** are not emissive in any organic solvent. It is probably because of the significant deviations from planarity of the electron-acceptor group (1-(dicyanomethylene)-3-indanone), which is in agreement with the DFT calculation results.

For the same acceptor units, diphenylamine-based derivatives showed red-shifted absorption and emission relative to the corresponding carbazole analogue, confirming the fact that diphenylamine is a stronger π-charge donor than carbazole. Compared to the lone pair electrons of nitrogen in diphenylamine, those of carbazole are preferentially delocalized within the carbazole ring due to the additional aromatic stabilization, which hinders the charge transfer from the carbazole nitrogen toward the acceptor and thus lowers the extent of

ICT, widening the optical bandgap.[256]

By comparing compounds **a5**, **a6**, **a7** and **a8**, with similar acceptor structure but different substituents, they all show a same trend in both absorption and emission maxima ($\lambda_5 > \lambda_6 > \lambda_8 > \lambda_7$), indicating the order of electron-accepting strength of the acceptors: TCF > 2,5-dihydro-4,5,5-trimethyl-2-oxofuran-3-carbonitrile > 3-(benzenesulfonyl)-4,5,5-trimethyl-2(*5H*) furano -ne > 3-(2-benzothiazolyl)-4,5,5-trimethyl- Δ^3-butenolide. Likewise, the comparison between the compounds **a3** and **a4** (or **a10** and **a11**) reveals that the 1-(dicyanomethylene)-3-indanone acceptor exhibits an increased electron–accepting ability compared with indane-1,3-dione.

In addition, time-resolved fluorescence measurements were performed and the detailed data are listed in **Table 3-1**. The decay behaviour of **a1**–**a3** and **a5**–**a10** is in a single-exponential manner in the solution obtained by monitoring at the monomer emission. The lifetimes of **a1**–**a3** and **a5**–**a10** are in the nanosecond range.

3.3.2. Solvatochromism

The linear absorption and emission spectra of compounds **a1**–**a11** in various solvents of different polarities at a concentration $c = 1 \times 10^{-6}$ mol L^{-1} were measured. Except compounds **a4** and **a11**, all other dipolar compounds **a1**-**a3** and **a5**-**a10** show interesting solvatochromic effect in different solvents. The photographs of representative compounds **a6** and **a10** in various solvents under UV illumination are shown in **Figure 3-19**. The absorption and emission spectra of **a1**-**a3** and **a5**-**a10** in different solvents are shown in **Figure 3-20**, **Figure 3-21**, and **Figure 3-22**. The spectroscopic dada in various solvents were presented in **Table 3-2** and **Table 3-3**.

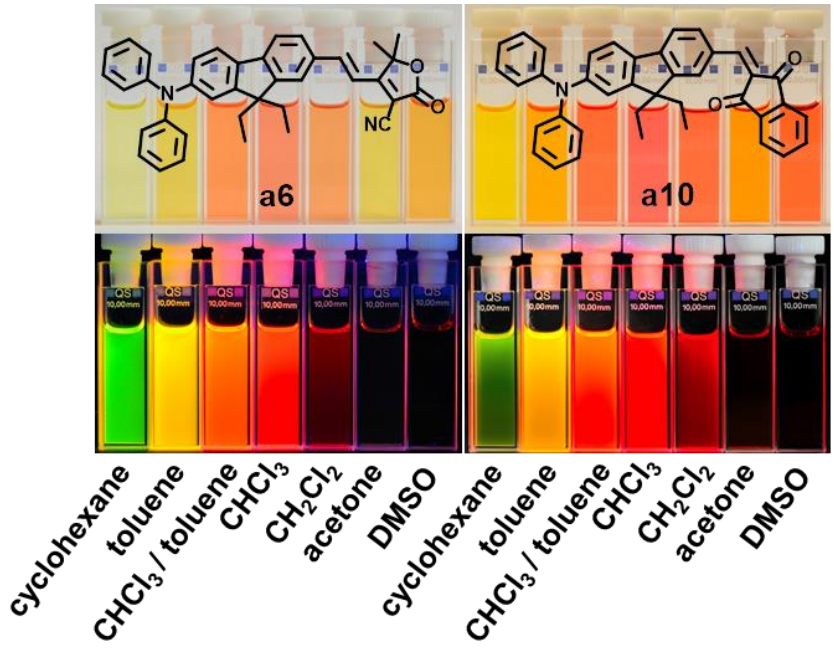

Figure 3-19. The UV–vis absorption and fluorescence photographs of compounds **a6** and **a10** in organic solvents of different polarity.

For each compound of **a1-a3** and **a5-a10**, the absorption spectra exhibit slight shift with increasing solvent polarity, showing weak solvatochromic behaviour distinctive of intramolecular charge transfer (ICT) transitions in push-pull dipolar molecules.

However, the D-π-A nature of these compounds produces a significant solvatochromic effect on their emission spectra (**Figure 3-20B**, **Figure 3-21B**, **Figure 3-22B**). For each compound of **a1-a3** and **a5-a10**, the emission spectrum in nonpolar cyclohexane reveals

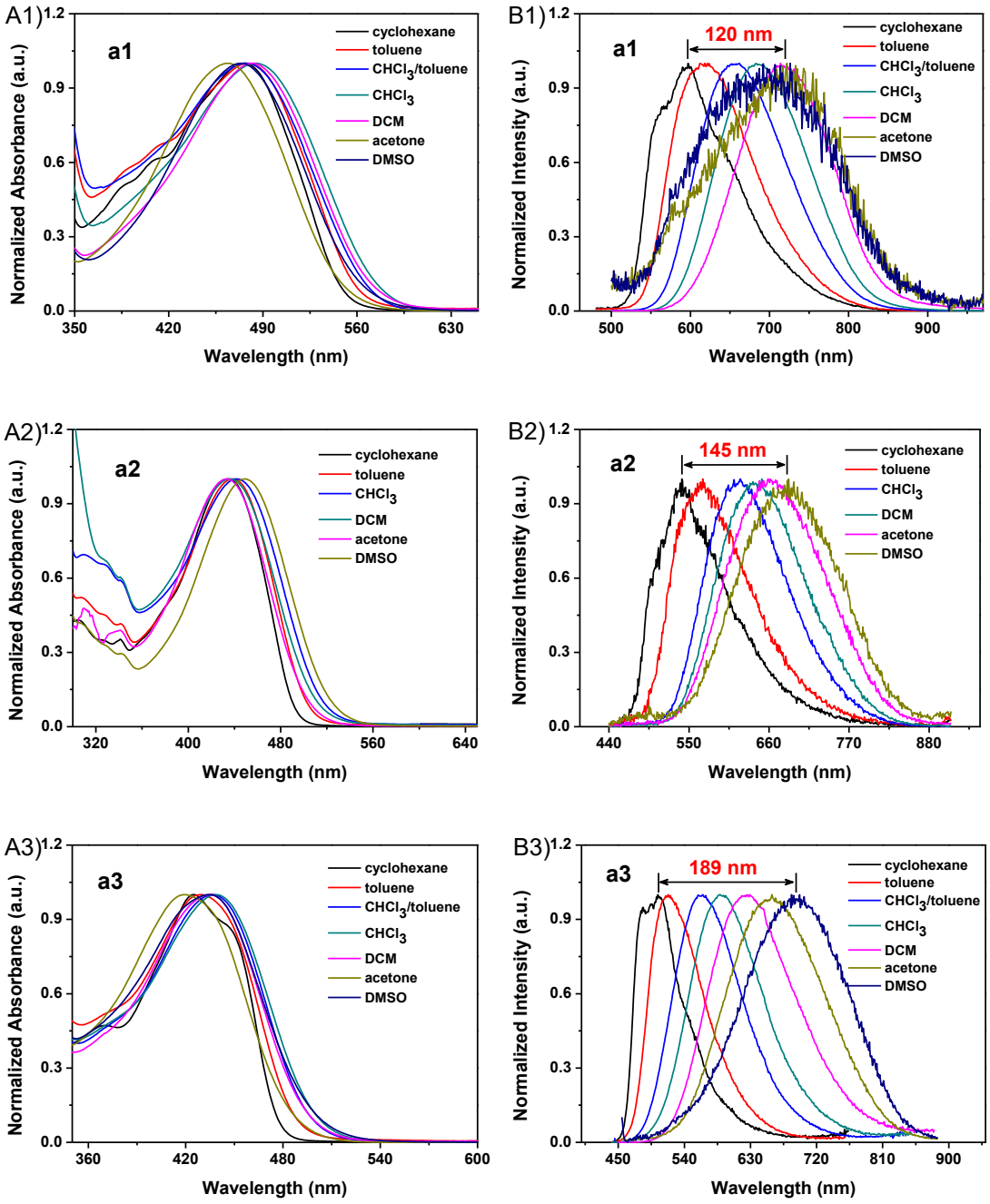

Figure 3-20. Linear absorption A) and normalized fluorescence B) of dyes **a1-a3** in organic solvents of different polarity.

vibronic definition, and shows a progressive red-shift and a loss of vibronic structure as the solvent polarity increases. As representatively shown for **a6** in **Figure 3-21B5**, a 225 nm bathochromic shift in the emission maximum is observed from 532 nm in cyclohexane to 757 nm in DMSO. Upon changing from apolar cyclohexane to polar DMSO, the emission maxima shift to the red by 120, 145, 189, 225, 213, 204, 187 and 215 nm for **a1**, **a2**, **a3**, **a6**, **a7**, **a8**, **a9** and **a10**, respectively. Except for **a1** and **a2**, all these values are larger than those of Prodan,[259] a well-known highly solvatochromic dye, and other fluorene-based D-π-A

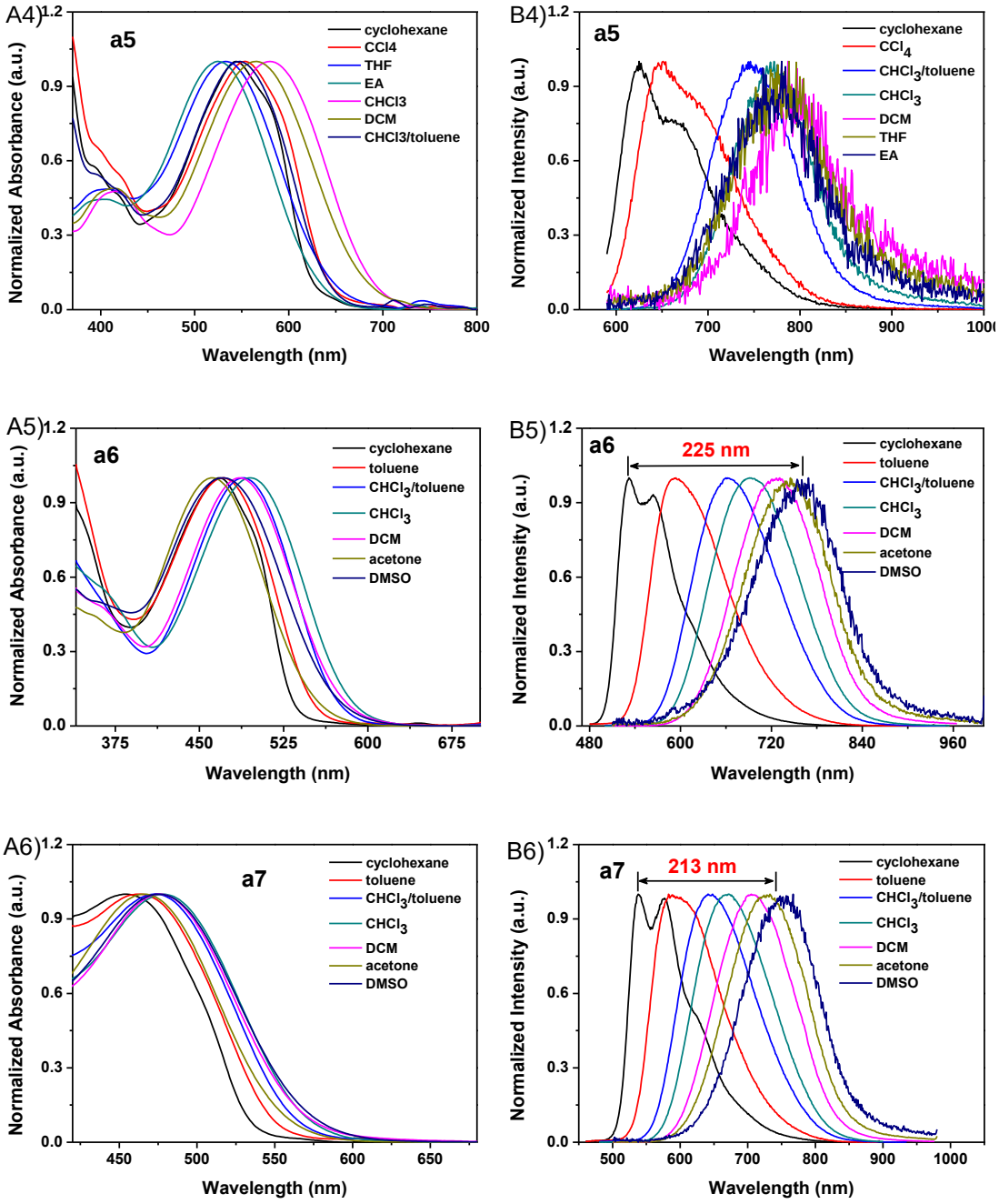

Figure 3-21. Linear absorption A) and normalized fluorescence B) of dyes **a5**-**a7** in organic solvents of different polarity

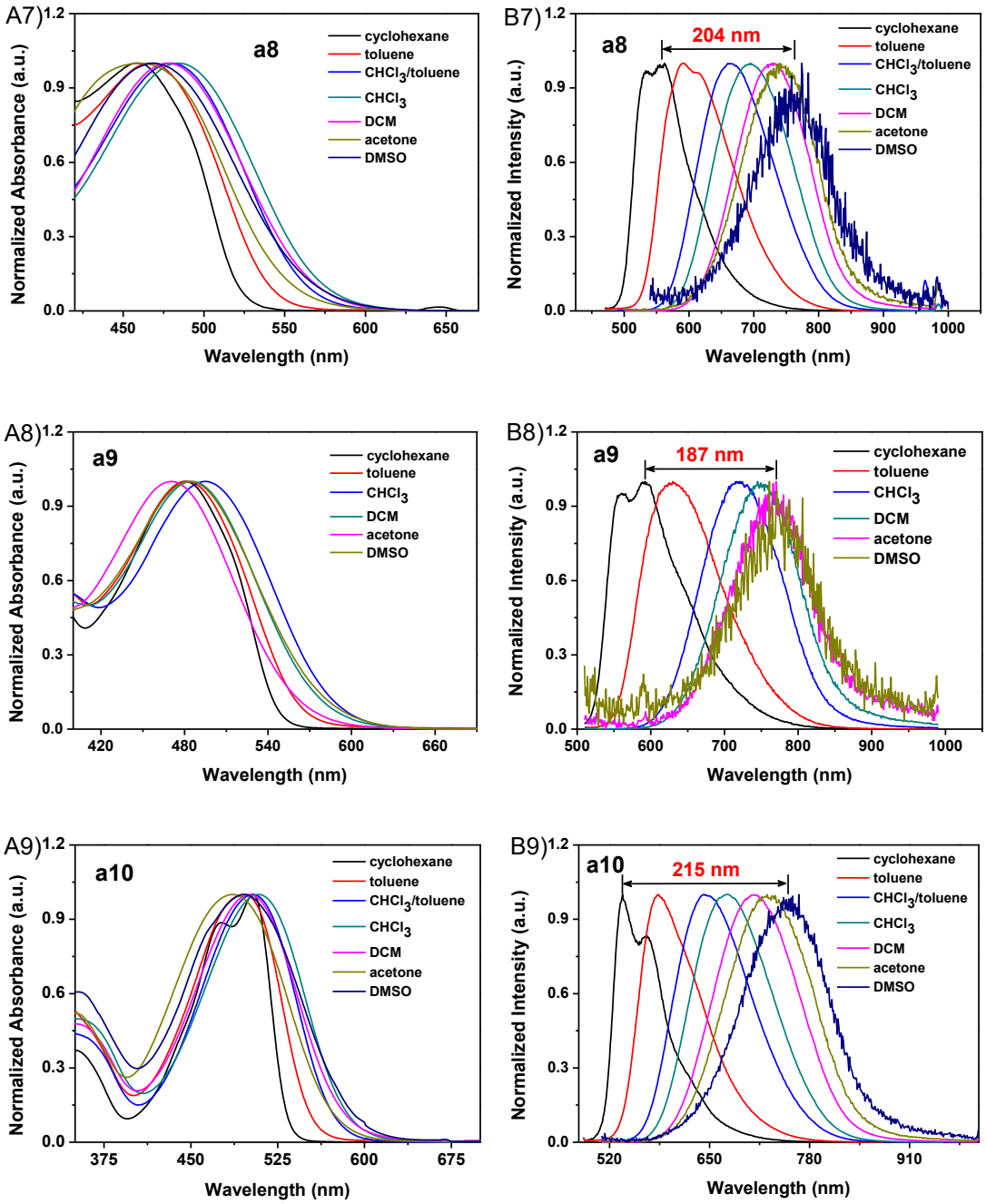

Figure 3-22. Linear absorption A) and normalized fluorescence B) of dyes **a8**-**a10** in organic solvents of different polarity

compounds (**Figure 3-23**).[260-261] In fact, the values of these samples are, to the best of our knowledge, the largest ever reported. Additionally, for each compound except **a2** and **a3**, the fluorescence intensity is greatly reduced in highly polar solvents (**Figure 3-20B**, **Figure 3-21B**, and **Figure 3-22B**). Take **a10** as an example (see **Table 3-3**), fluorescence quantum yields increase from 2% in apolar solvent (cyclohexane) to 51% in chloroform with medium polarity, then are greatly reduced in polar solvents dropping to 1% in DMSO. This is the common feature for most of strong dipolar molecules.

Table 3-2. Spectroscopic properties of **a1**-**a3** and **a5**-**a9** in different solvents.

	Solvent	λ_{abs} (nm)	λ_{em} (nm)	$\Delta\nu$ [a] (cm^{-1})		Solvent	λ_{abs} (nm)	λ_{em} (nm)	$\Delta\nu$ [a] (cm^{-1})
a1	Cyclohexane	476	596	4229	**a6**	Cyclohexane	468	532	2570
	Toluene	478	617	4713		Toluene	471	594	4396
	Toluene/$CHCl_3$	478	656	5676		Toluene/$CHCl_3$	489	661	5321
	$CHCl_3$	485	689	6230		$CHCl_3$	496	697	5997
	CH_2Cl_2	482	714	6741		CH_2Cl_2	486	727	6820
	Acetone	464	720	7662		Acetone	461	741	8196
	DMSO	474	698	6770		DMSO	471	760	8073
a2	Cyclohexane	434	541	4557	**a7**	Cyclohexane	454	538	3439
	Toluene	438	565	5131		Toluene	463	588	4591
	$CHCl_3$	443	623	6392		Toluene/$CHCl_3$	472	642	5610
	CH_2Cl_2	436	636	7212		$CHCl_3$	482	675	6019
	Acetone	436	663	7852		CH_2Cl_2	477	705	6779
	DMSO	449	682	7608		Acetone	466	726	7685
a3	Cyclohexane	425	505	3727		DMSO	475	751	7737
	Toluene	429	519	4042	**a8**	Cyclohexane	459	558	3865
	Toluene/$CHCl_3$	437	563	5121		Toluene	467	592	4521
	$CHCl_3$	439	590	5829		Toluene/$CHCl_3$	480	664	5773
	CH_2Cl_2	435	624	6962		$CHCl_3$	485	697	6474
	Acetone	419	657	8645		CH_2Cl_2	477	730	7265
	DMSO	434	691	8569		Acetone	460	740	8225
a5	Cyclohexane	544	626	2407		DMSO	469	764	8232
	CCl_4	553	650	2698	**a9**	Cyclohexane	481	591	3869
	Toluene/$CHCl_3$	548	748	4879		Toluene	481	629	4891
	THF	533	778	5908		$CHCl_3$	495	720	6596
	ethyl acetate	524	775	6180		CH_2Cl_2	485	748	7249
	$CHCl_3$	580	771	4865		Acetone	470	765	8204
	CH_2Cl_2	565	769	4695		DMSO	484	775	7757

[a] Stokes shift.

Table 3-3. Spectroscopic properties of **a10** in different solvents.

Solvent	λ_{abs} / nm	λ_{em} / nm	$\Delta\nu$ / cm^{-1} [a]	Φ_f / % [b]
Cyclohexane	504	537	1219	2
Toluene	495	584	3079	11
Toluene/$CHCl_3$	503	646	4425	38
$CHCl_3$	509	677	4897	58
CH_2Cl_2	501	707	5818	33
Acetone	486	725	6783	2
DMSO	496	754	6899	1

[a] Stokes shift. [b] Quantum yields determined by using rubrene in methanol (Φ_F = 27%) as the standard.

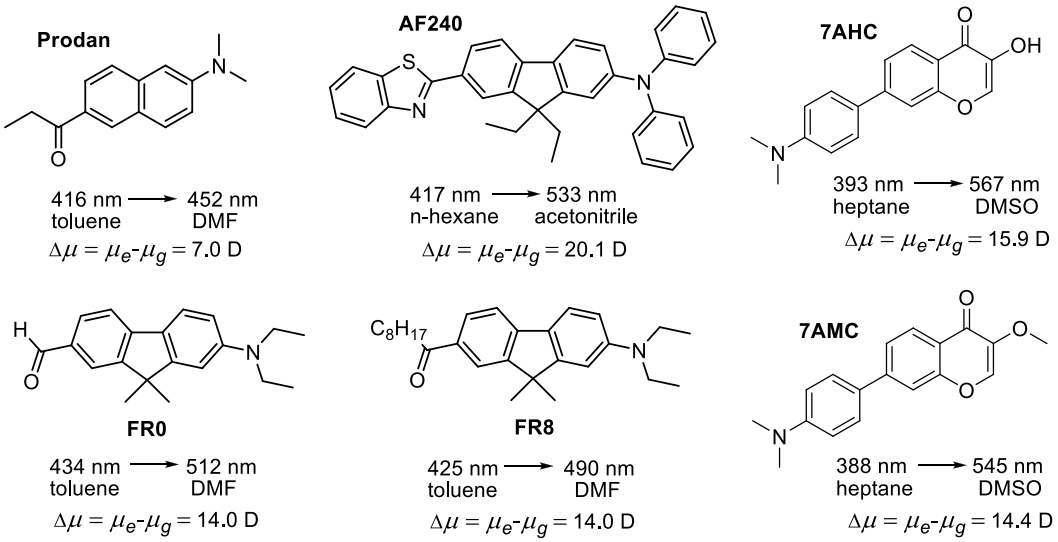

Figure 3-23. Molecular structure of solvatochromic fluorophores, bathochromic shift in emission between apolar and polar solvent, and corresponding $\Delta\mu$ reported.

Besides, large values of the Stokes shifts are observed for compounds **a1-a3** and **a5-a10** in seven solvents due to strong solvent-solute dipole-dipole interactions, a manifestation of the large dipole moment and orientational polarizability. The compound bear both electron-donor and -acceptor group, such that in the excited state, charge transfer occurs from the donor to the acceptor group through the conjugation core, strongly increasing the dipole moment. In aprotic solvents, Stokes shifts are approximately proportional to the orientational polarizability. Data were analyzed using the Lippert-Mataga model described in **Chapter 2** using equations (2-2) and (2-3). As indicated, $(\mu_e\text{-}\mu_g)^2$ is proportional to the slope of the Lippert -Mataga plot. Onsager radius *a* for each compound was obtained by DFT calculation and are listed in **Table 3-4**.

Table 3-4. Spectroscopic properties of **a1**–**a3** and **a5**–**a10**.

dye	*a* (Å) [a]	*s* (cm^{-1}) [b]	$\mu_e\text{-}\mu_g$ (D) [c]
a1	6.5	11158	17.5
a2	6.7	11772	18.8
a3	6.6	14451	20.3
a5	6.9	16532	23.3
a6	6.4	14859	19.6
a7	6.9	11295	19.4
a8	6.8	14508	21.2
a9	6.6	14854	20.6
a10	6.6	15195	20.9

[a] Onsager radius obtained from DFTcalculation. [b] The slopes of the best-fit line of Lippert-Mataga plot. [c] The dipole moment change.

Plots of the Stokes shifts as a function of the solvent polarity factor Δf are shown in **Figure 3-24**. The slopes of the best-fit lines were obtained for dyes **a1**, **a2**, **a3**, **a5**, **a6**, **a7**, **a8**, **a9** and **a10**, respectively, and presented in **Table 3-4**. Since the slope of the best-fit line is related to the dipole moment change (μ_e-μ_g) between the ground and excited states (eq 2-2, **Chapter 2**), so the values of μ_e-μ_g were further calculated and listed in **Table 3-4**. The μ_e-μ_g values obtained are much larger than those of the reported analogues **Figure 3-23**,[260-261] which infer larger dipole moment change for them with photoexcitation.

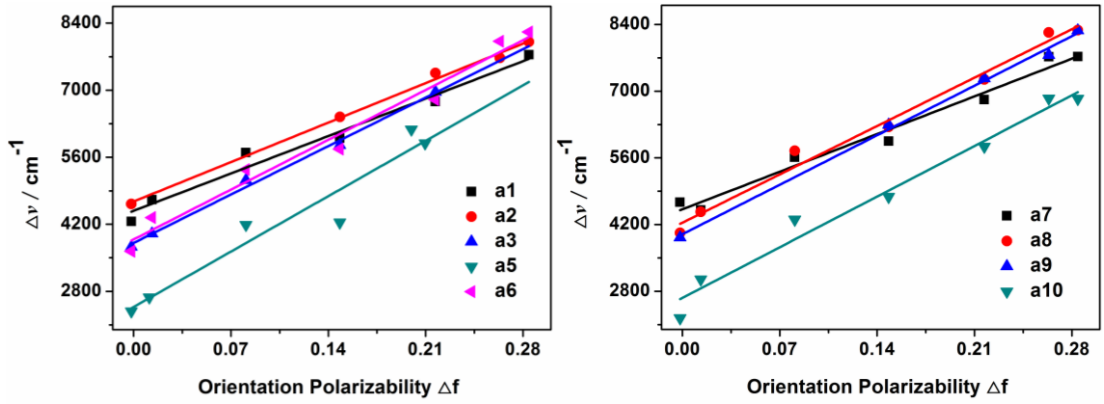

Figure 3-24. Lippert-Mataga plots for dyes **a1**–**a3** and **a5**–**a10**.

The μ_e-μ_g obtained were found to present similar values for **a3** and **a6**–**a10**. A slightly higher value for **a5** can be ascribed to an increase of the ICT due to a higher acceptor efficiency of TCF group with respect to other acceptors of diphenylamino derivatives. For the same reason, the carbazolyl substituted compounds (**a1**, **a2** and **a3**) with the relative weak ICT character show slightly lower values with respect to those of their diphenylamino analogues (**a5**, **a9** and **a10**). We also noticed that compound **a3** exhibits a most blue-shifted absorption (439 nm in chloroform) but shows a comparable value of μ_e-μ_g compared with those of compounds **a6–a10**, especially for its diphenylamino analogue **a10**. This result suggests that there is an ICT enhancement in the excited state and not in the ground state. The discussion above indicates that the synthesized dipolar molecules have an extremely polar structure in the excited state and thus their non-linear properties can be expected.

3.4. Two-Photon Absorption Properties

Owing to the strong push–pull dipolar character of compounds **a1**–**a3** and **a5**–**a10**, interesting nonlinear optical properties, and in particular two-photon absorption properties, can be expected. Thus the two-photon excitation spectra of **a1**–**a3** and **a6**–**a10** were recorded in chloroform (c = 1×10^{-4} mol L^{-1}) using a femtosecond laser pulse and a Ti: sapphire system (tunable range: 720–970 nm, 80 MHz, 140 fs) as the light source. The emission signals were collected upon excitation from 730 to 970 nm (at 10 nm intervals), in which compounds **a1**–**a3** and **a6**–**a10** have no linear absorption. Then two-photon absorption (2PA) cross-sections (σ_{2PA}) were subsequently calculated for them. However, for compound **a5** with a much more

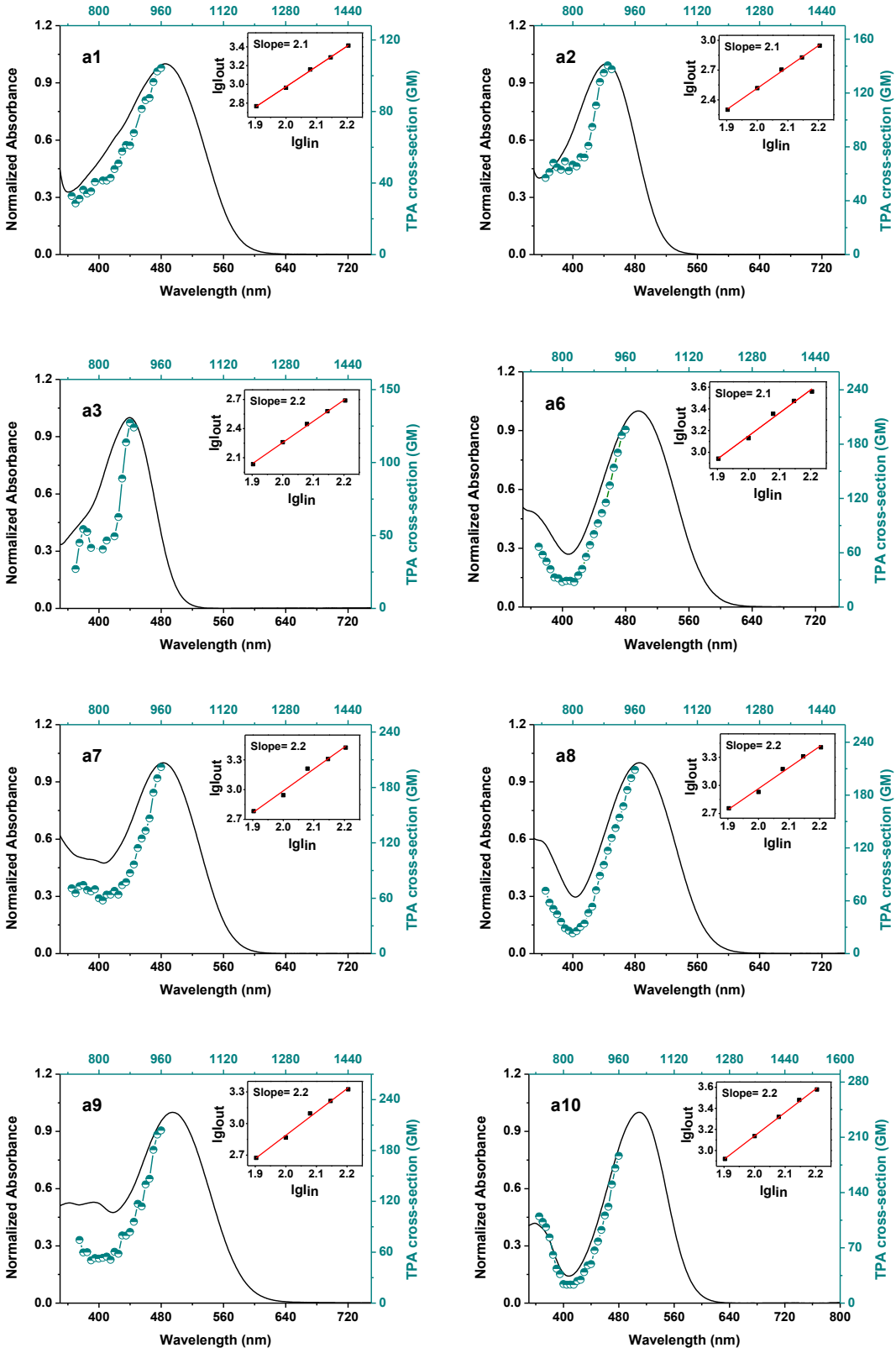

Figure 3-25. Absorption spectrum and two-photon absorption cross-sections of **a1**–**a3** and **a6**–**a10** in $CHCl_3$ solution in the 740–960 nm range. Insert shows the logarithmic plot of the fluorescence integral of chromophore versus different laser powers.

red-shifted linear absorption band (475–770 nm), the two-photon absorption measurement is limited by the wavelength range of the Ti: sapphire laser. Details of the measurement and calculation method are provided in **Experimental Section**.

The two-photon excitation spectrum as well as the linear absorption spectrum for each compound is illustrated in **Figure 3-25**. The insets show a logarithmic plot of the fluorescence integral versus laser powers with a slope around 2 when the input laser power is increasing, suggesting a two-photon excitation process. As expected, for these push-pull molecules that do not possess a centre of symmetry, the two-photon absorption spectra of compounds **a1**–**a3** and **a6**–**a10** correlated quite well with their linear absorption spectra. The two-photon excitation spectra of the dipolar compounds reveal a partial absorption band perfectly overlapping to twice the linear absorption band.

As shown in **Figure 3-25**, this series of compounds display moderate two-photon absorption activity in the range of 740–960 nm. Compound **a2** exhibits a maximum two-photon absorption cross-section of 140 GM at 890 nm. Similarly, a maximum value of 127 GM at 880 nm was observed for compound **a3**. Moreover, for the compounds whose 2PA cross-sections did not reach the maxima on the spectra, their maximum values were estimated referring to the linear absorption spectra as ~104 GM (**a1**), ~210 GM (**a6**), ~202 GM (**a7**), ~214 GM (**a8**), ~220 GM (**a9**) and ~240 GM (**a10**), respectively. These results are comparable to the previously reported values for similar fluorene-based push-pull fluorophores.[260, 262] In addition, for the compounds with same acceptor moiety, such as **a2** and **a9** (or **a3** and **a10**), increasing the strength of electron-donating end-groups results in a pronounced enhancement of the two-photon absorption cross-sections. These results demonstrate the design of the conjugated dipolar chromophores, possessing good two-photon excitation and photoluminescence in the transparency window in the range of 700-1000 nm.

4. Aggregation-Induced Emission and Solid Emission Properties of Push-Pull Fluorophores and Their Applications for Biphotonic in vivo Imaging

4.1. Aggregation-Induced Emission

4.1.1. One-Photon Properties

To investigate the AIE attributes of **a1**−**a11**, a simple precipitation method was employed to prepare stable nanoaggregates dispersed in water. Generally, we added different amounts of water, a poor solvent for the compounds, to pure acetone solutions by defining the water fractions (f_w between 0−90%) with the final concentration of 5×10^{-5} mol L^{-1}. The presence of water can lower the solubility of compounds and further stabilize the colloidal dispersion

formed by promoting surface charge. The absorption and photoluminescence spectra were subsequently recorded with the excitation wavelengths of 450 nm (**a2** and **a3**), 500 nm (**a1**, **a4** and **a6**–**a10**) and 580 nm (**a5** and **a11**). The experimental results show that all the compounds exhibit interesting AIE behaviour in the FR/NIR region except for compounds **a4**, **a5** and **a11**, which show a negligible AIE effect from solution to suspension.

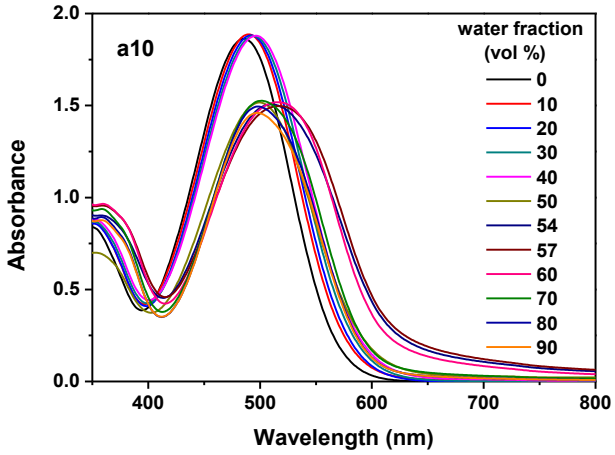

Figure 3-26. Absorption spectra of **a10** in acetone/water mixtures with different water fraction (f_w).

The absorption spectra of the representative compound **a10** in acetone/water mixtures with different water fraction (f_w) are shown in **Figure 3-26**. With increasing water fractions, the spectral profiles are significantly changed when f_w > 40 vol%. The red-shifted maximum absorption wavelength and the decreased absorption intensities are indicative of the formation of nanoscopic aggregates of compound **a10**. This result is consistent with its AIE behaviour. Meanwhile, the light scattering, or Mie effect, of the nanoaggregate suspensions effectively decreases light transmission in the mixture and causes the apparent high absorbance and level-off tail in the absorption spectrum.[263]

Figure 3-27 and **Figure 3-28** show the fluorescence spectra of compounds in acetone/water mixtures with different water fraction (f_w) as well as the variations of the intensity as a function of f_w. The insert pictures show the fluorescence of the pure acetone solution and the aggregates suspension under the UV lamp. As described before, a significant solvatochromic effect was observed for this series of compounds and their fluorescence is greatly decreased in polar environment because of inherent ICT character. For example, the fluorescence quantum yield of compound **a10** was calculated to be only 2% in acetone. As shown in **Figure 3-27** and **Figure 3-28** in pure acetone solutions, all the compounds display weak emission.

Upon gradually increasing the water fraction (f_w) from f_w = 0 to 40 or 50 vol%, the fluorescence intensities of compounds in the acetone/water mixtures are significantly decreased. This process is accompanied by a gradual red shift of emission bands. For example, the emission band of **a10** in the solvent mixture with f_w = 40 vol% is red-shifted to 755 nm, compared with 727 nm in pure acetone solution. At low water fraction, the dipolar compounds are completely dissolved in acetone. The decrease in fluorescence intensity and the red-shift of its peaks can be attributed to the twisted intramolecular charge-transfer (TICT)

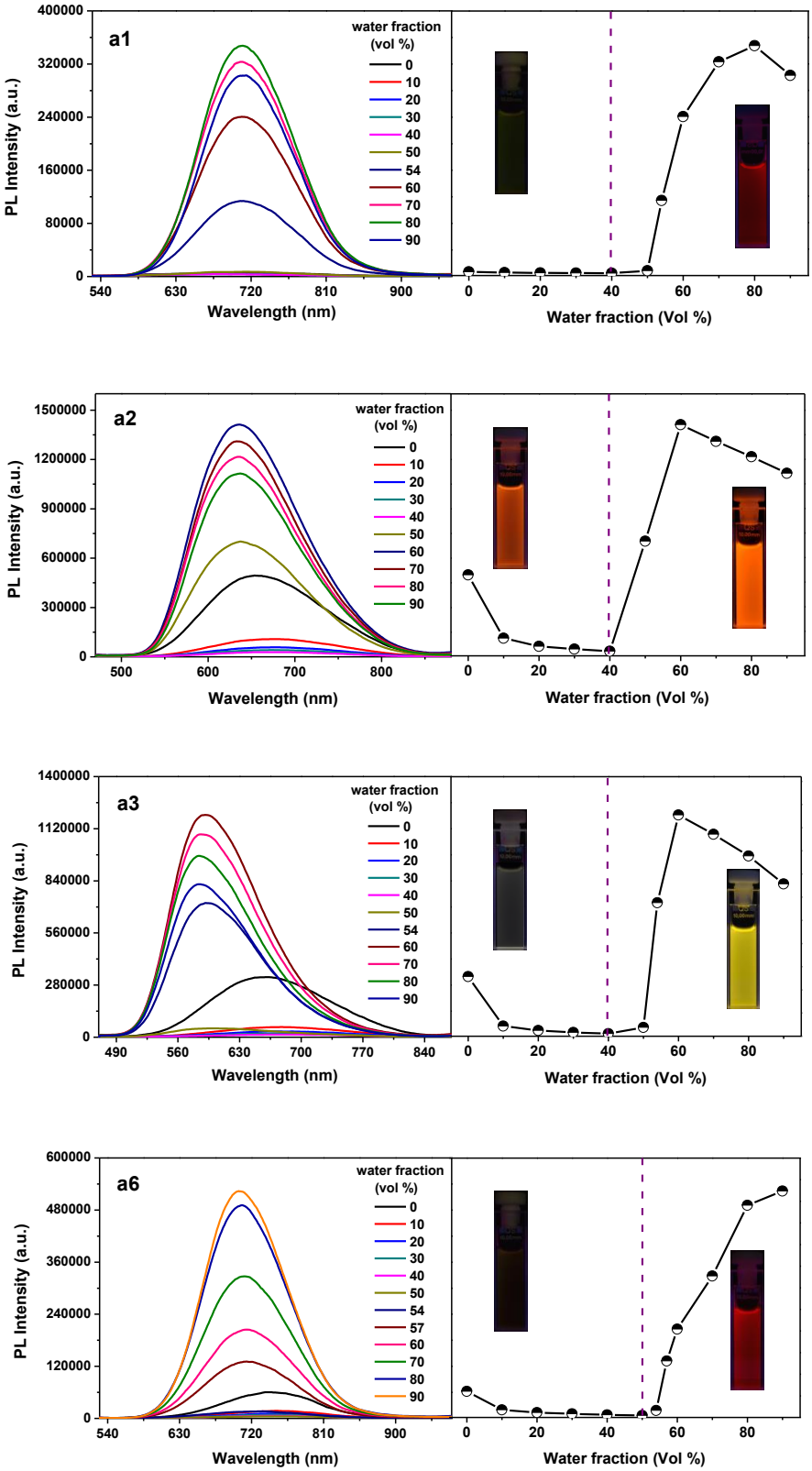

Figure 3-27. Left: emission spectra of compounds **a1**–**a3** and **a6** in acetone/water mixtures with different water fraction (f_w); Right: Plot of emission peak intensity *vs* f_w in the mixtures. Insert pictures show the fluorescence of the pure acetone solution and the aggregates suspension under the UV lamp.

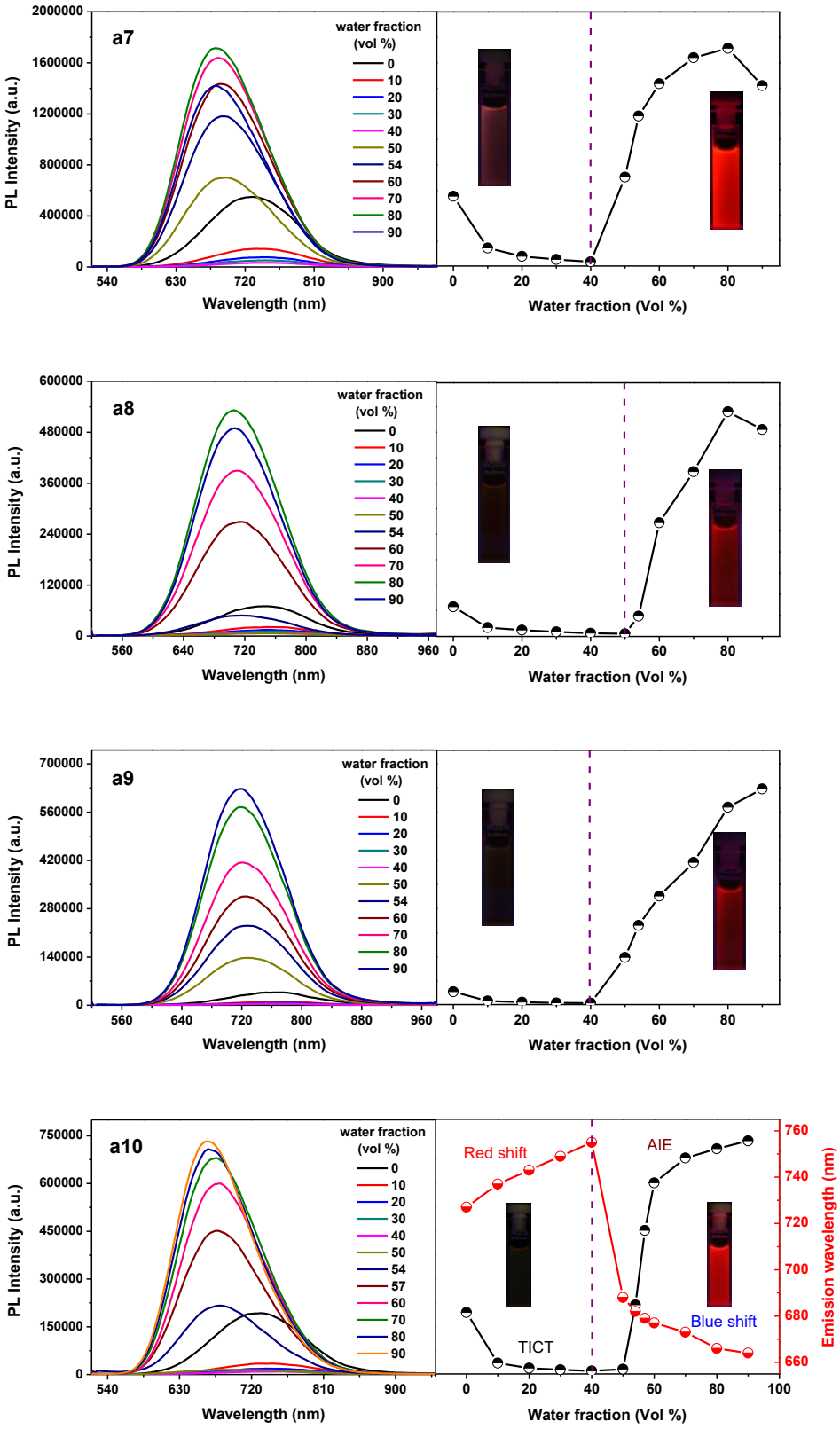

Figure 3-28. Left: emission spectra of compounds **a7**–**a10** in acetone/water mixtures with different water fraction (f_w); Right: Plot of emission peak intensity *vs* f_w in the mixtures. Insert pictures show the fluorescence of the pure acetone solution and the aggregates suspension under the UV lamp.

effect of push–pull compounds resulting from the increase in solvent polarity by gradually adding water. This result is also in agreement with the solvatochromic effect of compounds.

Once the f_w was increased beyond 40 or 50 vol%, a remarkable fluorescence enhancement with a blue-shift of peaks was observed, revealing the AIE feature of the compounds. In this process, the enhanced emission and the blue-shifted peak could be attributed to the formation of the nanoaggregates, which efficiently decrease the impact of the polarity of solvent on molecules. Simultaneously, rotations in the molecules are greatly restricted in the aggregate state, and thus the unique aggregation-induced emission occurs. For some of them, after reaching a maximum intensity, the fluorescence intensity slightly decreases upon further increasing the water fraction f_w. This decrease in fluorescence is probably due to the difference in aggregate morphology.[85]

To quantitatively evaluate the AIE properties of the fluorescent materials, the absorption and emission spectra were restricted to being taken in the suspension with the water fraction of 90 vol % (**Figure 3-29** and **Figure 3-30**), for which the maximum effect is observed. The optical data are collected in **Table 3-5**. As mentioned above, compared with the absorption of the compounds in pure acetone solution, the red-shifted and broadened absorption bands observed in suspension are indicative of the nanoaggregates formation. As expected, the designed compounds are AIE active with a wide emission range from 586 nm for **a3** to 717 nm for **a9** (**Figure 3-30**). The resulting emission colour of the formed nanoaggregates can be facilely turned through varying donor−acceptor combination. Furthermore, as shown in **Table 3-5**, the values of fluorescence quantum yield Φ_f were determined to be 4%-11% for the compounds by using rubrene in methanol (Φ = 27%) as the standard. In addition, it was interesting to find that all the compounds show very large Stokes shifts ($\Delta\nu$ = 5336–7077 cm^{-1}), which are favourable for bio-imaging due to the minimized interference between excitation and emission.

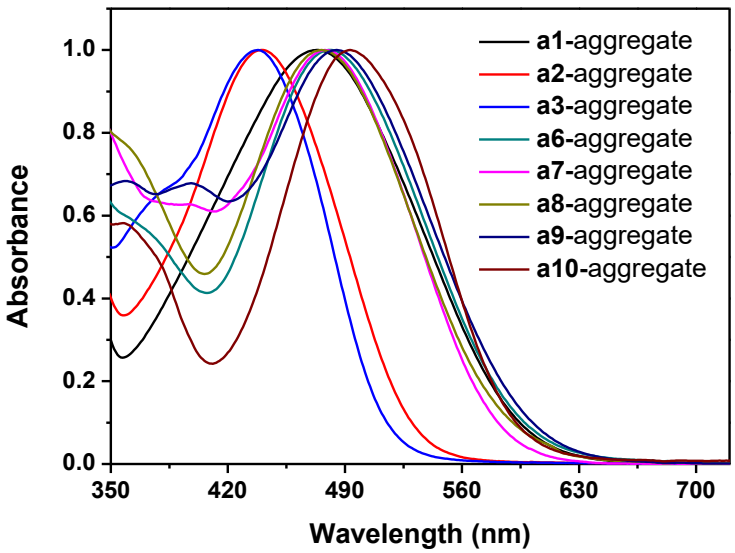

Figure 3-29. Absorption spectra of compounds in acetone/water mixtures with f_w = 90 vol%.

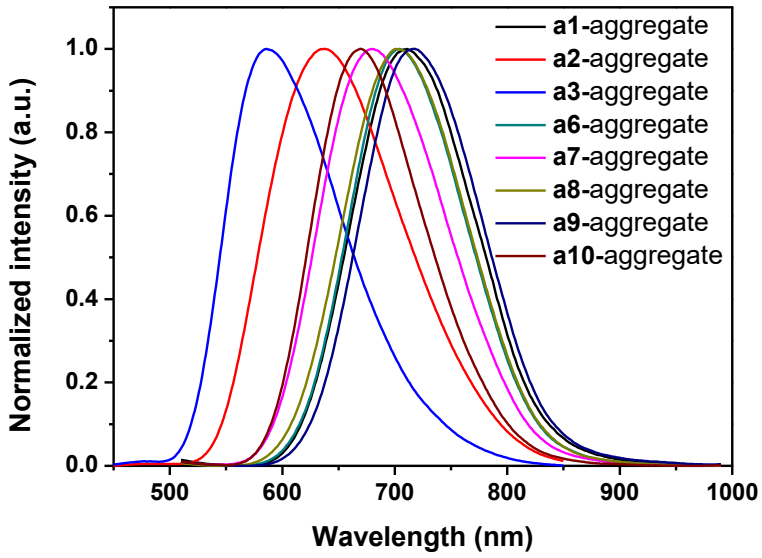

Figure 3-30. Emission spectra of compounds in acetone/water mixtures with f_w = 90 vol%.

At last, measurements of fluorescence lifetimes for all the prepared aggregates were performed and the detailed data of the fluorescence decay curves are listed in **Table 3-5**. The decay curves for the all aggregates can be fitted with a triple-exponential behaviour, which means the aggregates decay through three main relaxation pathways. This result could also indicate of the existence of different aggregation species in the suspension. Their weighted mean lifetimes are mainly from the contribution of the shortest lifetime species, consistent with the previous observation from solid materials.[263]

Table 3-5. Spectroscopic properties of chromophores in forms of self-aggregates.

Sample	λ_{max} [a]	λ_{max} [b]	$\Delta\nu$ [a]	Φ_f [d]	τ_1 [e]	A_1 [f]	τ_2 [e]	A_2 [f]	τ_3 [e]	A_3 [f]	$<\tau>$ [g]
a1-aggregate	473	711	7077	4	0.86	0.75	2.96	0.24	11.5	0.01	1.48
a2-aggregate	440	637	7027	11	0.75	0.84	2.71	0.15	11.6	0.01	1.10
a3-aggregate	438	586	5766	6	0.83	0.78	3.28	0.21	10.7	0.01	1.48
a6-aggregate	482	704	6542	4	0.98	0.65	2.89	0.34	9.62	0.01	1.76
a7-aggregate	478	679	6193	9	0.66	0.77	2.13	0.21	6.04	0.01	1.04
a8-aggregate	476	701	6743	4	0.75	0.68	2.58	0.30	8.44	0.02	1.44
a9-aggregate	485	717	6672	6	0.96	0.65	2.71	0.34	9.17	0.01	1.65
a10-aggregate	493	669	5336	5	0.85	0.70	3.27	0.28	8.14	0.02	1.66

[a] Absorption in nm. [b] Emission in nm. c Stokes shift in cm^{-1}. [d] Quantum yields determined by using rubrene in methanol (Φ = 27 %) as the standard. [e] Fluorescence lifetime (ns). [f] Fractional contribution (%). [g] Weighted mean lifetime (ns).

4.1.2. Characterization of Nanoaggregates

It is noteworthy that all the fluorescent aggregates suspensions are transparent and macroscopically homogeneous with no precipitation within one month, suggesting an excellent stability of the formed aggregates. The size distribution of the nanoaggregates in the

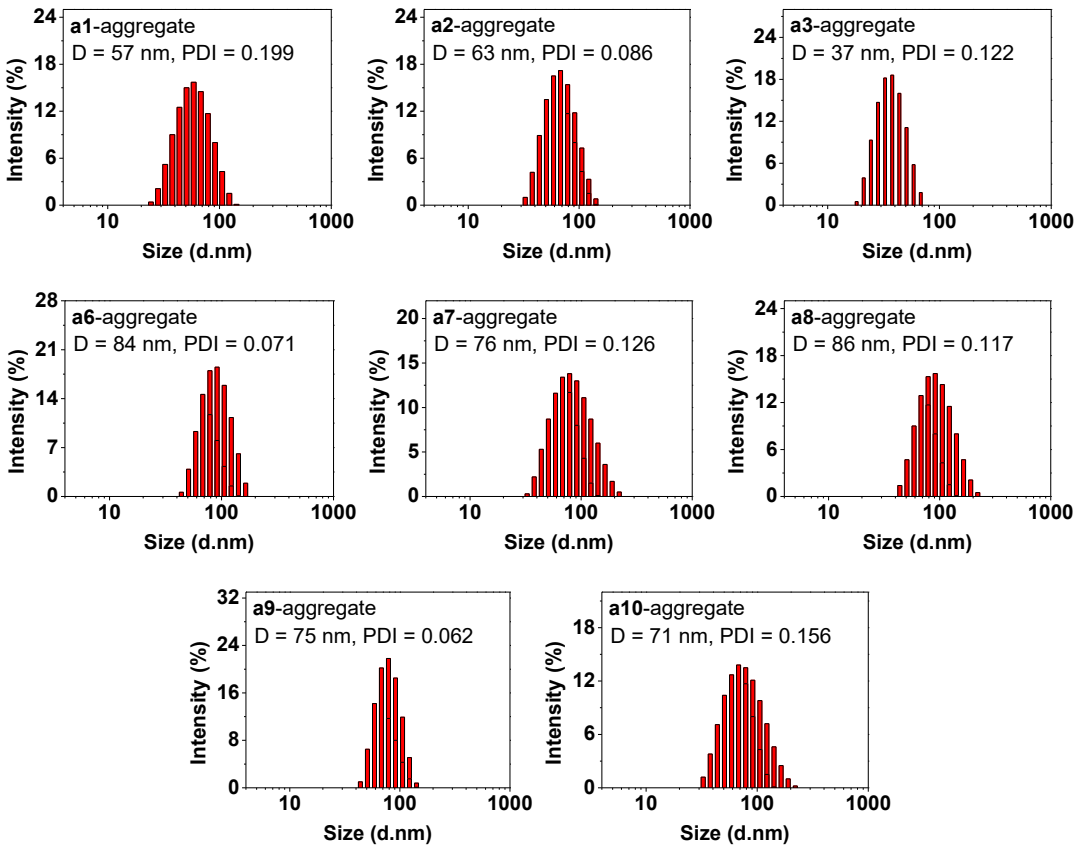

Figure 3-31. Particle size distribution of nanoaggregates of **a1**–**a3** and **a6**–**a10** in acetone/water mixtures with f_w = 90 vol%, measured by DLS.

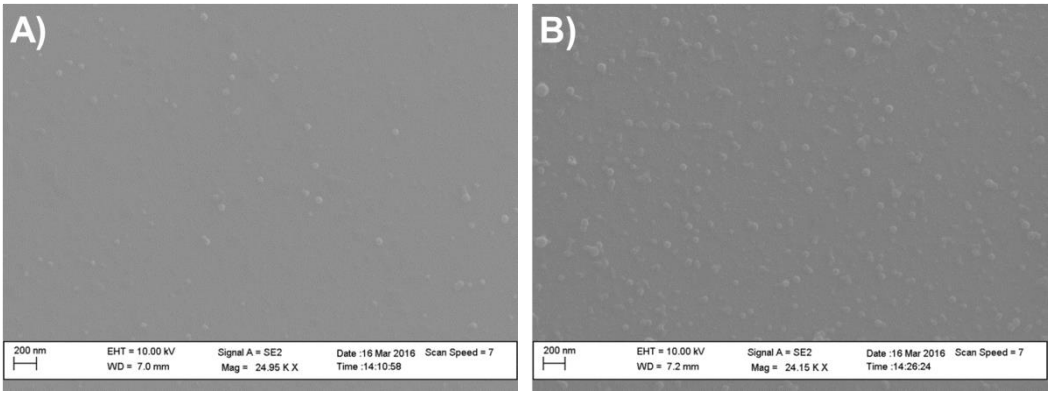

Figure 3-32. SEM images of A) **a1**-aggregates and B) **a9**-aggregates prepared in acetone/water mixtures with f_w = 90 vol% at 5 × 10 $^{-5}$ mol L^{-1}.

mixed solutions with f_w = 90 vol% was firstly determined by dynamic light scattering (DLS) measurements (**Figure 3-31**). The average diameters (D) of nanoaggregates were measured to be 57, 63, 37, 84, 76 and 86 nm for **a1**–**a3** and **a6**–**a10** in the mixed solutions with f_w = 90 vol%, respectively. For representative compounds **a1** and **a9**, the formation of nanoaggregates in acetone/water (f_w = 90 vol%) was further verified by scanning electron microscopy (SEM)

images (**Figure 3-32**). The result shows that the uniform spherical nanoaggregates were formed in the suspension. The size of nanoparticles obtained from SEM seems smaller than that from DLS.

4.1.3. Two-Photon Absorption Properties

Owing to the interesting two-photon absorption properties of compounds **a1**–**a3** and **a6**–**a10** in organic solvent chloroform, two-photon activity of their fluorescent nanoaggregates can also be expected. We further investigate the two-photon absorption spectra of the aggregates suspensions of **a1**–**a3** and **a6**–**a10** by the two-photon-excited fluorescence (2PEF) technique with a femtosecond laser pulse and a Ti: sapphire system (tunable range: 720–970 nm, 80 MHz, 140 fs). The emission signals were collected upon excitation from 740 to 960 nm at 10 nm intervals. Details of the measurement and calculation method are provided in the experimental part. The obtained 2PA spectra are shown in **Figure 3-33.** As expected, all the aggregates exhibit good two-photon absorption properties in the measuring range of 740–960 nm provided by the Ti:sapphire laser. The obtained two-photon excitation spectra for the aggregates composed of push–pull compounds are shifted with respect to twice their linear absorption band, which is a quite different behaviour from that in solution in chloroform. This result is probably related to the complexity of the molecular arrangement in aggregate. In this case, the estimation of maximum two-photon absorption cross-sections for the nanoaggregates becomes impossible. Due to the wavelength limitation of the Ti:sapphire laser, these values probably not the maximum for each aggregate. Even so, the value of two-photon absorption cross-section for each compound in aggregate is still larger than the maximum value estimated for the same compound in chloroform solution. This aggregation enhanced two-photon absorption of compound may be due to the considerably hindered internal rotation of the molecule in the aggregate.[252]

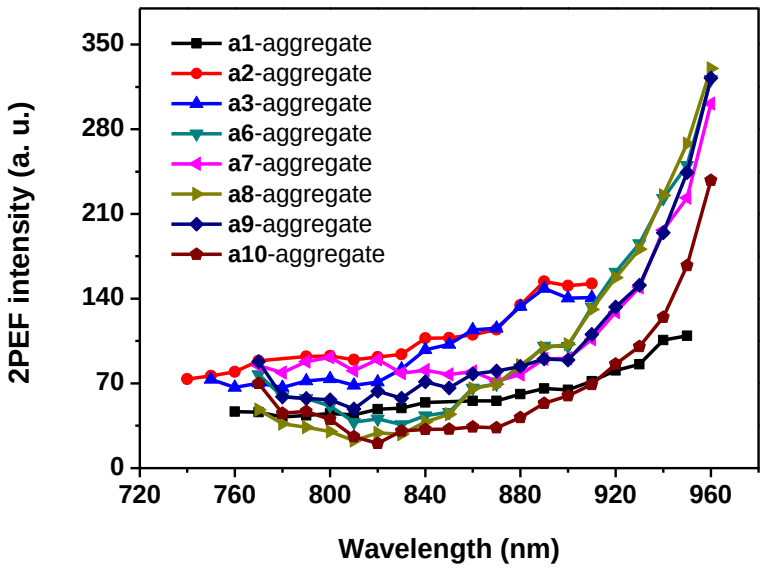

Figure 3-33. Two-photon absorption spectra of nanoaggregates of **a1**–**a3** and **a6**–**a10** in the range 740-960 nm in acetone/water mixtures with f_w = 90 vol%.

4.2. Optical Properties in the Solid State

4.2.1. Linear Optical Properties

To gain further insight into the AIE properties as well as solid state optical properties of **a1**–**a11**, we performed a series of spectroscopic measurements on the crystals. **Figure 3-34** shows the absorption spectra of crystals of **a1**, **a3**, **a6**–**a8** and **a10** grinded in anhydrous barium sulfate. All the absorption spectra are considerably broadened and red-shifted compared to those of the solution and the nanoaggregates suspension. For example, the absorption spectra of representative **a10** exhibit a gradual broadening and red-shift from solution to suspension and crystal (**Figure 3-35**).

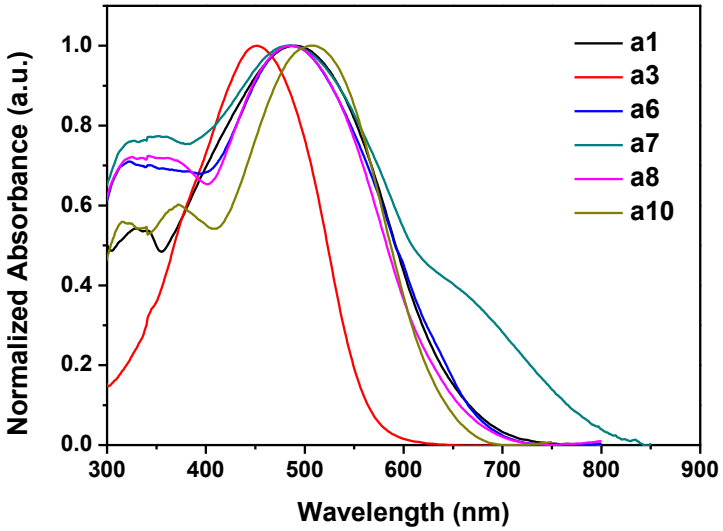

Figure 3-34. Absorption spectra of **a1**, **a3**, **a6**, **a7**, **a8** and **a10** crystals grounded in barium sulfate.

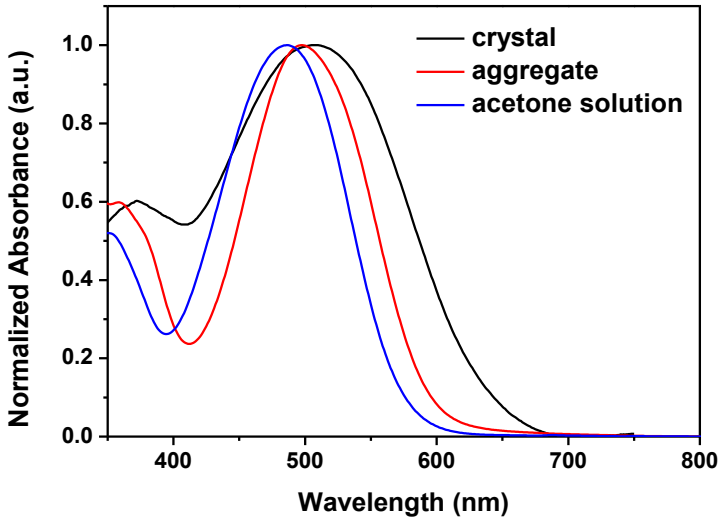

Figure 3-35. Absorption spectra of **a10** in the pure acetone solvent, the suspension with f_w = 90 vol% and the crystal grounded in barium sulfate.

Figure 3-36 shows the strong fluorescence from single crystal of **a10** under UV lamp at 365 nm, which is far from their excitation maximum. The emission spectra of crystals were subsequently recorded with an excitation wavelength at 450 nm (**a2** and **a3**), 500 nm (**a1**, **a4** and **a6**–**a10**) and 580 nm (**a5** and **a11**), close to their absorption maximum found in barium sulfate. All the crystals show a detectable emission in the FR/NIR region (**Figure 3-37**), even for **a4**, **a5** and **a11**, the three compounds that do not show obvious AIE effect. The fluorescence quantum yields of crystals were measured by using an integrating sphere and the values obtained are listed in **Table 3-6**.

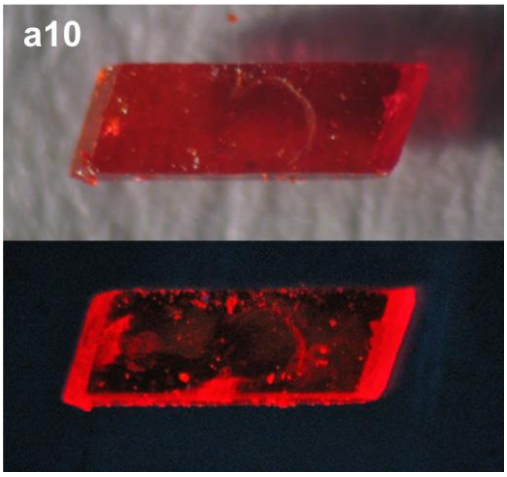

Figure 3-36. Photograph of crystal of **a10** (top) and the same under illumination of handled UV lamp at 365 nm (bottom).

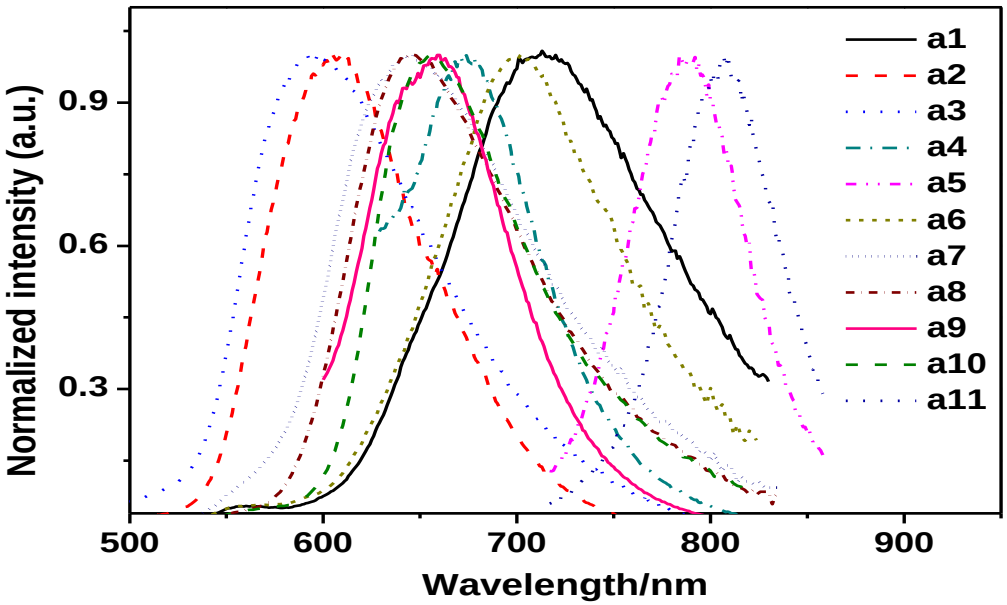

Figure 3-37. Emission spectra of **a1**–**a11** in the solid state (crystals).

Table 3-6. Spectroscopic properties of compounds **a1**–**a11** in solid.

Sample	λ_{abs} [a]	λ_{max} [b]	Φ_f [c]
a1	491	714	0.08
a2	–	608	0.03
a3	452	595	0.04
a4	–	672	<0.01
a5	–	788	<0.01
a6	486	701	0.03
a7	482	644	0.13
a8	485	646	0.08
a9	–	659	0.02
a10	507	656	0.20
a11	–	807	<0.01

[a] Grinded crystals in barium sulfate. [b] Steady-state fluorescence emission λ_{max} in solid. [c] Fluorescence quantum yield in crystal measured by using an integrating sphere.

The influence of the change of donors and acceptors on the solid state emission properties is especially evidenced by the variation of emission spectra (**Figure 3-37**). For all the crystals, emission spectra are broad and the emission maxima cover a wide spectral range from 595 nm for **a3** to 807 nm for **a11**. It is noteworthy that the greatly red-shifted emission at 788 and 807 nm were observed for crystals of **a5** and **a11**, respectively. These values are much larger than those of most of reported solid emitting materials. However, very low fluorescence quantum yields (< 1%) were determined for crystals of **a4**, **a5** and **a11**. These results are in good agreement with their negligible AIE behaviours. Interestingly, in this series of compounds, **a10** is the most emissive compound in crystalline state with Φ_f = 20% at 656 nm. Moreover, compounds **a1**, **a7** and **a8** also display rather intense fluorescence in their crystals with Φ_f = 8% (**a1**, **a8**) and 13% (**a7**). The less emissive crystalline compounds are **a2**, **a3**, **a6** and **a9** with Φ_f = 2–4%.

4.2.2. Multi-Photon (Two- and Three-Photon) Absorption Properties

Multi-photon absorption measurements were done through collaboration with Dr. Kenji Kamada in the National Institute of Advanced Industrial Science and Technology of Ikeda/Osaka in Japan. The two-photon absorption properties of the synthesized dipolar compounds have been demonstrated in the organic solution and the aggregate state. Owing to the strong push–pull dipolar character of compounds, higher-order nonlinear optical properties, such as three-photon absorption (3PA), can also be expected. Therefore, multi-photon absorption spectra of the following five representative compounds **a6**–**a10** (**Figure 3-38**) in solid state (powder) were measured by the multi-photon-induced fluorescence (MPIF) method for the wavelength range of 1160-1600 nm. The peak wavelength of the one-photon absorption spectra of the compounds **a6**–**a10** in aggregate state is 480-500 nm. So, the triples of them are 1440-1500 nm, which are covered by the

measurements above. The multi-photon-induced excitation spectra (in relative scale), the power dependence, and the comparison of the fluorescence spectra by one- and multi-photon excitations are presented.

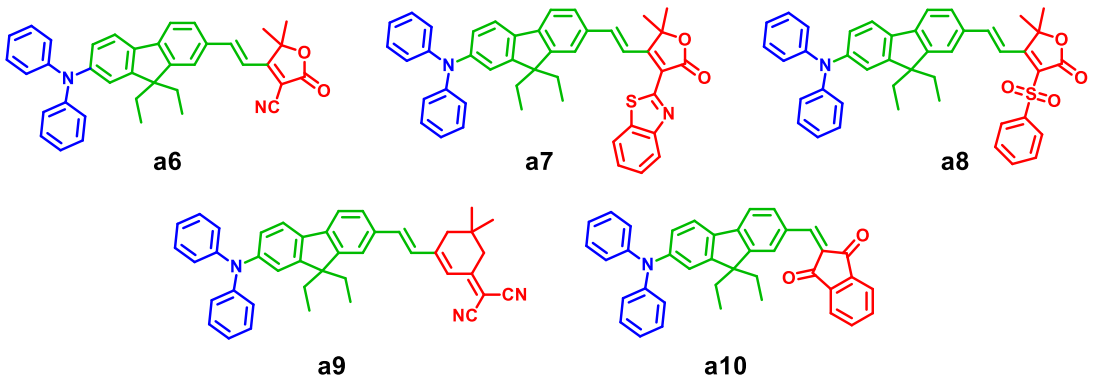

Figure 3-38. Molecular structures of **a6**–**a10**.

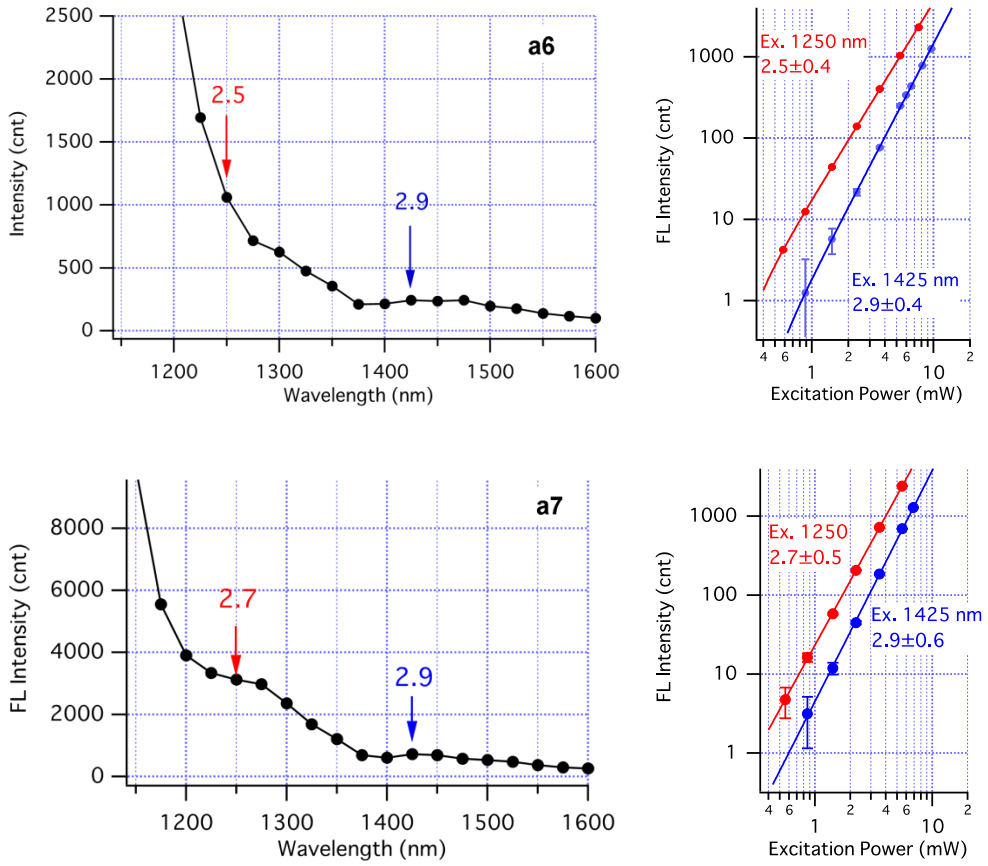

Figure 3-39. Left: multi-photon-induced excitation spectrum of the compounds **a6** and **a7** in powder form; Right: excitation-power-dependence of the fluorescence intensity at the peak wavelength of the fluorescence spectrum.

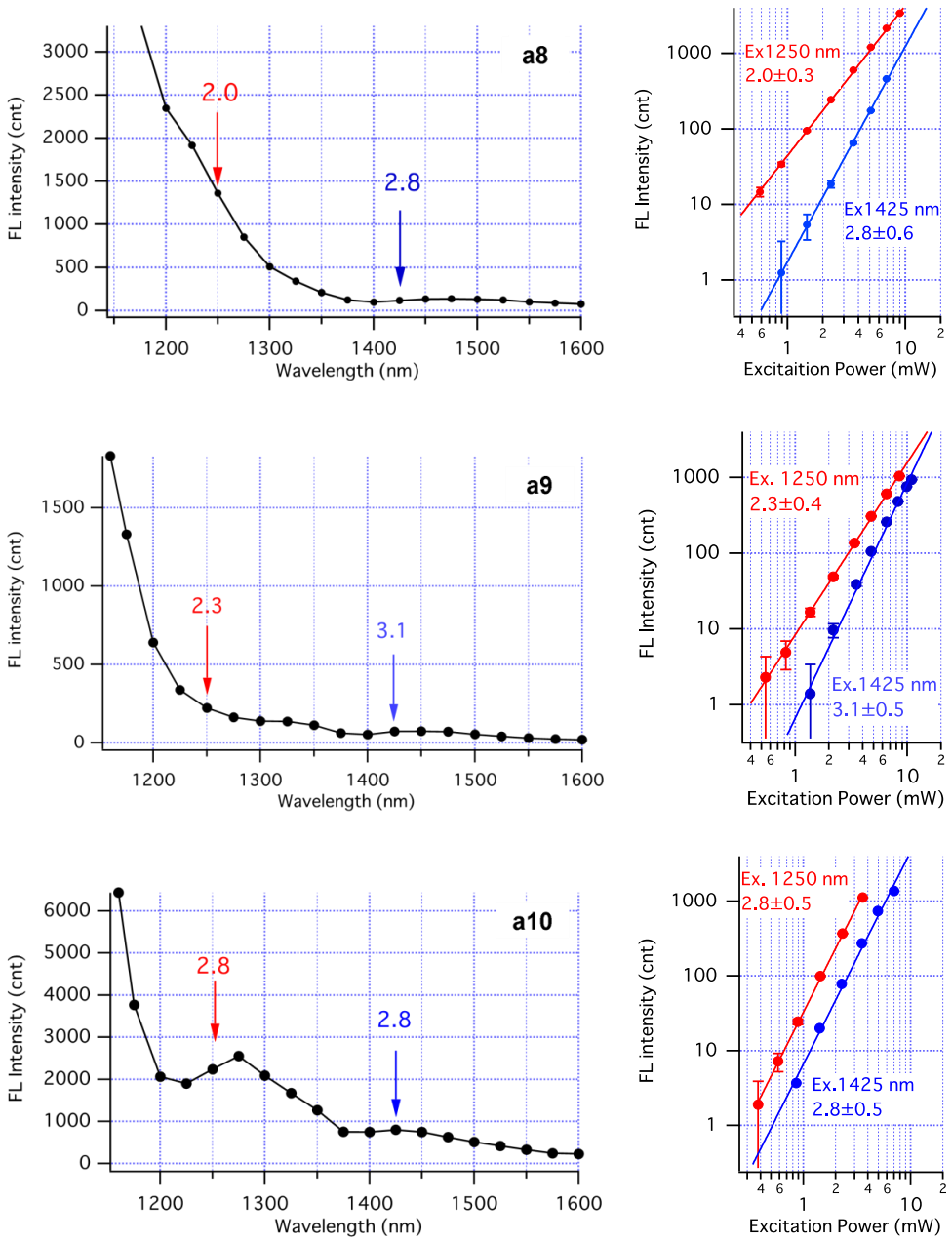

Figure 3-40. Left: multi-photon-induced excitation spectrum of the compounds **a8**, **a9** and **a10** in powder form; Right: excitation-power-dependence of the fluorescence intensity at the peak wavelength of the fluorescence spectrum.

Multi-photon excitation wavelength was scanned with a constant excitation power of 5 mW. The spectra were corrected for constant excitation "*intensity*" (*i.e.*, corrected with the laser pulse width and the focal length at each wavelength, see experimental part). Excitation power dependence was measured at 1250 nm and 1425 nm. The values of the slopes are shown in **Figure 3-39** and **Figure 3-40** (left column). All compounds showed similar excitation spectra: a tail from 1160 nm to 1250 nm (*Tail A*), a peak (or shoulder) around 1300 nm (*Band B*), and a small and broad band in the range 1400–1600 nm (*Band C*). At 1425 nm, the orders of the multi-photon absorption (slope) were determined to be 3 for all compounds, which mean that

3PA occurred at this wavelength for all compounds. Therefore, *Band C* is reasonably considered to be a 3PA band. While at 1250 nm, the slope was between 2 and 3, depending on the compounds. It seems that the spectra with intense *tail A* (**a 8** and **a9**) have the slope close to 2 while those with weaker *Tail A* and clear *Band B* (**a7** and **a10**) have the slope close to 3. Thus, it can be concluded that *Tail A* originates from 2PA and *Band B* originates from 3PA and they overlap the wavelengths. As a result, for all the compounds, the absorption band located around 1400-1600 nm can be assigned to 3PA, while there are another 3PA bands around 1200-1300 nm that overlap with the absorption tail of 2PA up to ~1350 nm; the degree of the overlap depends on the compound. However, quantitative comparison of the magnitudes among the spectra of compounds is difficult because of different packing density of compound in the tube cell.

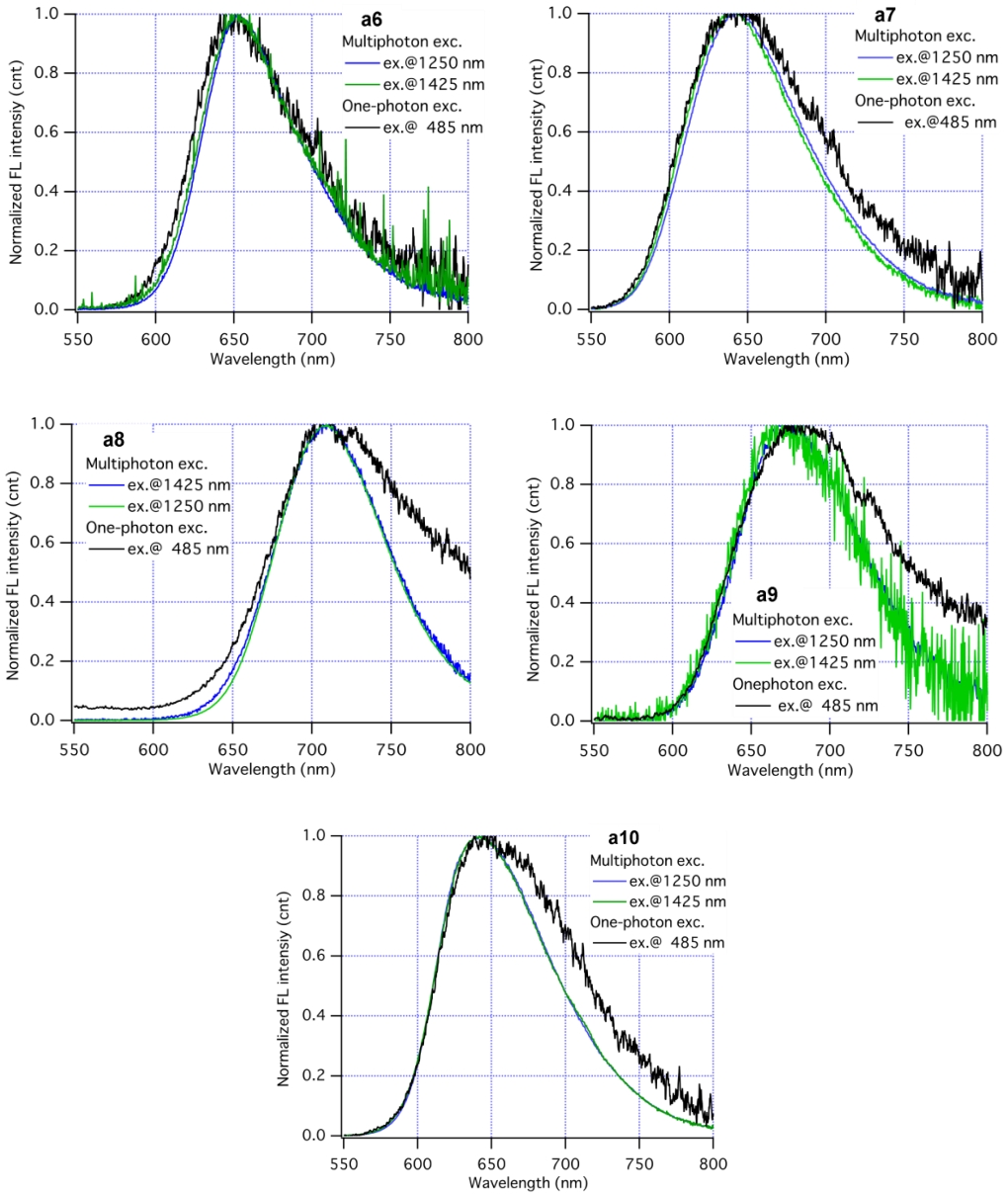

Figure 3-41. Normalized one-photon- and multi-photon-induced fluorescence spectra of the compounds **a6**–**a10** in powder form.

To further evaluate the difference in the fluorescence spectra of compounds **a6**–**a10** in solid with one-photon and multi-photon excitation, the spectra were subsequently recorded with one-photon excitation (recorded by a Hitachi F-4500 fluorescence spectrometer) and with the multi-photon excitation (at 1250 or 1425 nm, recorded by USB-2000FLG, corrected spectrum), respectively. As shown in **Figure 3-41**, for each compound, the spectra by one-photon excitation and by the multi-photon excitation agree well with each other. The fluorescence spectra under one-photon excitation (485 nm) show some deviation at wavelengths longer than 750 nm where the correction of the Hitachi F-4500 fluorescence spectrometer used is unreliable. In addition, the multi-photon-induced fluorescence spectra were unchanged in their shape for each compound by changing the excitation wavelength (**Figure 3-41**) and by changing the excitation power.

4.3. Crystal Structures

It is well known that the analysis of the crystal structures and crystal packing can help to understand the optical properties of compounds in the solid state. In our studies, the observations of AIE effect and solid state fluorescence of compounds triggered us to elucidate the molecular arrangement in their crystals. Crystals suitable for single crystal X-ray analysis were obtained for compounds **a2**, **a5**, **a6**, **a9**, **a10** and **a11** by slow evaporation from methanol/$CHCl_3$ mixture solution. Their crystal data and collection parameters are collected in tables in **Annexes**.

Compound **a2** crystallized in the triclinic $P\bar{1}$ group with an elemental cell containing two sets of two molecules. Compound **a5** crystallized in the monoclinic $P2_1/c$ group with an elemental cell containing four molecules. Compound **a6** crystallized in the monoclinic C2/c group with an elemental cell containing eight molecules. Compound **a9** and **a10** crystallized in the monoclinic $P\bar{1}$ group with an elemental cell containing two molecules. Finally, compound **a11** crystallized in the monoclinic $P2_1/n$ group with an elemental cell containing four molecules. The ORTEP diagrams with atom numbering scheme are depicted in **Figure 3-42**. Single crystal X-ray diffraction analyses provide direct evidence for the absolute structure of the compounds. All the compounds exhibit the *trans*-conformation except compound **a10**, which do not has conformation isomer.

The results indicate that the fluorene substructure is essentially planar for all six compounds. To further evaluate the planarity of the whole molecule, the dihedral angles between donor or acceptor and fluorene ring were listed in **Table 3-7**. For ease of understanding, the definitions of the angles were presented as well in **Table 3-7**. It should be noted that there are two different molecules in the crystal structure of **a2** and both of them were included in **Table 3-7**.

As we can see from **Table 3-7**, carbazolyl rings in molecules **a2** are greatly twisted with respect to the fluorene ring with dihedral angles of 68.3(0) and 70.4(3) °. For the other five diphenylamino compounds, phenyl rings from the diphenylamino donor group are also display large dihedral angles ranging from 64.8(1) to 87.2(8) ° with respect to the fluorene

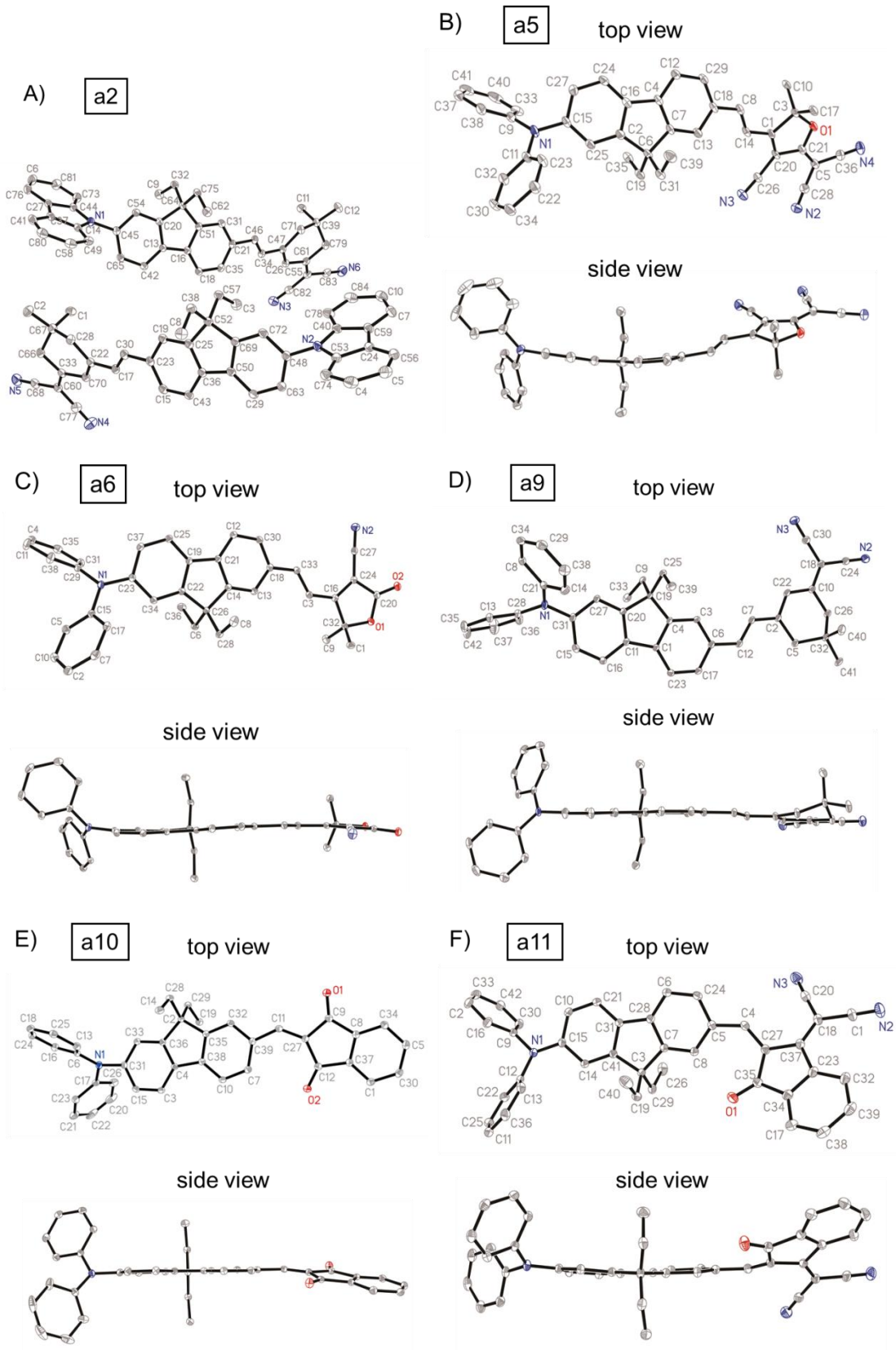

Figure 3-42. ORTEP drawings of **a2**, **a5**, **a6**, **a9**, **a10** and **a11** with the ellipsoids drawn at the 30% probability level.

bridge. These values are consistent with the reported data for similar unsymmetrical fluorene-based derivatives.[262] Besides, the acceptor groups of compounds **a2**, **a5** and **a11** revealed the large deviations from planarity of fluorene, manifested by the dihedral angles θ_3 of 37.4(8) and 28.3(4) ° for **a2**, 31.0(9) ° for **a5** and 36.3(8) ° for **a11**. The large dihedral angles between donor or acceptor and fluorene ring are probably associated with weak intermolecular interactions in the crystal packing, *i.e.*, the donors or acceptors of the fluorophores were twisted to fit into the crystalline lattices.[263-264]

Table 3-7. Dihedral angles (°) between donor or acceptor and fluorene ring in compounds **a2**, **a5**, **a6**, **a9**, **a10** and **a11**.

	a2	**a5**	**a6**	**a9**	**a10**	**a11**
θ_1 (°)	68.3(0), 70.4(3)	70.1(1)	72.4(2)	77.8(0)	77.1(2)	87.2(8)
θ_2 (°)		74.9(6)	70.9(3)	76.7(4)	70.0(4)	64.8(1)
θ_3 (°)	37.4(8), 28.3(4)	31.0(9)	6.6(9)	4.7(3)	15.3(0)	36.3(8)
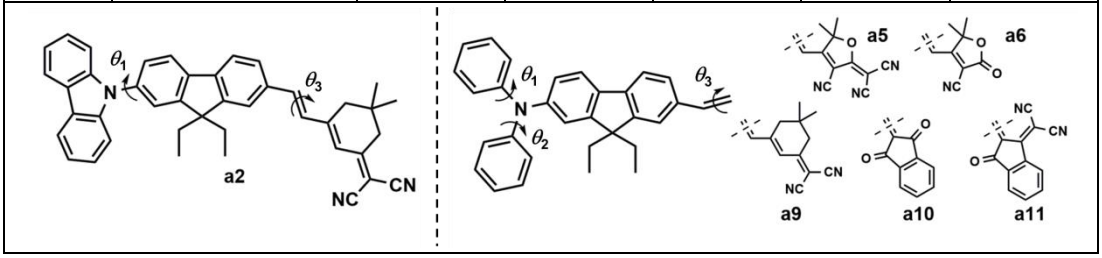						

As can be seen in **Figure 3-43** to **Figure 3-48**, obvious characteristic molecular pairs can be observed in the crystal packing diagram of the compounds **a2**, **a5**, **a6**, **a9**, **a10** and **a11**. The molecular pairs involve antiparallel dipole−dipole interactions between the molecules related by inversion centres. For all compounds except **a6**, the mean planes of conjugation skeleton of molecules are parallel to each other within molecular pairs. Moreover, the presence of multiple weak intramolecular interactions holds the molecule pairs together to result in the formation of crystal architecture. These phenomena are in line with our previous observations for the similar push-pull compounds.[253, 255]

Figure 3-43 shows four molecular pairs linked by weak C−H···π interactions in the packing structure of **a2**. For each molecular pair, two neighbour molecules are longitudinally slipped away with respect to each other forming a weakened π–π stacking (3.251 Å). As shown in **Figure 3-44**, the face-to-face *H*-aggregates can be observed in the crystal packing of the diethylamino **a5**, in which two adjacent molecules constitute the repeating molecular pairs through a weak π–π stacking (3.220 Å) between the fluorene ring of one molecule and the TCF acceptor of another molecule. The greatly twisted molecular structure of **a5** should be attributed to the space resistance of ethyl substituents on the fluorene moiety. These dimers are further stacked into crystal packing based on multiple weak C−H ···N interactions.

The packing structure of **a6** is quite different with respect to other compounds (**Figure 3-45**). It is composed of antiparallel chain of dipoles connected by C−H···O interactions (2.706 Å) between the oxygen atom of the carbonyl group and the aromatic hydrogen of its

neighbor molecule. In a chain, all dipoles are oriented in the same direction, whereas two adjacent chains have opposite direction. The neighboring chains are further linked by C−H···π interactions and $\pi \cdots \pi$ stacking along *a* axis, generating the crystal packing diagram. Moreover, the molecular pairs can be easily extracted from crystal packing. As shown in **Figure 3-45**, two molecules in the molecular pairs are not parallel to each other with a dihedral angle of 37.68 °.

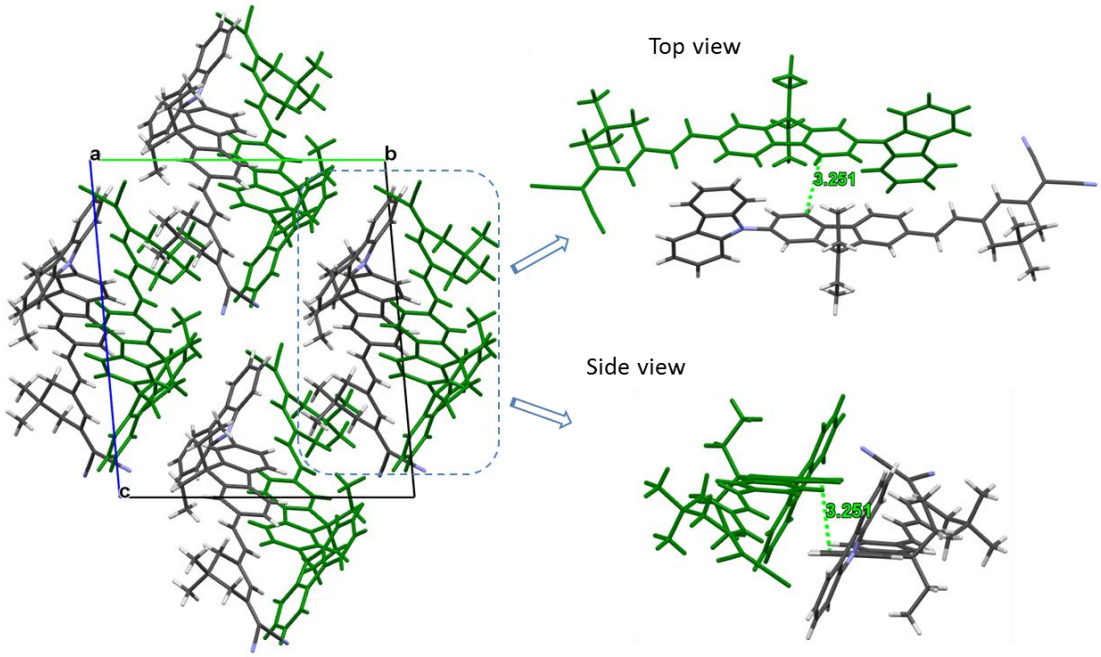

Figure 3-43. Crystal packing of **a2**, viewed down the crystallographic *a* axis.

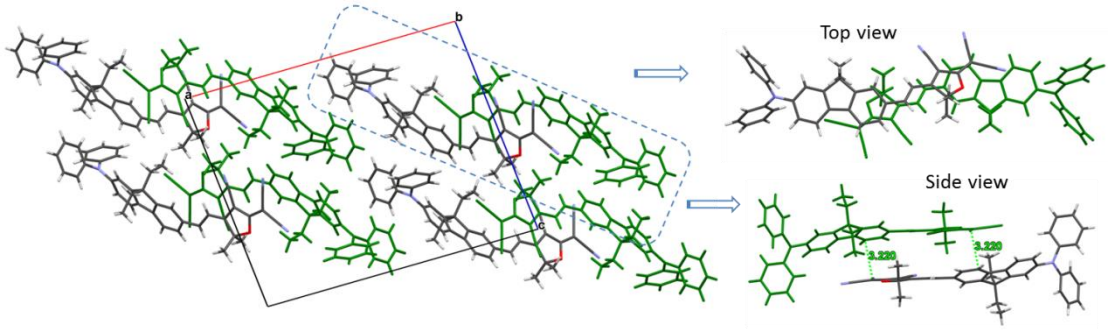

Figure 3-44. Crystal packing of **a5**, showing the *H*-type aggregates, viewed down the crystallographic *b* axis.

The crystal packing of **a9** shows a brickwork arrangement (**Figure 3-46**), in which the repeating molecular pairs bound by C−H···π interactions (2.891 Å) are arranged through another C−H···π interactions (2.881 Å), resulting in two anti-parallel stair-like chains of dipoles.

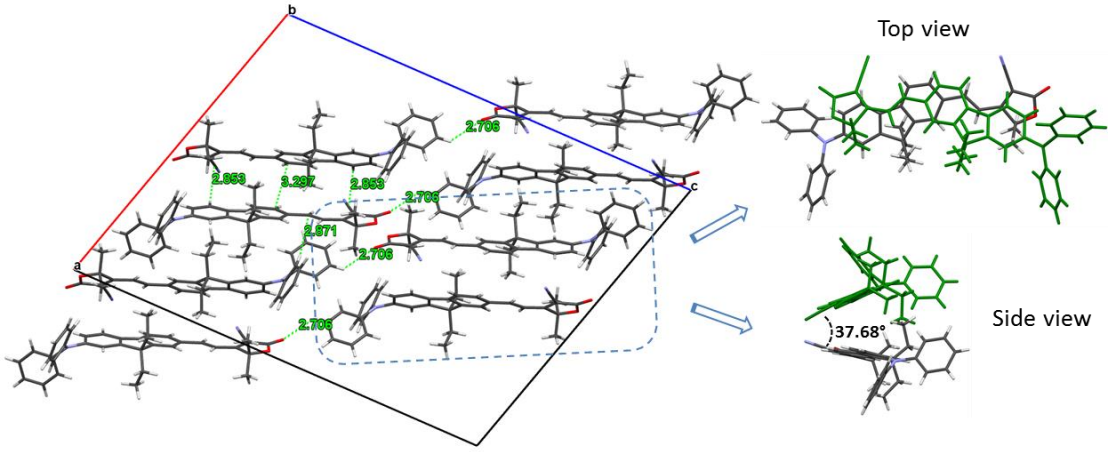

Figure 3-45. Crystal packing of **a6**, viewed down the crystallographic *b* axis.

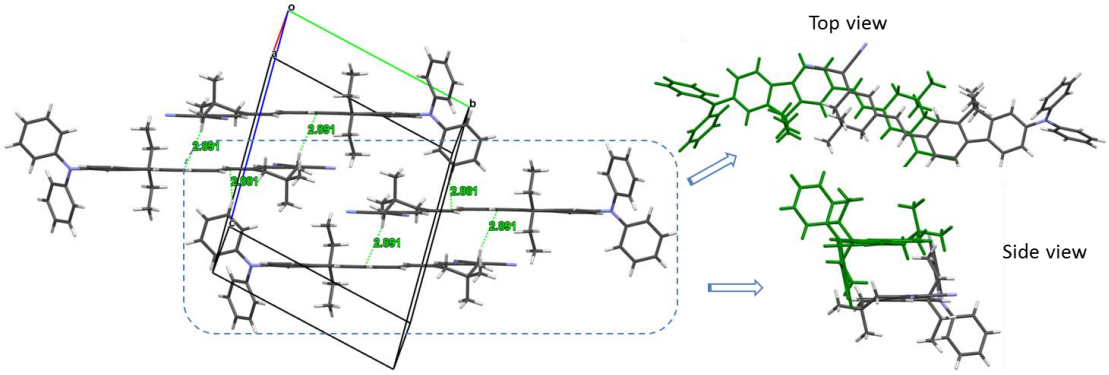

Figure 3-46. Crystal packing of **a9**, showing the brickwork arrangement.

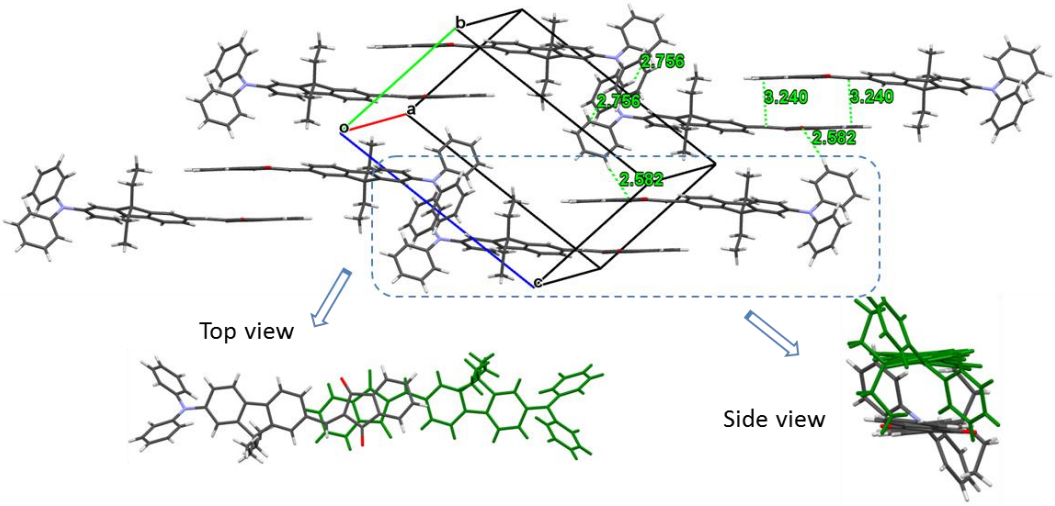

Figure 3-47. Crystal packing of **a10**, showing the *J*-type aggregates.

In contrast, the molecular pairs in the crystal packing of **a10** show the obvious *J*-aggregates with $\pi \cdots \pi$ interactions of 3.240 Å, in which only the acceptors of the adjacent molecules closely overlap with each other in opposite direction (**Figure 3-47**). Moreover, the adjacent

molecular pairs are horizontally linked together through C−H···π interactions with distances of 2.756 Å, and longitudinally linked together through C−H···O interactions with distances of 2.582 Å. The presence of *J*-aggregates in the packing of **a10** is in good agreement with the strong crystal fluorescence.

Similar to compound **a5**, in the molecular pairs of **a11**, $\pi\cdot\cdot\pi$ interaction between two head-to-tail dipoles results in face-to-face *H*-aggregates (**Figure 3-48**). The presence of ethyl groups on the fluorene greatly twists the molecular structure of **a11** and greatly weaken the $\pi\cdot\cdot\pi$ interaction. The molecular pairs are further connected *via* multiple C−H$\cdot\cdot\pi$ intermolecular interactions to generate packing diagram of **a11**.

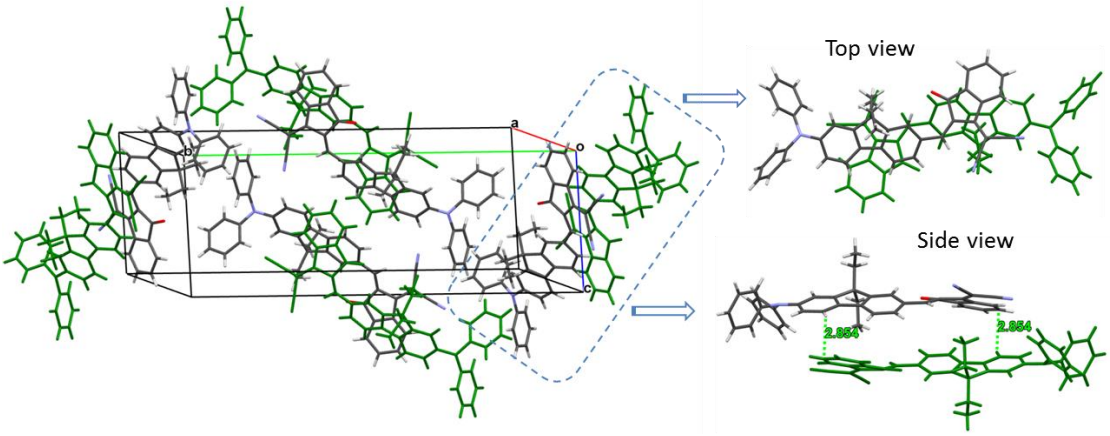

Figure 3-48. Crystal packing of **a11**, showing the *H*-type aggregates.

The crystal packing of compounds **a2**, **a5**, **a6**, **a9**, **a10** and **a11** indicate that the presence of bulky diphenylamino group, the carbazolyl group, ethyl substituents on the acceptor and ethyl substituents on the fluorene moiety could avoid the maximum face-to-face π–π intermolecular interactions. The strong red fluorescence of crystal **a10** can be attributed to the formation of *J*-aggregates. The presence of *H*-aggregates in **a5** and **a11** should be responsible for the feeble emission of crystals.

5. Two-Photon Blood Vasculature Imaging Using Aggregation-Induced Emission Active Nanoprobes

5.1. Preparation and Characterization

As described before, the designed compounds have been demonstrated to show the unique AIE feature, excellent two-photon activity and large Stokes shift with emission in the FR/NIR region. These advantages probably make them useful for biological applications. As a representative, the most red-shifted aggregate of **a9** was chosen as the fluorescent probe for

bio-imaging. According to our experience, the bare aggregates are not stable in physiological conditions and tend to assemble into larger aggregates (**Figure 3-49**). To improve the colloidal stability of AIE nanoaggregates, **a9**-aggregate was encapsulated into polymer nanoparticles through a nanoprecipitation method using a biocompatible polymeric surfactant, Pluronic F127. The small quantity of surfactant used not only can stabilize the nanoaggregates in physiological media but also can ensure the existence of the formed nanoaggregates working as bioprobes.

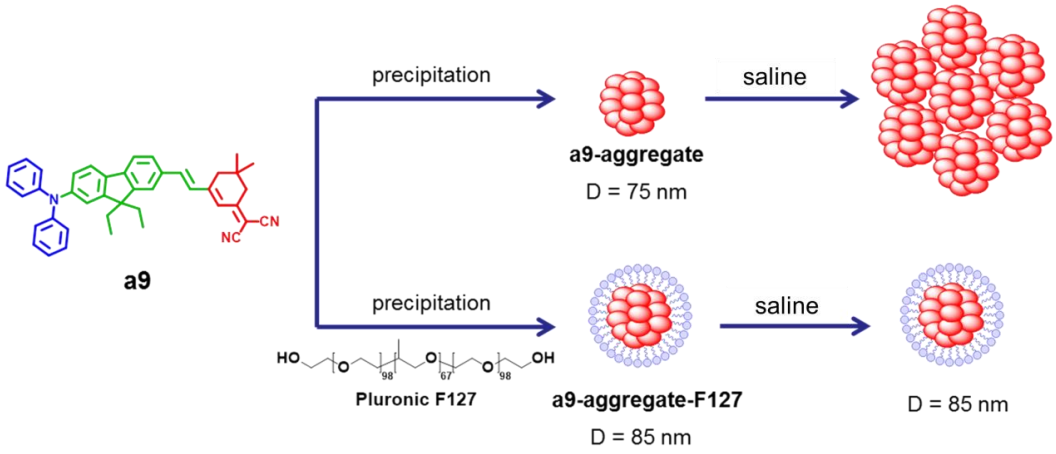

Figure 3-49. Illustration of the improvement of stability of AIE nanoaggregates.

The procedure for the preparation of the **a9**-aggregate-F127 is illustrated in **Figure 3-49**. A mixture acetone solution of **a9** and Pluronic F-127 with 1:1 weight ratio was injected into the water upon stirring, **a9** molecules aggregate and entangle with the hydrophobic chains of Pluronic F127. The acetone was then removed through slow evaporation upon stirring overnight, affording **a9**-aggregate-F127 suspension. The obtained nanoparticles were further purified by filtration through a 0.2 μm syringe filter to remove possible large particles. Final nanoparticles were directly used for optical measurements. For *in vivo* imaging, the prepared suspension was concentrated to a final concentration of 0.5–1×10^{-3} mol.L^{-1} in terms of compound **a9**. A saline suspension of **a9**-aggregate-F127 was prepared before injection into mice by adding sodium chloride pellet (specifically used for preparing physiological serum).

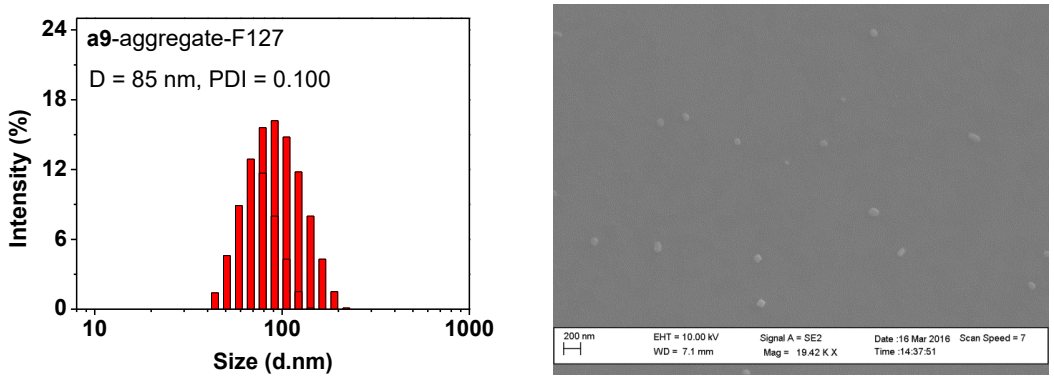

Figure 3-50. Left: Particle size distribution of **a9**-aggregate-F127 measured by DLS; Right: SEM images of **a9**-aggregate-F127.

The hydrodynamic diameters of **a9**-aggregate-F127 nanoparticles were studied by dynamic light scattering (DLS), suggesting an average size of 85 nm with a good size distribution (**Figure 3-50**, left). Furthermore, scanning electron microscopy (SEM) was utilized to study their morphologies, which revealed uniform distributed spherical nanoparticles for **a9**-aggregate-F127 (**Figure 3-50**, right). **a9**-aggregate-F127 show a similar value of size as that of bare **a9**-aggregate (D = 75 nm). It is worth noting that **a9**-aggregate-F127 nanoparticles are very stable in a saline solution as no large aggregation and obvious hydrodynamic diameter changes can be observed. This should be ascribed to the existence of PEG chains outside particles that suppress nonspecific interaction and further aggregation.

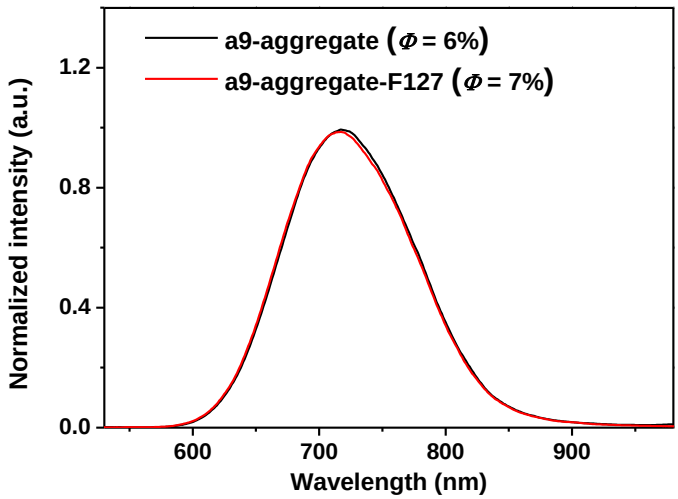

Figure 3-51. Emission spectra of **a9**-aggregate-F127 in the aqueous suspension and **a9**-aggregate in acetone/water mixtures (f_w = 90 vol%).

The emission spectrum of **a9**-aggregate-F127 nanoparticles is shown in **Figure 3-51**, which exhibits same spectrum as that of **a9**-aggregate dispersed in acetone/water mixtures (f_w = 90 vol%). It should be noted that **a9**-aggregate-F127 nanoparticles in water showed a Φ_f value of 7%, measured using rubrene in methanol as the standard, which is identical to 6% for the corresponding **a9**-aggregate. These similarities between **a9**-aggregate-F127 and **a9**-aggregate indicate compact encapsulation of compound **a9** in the nanoparticles, revealing that pluronic F127 added do not modify the aggregate state.

5.2. Importance of Imaging Tumour Vasculature

Dysfunction of the vascular system is associated with various diseases like cardiovascular, kidney, renal, rheumatoid, eyes diseases or cancer.[265-267] Angiogenesis plays a major role in tumour growth and metastasis.[268] *In vivo* optical imaging of the vascular system gives valuable information on the vascular morphology, the blood flow, the vascular permeability and abnormality in blood vessel endothelial cells and their interactions with cancer or cells of the immune system. Only a few probes are available, which stay in the leaky tumour

vasculature to access changes in tumour blood volume and vessel permeability before and after treatment.[269-271] Indeed, most probes diffuse across the tumour vascular endothelium and can therefore not be used to detect changes in these parameters.

Moreover, in depth *in vivo* optical vascular imaging needs long wavelength fluorophores absorbing and emitting in the FR/NIR region (650–1300 nm), which corresponds to the optical transparency window of tissues. The pulsed IR lasers in two-photon microscopy use this window for deep fluorescence imaging in whole animals. In this region, light photon absorption by endogenous molecules (hemoglobin, H_2O...) is minimal for maximum penetration depth [44, 270, 272-274] and photon scattering is reduced. These phenomena are, however, high in tumours due to their high cell and cell organelles densities.[275-280] Therefore, the probe with efficient two-photon absorption and emission properties in the FR/NIR is much more interesting for imaging tumour tissues.[81, 102, 108, 247, 252, 281-283]

5.3. Biphotonic *in vivo* Imaging Using a9-Aggregate-F127

After preparing the surfactant stabilized nanoaggregates of **a9**, **a9**-aggregate-F127 was subsequently used to image blood vasculature of a tumour in mouse ear using two-photon fluorescence microscope (2PFM) through the collaboration with Dr. Flavien Caraguel and Dr. Boudewijn van der Sanden in CEA-INSERM-Grenoble Alps University. Before imaging, **a9**-aggregate-F127 nanoparticles ($0.5–1\times10^{-3}$ mol L^{-1}) were intravenously injected into the tail vein of mice. During 60 minutes circulation of **a9**-aggregate-F127 in the body, bright red

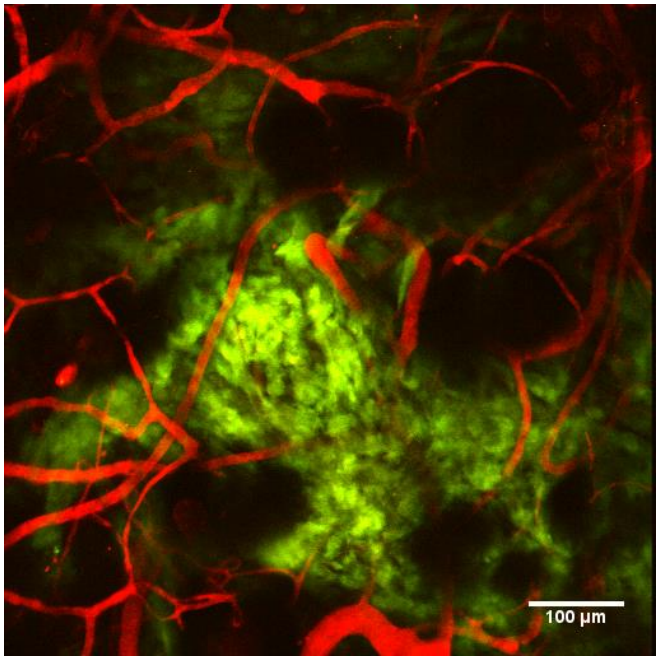

Figure 3-52. Two-photon microscopic image of **a9**-aggregate-F127 (red signal) circulating in the tumour vasculature of a human glioma U87MG (glioma cells express GFP = green signal) xenografted in the ear of a nude mouse. The image is a z-projection (52 images with a step size of 3 µm, thickness = 156 µm) of the standard deviation of the fluorescence intensities (higher intensity for circulating NPs).

fluorescence from the blood vasculature network in mice ear was clearly observed upon two-photon excitation at 1000 nm (**Figure 3-52**). Moreover, not only the blood vessels, but also small capillaries could be clearly observed by the **a9**-aggregate-F127 nanoparticles (**Figure 3-52**). The Z-projected and 3D (**Figure 3-53**) images illustrate that **a9**-aggregate-F127 nanoparticles can efficiently label the blood vasculature under *in vivo* conditions. No diffusion of the **a9**-aggregate-F127 in the extravascular–extracellular space was observed during one hour after injection.

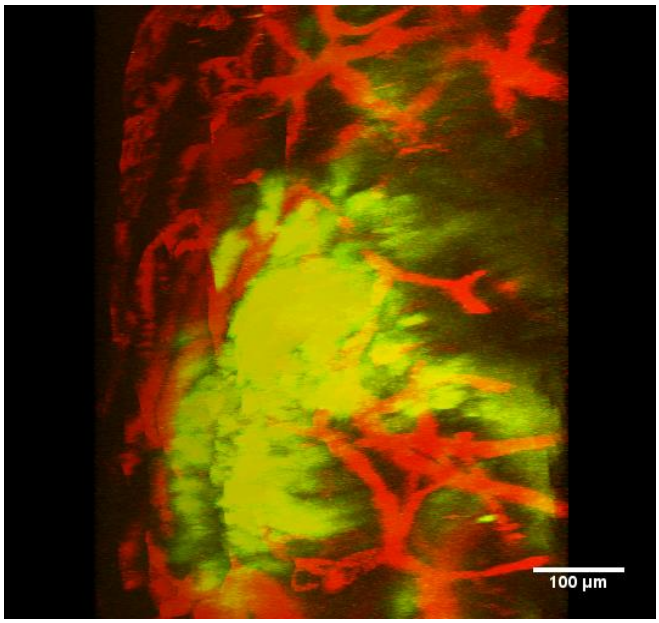

Figure 3-53. 3D two-photon microscopic image of the z-stack in **Figure 3-52**. The imaging depth is exceptional for tumours with a high cell density (160 µm), which normally show an important diffusion of light photons and consequently loss of photons for excitation and detection.

6. Preparation of FRET-based Co-assembled Nanoparticles with Aggregation Induced Near-Infrared Emission for Biphotonic in vivo Imaging

In the last section, we have developed a novel class of organic fluorophores with an extraordinary AIE feature and most of them are located in the NIR region. The obtained NIR NPs have been successfully utilized in two-photon excited *in vivo* fluorescence imaging. In fact, most of the reported AIE fluorophores loaded NPs show emission in the visible region, which is not ideal for *in vivo* imaging.[109] Although several studies reported AIE NPs with FR/NIR emission, their emission maxima were mainly located at wavelengths shorter than 650 nm and only part of their emission spectra was located in the NIR range. Different from the small molecule engineering, a second strategy will be explored in this section to reach

NIR emission by keeping a good emission quantum yield.

6.1. Design of Co-assembled Nanoparticles

6.1.1. FRET-based Co-assembled Nanoparticles

FRET is a distance dependent interaction between two chromophores in which excitation is transferred from the donor to the acceptor. This process has been discussed in details in **Chapter 2**. Upon encapsulation of a FRET pair into one matrix, efficient FRET occurs between the donor and the acceptor when there is substantial overlap between the emission of donor and the absorption of acceptor. As compared to sophisticated chemical modification, the FRET strategy should provide a more straightforward and efficient method to red-shift the emission of AIE nanoaggregates. Encapsulation of a suitable organic fluorophore into AIE nanoaggregates might be able to quench the fluorescence from AIE fluorophores and amplify the emission of the doped dyes. The appropriate choice of AIE fluorophores and loaded NIR fluorophores would offer NIR fluorescence signals.

In addition, due to the signal amplification provided by the energy donor, these nanoparticles are also expected to show higher brightness than those based on traditional NIR dyes alone. When the hydrophobic ACQ donors are encapsulated in nanoparticles, they aggregate and lead to fluorescence quenching, which subsequently reduce the nanoparticles fluorescence intensities. This disadvantage can be overcome by using AIE fluorophores, which emit stronger fluorescence at higher concentration in the nanoparticles formulation. In addition, the low concentration of doped dyes in AIE nanoparticles should be diluted and separated by AIE fluorophores. As a result, the doped dyes could be stabilized in the AIE nanoparticles with enhanced fluorescence *via* FRET from AIE fluorophores, resulting in nanoparticles with strong amplified fluorescence and good photostability.

As shown in **Figure 3-54**, the above FRET strategy has been successfully applied to prepare fluorescence amplified organic nanoparticles by incorporation of two hydrophobic AIE fluorophores, **BOSA** donor and **NPAPF** acceptor, using biocompatible Pluronic F127–folic acid adduct (F127–FA) as the encapsulation matrix.[284] A 3.0-fold amplified **NPAPF** emission signal was achieved *via* FRET as a result of good spectra overlap between the emission spectrum of **BOSA** donor and the absorption spectrum of **NPAPF** acceptor. The emission of **BOSA** loaded nanoparticles was greatly red-shifted from 503 to ~620 nm after doping **NPAPF** acceptor. As a result, the obtained **BOSA–NPAPF** co-loaded F127–FA nanoparticles show a large Stokes shift of 245 nm and bright fluorescence signals. The cellular imaging studies indicated that the F127–FA encapsulated AIE NPs are efficient fluorescent probes for biological imaging.

In another case, nanoparticles of an AIE active **TPETPAFN** (donor) was doped with a non-AIE active NIR fluorophore **NIR775** aiming to obtain NIR emission with high brightness (**Figure 3-55**).[248] The good spectral overlap between the emission of **TPETPAFN** and the absorption of **NIR775** leads to efficient energy transfer, resulting in a 47-fold enhancement of

the **NIR775** emission intensity upon excitation of **TPETPAFN** donor as compared to that upon direct excitation of **NIR775**. The obtained fluorescent nanoparticles show sharp NIR emission at ~780 nm with a band width of 20 nm, a large Stokes shift of 275 nm, good photostability and low cytotoxicity. *In vivo* imaging study revealed that the synthesized nanoparticles are able to provide high fluorescence contrast in live animals.

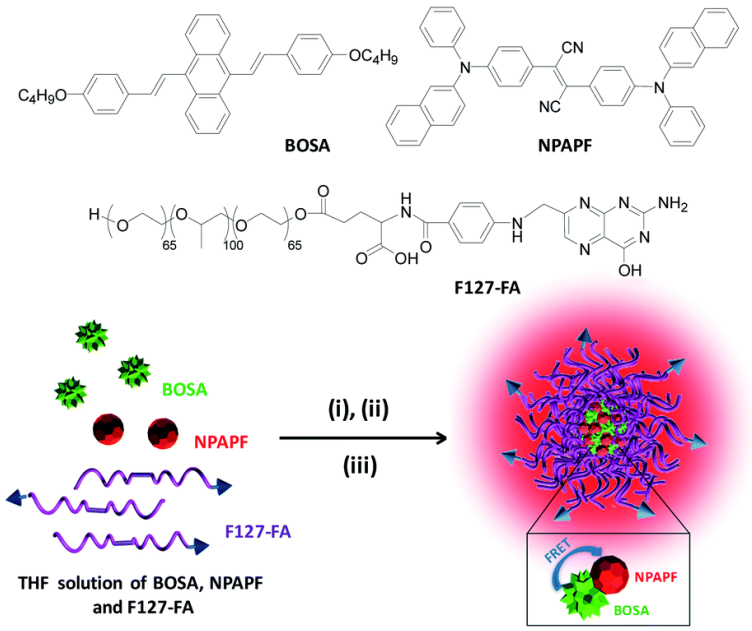

Figure 3-54. Chemical structures of **BOSA**, **NPAPF** and **F127–FA**, and schematic illustration of the fabrication of **BOSA–NPAPF** co-loaded **F127–FA** NPs. (i) mix with water; (ii) sonication; (iii) THF removal.[284]

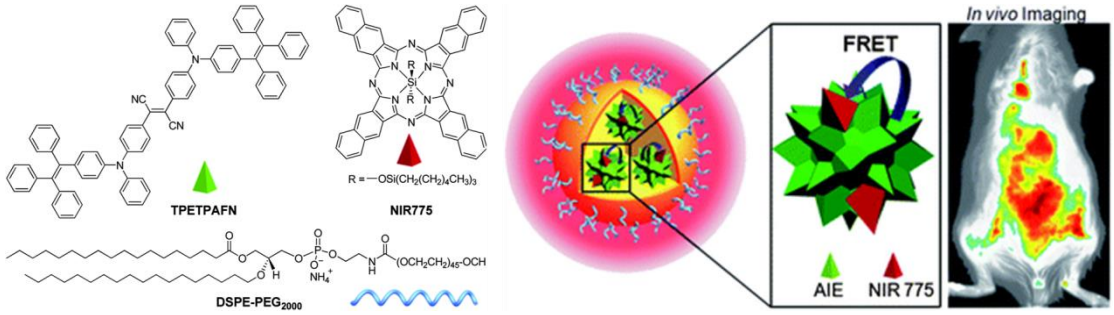

Figure 3-55. Chemical structures of **TPETPAFN**, **NIR775** and **DSPEPEG$_{2000}$**; Near-infrared fluorescence amplified organic nanoparticles with aggregation-induced emission characteristics for *in vivo* imaging.[248]

In principle, this FRET strategy could be generally applied to other AIE fluorophores to yield bright fluorescent nanoparticles with large Stokes shift for biological applications. Moreover, this is a very efficient way of red-shifting the emission and having high quantum yield of emission.

6.1.2. Design of FRET-based Co-assembled Nanoparticles

Based upon this literature, the FRET strategy can endow the nanoparticles with the optical properties of both donor fluorophore and acceptor fluorophore. Since we aim to develop NIR nanoparticles for two-photon fluorescence bio-imaging, a proper two-photon FRET donor and a suitable NIR acceptor are required for constructing co-assembled nanoparticles. In the context, the AIE active **a3** (**Figure 3-56**) was chosen as the two-photon FRET donor for harvesting energy, which displays good two-photon absorption properties in the range of 800–1000 nm in the aggregate state (**Figure 3-57**). Considering the rule of substantially spectral overlap between donor emission and acceptor absorption, two non-AIE active hydrophobic fluorophores **a5** and **a12** with strong push-pull strength were chosen as FRET acceptor candidates (**Figure 3-56**). The nanoparticles **a3**-NPs, **a5**-NPs and **a12**-NPs were prepared easily and repeatedly by using rapid injection method, which will be described after.

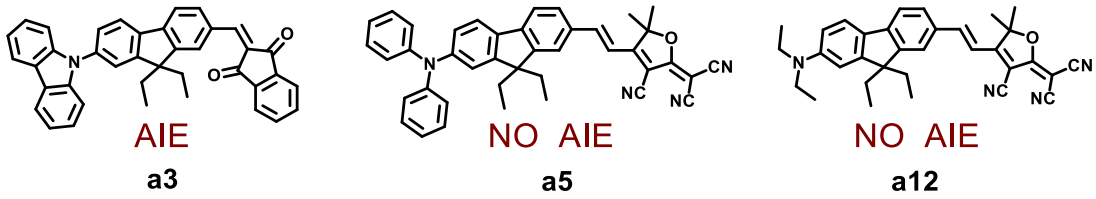

Figure 3-56. Molecular structures of **a3**, **a5** and **a12**.

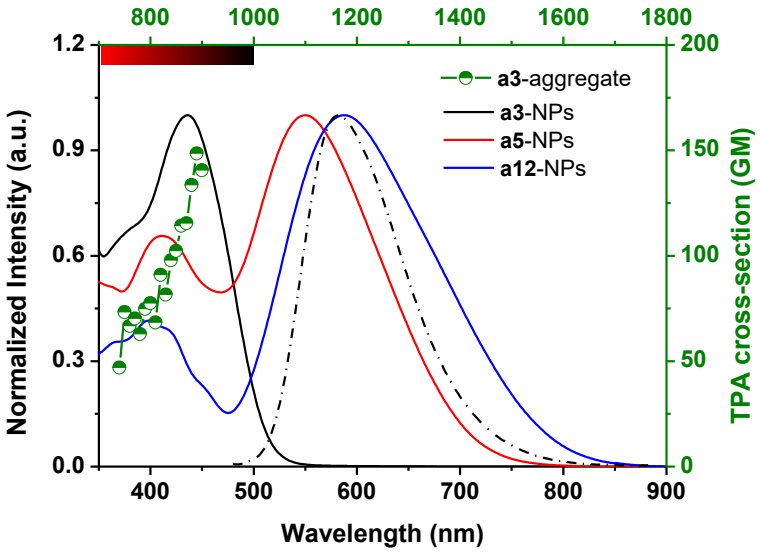

Figure 3-57. Normalized absorption spectra (solid line) of **a3**-NPs, **a5**-NPs and **a12**-NPs, PL spectrum (dash line) of **a3**-NPs and two-photon absorption spectrum of **a3**-aggregate. All the samples were dispersed in water.

The absorption spectra of **a3**-NPs, **a5**-NPs and **a12**-NPs in water as well as the photoluminescence (PL) spectrum of **a3**-NPs in water are shown in **Figure 3-57**. **a3**-NPs have absorption and emission maxima at 436 nm and 582 nm, respectively. The maximum absorption of **a5**-NPs and **a12**-NPs are located at 550 and 588 nm, respectively. Importantly,

preliminary result show that the emission spectrum of **a3**-NPs overlaps well with the absorption spectra of **a5**-NPs and **a12**-NPs, which implies that they could be used as FRET donor–acceptor pairs.

6.2. Preparation of Co-loaded Nanoparticles

a3 and **a5** (or **a12**) co-loaded nanoparticles were synthesized through a modified precipitation method using pluronic F127 as the matrix compared with **a9**-aggregate-F127 (**Figure 3-58**). A small quantity of amphiphilic copolymer pluronic F127 not only can enhance the biocompatibility of aggregates but also can ensure the aggregate state of molecules. An acetone solution containing **a3**, **a5** (or **a12**) and pluronic F127 was injected into water under stirring. The nanoparticles suspension was obtained after acetone evaporation under stirring overnight. The nanoparticles suspension was further purified with a 0.2 μm syringe filter to obtain **a3** and **a5** (or **a12**) co-loaded nanoparticles (**a3**-**a5**-NPs and **a3**-**a12**-NPs). Based on a similar procedure, **a3**, **a5** or **a12** loaded pluronic F127 nanoparticles (namely **a3**-NPs, **a5**-NPs and **a12**-NPs) were also synthesized separately without doping other compound. No obvious precipitation from the prepared nanoparticle suspensions was observed after being stored at room temperature for at least one month, indicating their excellent colloidal stability.

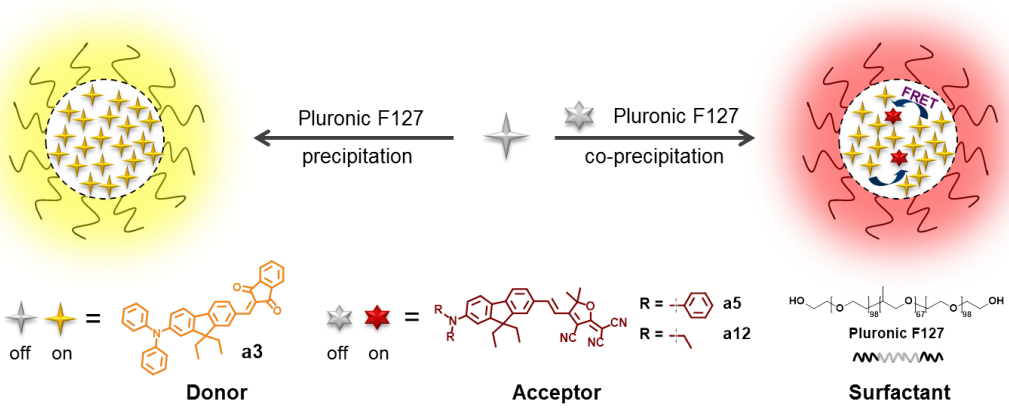

Figure 3-58. Schematic illustration of the fabrication of **a3** and **a5** or **a12** co-loaded NPs using pluronic F127 as the matrix through a co-precipitation method.

6.3. Optical Properties of Co-loaded Nanoparticles

6.3.1. Absorption and Emission Properties

As the FRET efficiency is related to the ratio of acceptor to donor, to optimize the fluorescence signal output of **a3**-**a5**-NPs and **a3**-**a12**-NPs, the influence of the mass ratios of acceptor (**a5** or **a12**) to donor **a3** on the nanoparticle emission was investigated. In these experiments, the amounts of **a3** and pluronic F127 were fixed, while the mass ratio of

acceptor to donor changed from 0.2% to 10% for **a5**-**a3** pair and from 0.2% to 4% for **a12**-**a3** pair. Absorption spectra of **a3**-**a5**-NPs and **a3**-**a12**-NPs with various mass ratio of acceptor to donor are shown in **Figure 3-59**. The absorption maxima for **a3** in both **a3**-**a5**-NPs and **a3**-**a12**-NPs are located at 436 nm, only 2 nm blue-shifted as compared to that of pure **a3** aggregates (438 nm) in acetone/water mixtures with f_w = 90 vol%. This comparable absorption demonstrates the aggregation of **a3** molecules in co-loaded **a3**-**a5**-NPs and **a3**-**a12**-NPs is the same.

As shown in insets of **Figure 3-59**, the absorbance of acceptor (**a5** or **a12**) in co-loaded nanoparticles increases with the increased mass ratio of acceptor. Meanwhile, the absorbance of **a3**-**a5**-NPs at 436 nm shows a slight increase with increasing the quantity of acceptor **a5**, probably due to the overlap of absorption spectra of **a3** and **a5**. The same absorbance increase at 436 nm can also be found for **a3**-**a12**-NPs.

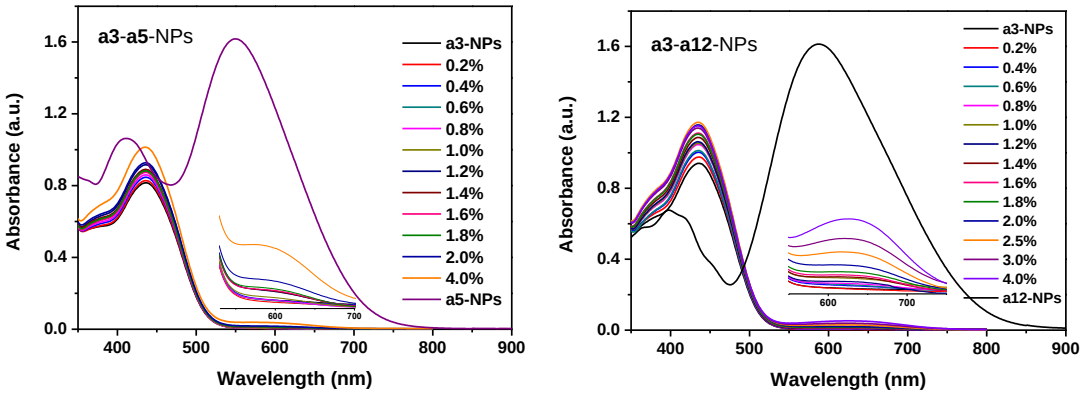

Figure 3-59. Absorption spectra of **a3**-**a5**-NPs (left) and **a3**-**a12**-NPs (right) with different mass ratio (wt %) of acceptor (**a5** or **a12**) to donor **a3**. **3-NPs**, **5-NPs** and **12-NPs** represent the pure nanoparticles without doping other fluorophore. Inset is an enhanced view of the range 550-700 nm.

The emission spectra of **a3**-**a5**-NPs and **a3**-**a12**-NPs with various acceptor–donor mass ratios were recorded upon direct excitation of donor **a3** at 460 nm, where the acceptors **a3** and **a5** have less absorption. As shown in **Figure 3-60**, with increasing acceptor **a5** mass ratio (wt %) from 0.2% to 1.2%, the emission of donor **a3** centred at 582 nm is gradually quenched, while, as expected, the intensity of NIR emission from acceptor **a5** increases greatly. This is the result of significant FRET process between donor **a3** and acceptor **a5**. However, further increase of the acceptor mass ratio up to 10%, the fluorescence intensity of **a5** in **a3**-**a5**-NPs is gradually decreased because of the self-quenching of **a5** molecules, since any back transfer seems impossible as regards to the position of the different excited states. These probably illustrate that the acceptor **a5** is largely separated rather than aggregated in the co-loaded nanoparticles at low doping, which should not only minimize self-quenching of acceptor dyes but also facilitate energy transfer from the donor **a3** to the acceptor **a5**. It is worth noting that the amplified emission of **a3**-**a5**-NPs is gradually red-shifted from 669 to 753 nm with increasing the **a5** mass ratio from 0.2% to 10%. This phenomenon should be related to the intermolecular interactions among **a5** molecules in **a3**-**a5**-NPs. As a result, co-loaded

nanoparticles prepared with 1.2% feeding ratio of **a5** (abbreviated as **a3**-1.2%**a5**-NPs) offer the strongest NIR fluorescence signal at 711 nm with a large Stokes shift of 275 nm. The fluorescence quantum yield of **a3**-1.2%**a5**-NPs was determined to be 14 % using rubrene in methanol as a standard.

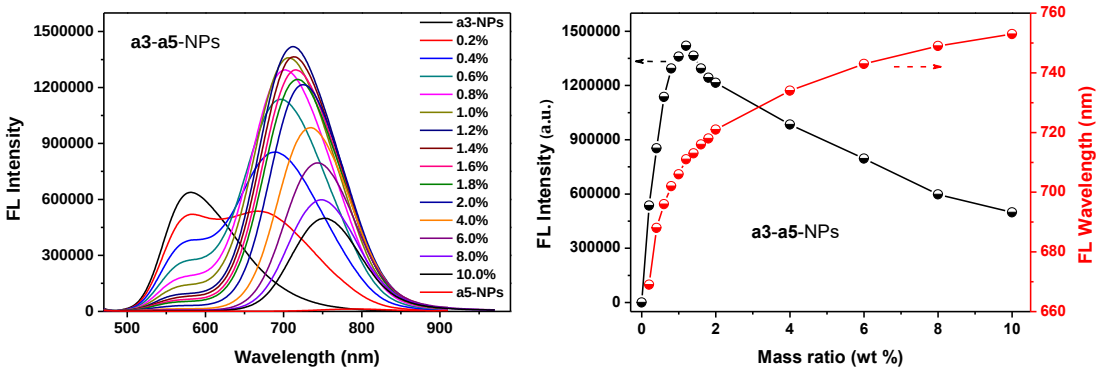

Figure 3-60. Left: PL spectra of **a3**-**a5**-NPs with different mass ratio (wt %) of **a5** to **a3**; Right: Plot of PL intensity (black) and wavelength (red) versus wt % in **a3**-**a5**-NPs. Excitation at 460 nm.

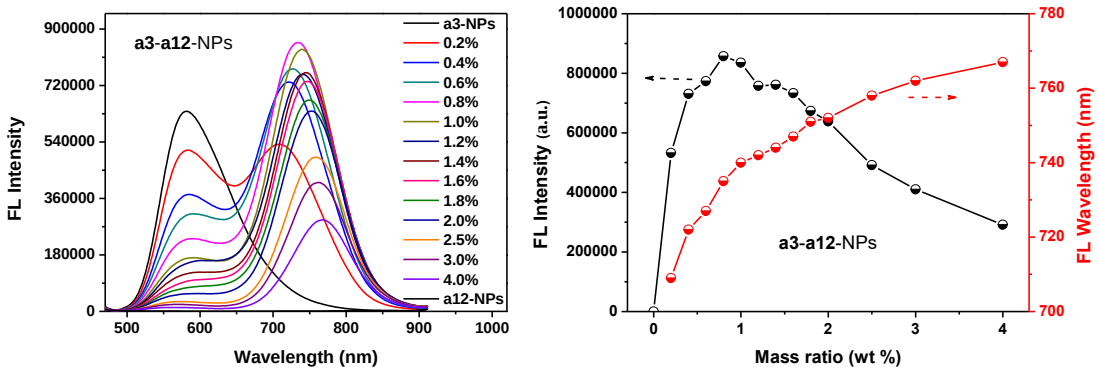

Figure 3-61. Left: PL spectra of **a3**-**a12**-NPs with different mass ratio (wt %) of **a12** to **a3**; Right: Plot of PL intensity (black) and wavelength (red) versus wt % in **a3**-**a12**-NPs. Excitation at 460 nm.

As we can see in **Figure 3-61**, **a3**-**a12**-NPs display the similar FRET phenomenon as **a3**-**a5**-NPs. Upon the excitation of 460 nm, the fluorescence originates from donor **a3** is quenched gradually and the intensity of NIR emission from acceptor **a12** is remarkable increased with increasing wt % from 0.2% to 0.8%. Afterwards, the emission of loaded **a12** in **a3**-**a12**-NPs is decreased when wt % increases up to 4%. Meanwhile, the emission maximum is gradually red-shifted from 709 to 767 nm when wt % increases from 0.2% to 4%. The most fluorescent **a3**-**a12**-NPs with 0.8% feeding ratio of **a12** (abbreviated as **a3**-0.8%**a12**-NPs) show a fluorescence quantum yield of 9 % at 735 nm. It is worth noting that **a3**-0.8%**a12**-NPs exhibit a larger Stokes shift (299 nm) than those of **a3**-1.2%**a5**-NPs and other reported FRET-based nanoparticles.[244, 284] Moreover, compared with **a3**-1.2%**a5**-NPs, **a3**-0.8%**a12**-NPs show a 24 nm red-shifted emission with a slightly lower fluorescence quantum yield.

6.3.2. Characterization of Co-loaded Nanoparticles

The average diameters of **a3**-**a5**-NPs and **a3**-**a12**-NPs with various acceptor–donor mass ratios were measured with dynamic light scattering (DLS) (**Figure 3-62**). The DLS results indicate that both the average diameters of **a3**-**a5**-NPs and **a3**-**a12**-NPs are around 57 nm, which are not influenced by the acceptor–donor mass ratios.

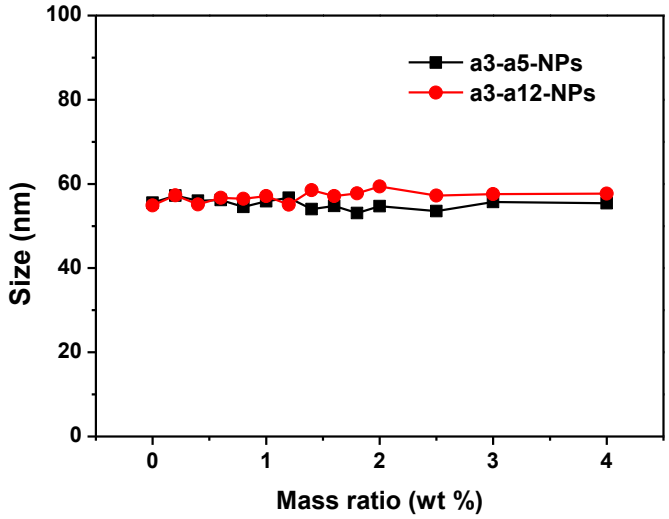

Figure 3-62. Particle size of **a3**-**a5**-NPs and **a3**-**a12**-NPs with different mass ratio (wt %) of acceptor (**a5** or **a12**) to donor **a3**, measured by DLS.

Figure 3-63 and **Figure 3-64** exhibit the DLS and scanning electron microscopy (SEM) characterization results of the optimized **a3**-1.2%**a5**-NPs and **a3**-0.8%**a12**-NPs. DLS measurement result shows an average hydrodynamic diameters of 57 nm for **a3**-1.2%**a5**-NPs and of 56 nm for **a3**-0.8%**a12**-NPs, and the SEM characterization of the same nanoparticle samples reveal their spherical shape with diameter roughly consistent with the DLS measurement results.

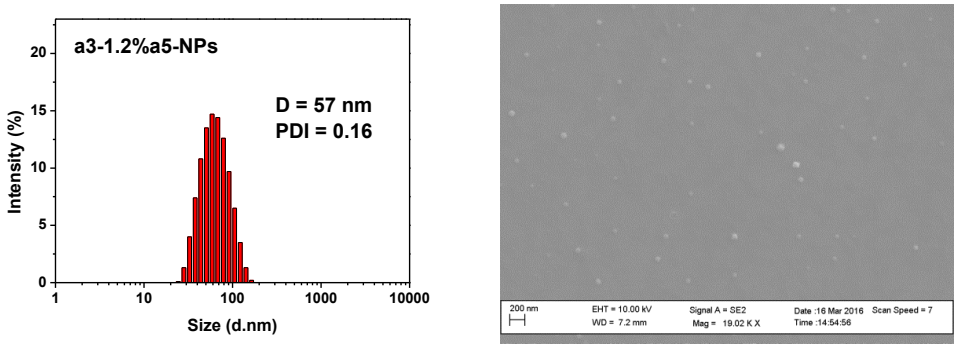

Figure 3-63. Left: Particle size distribution of **a3**-1.2%**a5**-NPs measured by DLS; Right: SEM images of **a3**-1.2%**a5**-NPs.

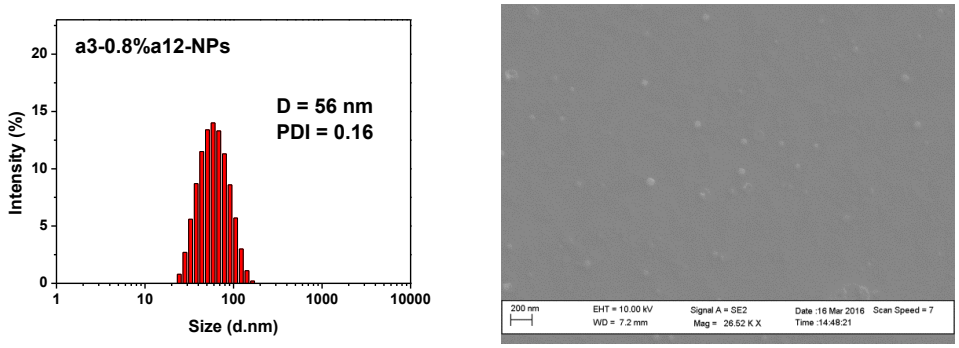

Figure 3-64. Left: Particle size distribution of **a3**-0.8%**a12**-NPs measured by DLS; Right: SEM images of **a3**-0.8%**a12**-NPs

6.3.3. Study of the Energy Transfer Process in Nanoparticles

Significant FRET process in co-loaded nanoparticles (**a3**-**a5**-NPs and **a3**-**a12**-NPs) has been identified. To further evaluate the energy transfer efficiency between the donor (**a3**) and the acceptor (**a5** or **a12**) in nanoparticles, the study of the fluorescence quenching of the donor dyes by the acceptor was performed. Moreover, the excitation and time resolved fluorescence spectra at room temperature were also measured for the analysis of energy transfer process.

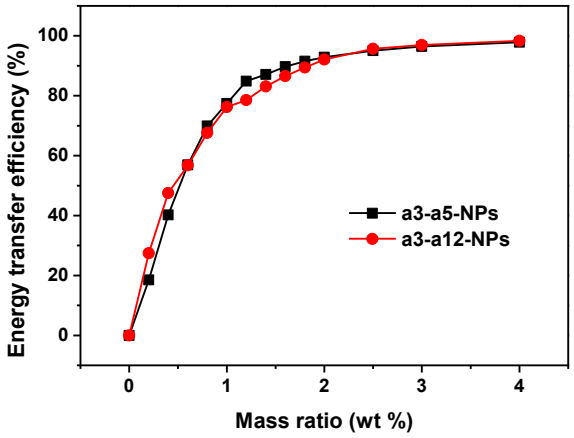

Figure 3-65. The energy transfer efficiency between the donor (**a3**) and the acceptor (**a5** or **a12**) in **a3**-**a5**-NPs and **a3**-**a12**-NPs with different mass ratio (wt %) of acceptor to donor.

Firstly, the FRET efficiency is determined by studying the quenching of **a3** donor fluorescence in the presence of different quantity of the acceptor (**a5** or **a12**). As shown in **Figure 3-65**, **a3**-**a5**-NPs and **a3**-**a12**-NPs display the similar FRET efficiency curves as a function of mass ratio of acceptor to donor. More importantly, mass ratios of acceptor to donor have a significant influence on the FRET efficiency. For example, for **a3**-**a5**-NPs, only 18% of FRET efficiency from **a3** to **a5** was observed with the acceptor–donor mass ratio (wt %) of 0.2%. With increasing wt % from 0.2% to 4%, the FRET efficiency initially increases rapidly and then slowly. It eventually reaches a value of 98% at a mass ratio of 4 %. Moreover,

84% and 68% of FRET efficiencies can be obtained for the most fluorescent nanoparticles **a3**-1.2%**a5**-NPs and **a3**-0.8%**a12**-NPs, respectively.

To further confirm the energy transfer process in nanoparticles, the excitation spectra of **a3**-1.2%**a5**-NPs and **a3**-0.8%**a12**-NPs were recorded at their amplified emission peaks at room temperature. Both the excitation spectra of **a3**-1.2%**a5**-NPs and **a3**-0.8%**a12**-NPs show a prominent peak at around 410 nm and a weak peak from acceptor, corresponding to their absorption spectra, respectively (**Figure 3-66**). This result provides a direct evidence of FRET between donor (**a3**) and acceptor (**a5** or **a12**).

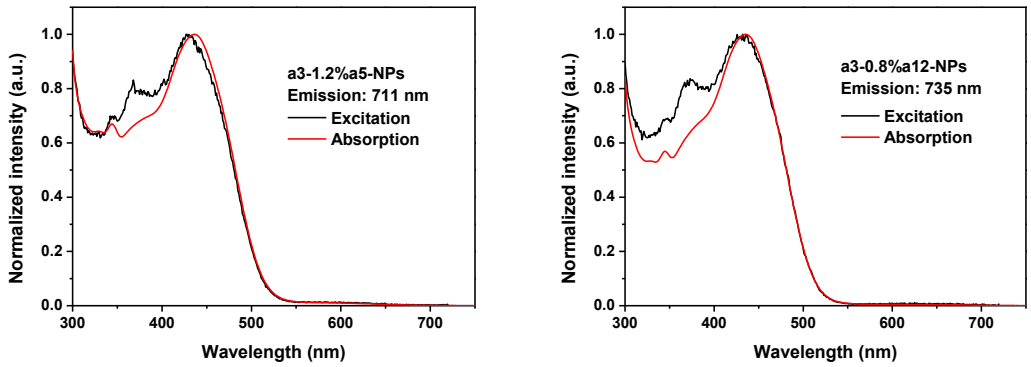

Figure 3-66. Excitation and absorption spectra of **a3**-1.2%**a5**-NPs (left) and **a3**-0.8%**a12**-NPs (right). Excitation spectra detected at their amplified emission peaks.

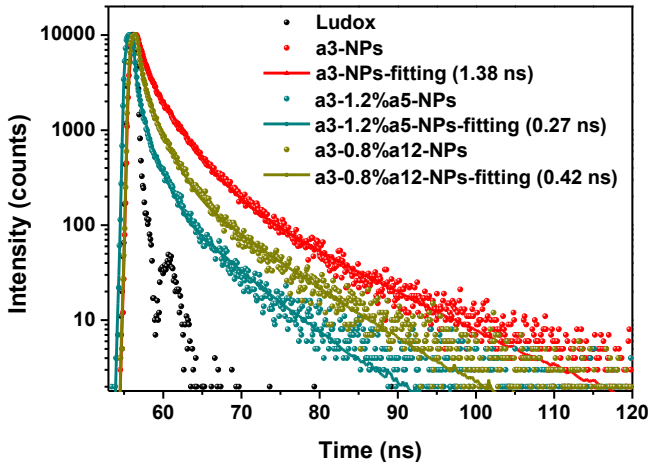

Figure 3-67. Fluorescence decay curves of **a3**-1.2%**a5**-NPs and **a3**-0.8%**a12**-NPs detected at their amplified emission peaks.

Furthermore, energy transfer between the donor and the acceptor is usually associated with the lifetime change of the donor in the absence and presence of the acceptor, and larger obvious lifetime changes indicate more efficient energy transfer between the FRET pair.[285] Thus, the lifetime measurements were conducted for **a3**-NPs in the absence and presence of **a5** (1.2% mass ratio) or **a12** (0.8% mass ratio) (**Figure 3-67**). **a3**-NPs without doping

acceptor fluorophore have an average lifetime of 1.38 ns, which decreases to 0.27 ns by doping with 1.2% **a5** and to 0.42 ns by doping with 0.8% **a12**. The obvious lifetime decrease of **a3** in co-loaded nanoparticles further demonstrates the efficient energy transfer between donor **a3** and acceptor (**a5** or **a12**).

6.3.4. Two-Photon Absorption Properties

After confirming the FRET process in co-loaded nanoparticles **a3**-**a5**-NPs and **a3**-**a12**-NPs, this process was further studied by two-photon fluorescence spectroscopy. The emission spectra of **a3**-**a5**-NPs and **a3**-**a12**-NPs with various acceptor–donor mass ratios were recorded under two-photon excitation of donor **a3** at 900 nm by femtosecond laser. The two-photon fluorescence spectra of **a3**-**a5**-NPs and **a3**-**a12**-NPs display the similar profiles with respect to their one-photon fluorescence spectra as a result of same relaxation pathway for one- and two-photon excited emission. As shown in **Figure 3-68**, the **a3**-1.2%**a5**-NPs (**a3**-**a5**-NPs with wt % of 1.2%) show a strongest amplified emission at 711 nm, moreover, **a3**-0.8%**a12**-NPs (**a3**-**a12**-NPs with wt % of 0.8%) was found to exhibit a most pronounced emission at 740 nm, suggesting the effective FRET from donor (**a3**) to acceptor (**a5** or **a12**) under two-photon excitation of donor **a3**. These results demonstrate the design of the FRET-based co-assembled nanoparticles.

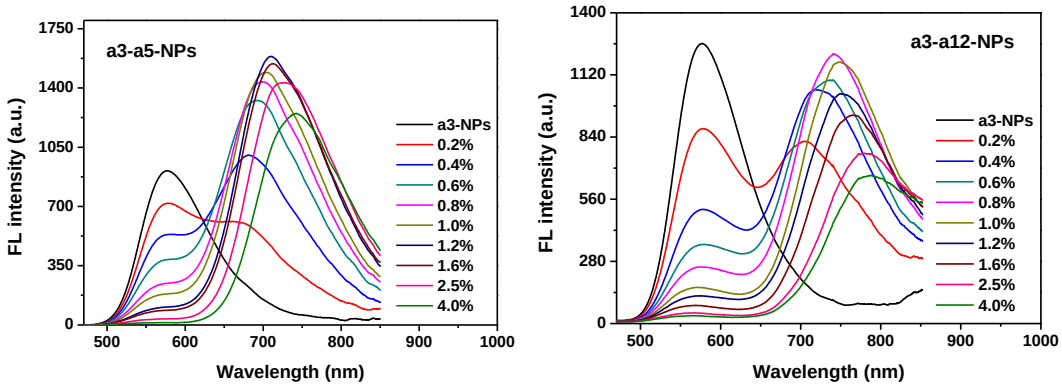

Figure 3-68. Two-photon fluorescence spectra of **a3**-**a5**-NPs (left) and **a3**-**a12**-NPs (right) with different mass ratio (wt %) of acceptor (**a5** or **a12**) to donor **a3** pumped by femtosecond laser pulses at 150 mW at 900 nm.

6.3.5. Photostability

As a bioprobe for practical imaging applications, **a3**-1.2%**a5**-NPs and **a3**-0.8%**a12**-NPs are required to have an excellent photostability for long-term imaging process. Thus, the photostability of **a3**-1.2%**a5**-NPs and **a3**-0.8%**a12**-NPs in water was evaluated under the continued irradiation at 460 nm for 40 min (**Figure 3-69**). Here, the typical photobleaching agent fluorescein in 0.1 M NaOH was used as a contrast. The result demonstrates that, during the irradiation time, the fluorescence intensity of **a3**-1.2%**a5**-NPs and **a3**-0.8%**a12**-NPs was almost kept constant without significant photobleaching.

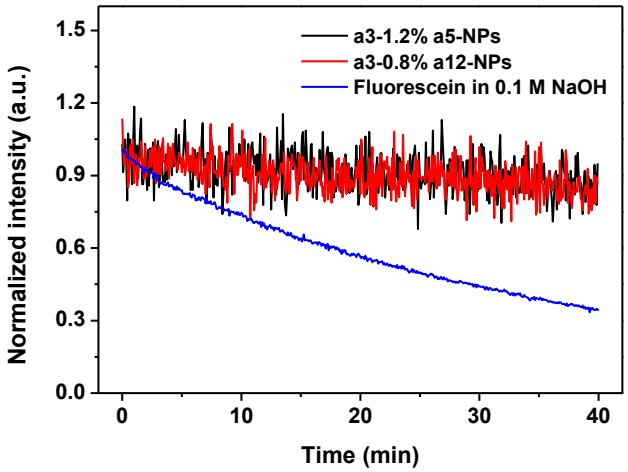

Figure 3-69. Photostability of **a3**-1.2%**a5**-NPs and **a3**-0.8%**a12**-NPs compared with fluorescein. Samples were excited at 460 nm and monitored at their amplified emission peaks.

7. Two-Photon Blood Vasculature Imaging Using Co-loaded Aggregation-Induced Emission Active Nanoprobes

Both **a3**-1.2%**a5**-NPs and **a3**-0.8%**a12**-NPs have shown the unique AIE amplified NIR emission, good 2PA capacity, large Stokes shift, good photostability and high brightness in the NIR region. The applicability of **a3**-1.2%**a5**-NPs for real-time *in vivo* two-photon fluorescence imaging of the blood vasculature of mouse ear was studied by two-photon fluorescence microscope (2PFM). The preparation of **a3**-1.2%**a5**-NPs for *in vivo* imaging is same as for **a9**-aggregate-F127.

a3-1.2%**a5**-NPs were administered intravenously prior to imaging and the two-photon excited fluorescence was collected at two individual channels, *i.e.*, green and red channels, upon two-photon excitation at 900 nm. The result shown that only bright red emission was observed from the red channel, whereas no signal was observed from the green channel, which means that the signal are from the amplified NIR emission of acceptor **a5** rather than donor **a3**. This result is consistent with the two-photon excited fluorescence spectra of **a3**-1.2%**a5**-NPs. The Z-projected image (**Figure 3-70**) demonstrates that the blood vascular network including the major blood vasculature, small capillaries and even arteries could be visualized, providing spatiotemporal information about the whole blood vascular network. The 'butterfly structures' are sebaceaous glands with endogenous fluorescence. Note that some nanoparticles formed large aggregates in the blood circulation. In the associated film of the time series, perivascular phagocytes ingest the nanoparticles and move on the surface of the vessel. However, some diffusion of **a3**-1.2%**a5**-NPs was observed out of vasculature during 52 min of circulation (**Figure 3-71**).

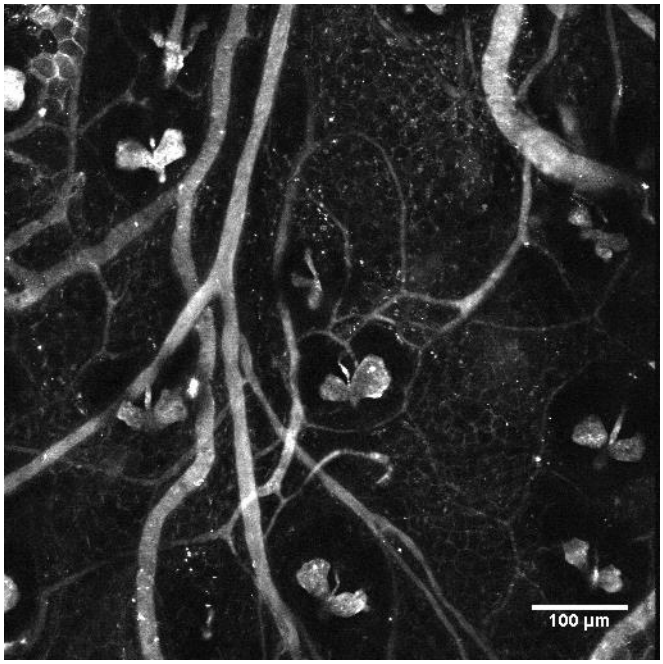

Figure 3-70. Two photon microscopic image of the circulation of **a3**-1.2%**a5**-NPs (λ_{exc} = 900 nm) in the normal ear of a nude mouse. The image is a z-projection of the standard deviations of the fluorescence intensities: 19 images, step size 3 µm = thickness of 60 µm.

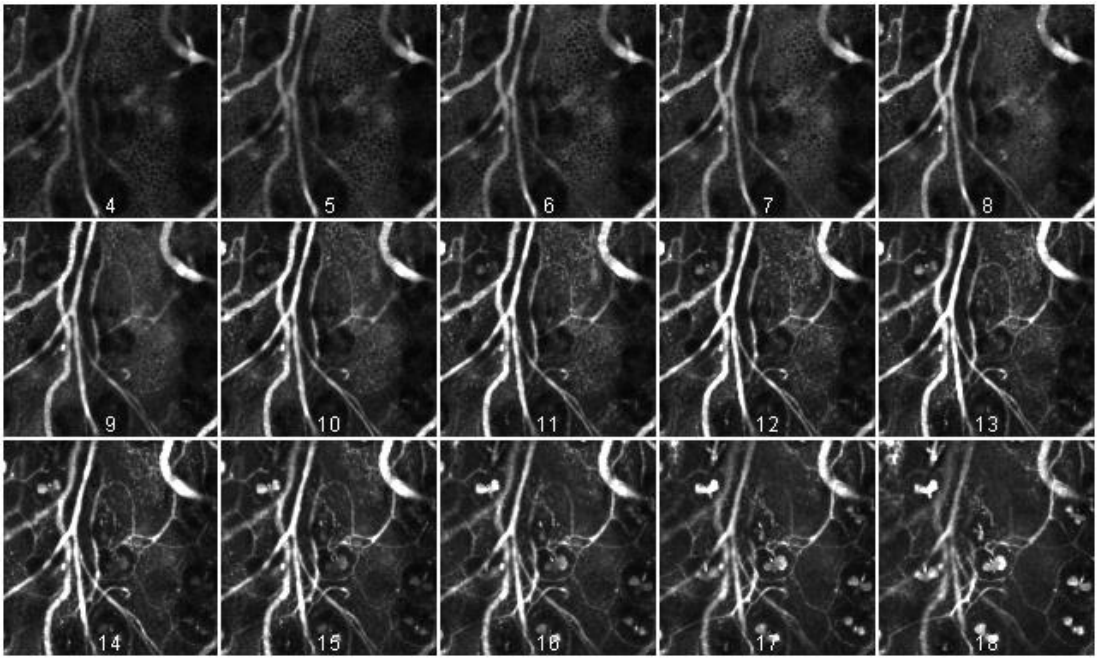

Figure 3-71. Time lapse acquisition over 52 minutes (20 seconds for 1 stack of 19 images) showing the diffusion of **a3**-1.2%**a5**-NPs in the vasculature (two-photon excitation at 900 nm).

In order to further check the behaviour of nanoparticles in *in vivo* circulation, the *ex vivo* fluorescence images of the internal organs of mice were recorded in **Figure 3-72**. In most cases, the nanoaggregates formed aggregates in the micro-blood circulation of these organs.

The circulation time was too short for accumulation in the macrophages (Kupfer cells in the liver). Note that the formation of large aggregates was merely seen in the kidney with a low accumulation in the tubules. All excised organs were analyzed as a whole to avoid artifacts in the nanoparticles distribution during slicing.

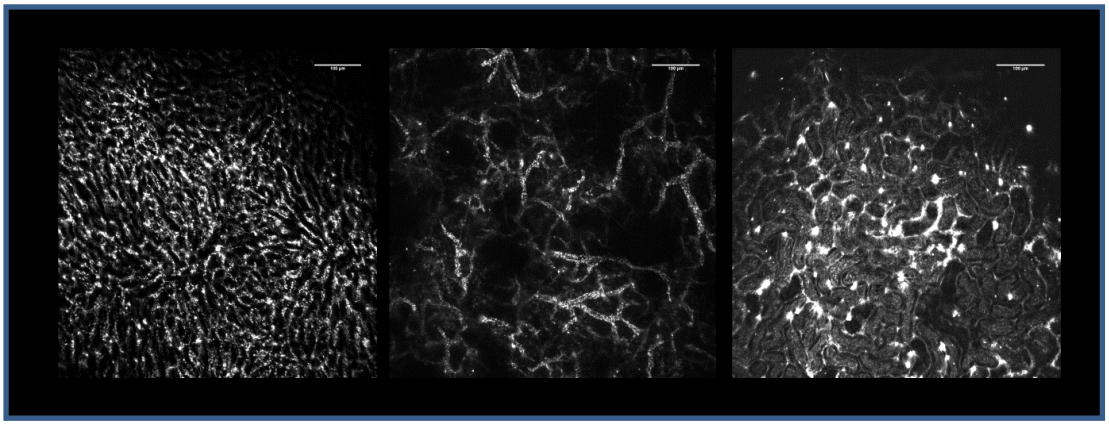

Figure 3-72. Two photon microscopic images of the **a3**-1.2%**a5**-NPs distributions in the excised organs: liver (left); spleen (centre); kidney (right), at 1 h and 15 min after injection in the tail vein of nude mouse.

Figure 3-73 shows the two photon microscopic images of the same mouse ear at another location after injection of **a3**-1.2%**a5**-NPs. The excitation wavelength was 1200 nm instead of 900 nm in the previous images. At this wavelength three-photon excitation is possible, but the images are disturbed by strong SHG signals from collagen type 1 and 3 fibers that show a high intensity in the red detection channel around 600 nm.

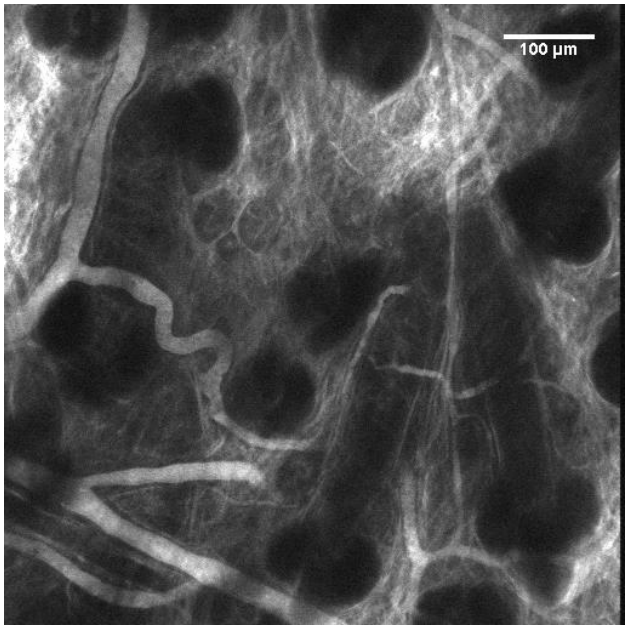

Figure 3-73. Image of the vasculature (two-phton excitation at 1200 nm). Detection channel at around 600 nm.

8. Conclusion

The goal of this chapter was to design and prepare near-fluorescent nanoparticles for imaging vasculature system for two-photon microscopy. A new series of asymmetrical fluorene-based push-pull chromophores was designed and synthesized. Structure-property relationships were systematically investigated. Except two non-fluorescent fluorophores, all the dipolar fluorophores display very strong solvatochromism effect, and a very large dipole moment change (17–23 D) were obtained. The two-photon excited fluorescence (2PEF) measurements indicated that the fluorophores display obvious two-photon absorption activities (estimated maximum: 100–240 GM) in chloroform in the range of 740–960 nm. Density functional theory (DFT) calculations were also carried out for analysing the optical properties and electronic structure using the Gaussian 03 program.

It was found that most of the chromophores exhibit aggregation-induced emission (AIE) behaviours in the FR/NIR region. By using a simple precipitation way, nanoaggregates of fluorophores were prepared separately with sizes of 37–86 nm (determined by DLS and SEM). Fluorescence quantum yiels Φ_f were determined to be 4–11% for the obtained nanoaggregates, and they also show very large Stokes shifts ($\Delta\nu$ = 5336–7077 cm^{-1}), which is favourable for bio-imaging. The two-photon properties of the nanoaggregates were demonstrated. Study of solid state optical properties of the synthesized fluorophores revealed that all the fluorophores show an interesting FR/NIR emission and fluorophore **a10** exhibit the highest fluorescence quantum yield Φ_f of 20% at 656 nm. Moreover, the three-photon properties of fluorophores in solid state were studied by multi-photon-induced fluorescence (MPIF) method, revealing interesting three-photon absorption properties in the range 1400–1600 nm. Several single crystals of fluorophores were obtained and analysed for understanding the optical properties of compounds in the solid state. The result showed that *J*-type aggregation in the crystal structure is in favour of strong solid state fluorescence. To further demonstrate the applicability of the nanoaggregates in two-photon biological imaging, the most red-shifted nanoaggregates (**a9**-aggregate-F127, λ_{em} = 717 nm) were stabilized by a small amount of surfactant (pluronic F127). The stabilized nanoparticles can efficiently label the blood vasculature in mice ear in two-photon microscopy. However, an obvious diffusion effect was observed after a long circulation and the particles accumulate in the liver and the spleen and are not filtrated through the kidney. This is probably due to excessive size of the aggregates obtained by simple precipitation.

As another part of this chapter, two new FRET-based co-assembled nanoparticles (**a3**-**a5**-NPs and **a3**-**a12**-NPs) were fabricated based on a two-photon absorbing AIE fluorophore. For preparing nanoparticles, an AIE active fluorophore (**a3**) and an AIE-inactive fluorophore (**a5** or **a12**) were co-precipitated along with a small quantity of surfactant (pluronic F127). Good spectra overlap between donor and acceptor makes them suitable FRET donor/acceptor pairs and the FRET process occured when they were co-loaded in nanoparticles. The FRET strategy was demonstrated to endow the nanoparticles with the optical properties of both donor fluorophore (NIR two-photon absorption) and acceptor

fluorophore (NIR emission). The optimization of nanoparticles was first performed by varying the ratio of acceptor to donor (wt %) and gave the optimal nanoparticles **a3**-1.2%**a5**-NPs (λ_{em} = 711 nm, Φ_f = 14%) and **a3**-0.8%**a12**-NPs (λ_{em} = 735 nm, Φ_f = 9%), which showed strongest fluorescence in the series. The emission spectra of two series of nanoparticles were also recorded under two-photon excitation (λ_{em} = 900 nm), revealing same spectra profile as those with one-photon excitation. Then the energy transfer efficiency between the donor and the acceptor in nanoparticles was evaluated by the fluorescence quenching of donor, excitation spectra and lifetime study. 84% and 68% of FRET efficiency can be obtained for the most fluorescent nanoparticles **a3**-1.2%**a5**-NPs and **a3**-0.8%**a12**-NPs, respectively. The size (56 nm for both) and photostability of **a3**-1.2%**a5**-NPs and **a3**-0.8%**a12**-NPs were also studied. Similar to **a9**-aggregate-F127, the potential of **a3**-1.2%**a5**-NPs in two-photon biological imaging was demonstrated.

These results are very promising for the development of efficient NIR fluorescent probes. In this case, structures of the donor and the acceptor were similar. Further works will therefore include changing the nature of both the donor and the acceptor in order to understand the requirement to obtain particles in which efficient energy transfer occurs and displaying an even more shifted emission. Provided control of the size is achieved, interesting blood-pool agents can be obtained. To that end, extensive study of the physico-chemical parameters controlling the nanoparticles size and understanding of theses parameters is of utmost importance. Establishing phase diagrams of fluorophore/solvent/water ternary systems could provide valuable information by defining different areas for certain proportions of solute, solvent and water, where dispersion of submicronic droplets or particles are spontaneously generated. In particular, it could be worth estimating the bimodal curve characterizing the fluorophore solubility and the Ouzo limit separating a domain where aggregation occurs from the “ouzo” domain where fluorescent nanocrystals of controlled size are obtained. Finally, changing the nature of the surfactant used to stabilize the system will also be investigated.

Chapter 4. Far-Red/Near-Infrared Emitting Micelle/Silica-Encapsulated Nanoparticles for Biphotonic *in vivo* Imaging

1. Design of Micelle/Silica-Encapsulated Nanoparticles

As we have described above, two different kinds of NIR emissive nanoaggregates based on the synthesized dipolar fluorophores were prepared and finally applied to the biphotonic *in vivo* imaging of the tumour vasculature. However, all these nanoaggregates display a low fluorescence quantum yield at NIR wavelength, and also no satisfying behaviour in *in vivo* imaging. In order to improve the stay in the vascular system, new nano-objects will be envisaged for our dipolar molecules in this section.

1.1. Micelle/Silica-Encapsulated Nanoparticles

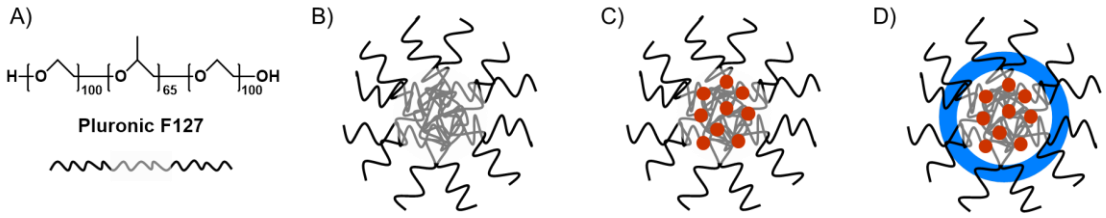

Figure 4-1. A) Pluronic F127 block copolymer surfactant; B) Pluronic F127 micelles; C) Pluronic F127 stabilized nanoparticles; D) Micelle/silica-encapsulated nanoparticles.

Amphiphilic block copolymers, including Pluronic F127 (**Figure 4-1A**), a triblock EO_{100}–PO_{65}–EO_{100} copolymer made of hydrophilic ethylene oxide (EO) and hydrophobic propylene oxide (PO) moieties, have been extensively investigated for drug delivery.[286] In an aqueous environment, the molecules of Pluronic F127 can aggregate into spherical, core-shell-like particles above their critical micelle concentrations (CMCs) (**Figure 4-1B**) The core is formed by the hydrophobic PO segments and is separated from the aqueous environment by the hydrophilic shell containing the hydrophilic EO segments. As a result, micelles can be used to effectively solubilize and carry compounds that have poor solubility, low stability, or undesirable pharmaceutical properties in the core structure.[286] With these interesting advantages, Pluronic F127 is widely used to form and stabilize fluorescent organic nanoparticles (**Figure 4-1C**) for various bio-applications.[287] In the context of angiogenesis imaging, Pluronic F127 based fluorescent nanoparticles show great potential as blood pool dye for intravital microscopy, displaying efficient and long time homogeneous blood plasma

staining, probably due to the protective hydrophilic shell formed by the EO segments that prevents the adsorption of proteins, adhesion to tissues, and recognition by the reticuloendothelial system.[287-289] However, Pluronic micelles are known to easily dissociate upon dilution.[290] Shielding of polymeric micelle with a silica shell remarkably improves the resistance to dissociation or highly salted buffer (**Figure 4-1D**).[291-292] This original micelle/silica coprotection strategy was firstly proposed by Liu and co-workers in 2006.[293] Afterwards, this strategy was widely used to encapsulate various hydrophobic dyes.

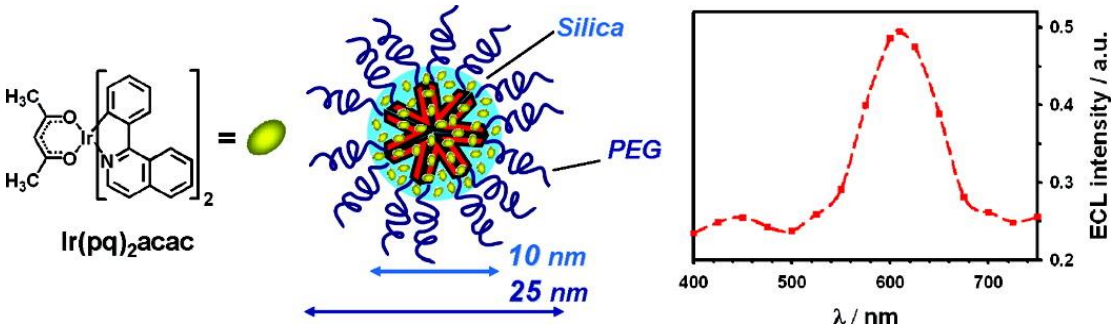

Figure 4-2. Iridium doped micelle/silica-encapsulated nanoparticles: enabling electrochemilumine-scence of neutral complexes in aqueous media.

As shown in **Figure 4-2**, this strategy was used by Prodi and co-workers in 2009 for the preparation of stable luminescent nanoparticles doped with highly hydrophobic materials **Ir(pq)$_2$acac**.[292] Then, Prodi and co-workers further applied the methodology to a number of hydrophobic organic emitters, which were functionalized with triethoxysilane groups to be part of the silica shell.[294-297] They reported a series of multifluorophoric silica nanoparticles and the unprecedented efficiencies in the energy-transfer processes were observed among the doping dyes (**Figure 4-3**). These nanomaterials show a very high overall sensitization, allowing under a single wavelength excitation to obtain many different colours (one per nanoparticle) in emission with negligible crosstalk. Moreover, each particle can present very large and tuneable pseudo-Stokes shifts (up to 435 nm), a very high brightness even exciting the bluest donor, and a negligible residual emission intensity from all donor dyes. All these features, combined with colloidal stability and synthetic method reliability, make these multicomponent nanoparticles very promising for multiplex analysis and for all the diagnostic techniques requiring high sensitivity associated with a large Stokes shift. In addition, they also concluded that the optical properties, in particular emission, of dye in NPs are affected by the dye doping degree. The low doping degrees make it possible to rule out the formation of appreciable quantities of aggregates.

In 2014, the same strategy was employed by Liu and co-workers to effectively increase the fluorescence quantum yield (Φ_f = 75%) as well as two-photon action cross section of the conjugated polymer poly(9,9-dihexylfluorenealt-2,1,3-benzothiadiazole) (**PFBT**) in NPs (**Figure 4-4**).[298] The result further demonstrates that the micelle/silica-encapsulated nanoparticles are very efficient at reducing aggregation and preventing self-quenching of the dye, resulting in restoration of an intense fluorescence in aqueous media. Moreover,

PFBT-F127-SiO_2 NPs showed a large two-photon cross section, good photostability and nontoxic biocompatibility, benefiting their biological applications as two-photon fluorescent probe. Finally, real-time *in vivo* two-photon fluorescent imaging revealed that **PFBT**-F127-SiO_2 NPs could be utilized as an effective two-photon probe for *in vivo* blood vascular imaging with a deep depth of 500 μm and high contrast.[298]

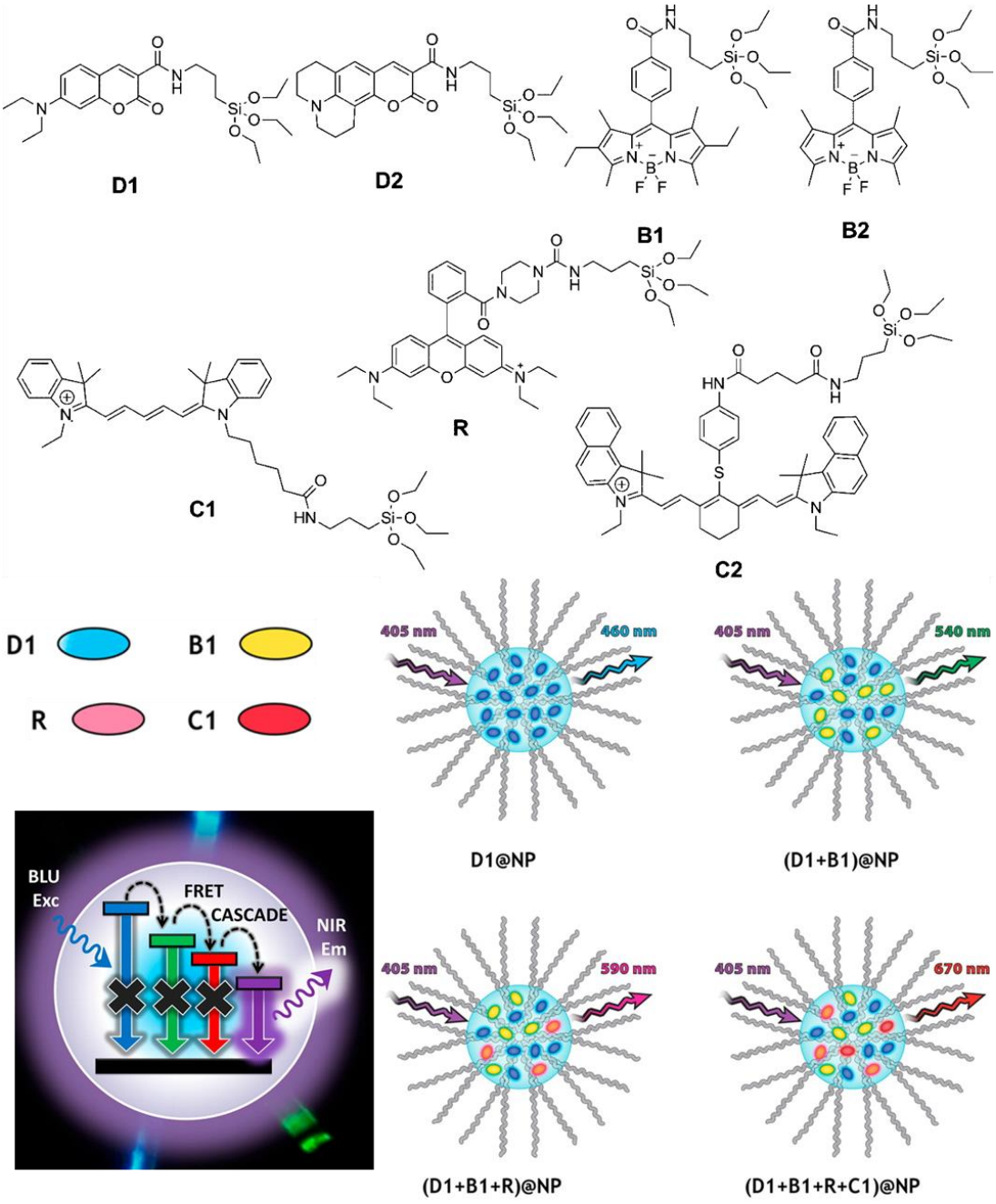

Figure 4-3. Pluronic-silica nanoparticles doped with multiple dyes featuring complete energy transfer.[295-297]

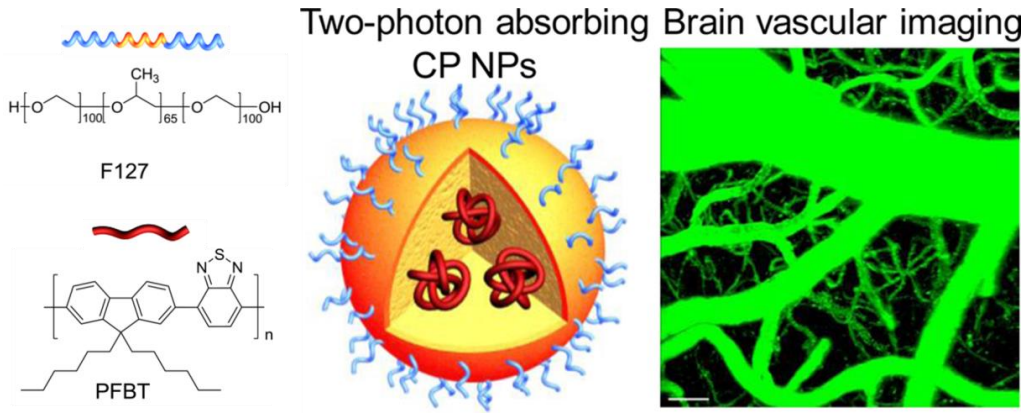

Figure 4-4. Micelle/silica co-protected conjugated polymer nanoparticles for two-photon excited brain vascular imaging.[298]

Very recently, paradoxically, the same system was later used by the same group to favour the aggregation and encapsulate dye showing AIE (**Figure 4-5**).[299] The high quantum yield (50%) of AIE-F127-SiO_2 NPs was attributed to the relatively non-polar microenvironment provided by the silica shell and the reduced water and oxygen attack to dye. In fact, the molecules in aggregates (if they exist) are protected from exposure to non-polar NPs core and not affected by the microenvironment provided by the nanoparticles. Unfortunately, this work was reported during the course of my work…

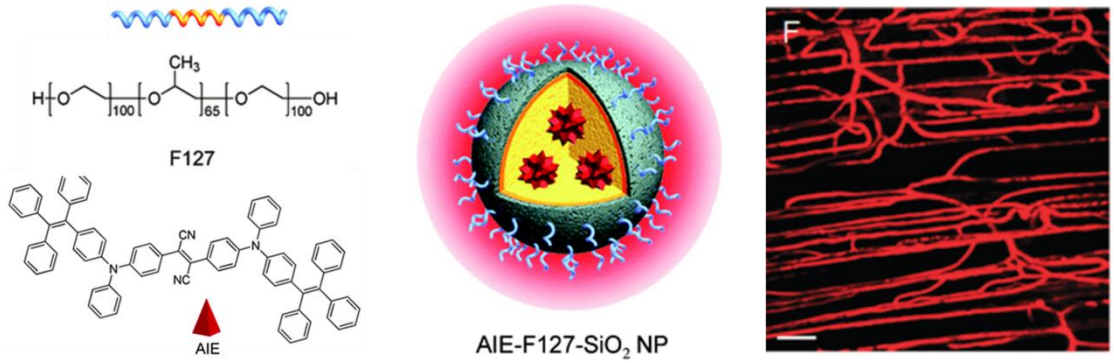

Figure 4-5. Micelle/silica-encapsulated red-emissive AIE nanoparticles for two-photon excited vascular imaging.[299]

1.2. Design of Micelle/Silica-Encapsulated Nanoparticles

Based on these literatures, the micelle/silica co-protection strategy has been demonstrated to show a high efficiency in encapsulation of hydrophobic dyes, resulting in robust, ultrabright, biocompatible and stable core-shell polymer-silica colloidal particles. Most importantly, the polymer matrix in micelle/silica co-protected nanoparticles can efficiently isolate the dye molecules from each other and provide a less polar microenvironment for the isolated dye molecules. Thus, the dye molecules in resulting nanoparticles are protected from

environment quenching by minimizing their contact with water. Because of all these advantages, we employed the micelle/silica co-protection strategy to directly encapsulate our push-pull dipolar fluorophores (**Figure 4-6**), which show very strong fluorescence in apolar and less polar solvents while the fluorescence is greatly quenched in high polarity solvents. In addition, the fluorophores were chosen to take advantage of the large solvatochromic shift usually associated with emission originating from charge transfer transition that may help shifting the fluorescence to the FR. Overall, the strategy is expected to conserve both the fluorescence property and two-photon activity of the fluorophores by providing a less-polar environment inside micelle/silica nanoparticles.

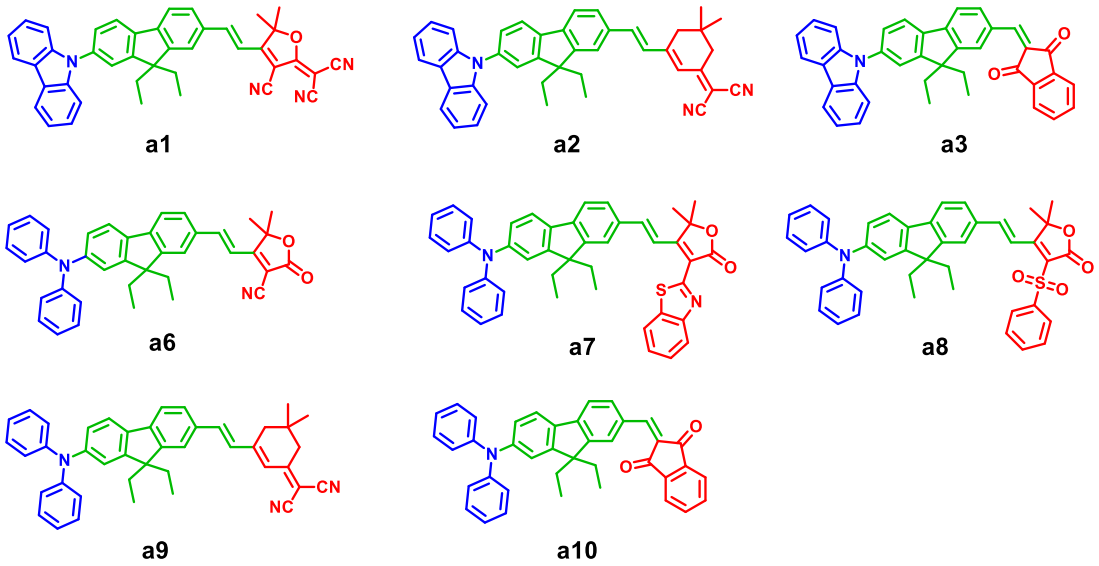

Figure 4-6. Molecular structures of **a1**–**a3** and **a6**–**a10**.

2. Preparation of Micelle/Silica-Encapsulated Nanoparticles Two-Photon in vivo Imaging

2.1. Preparation and Characterization of Micelle/Silica-Encapsulated Nanoparticles

2.1.1. Preparation

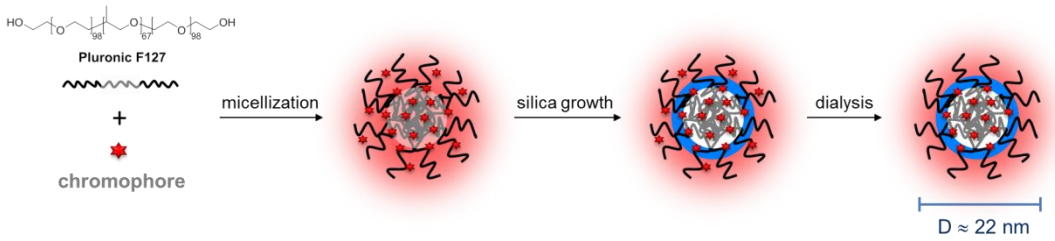

Figure 4-7. Illustration of the formation of fluorophore loaded F127-SiO2 NPs.

The procedure for the preparation of the compound-loaded F127-SiO_2 NPs is illustrated in **Figure 4-7**, using a triblock copolymer Pluronic F127 as the encapsulation matrix. It started with the preparation of a dichloromethane solution of pluronic F127 and compound. The solution was then dried with argon blow and further dissolved in 0.85 N hydrochloric acid to yield compound-loaded F127-micelles. The result micelles were further coated with a silica shell through TEOS hydrolysis under acidic condition. Addition of diethoxydimethylsilane (DEDMS) into the NP suspension could terminate the silicate cross-linking and provide micelles with thin silica shells. The mixtures were then dialyzed to remove excess hydrochloric acid and some impurity. At last, the nano-suspension was finally obtained through filtration with 0.2 μm syringe filter to remove large aggregates.

For preparing F127-SiO_2 NPs for our fluorophores, we initially investigated the encapsulation efficiencies of the F127-SiO_2 NPs toward the fluorophore. This study was carried out by using the representative fluorophore **a10** as a candidate. **a10** loaded F127-SiO_2 NPs with different feeding ratios of **a10** were prepared. In the preparation, the amount of pluronic F127 was fixed, while the mass ratio of dye to pluronic F127 (feeding ratio) changed from 0.05% to 0.4%. After the preparation, the quantity of fluorophore **a10** encapsulated into the F127-SiO_2 NPs (loading ratio) was estimated according to the absorption spectra after dissolving in DMF. The encapsulation efficiency of F127-SiO_2 NPs toward **a10** is defined as the ratio of the amount of the **a10** loaded in the NPs to the total amount of **a10** initially added in the preparing mixture.

Table 4-1. **a10**@ F127-SiO_2 NPs synthesis.

Entry	**a10** feeding ratio (wt%) [a]	**a10** loading ratio (wt%) [b]	Encapsulation efficiency (%)
1	0.05	0.048	96
2	0.10	0.093	93
3	0.15	0.14	93
4	0.20	0.15	73
5	0.30	0.15	51
6	0.40	0.17	43

[a] weight ratio of dye **a10** to that of F127 in the feed mixture; [b] weight of loaded **a10** to that of the F127 matrix in the NPs.

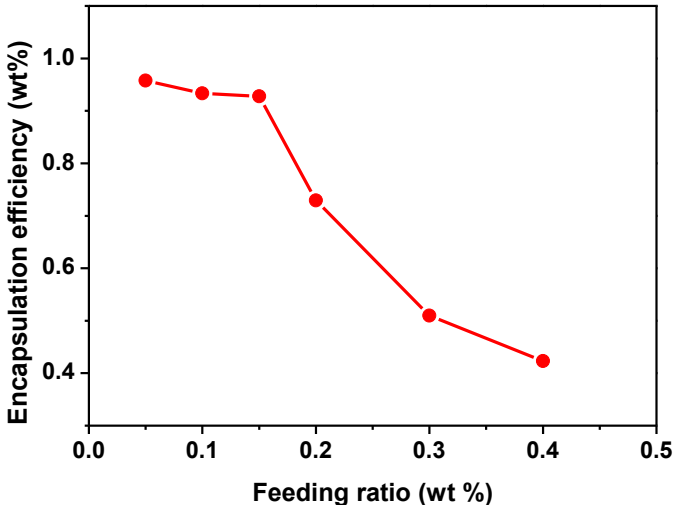

Figure 4-8. Encapsulation efficiency as a function of **a10** feeding ratio.

As shown in **Table 4-1**, the results indicate that the fluorophore loading ratio increases with an increase in the fluorophore feeding ratio. The encapsulation efficiencies of the fluorophore was ≥ 93% when the fluorophore **a10** feeding ratio was ≤ 0.15 wt%, while an sharp decrease in the encapsulation efficiencies was observed when the fluorophore feeding ratio was increased to > 0.15 wt% (**Figure 4-8**). Therefore, an optimized **a10** loading ratio of 0.15 wt% was obtained for F127-SiO_2 NPs. Since all the fluorophores display the similar molecular structure, we chose this loading ratio to prepare the F127-SiO_2 NPs for fluorophores **a1**, **a2**, **a3**, **a6**, **a7**, **a8**, **a9** and **a10** respectively for further optical study and practical *in vivo* imaging.

2.1.2. Characterization

After preparing the nanoparticles, the diameters of all the nanoparticles were firstly studied by the dynamic light scattering (DLS) measurements. As shown in **Figure 4-9**, the DLS results show that all nanoparticles have the similar size of 22 nm with good distribution,

which is similar to the size of nanoparticles reported in the literature.[291] **Figure 4-10** shows the transmission electron microscopy (TEM) image of **a10**@F127-SiO_2 NPs, which is agreement with DLS result.

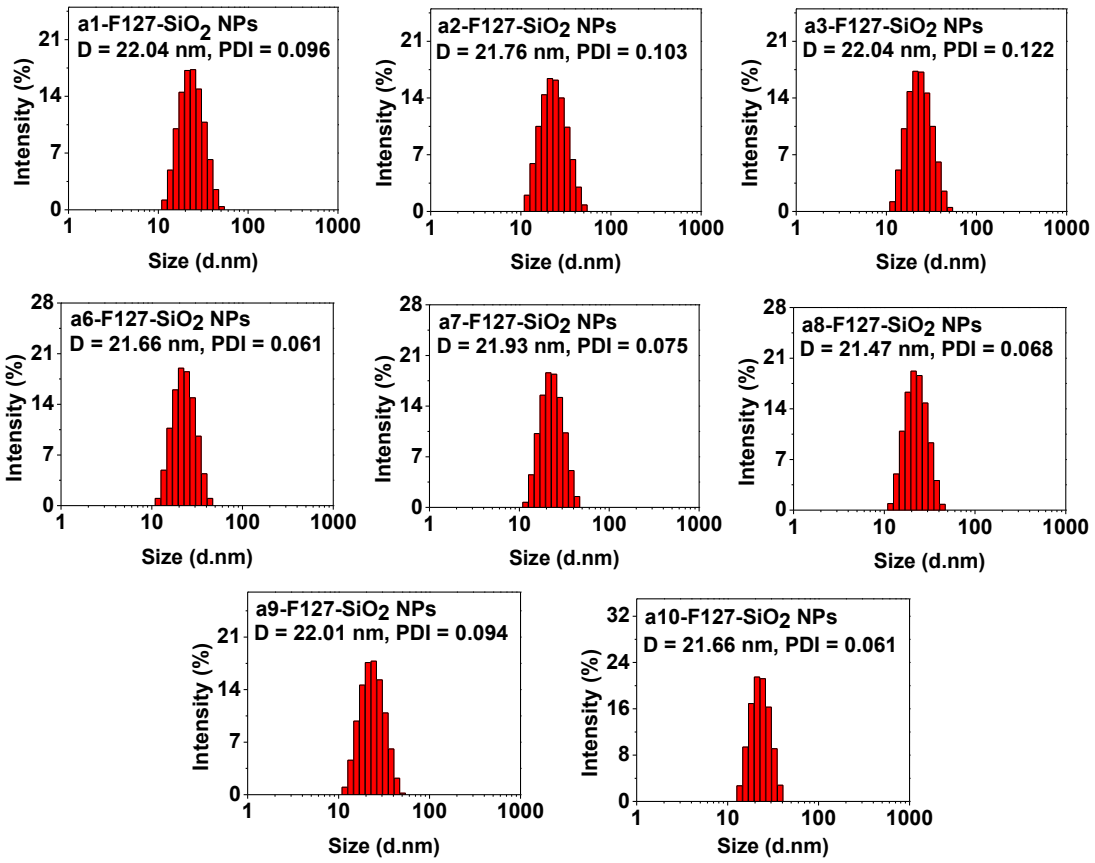

Figure 4-9. Particle size distribution of F127-SiO_2 NPs dispersed in water, measured by DLS.

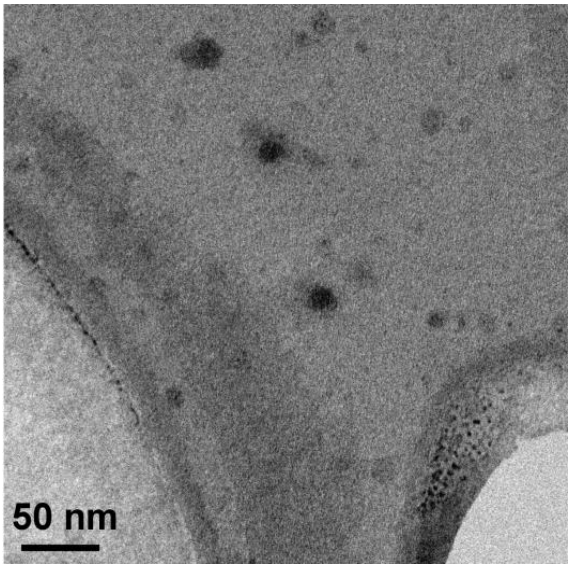

Figure 4-10. TEM image of **a10**@F127-SiO_2 NPs.

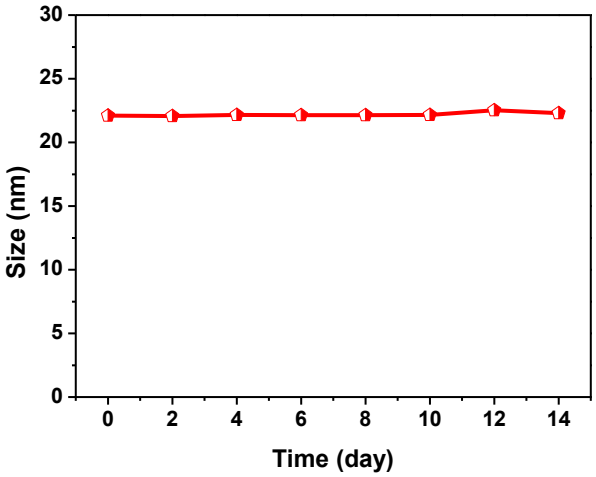

Figure 4-11. The DLS size evolution of **a10**@F127-SiO_2 NPs in PBS buffer with storing time up to two weeks.

Moreover, the colloidal stability of **a10**@F127-SiO_2 NPs was checked by recording the evolution of the DLS size distribution in 1× DPBS over a two weeks period of time. As shown in **Figure 4-11**, the sizes of a**10**-F127-SiO_2 NPs have no changes upon incubation with 1× DPBS and remain constant for at least two weeks, demonstrating their excellent colloidal stability.

2.2. Optical Properties

2.2.1. Linear Optical Properties

Figure 4-12. The UV–vis absorption and fluorescence emission photographs of dye@F127-SiO_2 NPs in water under UV lamp.

As expected, the resulting nanoparticles display interesting optical properties as shown in **Figure 4-12**. Their linear absorption and emission spectra were subsequently recorded. The relevant photophysical data are collected in **Table 4-2**, including the fluorescence quantum yields and lifetimes. **Figure 4-13** shows the absorption and emission spectra of all the dye@F127-SiO_2 NPs in aqueous media. The main absorption of the fluorophore in F127-SiO_2 NPs is similar to that of corresponding fluorophore in aggregate state. However, for each

dye@F127-SiO_2 NPs, the emission maximum shows an obvious red shift (18–61 nm) with respect to that of corresponding dye in aggregate state. For example, **a1**@F127-SiO_2 NPs exhibits an emission at 650 nm, which is 61 nm blue-shifted compared with that of **a1** in aggregate state (711 nm).

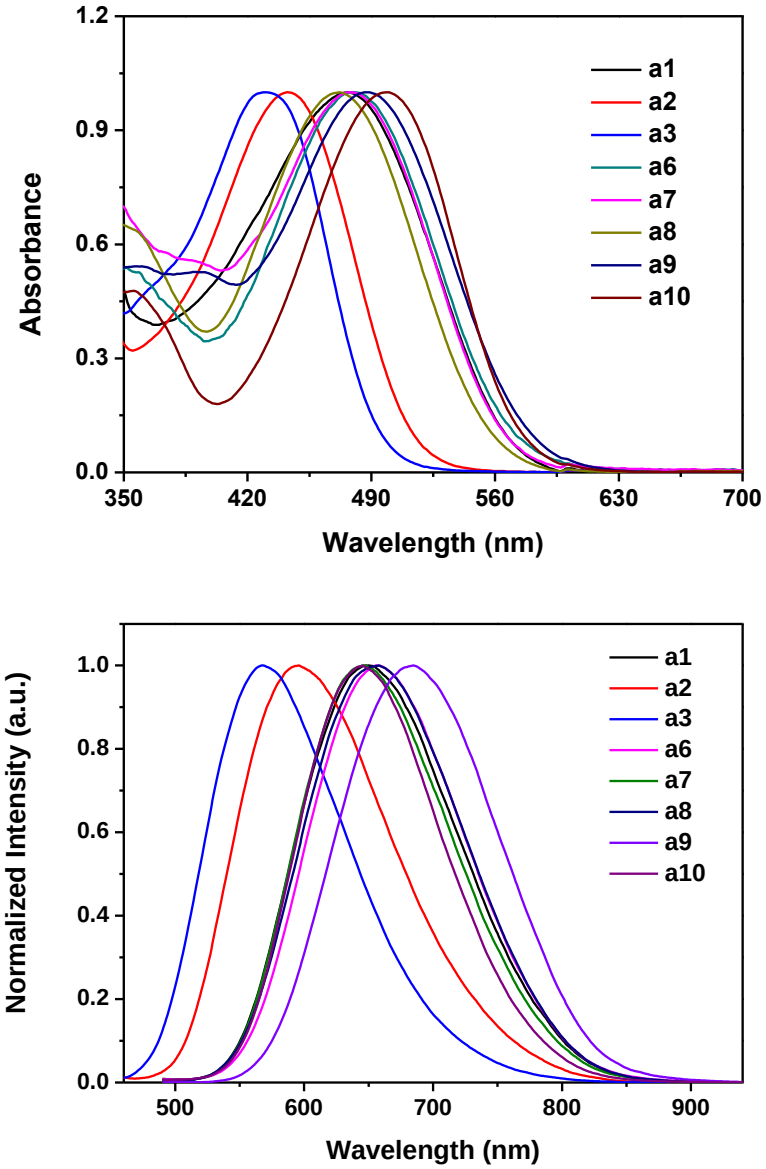

Figure 4-13. One-photon absorption (top) and emission (bottom) spectra of dye@F127-SiO_2 NPs in water.

The fluorescence quantum yields of fluorophore-loaded F127-SiO_2 NPs in water were measured using rubrene in methanol (Φ = 27%) as the standard. It is interesting to find that the fluorophore in F127-SiO_2 NPs displays a greatly enhanced fluorescence quantum yield (Φ_f = 14–39%) with respect to that of corresponding fluorophore in aggregate state (Φ_f = 4–9%) except for **a2** and **a3**, which display low Φ_f in solvent with moderate polarity such as chloroform (3% for **a2** and 1% for **a3**) while relatively high Φ_f in aggregate state (11% for **a2**

and 6% for **a3**). Such Φ_f values of dye@F127-SiO_2 NPs, especially for **a6**, **a7**, **a8**, **a9** or **a10**, are much higher than those of most of reported red/NIR emissive nanoparticles.[240, 251, 300] Moreover, the emission properties (λ_{emi} and Φ_f) of **a10**@F127-SiO_2 NPs in aqueous media are actually comparable to what is obtained in toluene/$CHCl_3$ (1:1) mixture (**Table 3-3** in **Chapter 3**), providing a possibility to know roughly the optical properties of a new chromophore loaded F127-SiO_2 NPs before preparation.

Table 4-2. Spectroscopic properties of dye@F127-SiO_2 NPs.

Sample	λ_{abs} [a]	λ_{em} [b]	$\Delta\nu$ [c]	Φ_f [d]	τ_1 [e]	A_1 [f]	τ_2 [e]	A_2 [f]	$<\tau>$ [g]	χ^2
a1	477	650	5580	14	1.11	0.64	2.30	0.36	1.54	1.00
a2	443	596	5795	5	0.64	0.85	1.76	0.15	0.81	1.00
a3	430	568	5650	8	1.35	0.74	3.38	0.26	1.87	1.04
a6	479	656	5633	25	1.73	0.54	2.86	0.46	2.25	1.00
a7	478	646	5441	30	2.19	0.56	3.45	0.44	2.75	1.02
a8	472	656	5943	30	1.89	0.61	3.04	0.39	2.34	1.00
a9	488	685	5893	25	0.90	0.56	2.06	0.44	1.41	1.00
a10	498	650	4696	39	2.34	0.48	3.46	0.52	2.92	1.00

[a] Absorption peak in nm. [b] Emission peak in nm. [c]Stokes shift in cm^{-1}. [d] Quantun yields determined by using rubrene in methanol (Φ = 27 %) as the standard. [e] Lifetime (ns). [f] Fractional contribution (%). [g] Weighted mean lifetime (ns).

The excellent optical properties of dye@F127-SiO_2 NPs clearly indicate that, in nanoparticles, hydrophobic segments of pluronic F127 and the protective silica layer provide a relatively less polar environment isolating the chromophore molecules from contact with polar medium (water) and preserving their optical properties. The different optical behaviour of fluorophore in dye@F127-SiO_2 NPs and aggregate state further demonstrate the existence of isolated fluorophore molecules rather than molecular aggregate. In addition, the large Stokes shifts for dye@F127-SiO_2 NPs (4696–5943 cm^{-1}) are favourable for bioimaging due to the minimized interference between excitation and emission.

2.2.2. Study of Fluorescence Lifetime

To further investigate the influence of F127-SiO_2 matrix on the fluorescence properties of molecules, the lifetime of fluorophore-loaded F127-SiO_2 NPs was recorded. As shown in **Figure 4-14**, all the decay curves were well-fitted by in a double-exponential manner, indicating that there were two relaxation pathways in the decay process. We can see from **Table 4-2**, dye@F127-SiO_2 NPs exhibit an increased weighted mean lifetime compared with compound in aggregate state. The longer lifetime of dye@F127-SiO_2 NPs can be atributed to the good isolation of molecules in the core of F127-SiO_2 NPs.[298] The F127-SiO_2 matrix could block the non-radiative decay pathways of molecules and also protect the chromophore from environmental quenching. Those two functions are beneficial to maintain the optical properties of compounds with well-defined FR/NIR fluorescence, which originate from the delocalized excited state of molecules without molecule aggregation.

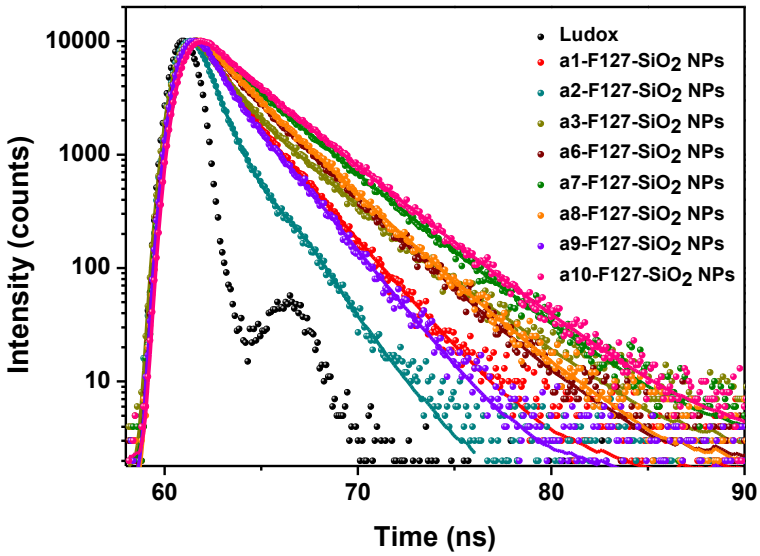

Figure 4-14. Fluorescence decay curves of dye@F127-SiO_2 NPs. Instrument response (Ludox) is also indicated.

2.2.3. Two-Photon Absorption Properties

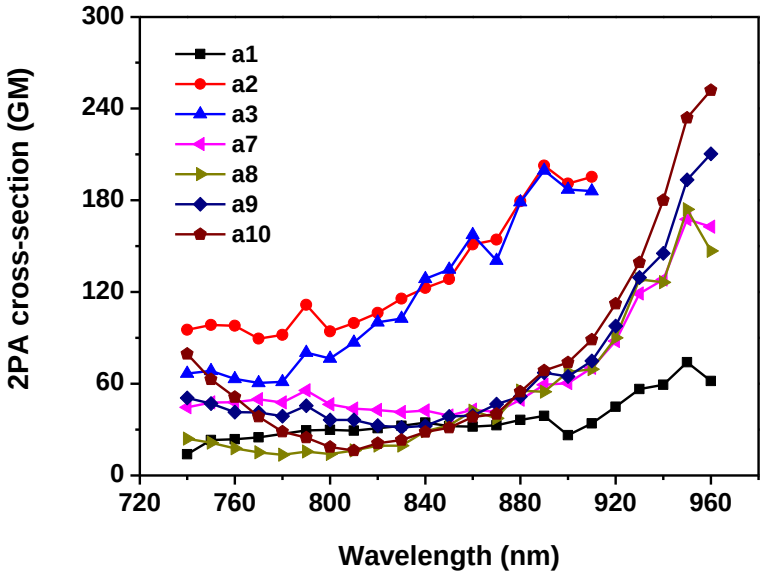

Figure 4-15. Two-photon absorption cross-sections of dye@F127-SiO_2 NPs in 740-960 nm range.

Two-photon absorption properties of dye@F127-SiO_2 NPs in water were performed and compared with those of bare molecules in chloroform, in order to determine whether our strategy also allowed an adequate conservation of this parameter. The two-photon excitation spectra of dye@F127-SiO_2 NPs were recorded under the same conditions as for fluorophore in chloroform. From these experiments, as seen in **Figure 4-15**, it is clear that the two-photon absorption behaviour of dye@F127-SiO_2 NPs is consistent with what is observed in chloroform. This result demonstrates that the

fluorophore-loaded F127-SiO_2 NPs, with good $\sigma_{2PA,}$ are the valuable candidates for the two-photon fluorescence bioimaging applications.

2.3. Stability and Cytotoxicity

For a bioprobe, excellent fluorescence stability and photostability, and low toxicity in aqueous media are essential for its biological applications, especially in long-term studies. In this part, these parameters will be evaluated for representative **a10**@F127-SiO_2 NPs.

Considering the applications of dye@F127-SiO_2 NPs for *in vivo* imaging, the fluorescence stability of representative **a10**@F127-SiO_2 NPs was performed by monitoring their fluorescence changes upon incubation with 1× DPBS over a two weeks period. **Figure 4-16** and its inset show no obvious fluorescence decrease after two weeks incubation of **a10**@F127-SiO_2 NPs with 1× DPBS, suggesting excellent fluorescence stability of the prepared nanoparticles.

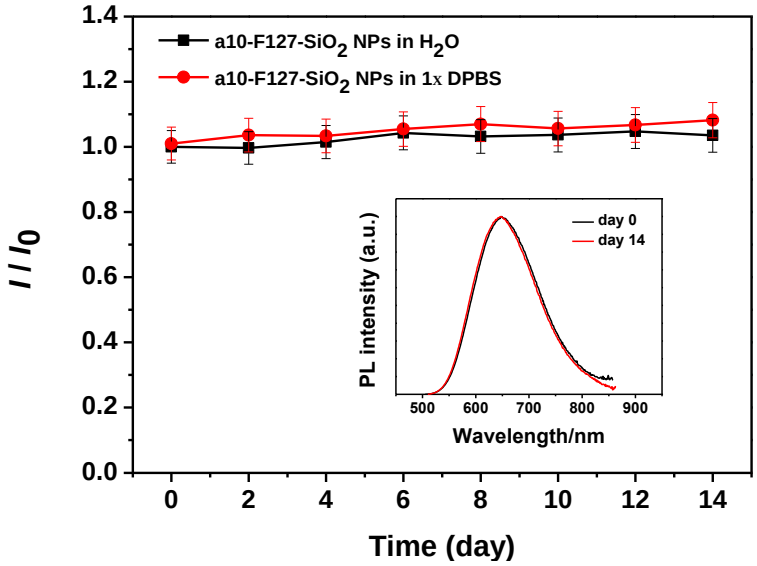

Figure 4-16. PL intensity evolution of **a10**@F127-SiO_2 NPs upon incubation with 1 × DPBS for two weeks, where I_0 is the fluorescence intensity at 650 nm for the fresh NP suspension and I is that for NPs after incubation for different time, respectively. The inset shows the PL spectra of freshly prepared **a10**@F127-SiO_2 NPs (black) and after two weeks incubation with 1 × DPBS (red).

Besides, the photostability of **a10**@F127-SiO_2 NPs in water and 1x DPBS was also checked under the continued irradiation at 460 nm for 60 min (**Figure 4-17**). In this experiment, the photostability of **a10** in dilute chloroform solution and a typical photobleaching fluorescein (0.1 M NaOH) was studied for comparison. It was found that the photostability of **a10**-F127-SiO_2 NPs is improved as compared to that for bare chromophore in chloroform without protection.

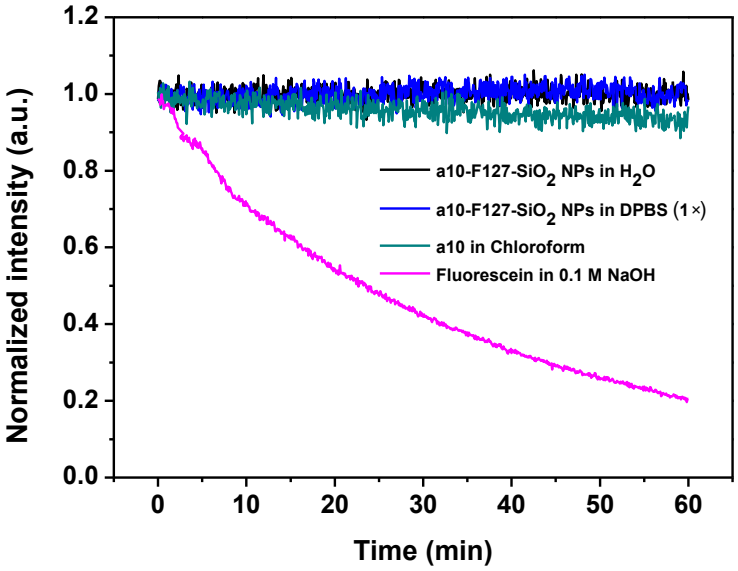

Figure 4-17. Photostability of **a10** and a**10**@F127-SiO2 NPs compared with fluorescein. Samples were excited at 500 nm and monitored at their maximum emission peaks.

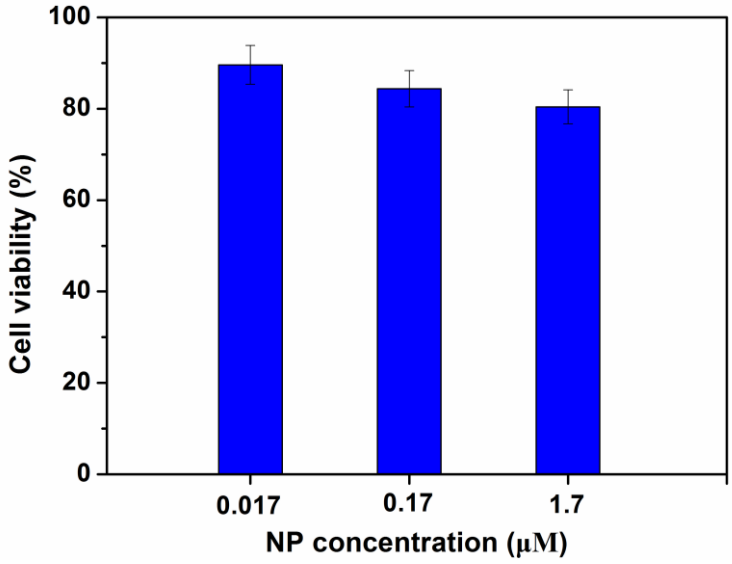

Figure 4-18. MTT assay of HepG2 cells treated with **a10**@F127-SiO_2 NPs suspensions at different concentrations for 24 h.

To evaluate the cytotoxic effect of the **a10**-F127-SiO_2 NPs, an MTT assay was performed to ascertain the cytotoxicity of NPs against HepG2 cells over a 24 h period. **Figure 4-18** shows the cell viability for HepG2 cells treated with NPs at different concentrations for 24 h. The results clearly indicated that the cell viabilities remain 80% upon incubation with **a10**-F127-SiO_2 NPs for 24 h at 0.017 μM concentration, indicating the low cytotoxicity of the NPs, demonstrating the superior biocompatibility of prepared NPs. In addition, it was found

that a high concentration only leads to a gradual decrease of viable cells as shown in **Figure 4-18**. As a result, cytotoxicity tests definitely indicate that low concentrations of NPs have small toxic effects on living cells over a period of 24 h, which has great potential for biological imaging.

2.4. Micelle/Silica-Encapsulated Nanoparticles for Biphotonic *in vivo* Imaging of the Leaky Tumour Vasculature

Owing to the good two-photon activity, large Stokes shift, good photostability, good biocompatibility and high brightness in the red/NIR region, the potential of **a10**@F127-SiO_2 NPs for real-time two-photon blood vasculature imaging was investigated on mice bearing tumours in the ear. FR emitting **a10**@F127-SiO_2 NPs were compared to commercial blood pool fluorophores **Rhodamin B dextran** (70 kDa) and to similar NPs bearing the blue emitting dye **46** (**Figure 4-19**). **Rhodamin B dextran** has comparable molecular weight than the most abundant blood plasma protein, albumin (65 kDa). The leakage of this protein is often observed in tumours and related to a higher interstitial fluid pressure.[301]

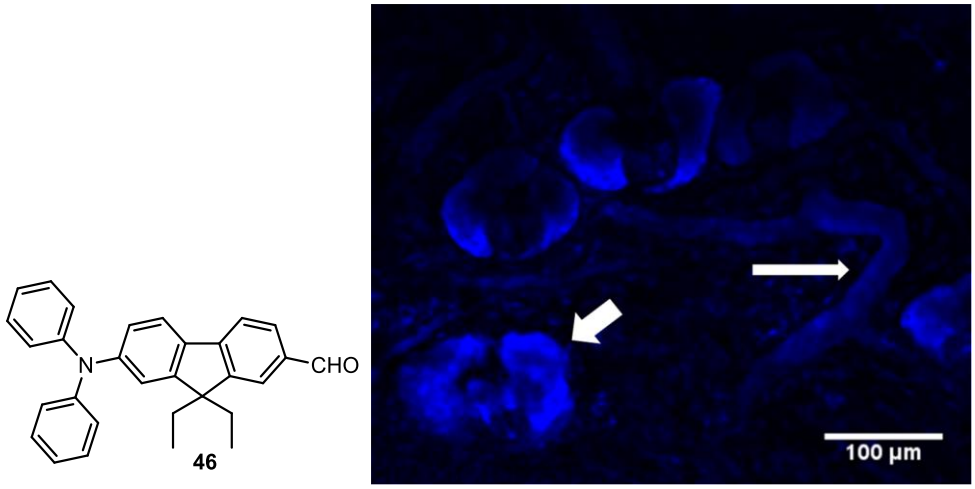

Figure 4-19. Left: Molecular structure of dye **46**; Right: Two-photon microscopy image of the maximum intensity projection of 1 minute circulation of blue NPs in a mouse ear. The longest arrow indicate the heterogeneous circulation of the NP in a capillary: areas with the slowest perfusion are associated to higher maximum intensity projections. The smallest arrow shows endogenous fluorescence signals from sebaceous glands. These glands are at the surface of the skin, indicating that the imaging depth is less than 100 µm. Two-photon excitation at 750 nm, scale bare = 100 µm.

Before imaging, the **a10**@F127-SiO_2 NPs were intravenously injected into the tail vein of mice. Immediately after injection of NPs, bright fluorescence from the whole blood vasculature network of mice ear was observed. **Figure 4-20** shows images of the blood vessels at 360 µm in depth, obtained with FR emitting **a10**@F127-SiO_2 NPs 1 h after injection and using a 1000 nm excitation wavelength. The main blood vessels but also small

capillaries deep below the tumour can clearly be observed, whereas the penetration depth with the blue emitting NPs is limited to the surface of the mouse ear (**Figure 4-19**), highlighting the benefits of combined NIR excitation/red emission for deep *in vivo* imaging.

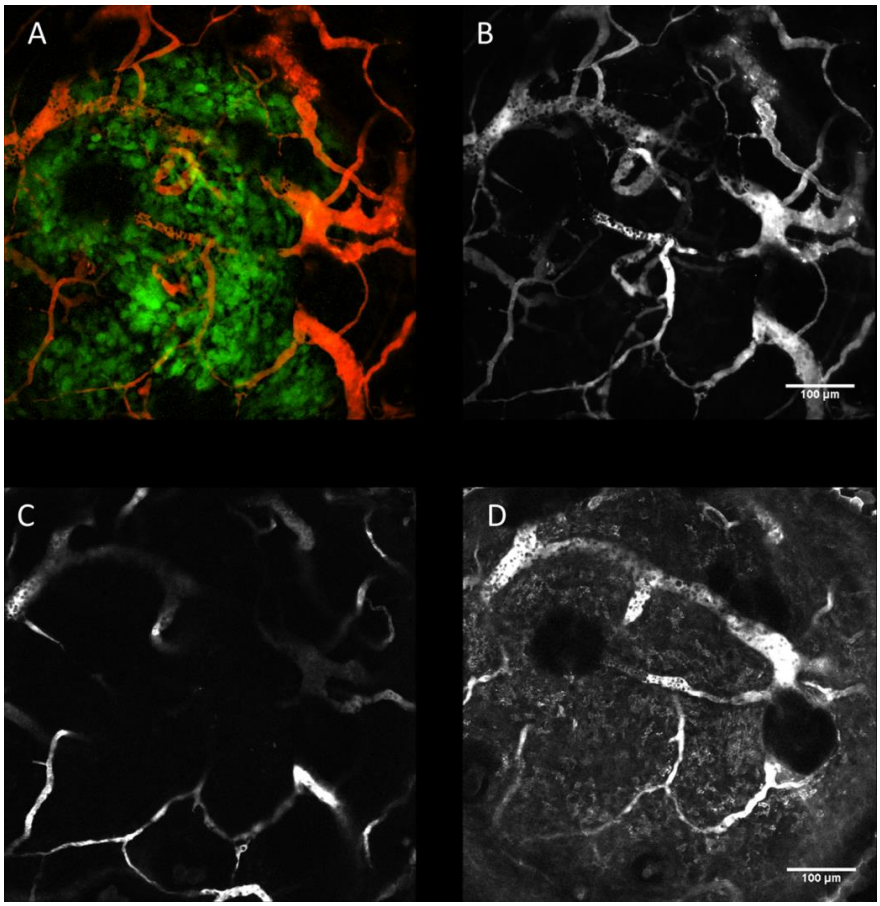

Figure 4-20. A) 3D two-photon image (z-projection standard deviations of fluorescence intensities, z-stack 91 slices, step-size 2 µm, imaging depth 360 µm, excitation wavelength 1000 nm) at 1 h after injection of **a10**@F127-SiO_2 NPs showing the vasculature (red signals) and the tumour cells (Glioma U87 green GFP signals); B) The same as (A) without the cancer cells; C) and D) One slice of the z-stack: (C) is before injection of **rhodamin-B dextran** 70 kDa and (D) is at 1 h after injection with a diffusion of **rhodamin-B dextran** in the extravascular space of the tumour. Scale bar = 100 µm.

Figure 4-20 and **Figure 4-21** also clearly showed no leakage of **a10**@F127-SiO_2 NPs into the extra vascular tumour space during 1 h after intravenous injection. In comparison, **rhodamine B dextran** 70 kDa diffused in the extra-vascular tumour space, which blurred the two-photon image of the tumour vasculature (**Figure 4-20D** and **Figure 4-22**). The absence of **a10**@F127-SiO_2 NPs diffusion enables a time consuming 3D mosaic acquisition of the tumour vasculature in time (**Figure 4-23**). Diffusion of a fluorophore into the extra-vascular space during the acquisition would have over-estimated the blood volume as a function of acquisition time, making impossible comparisons of the blood volume in between tumour areas and normal tissue regions before and after an anti-angiogenic therapy.

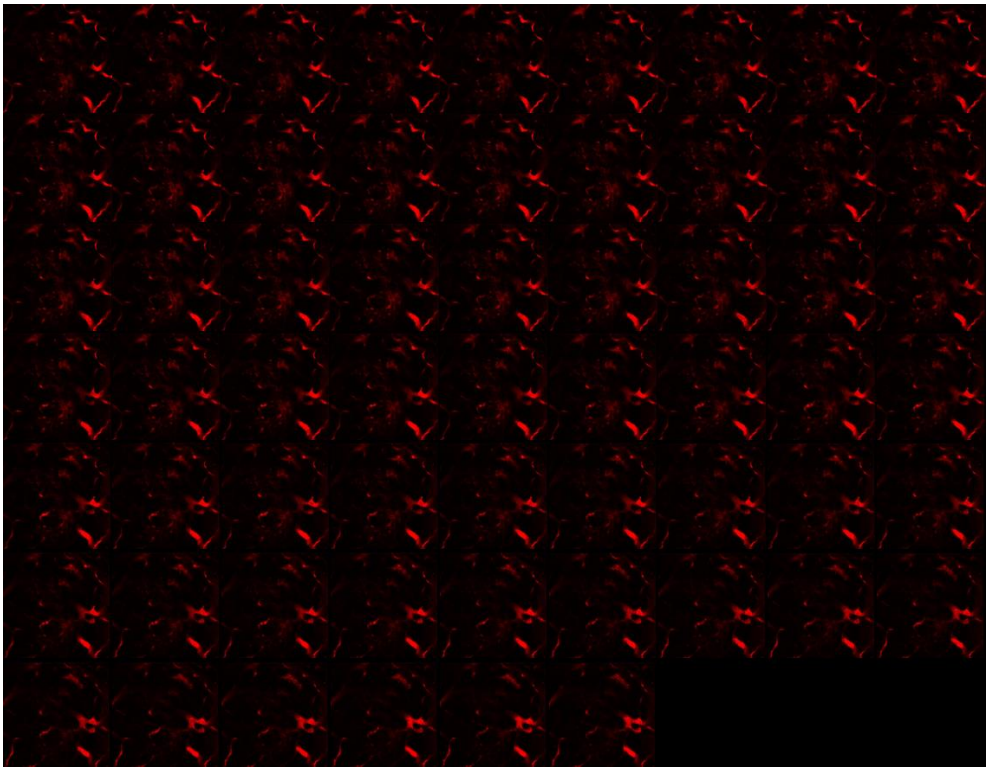

Figure 4-21. **a10**@F127-SiO_2 NPs: time lapse acquisition over 1 hour (1 image per minute) showing the vasculature and the lack of diffusion in the tumour (2PA excitation at 1000 nm).

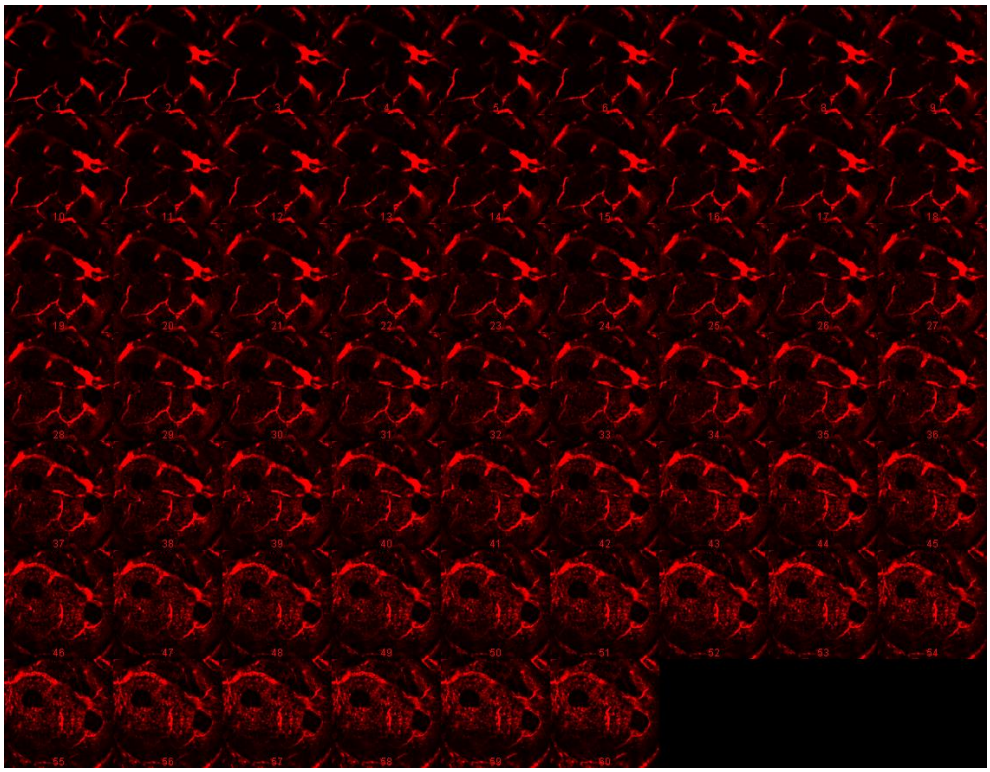

Figure 4-22. **RhB-dextran** 70 kDa: time lapse acquisition over 1 hour (1 image per minute) showing the vasculature and the diffusion of **RhB-dextran** 70 kDa in tumour (2PA excitation at 800 nm).

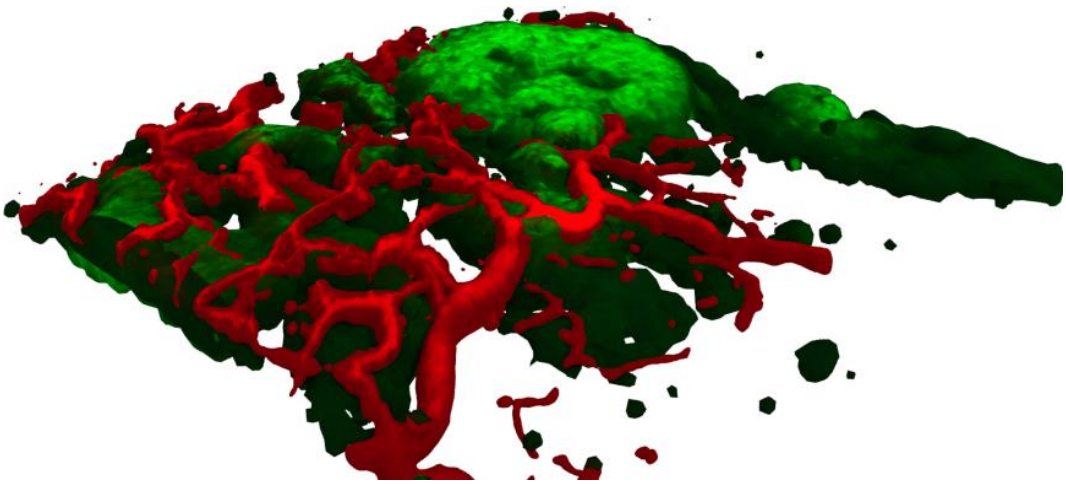

Figure 4-23. 3D two-photon microscopy image of the functional vasculature (red signal of circulating **a10**@F127-SiO_2 NPs) at the surface of a tumour (Glioma U87 GFP cells in green) growing subcutaneously in a mouse ear. The image is a 3D reconstruction using free software (Blender) after a 3D mosaic acquisition (x-y plane: 6x6 images of 512^2 pixels with 91 slices in the z-direction, step-size 2 µm, imaging depth 360 µm, total acquisition time 5600 s).

3. Conclusion

In this chapter, a micelle/silica coprotection strategy was proposed to prepare nanoparticles with a less polar interior, which can be used to conserve optical properties of dipole chromophores in aqueous solution. First of all, the loading efficiency of nanoparticles towards dipolar fluorophore **a10** was optimized by varying the quantity of fluorophore. The optimum conditions were applied to prepare the nanoparticles for the other synthesized dipolar fluorophores and the obtained nanoparticles provide emission from green (568 nm) to FR (685 nm). The size was determined to be 22 nm for all the nanoparticles. The studies indicated that the prepared nanoparticles show excellent colloidal stability, fluorescence stability and photostability, and low toxicity. The similar two-photon properties were found for the nanoparticles as those in chloroform. One of the FR emissive nanoparticles (**a10**@F127-SiO_2 NPs) has been successfully used for two-photon excited fluorescence imaging of blood vessels in tumour inside mouse ear. The nanoparticles show outstanding staining of the vascular system making them perfect blood pool markers. Since different emission wavelengths are available with the prepared nanoparticles, the multiple-colour (two or three) imaging of vasculature system in tumour for two-photon microscopy is in progress.

Chapter 5. Conclusion and Perspectives

This thesis dealt with the development of new far red/near-infrared luminescent probes for *in vivo* two-photon microscopy, focusing on two main projects: oxygen pressure sensing and vasculature system imaging.

In the first part, we presented the synthesis and the study of two new phosphorescent oxygen sensitive probes specifically designed for two-photon absorption. Probes **P-1** and **P-2** (**Chapter 2**) operate through Förster Resonance Energy Transfer (FRET) between suitable two-photon chromophore acting as antenna and harvesting light, and the phosphorescent part composed by a *meso*-tetraphenylporphyrin-Pd(II) core. Prior to the synthesis, four different fluorene-based two-photon absorbing chromophores and two different phosphorescent cores were designed and studied for the optimization of optical properties such as emission and two-photon absorption in the range 750-850 nm. The optimal antenna was covalently grafted to the phosphorescent cores by an efficient Cu(I) catalyzed alkyne-azide cycloaddition (click reaction), affording **P-1** and **P-2** in high yield. These two new compounds contain four or eight two-photon absorbing chromophores connected to the phosphorescent core. Optical study demonstrated an efficient FRET between the different moieties, allowing efficient sensitivity towards oxygen under two-photon excitation. Finally, preliminary steps towards improving the water solubility by modifying the structure have been attempted.

The second part of this thesis work introduced a new series of unsymmetrical fluorene-based push-pull chromophores showing far-red emission along with outstanding solvatochromic properties and interesting two-photon absorption cross-section in the range 800-1200 nm (**Chapter 3**). Interestingly, most of the fluorophores were found to display aggregation-induced emission (AIE) in the far red/near-infrared region. As a consequence, the solid state optical properties including two- and three-photon absorption were investigated together with crystal packing to explain the origin of the solid state emission. Emissive nanoaggregates stable in physiological serum were prepared by using a simple co-precipitation with pluronic F127, the bloc copolymer used to stabilize the nanoparticles. Besides, a new kind of FRET-based co-assembled nanoparticles was prepared using the same protocol, starting from AIE fluorophore and non-AIE fluorophore. This strategy allowed obtaining near-infrared emitting nanoparticles. Deep *in vivo* imaging of the mice vascular system by two-photon microscopy following intra-venous injection was possible using 900 and 1200 nm excitation wavelength. However, diffusion of the fluorescent probes out of the vasculature and accumulation in the liver and the spleen were observed that hampered the use of such aggregates for long-term imaging.

To tackle this issue, an original micelle/silica co-protection nanoparticles was adopted to restore the far-red emission of dipolar fluorophores in aqueous environment. The resulting nanoparticles were demonstrated to be perfect blood pool probes for two-photon imaging of leaky tumour vasculature. No diffusion in the extra vascular space was observed for at least one hour, enabling long three dimensional mosaic acquisitions for the whole tumour area (**Chapter 4**). Different fluorophores giving different emission, two-photon multi-colour

imaging was also performed.

These different *in vivo* two-photon microscopy studies highlight the benefits of combined NIR excitation/red emission for deep *in vivo* imaging and the interest of a specific design of new far-red/NIR fluorophores displaying high two-photon absorption cross-section. Of particular interest is the possibility of two-photon multi-colour imaging in order to analyze the effects of anti-angiogenic therapies by imaging before and after the treatment and comparing the evolution of the neovasculature.

We have seen that formulation in nanoparticles may offer considerable advantages over a single (soluble) fluorophore approach, not only in view of the spectroscopic properties (enhance photostability and quantum yield), but also for solubility and practical *in vivo* use. Considering the difficulties we faced in modifying the structure of big molecules such as compounds **P-1** and **P-2**, formulation in nanoparticles with lessons learnt from this work, may be the answer to provide adequate water solubility. Preliminary works reveal that a simple precipitation method (identical to the one employed for dipolar fluorophores in this thesis), always gives large nanoparticles size over 200 nm, probably because of the bigger size of molecules **P-1** and **P-2**. Micelle/silica-encapsulated strategy seems more suited in that prospect if sophisticated molecule such as **P-1** and **P-2** have to be used.

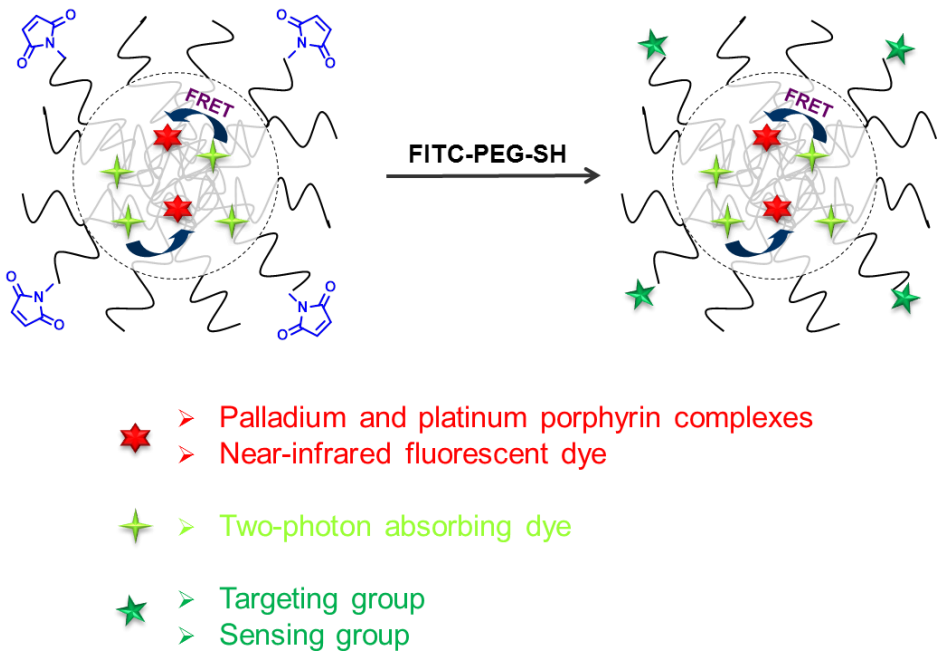

Figure 5-1. Illustration of the strategy for designing new nanoparticles with different functionalities.

However, if simplification of the system is looked after, FRET-based co-assembled nanoparticles, in which the previous antenna act as donor and a suitable Pd-porphyrin complex acts as acceptor appears particularly attractive. Inspired by our work on FRET-based co-assembled nanoparticles, we believe that such a strategy will be a good alternative to sophisticated synthesis for developing oxygen sensitive two-photon phosphorescent probes

(**Figure 5-1**). By using this strategy, the solubility of probes can be easily solved because the nanoparticles can be well dispersed in water. Moreover, it is very flexible to change the component (donor and/or acceptor) as well as the ratio between donor and acceptor. Work in that direction has started.

Since the size of organic nanoparticles has great effect on their optical properties (emission wavelength and fluorescence quantum yield) and their practical *in vivo* applications, control of the size and understanding the physico-chemical parameter controlling the size is of utmost importance. The nanoparticles size is always associated with the preparation protocols and surfactant polymers used. So far, there is no clear explanation on the effect of the particle size on fluorescence, nor degradation *in vivo* has been provided. Colloidal stability and dye leakage issues have also not been addressed specifically. To carry on these studies, a related project was proposed very recently in our laboratory, aiming at developing very stable, ultrabright, non toxic and biodegradable tracers based on new near-infrared organic fluorophores emitting in the solid-state and embedded in polymer shells for practical application in *in vivo* imaging. On the other hand, the potentials of the presented nanoparticles in vasculature imaging have been demonstrated; however, all of them do not possess specific targeting functionality. An interesting continuing work would be to functionalize the surfactant polymers on the surface of nanoparticles with targeting moiety, such as cyclic arginine-glycine-aspartic acid (cRGD) tripeptide, which can specifically recognize cancer cells with overexpressed $\alpha_v\beta_3$ integrin (**Figure 5-1**).[302]

Chapter 6. Experimental Section

1. Synthesis

1.1. General Information

All commercially available chemicals were used as received without further purification. All solvents used for optical measurement were of spectrophotometric grade. Anhydrous solvents (THF and CH_2Cl_2) were dried over a drying column of activated alumina. Dry DMF was purchased over activated molecular sieves and used as received. Analytical thin-layer chromatography (TLC) was performed on Merck 60 F_{254} precoated silica gel plates (0.2 mm thickness). Column chromatography was carried out using Merck silica gel 60 (70−230 mesh). NMR spectra (^{1}H NMR and ^{13}C NMR) were recorded at ambient temperature on a 300 or 500 MHz NMR instrument. Chemical shifts are reported in parts per million (ppm) relative to internal TMS (0 ppm) and coupling constants in hertz (Hz). Splitting patterns were described as singlet (s), doublet (d), triplet (t), quartet (q), or multiplet (m). High-resolution mass spectrometry (HRMS) measurements were performed by ESI-TOF (Bruker Daltonics® Micro TOF-Q II) at the Centre Commun de Spectrométrie de Masse (UCBL, Villeurbanne, France). Mass spectrometry of porphyrin antennae adducts **P-1** and **P-2** was performed by the Pôle Chimie Moléculaire / plateau technique de Welinece in Dijon.

1.2. Synthesis and Characterization

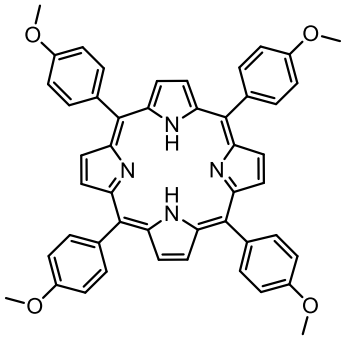

5,10,15,20-tetrakis(4-methoxyphenyl)porphyrin (2)

A solution of pyrrole (2.0 g, 30 mmol) in propionic acid (45 mL) was added dropwise into a solution of 4-anisaldehyde (**1**) (4.1 g, 30 mmol) in propionic acid (135 mL) at 120 °C. When it is completed, the temperature was raised up to 140 °C. After refluxing for 3 h, the propionic acid was distilled off under reduced pressure. The crude product was purified by chromatography on silica gel eluting with CH_2Cl_2/EtOAc (20:1, v:v) to give a purple solid

(1.4 g, yield: 25%). ^{1}H NMR (300 MHz, $CDCl_3$, ppm): δ 8.84 (s, 8H), 8.12 (d, J = 8.6 Hz, 8H), 7.28 (d, J = 8.7 Hz, 8H), 4.08 (s, 12H), -2.76 (s, 2H). ^{13}C NMR (75 MHz, $CDCl_3$, ppm): δ 159.4, 135.6, 134.6, 119.7, 112.2, 55.6. HR-MS (ESI-QTOF): m/z calcd for $[M + H]^+$, 735.2966; found, 735.2945. CAS number: 22112-78-3.

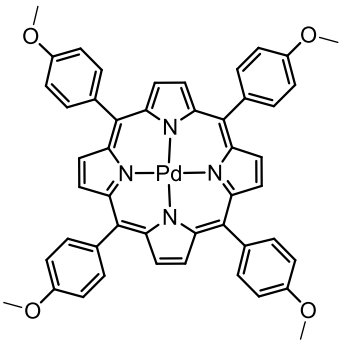

Pd (II)-5,10,15,20-tetrakis(4-methoxyphenyl)porphyrin (Pd-por-1)

In a round-bottom flask, palladium (II) chloride (0.26 g, 1.47 mmol) was added to a solution of **2** (0.54 g, 0.74 mmol) in benzonitrile (370 mL). The mixture was heated to reflux for 3 h. The solution was then cooled to room temperature, and the solvent was distilled off under reduced pressure. The crude product was purified by chromatography on silica gel eluting with CH_2Cl_2 to give a red solid (0.16 g, yield: 26%). ^{1}H NMR (300 MHz, $CDCl_3$, ppm): δ 8.81 (s, 8H), 8.07 (d, J = 8.6 Hz, 8H), 7.27 (d, J = 8.7 Hz, 8H), 4.07 (s, 12H). ^{13}C NMR (75 MHz, $CDCl_3$, ppm): δ 159.4, 141.8, 135.10, 134.2, 130.8, 121.3, 112.2, 55.5. HR-MS (ESI-QTOF): m/z calcd for $[M]^+$, 838.1766; found, 838.1786.

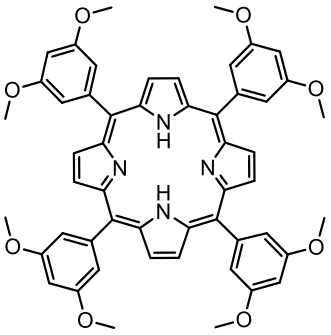

5,10,15,20-tetrakis(3,5-dimethoxyphenyl)porphyrin (4)

A solution of pyrrole (1.30 g, 19.45 mmol) in propionic acid (30 mL) was added dropwise into a solution of 3,5-dimethoxybenzaldehyde (**3**) (3.23 g, 19.45 mmol) in propionic acid (90 mL) at 120 ℃. When it is completed, the temperature was raised up to 140 ℃. After refluxing for 3 h, the propionic acid was distilled out under reduced pressure. The crude product was purified by chromatography on silica gel eluting with CH_2Cl_2/EtOAc (50:1, v:v) to give a purple solid (0.8 g, yield: 20%). ^{1}H NMR (300 MHz, $CDCl_3$, ppm): δ 8.93 (s, 8H), 7.40 (d, J = 2.3 Hz, 8H), 6.91 (t, J = 2.3 Hz, 4H), 3.96 (s, 24H), -2.84 (s, 2H). ^{13}C NMR (75

MHz, $CDCl_3$, ppm): δ 158.9, 144.0, 119.8, 113.9, 100.2, 55.6. HR-MS (ESI-QTOF): m/z calcd for $[M + H]^+$, 855.3388; found, 855.3364. CAS number: 74684-34-7.

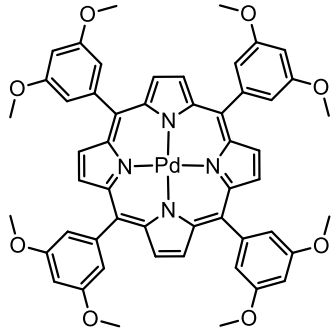

Pd (II)-5,10,15,20-tetrakis(3,5-dimethoxyphenyl)porphyrin[171] (Pd-por-2)

In a round-bottom flask, palladium (II) chloride (0.26 g, 1.47 mmol) was added to a solution of **4** (0.63 g, 0.74 mmol) in benzonitrile (370 mL). The mixture was heated to reflux for 3 h. The solution was then cooled to room temperature, and the solvent was distilled out under reduced pressure. The crude product was purified by chromatography on silica gel eluting with CH_2Cl_2 to give a red solid (0.28 g, yield: 40%). ^{1}H NMR (300 MHz, $CDCl_3$, ppm): δ 8.90 (s, 8H), 7.35 (d, J = 2.2 Hz, 8H), 6.89 (t, J = 2.1 Hz, 4H), 3.95 (s, 24H). ^{13}C NMR (75 MHz, $CDCl_3$, ppm): δ 158.9, 143.6, 141.3, 130.9, 121.4, 113.3, 100.3, 55.6. HR-MS (ESI-QTOF): m/z calcd for $[M]^+$, 958.2189; found, 958.2218.

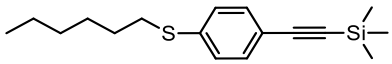

1-hexylsulfanyl-4-(2-(trimethylsilyl)ethynyl)benzene (6)

In a 100 mL two-neck flask, 1-bromo-4-hexylsulfanylbenzene (**5**) (1.00 g, 3.66 mmol) was dissolved in a mixture of DMF and triethylamine (13 mL/13 mL). The solution was degassed by argon bubbling for 20 min and trimethylsilylacetylene (1.08 g, 11.0 mmol), copper iodide (0.14 g, 0.73 mmol) and $(Ph_3P)_2PdCl_2$ (0.26 g, 0.37 mmol) were added under a flux of argon. The mixture was stirred at 100 ℃ for 20 h. The solution was evaporated under vacuum and the resulting oil was dissolved in EtOAc and washed with saturated NH_4Cl aqueous solution and with brine. The crude product was purified by chromatography on silica gel eluting with petroleum ether to afford a colorless oil (0.6 g, yield: 56%). ^{1}H NMR (300 MHz, $CDCl_3$, ppm): δ 7.36 (d, J = 8.7 Hz, 2H), 7.19 (d, J = 8.4 Hz, 2H), 2.89 (t, J = 7.5 Hz, 2H), 1.66 (m, 2H), 1.44 (m, 2H), 1.28 (m, 4H), 0.90 (t, J = 6.8 Hz, 3H), 0.24 (s, 9H). ^{13}C NMR (75 MHz, $CDCl_3$, ppm): δ 138.5, 132.2, 127.5, 119.8, 104.9, 94.2, 32.8, 31.4, 28.9, 28.5, 22.5, 14.0, 0.06. HR-MS (ESI-QTOF): m/z calcd for $[M + H]^+$, 291.1597; found, 291.1601.

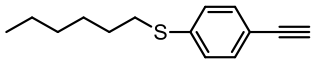

1-ethynyl-4-hexylsulfanylbenzene (7)

In a 100 mL round bottom flask, **6** (0.30 g, 1.03 mmol) and K_2CO_3 (0.43 g, 3.10 mmol) were dissolved in a mixture of THF and methanol (2 mL/2 mL) and the reaction was stirred at room temperature for 2 h. Then, CH_2Cl_2 was added, the suspension was filtered off and the solvent was removed under vacuum. The crude product was purified by chromatography on silica gel eluting with petroleum ether to afford a colorless oil (0.20 g, yield: 90%). ^{1}H NMR (300 MHz, $CDCl_3$, ppm): δ 7.42 (d, J = 8.5 Hz, 2H), 7.26 (d, J = 8.5 Hz, 2H), 3.09 (s, 1H), 2.97 (t, J = 7.4 Hz, 2H), 1.73 (m, 2H), 1.50 (m, 2H), 1.34 (m, 4H), 0.93 (t, J = 6.9 Hz, 3H). ^{13}C NMR (75 MHz, $CDCl_3$, ppm): δ 138.9, 132.4, 127.6, 118.8, 83.4, 77.3, 32.9, 31.3, 28.9, 28.5, 22.5, 14.0. HR-MS (ESI-QTOF): m/z calcd for $[M + H]^+$, 219.1202; found, 219.1206.

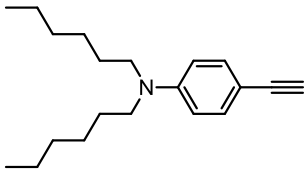

4-ethynyl-*N*,*N*-dihexylaniline[210] (10)

In a 25 mL round bottom flask, *N*,*N*-dihexyl-4-((trimethylsilyl)ethynyl)aniline (**9**) (0.94 g, 2.63 mmol) was dissolved in a mixture of THF and methanol (5 mL/5 mL) and K_2CO_3 (1.09 g, 7.89 mmol) was added. The reaction was stirred at room temperature for 2 h. Then, CH_2Cl_2 was added and the suspension was filtered off. The solvents were removed under reduced pressure. The crude product was purified by chromatography on silica gel eluting with petroleum ether to afford a colorless oil (0.71 g, yield: 95%). ^{1}H NMR (300 MHz, $CDCl_3$, ppm): δ 7.31 (d, J = 9.0 Hz, 2H), 6.51 (d, J = 9.0 Hz, 2H), 3.25 (t, J = 7.7 Hz, 4H), 2.94 (s, 1H), 1.54 (m, 4H), 1.29 (m, 12H), 0.87 (t, J = 6.5 Hz, 6H).

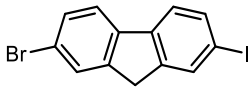

2-bromo-7-iodo-9*H*-fluorene (12)

2-bromofluorene (**11**) (5.0 g, 20.4 mmol) was dissolved in a mixture of glacial acetic acid (90 mL), concentrated H_2SO_4 (2.1 mL) and water (4.2 mL). The mixture was heated at 85 ℃ for 10 min, followed by the addition of iodic acid (0.9 g) and I_2 (2.2 g, 8.5 mmol). The mixture was cooled down to room temperature after keeping the reaction at 85 ℃ for 2 h. The solid was filtered and washed with glacial acetic acid and water. A white product was obtained (6.5 g, yield: 86%). ^{1}H NMR (300 MHz, $CDCl_3$, ppm): δ 7.86 (s, 1H), 7.67 (m, 2H), 7.60 (m, 1H), 7.48 (m, 2H), 3.87 (s, *2*H). ^{13}C NMR (75 MHz, $CDCl_3$, ppm): δ 145.0, 144.6, 140.3, 139.7, 136.0, 134.2, 130.1, 128.2, 121.5, 121.2, 121.1, 92.2, 36.4. HR-MS (EI-QTOF):

m/z calcd for $[M]^+$, 369.8849; found, 369.8846. CAS number: 123348-27-6.

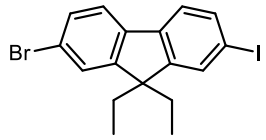

2-bromo-9,9-diethyl-7-iodofluorene (13)

12 (0.5 g, 1.35 mmol) and benzyltriethylammonium chloride (0.15 g, 0.68 mmol) were dissolved in DMSO (8 mL) under argon atmosphere. NaOH (1.25 mL, 50 wt%) was added to this mixture portion-wise over 5 min. Bromoethane (0.44 g, 4.04 mmol) was slowly dropped to the reaction mixture. The mixture was stirred at room tempreature for 2 days. EtOAc (50 mL) was added to the reaction mixture and then this mixture was washed by HCl (35 wt%) and water. The organic layer was dried over Na_2SO_4 and filtered. The solution was evaporated to afford compound **13** (0.56 g, yield: 97%). ^{1}H NMR (300 MHz, $CDCl_3$, ppm): δ 7.64 (m, 2H), 7.51 (m, 1H), 7.44 (m, 3H), 2.01 (q, J = 7.5 Hz, 4H), 0.31 (t, J = 7.3 Hz, 6H). ^{13}C NMR (75 MHz, $CDCl_3$, ppm): δ 151.9, 151.5, 140.1, 139.5, 136.1, 132.1, 130.2, 126.2, 121.6, 121.4, 121.1, 92.9, 56.6, 32.5, 8.4. HR-MS (EI-QTOF): m/z calcd for $[M]^+$, 425.9475; found, 425.9486.

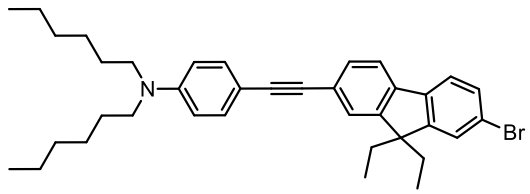

4 -(2-(2–bromo -9,9–diethylfluoren-7-yl)ethynyl)-*N*,*N*-dihexylbenzenamine (14)

In a 50 mL two-neck flask, **13** (0.81 g, 1.89 mmol) was dissolved in a mixture of THF and triethylamine (12 mL/12 mL). The solution was thoroughly degassed by argon bubbling for 20 min and **10** (0.45 g, 1.58 mmol), copper iodide (0.07 g, 0.38 mmol) and $(Ph_3P)_2PdCl_2$ (0.13 g, 0.19 mmol) were added under a flux of argon. The reaction was stirred at room temperature for one day. The solution was evaporated under vacuum and the resulting oil was dissolved in EtOAc and washed with saturated NH_4Cl aqueous solution and with brine. The crude product was purified by chromatography on silica gel eluting with pentane/CH_2Cl_2 (10:1, v:v) to afford a colorless oil (0.66 g, yield: 71%). ^{1}H NMR (300 MHz, $CDCl_3$, ppm): δ 7.60 (d, J = 7.9 Hz, 1H), 7.53 (d, J = 8.5 Hz, 1H), 7.47-7.42 (m, 4H), 7.38 (d, J = 8.9 Hz, 2H), 6.58 (d, J = 8.9 Hz, 2H), 3.29 (t, J = 7.5 Hz, 4H), 2.00 (m, 4H), 1.57 (m, 4H), 1.30 (s, 12H), 0.91 (t, J = 6.6 Hz, 6H), 0.33 (t, J = 7.3 Hz, 6H). ^{13}C NMR (75 MHz, $CDCl_3$, ppm): δ 152.4, 149.5, 148.0, 140.2, 139.8, 132.9, 130.5, 130.1, 126.3, 125.7, 123.3, 121.24, 121.19, 119.7, 111.3, 108.8, 91.5, 88.0, 56.5, 51.0, 32.8, 31.8, 27.3, 26.9, 22.8, 14.1, 8.5. HR-MS (ESI-QTOF): m/z calcd for $[M + H]^+$, 584.2886; found, 584.2853.

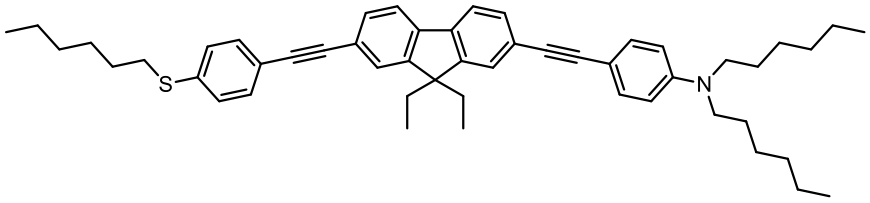

4-((9,9-diethyl-7-((4-(hexylthio)phenyl)ethynyl)fluoren-2-yl)ethynyl)-*N*,*N*-dihexylbenzen amine (NS)

In a 100 mL two-neck flask, **14** (0.66 g, 1.13 mmol) was dissolved in a mixture of DMF and triethylamine (12 mL/12 mL). The solution was thoroughly degassed by argon bubbling for 20 min and **7** (0.74 g, 3.38 mmol), copper iodide (0.04 g, 0.21 mmol) and $(Ph_3P)_2PdCl_2$ (0.07 g, 0.10 mmol) were added under a flux of argon. The reaction was stirred at 100 ℃ for 20 h. The solution was evaporated under vacuum and the resulting oil was dissolved in EtOAc and washed with saturated NH_4Cl aqueous solution and with brine. The crude product was purified by chromatography on silica gel eluting with petroleum ether/EtOAc (2:1, v:v) to afford a light yellow oil (0.60 g, yield: 74%). ^{1}H NMR (300 MHz, $CDCl_3$, ppm): δ 7.64-7.60 (m, 2H), 7.49-7.45 (m, 4H), 7.44 (d, *J* = 8.3 Hz, 2H), 7.38 (d, *J* = 8.9 Hz, 2H), 7.26 (d, *J* = 8.5 Hz, 2H), 6.57 (d, *J* = 9.0 Hz, 2H), 3.28 (t, *J* = 7.6 Hz, 4H), 2.95 (t, *J* = 7.4 Hz, 2H), 2.06 (m, *J* = 7.3 Hz, 4H), 1.57 (m, 6H), 1.47 (m, 2H), 1.30 (m, 16H), 0.88 (m, 9H), 0.34 (t, *J* = 7.3 Hz, 6H). ^{13}C NMR (75 MHz, $CDCl_3$, ppm): δ 150.2, 150.1, 147.9, 141.3, 140.1, 138.0, 132.8, 131.8, 130.7, 130.4, 127.8, 125.9, 125.6, 123.2, 121.6, 120.2, 119.8, 119.7, 111.2, 108.7, 91.4, 90.7, 89.4, 88.0, 56.2, 50.9, 33.0, 32.7, 31.7, 31.3, 28.9, 28.5, 27.2, 26.8, 22.7, 22.5, 14.1, 14.0, 8.4. HR-MS (ESI-QTOF): m/z calcd for $[M + H]^+$, 722.4754; found, 722.4720.

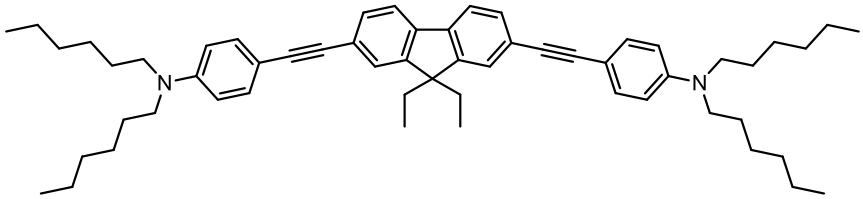

4,4'-((9,9-diethylfluorene-2,7-diyl)di-2,1-ethynediyl)bis(*N*,*N*-dihexylbenzenamine) (NN)

In a 25 mL two-neck flask, 2,7-diiodo-9,9-diethylfluorene (**8**) (0.50 g, 1.05 mmol) was dissolved in a mixture of THF and triethylamine (5 mL/5 mL). The solution was thoroughly degassed by argon bubbling for 20 min and **10** (0.90 g, 3.16 mmol), copper iodide (0.14 g, 0.76 mmol) and $(Ph_3P)_2PdCl_2$ (0.26 g, 0.38 mmol) were added under a flux of argon. The reaction was stirred at room temperature for one day. Then the solution was diluted by diethyl ether (150 mL) and washed with saturated NH_4Cl aqueous solution and with brine. The organic phase was evaporated and the crude product was purified by chromatography on silica gel eluting with CH_2Cl_2 to afford a colorless oil (0.41 g, yield: 50%). ^{1}H NMR (300 MHz, $CDCl_3$, ppm): δ 7.61 (d, *J* = 7.8 Hz, 2H), 7.46-7.42 (m, 4H), 7.37 (d, *J* = 8.8 Hz, 4H), 6.57 (d, *J* = 8.9 Hz, 4H), 3.28 (t, *J* = 7.6 Hz, 8H), 2.05 (q, *J* = 7.3 Hz, 4H), 1.56 (m, 8H), 1.30

(m, 24H), 0.98 (t, J = 6.6 Hz, 12H), 0.33 (t, J = 7.2 Hz, 6H). ^{13}C NMR (75 MHz, $CDCl_3$, ppm): δ 147.9, 140.4, 132.8, 130.3, 125.6, 122.7, 119.6, 111.2, 108.8, 91.1, 88.1, 56.1, 50.9, 32.7, 31.7, 27.2, 26.8, 22.6, 14.0, 8.4. HR-MS (ESI-QTOF): m/z calcd for $[M + H]^+$, 789.6081; found, 789.6058.

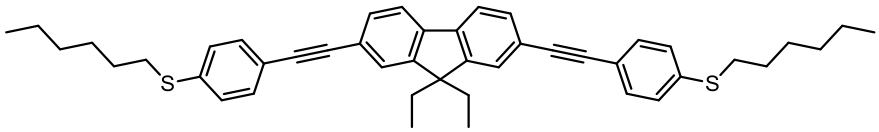

4,4'-[(9,9-diethylfluorene-2,7-diyl)di-2,1-ethynediyl]bishexylsulfanylbenzene (SS)

Compound **SS** was prepared according to the same procedure than **NN** using **7** (0.69 g, 3.16 mmol) instead of **10** (0.90 g, 3.16 mmol). Purification by chromatography on silica gel afford a yellow-green powder (0.53 g, yield: 76%). ^{1}H NMR (300 MHz, $CDCl_3$, ppm): δ 7.66 (d, J = 7.7 Hz, 2H), 7.51-7.47 (m, 4H), 7.45 (d, J = 8.5 Hz, 4H), 7.26 (d, J = 8.5 Hz, 4H), 2.95 (t, J = 7.4 Hz, 4H), 2.07 (q, J = 7.3 Hz, 4H), 1.70 (m, 4H), 1.47 (m, 4H), 1.30 (m, 8H), 0.90 (t, J = 6.7 Hz, 6H), 0.34 (t, J = 7.3 Hz, 6H). ^{13}C NMR (75 MHz, $CDCl_3$, ppm): δ 150.3, 141.1, 138.1, 131.8, 130.8, 127.8, 126.0, 122.0, 120.1, 119.9, 90.6, 89.6, 56.3, 33.0, 32.7, 31.4, 28.9, 28.6, 22.5, 14.0, 8.4. HR-MS (ESI-QTOF): m/z calcd for $[M + H]^+$, 655.3427; found, 655.3412.

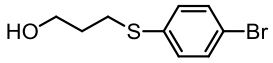

3-((4-bromophenyl)thio)propan-1-ol (17)

Sodium hydride (0.79 g, 60% dispersion in mineral oil, 19.8 mmol) was added to a solution of 4-bromothiophenol (**15**) (2.5 g, 13.2 mmol) in DMF (20 mL), followed by the addition of 3-bromo-1-propanol (**16**) (3.68 g, 26.4 mmol). The resulting mixture was stirred for 18 h at room temperature. The reaction mixture was diluted with water (40 mL) and extracted with EtOAc (2×50 mL). The combined organic phases were dried over $MgSO_4$, filtered and concentrated. The crude product was purified by chromatography on silica gel eluting with petroleum ether/EtOAc (2:1, v:v) as eluent to afford colorless oil (2.71 g, yield: 83%). ^{1}H NMR (300 MHz, $CDCl_3$, ppm): δ 7.39 (d, J = 8.6 Hz, 2H), 7.19 (d, J = 8.6 Hz, 2H), 3.75 (q, 2H), 3.02 (t, J = 7.1 Hz, 2H), 1.88 (m, 2H), 1.38 (t, J = 5.2 Hz, 1H).

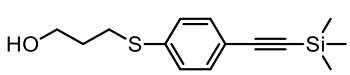

3-((4-((trimethylsilyl)ethynyl)phenyl)thio)propan-1-ol (18)

In a 100 mL two-neck flask, **17** (2.71 g, 10.97 mmol) was dissolved in a mixture of DMF and triethylamine (40 mL/40 mL). The solution was thoroughly degassed by argon bubbling for 20 min and trimethylsilylacetylene (3.23 g, 32.90 mmol), copper iodide (0.42 g, 2.2 mmol) and $(Ph_3P)_2PdCl_2$ (0.77 g, 1.1 mmol) were added under a flux of argon. The reaction was

stirred at 100 ℃ for 20 h. The solution was evaporated under vacuum and the resulting oil was dissolved in EtOAc and washed with saturated NH_4Cl aqueous solution and with brine. The crude product was purified by chromatography on silica gel eluting with petroleum ether/EtOAc (2:1, v:v) to afford a colorless oil (1.39 g, yield: 48%). ^{1}H NMR (300 MHz, $CDCl_3$, ppm): δ 7.36 (d, J = 8.6 Hz, 2H), 7.22 (d, J = 8.6 Hz, 2H), 3.78 (q, 2H), 3.06 (t, J = 7.1 Hz, 2H), 1.92 (m, 2H), 1.38 (t, J = 5.2 Hz, 1H), 0.22 (s, 9H). ^{13}C NMR (75 MHz, $CDCl_3$, ppm): δ 138.1, 132.5, 127.9, 119.2, 83.3, 61.3, 31.5, 29.5. HR-MS (ESI-QTOF): m/z calcd for $[M + H]^+$, 265.1077; found, 265.1071.

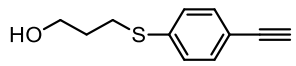

3-((4-ethynylphenyl)thio)propan-1-ol (19)

In a 100 mL round bottom flask, **18** (1.39 g, 5.26 mmol) was dissolved in a mixture of THF and methanol (1 mL/1 mL) and K_2CO_3 (2.18 g, 15.7 mmol) was added. The reaction was stirred at room temperature for 2 h. Then, CH_2Cl_2 was added and the suspension was filtered off. The solvent were removed under reduced pressure. The crude product was purified by chromatography on silica gel eluting with petroleum ether/EtOAc (2:1, v:v) to afford a colorless oil (0.8 g, yield: 82%). ^{1}H NMR (300 MHz, $CDCl_3$, ppm): δ 7.39 (d, J = 8.5 Hz, 2H), 7.25 (d, J = 8.6 Hz, 2H), 3.77 (q, 2H), 3.07 (t, J = 7.1 Hz, 2H), 3.06 (s, 1H), 1.94 (m, 2H), 1.40 (t, J = 5.2 Hz, 1H). ^{13}C NMR (75 MHz, $CDCl_3$, ppm): δ 138.1, 132.5, 127.9, 119.2, 90.1, 83.3, 61.3, 31.5, 29.5. HR-MS (ESI-QTOF): m/z calcd for $[M + H]^+$, 193.0682; found, 193.0677.

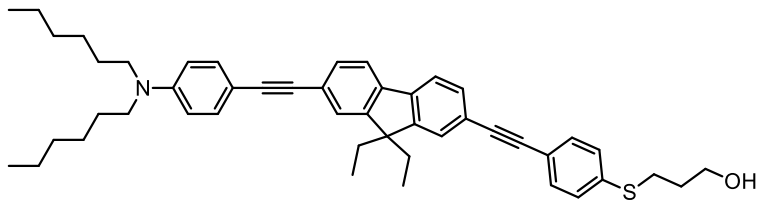

3-((4-((7-((4-(dihexylamino)phenyl)ethynyl)-9,9-diethylfluoren-2-yl)ethynyl)phenyl)thio)propan-1-ol (20)

In a 100 mL two-neck flask, **14** (0.66 g, 1.13 mmol) was dissolved in a mixture of DMF and triethylamine (12 mL/12 mL). The solution was thoroughly degassed by argon bubbling for 20 min. **19** (0.65 g, 3.38 mmol), copper iodide (0.04 g, 0.21 mmol) and $(Ph_3P)_2PdCl_2$ (0.07 g, 0.10 mmol) were added under a flux of argon. The reaction was stirred at 100 ℃ for 20 h. The solvents were removed under reduced pressure. The resulting oil was dissolved in EtOAc and washed with saturated NH_4Cl aqueous solution and with brine. The crude product was purified by chromatography on silica gel eluting with petroleum ether/EtOAc (2:1, v:v) to afford a light yellow oil (0.65 g, yield: 83%). ^{1}H NMR (300 MHz, $CDCl_3$, ppm): δ 7.65 (dd, 2H), 7.50-7.43 (m, 6H), 7.39 (d, J = 8.9 Hz, 2H), 7.30 (d, J = 8.5 Hz, 2H), 6.58 (d, J = 9.0 Hz, 2H), 3.79 (t, J = 6.0 Hz, 2H), 3.29 (t, J = 7.4 Hz, 4H), 3.09 (t, J = 7.1 Hz, 2H), 2.05 (q, 4H), 1.91 (m, 2H), 1.60 (m, 4H), 1.31 (s, 12H), 0.92 (t, J = 6.6 Hz, 6H), 0.34 (t, J = 7.2 Hz, 6H).

^{13}C NMR (75 MHz, $CDCl_3$, ppm): δ 150.21, 150.18, 147.9, 141.4, 140.2, 137.2, 132.9, 131.9, 130.7, 130.4, 128.1, 125.9, 125.7, 123.2, 121.6, 120.6, 119.9, 119.8, 111.2, 108.7, 91.4, 90.9, 89.3, 88.1, 61.3, 56.3, 50.9, 32.8, 31.7, 31.6, 29.6, 27.2, 26.8, 22.7, 14.1, 8.5. HR-MS (ESI-QTOF): m/z calcd for $[M + H]^+$, 696.4234; found, 696.4190.

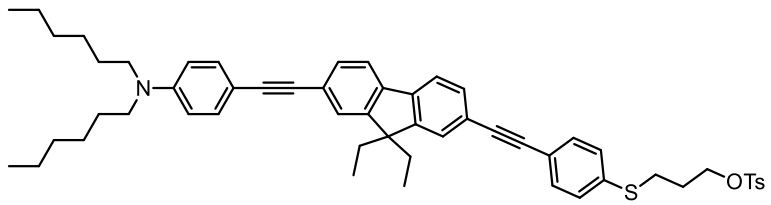

3-((4-((7-((4-(dihexylamino)phenyl)ethynyl)-9,9-diethylfluoren-2-yl)ethynyl)phenyl)thio)propyl(4-methylbenzenesulfonate) (21)

In a round bottom flask, a solution of **20** (0.20 g, 0.29 mmol) in dried CH_2Cl_2 (25 mL) was cooled to 0 ℃. Triethylamine (3 mL), DMAP (8 mg) and tosyl chloride (0.15 g) were added. After stirring for 30 min at 0 ℃, the ice bath was removed and the reaction mixture was subsequently stirred for 3 h at room temperature under argon atmosphere. The solvent was evaporated under reduced pressure, and the crude oil was purified by chromatography on silica gel eluting with petroleum ether/EtOAc (2:1, v:v) to afford a light yellow oil (0.20 g, yield: 82%). ^{1}H NMR (300 MHz, $CDCl_3$, ppm): δ 7.79 (d, J = 8.3 Hz, 2H), 7.65 (dd, 2H), 7.50-7.41 (m, 6H), 7.39 (d, J = 8.9 Hz, 2H), 7.34 (d, J = 8.0 Hz, 2H), 7.21 (d, J = 8.5 Hz, 2H), 6.58 (d, J = 9.0 Hz, 2H), 4.17 (t, J = 5.9 Hz, 2H), 3.29 (t, J = 7.5 Hz, 4H), 2.97 (t, J = 7.0 Hz, 2H), 2.43 (s, 3H), 2.07 (q, 4H), 1.96 (m, 2H), 1.57 (m, 4H), 1.31 (s, 12H), 0.91 (t, J = 6.6 Hz, 6H), 0.34 (t, J = 7.2 Hz, 6H). ^{13}C NMR (75 MHz, $CDCl_3$, ppm): δ 150.22, 150.17, 147.9, 144.9 141.5, 140.1, 136.1, 132.9, 132.1, 131.9, 130.7, 130.4, 129.9, 128.6, 127.9, 125.9, 125.7, 123.2, 121.4, 121.1, 119.9, 119.8, 111.2, 108.7, 91.5, 91.1, 89.1, 88.0, 68.5, 56.3, 50.9, 32.8, 31.7, 29.1, 28.3, 27.2, 26.8, 22.7, 21.7, 14.1, 8.5. HR-MS (ESI-QTOF): m/z calcd for $[M + H]^+$, 850.4322; found, 850.4275.

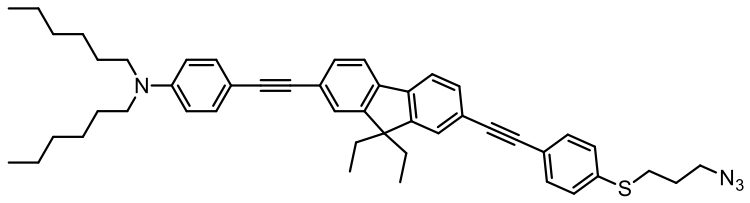

4-((7-((4-((3-azidopropyl)thio)phenyl)ethynyl)-9,9-diethylfluoren-2-yl)ethynyl)-*N,N*-dihexylbenzenamine (22)

A suspension of **21** (0.20 g, 0.23 mmol) and sodium azide (0.05 g, 0.70 mmol) in DMF (5 mL) was stirred at 80 ℃ for 24 h. The reaction mixture was concentrated under reduced pressure and the crude purified by chromatography on silica gel eluting with petroleum ether/EtOAc (20:1, v:v): light yellow oil (0.15 g, yield: 88%). ^{1}H NMR (300 MHz, $CDCl_3$, ppm): δ 7.65 (dd, 2H), 7.50-7.44 (m, 6H), 7.38 (d, J = 8.8 Hz, 2H), 7.29 (d, J = 8.4 Hz, 2H), 6.57 (d, J = 8.9 Hz, 2H), 3.47 (t, J = 6.5 Hz, 2H), 3.28 (t, J = 7.5 Hz, 4H), 3.05 (t, J = 7.0 Hz,

2H), 2.07 (q, 4H), 1.91 (m, 2H), 1.57 (m, 4H), 1.31 (s, 12H), 0.91 (t, J = 6.5 Hz, 6H), 0.33 (t, J = 7.2 Hz, 6H). ^{13}C NMR (75 MHz, $CDCl_3$, ppm): δ 150.21, 150.17, 147.9, 141.5, 140.1, 136.5, 132.9, 132.0, 130.7, 130.4, 128.5, 125.9, 125.7, 123.2, 121.5, 120.9, 119.8, 119.7, 111.2, 108.7, 91.4, 91.1, 89.2, 88.0, 56.3, 50.9, 49.9, 32.8, 31.7, 31.5, 29.7, 27.2, 26.8, 22.7, 14.1, 8.5. HR-MS (ESI-QTOF): m/z calcd for $[M + H]^+$, 721.4298; found, 721.4284.

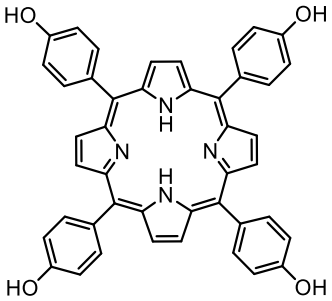

5,10,15,20-tetrakis(4-hydroxyphenyl)porphyrin (24)

A solution of pyrrole (2.0 g, 30 mmol) in propionic acid (45 mL) was added dropwise into a solution of *para*-hydroxybenzaldehyde (**23**) (3.6 g, 30 mmol) in propionic acid (135 mL) heated at 120 ℃. When the addition was completed, the temperature was raised up to 140 ℃. After refluxing for 3 h, propionic acid was distilled off under reduced pressure. Purification of the crude by chromatography on silica gel eluting with acetone/petroleum ether (1:1, v:v) gave a purple solid (1.0 g, yield: 20%). ^{1}H NMR (300 MHz, $(CD_3)_2CO$, ppm): δ 8.93 (s, 8H), 8.09 (d, J = 8.5 Hz, 8H), 7.32 (d, J = 8.5 Hz, 8H), -2.70 (s, 2H). ^{13}C NMR (75 MHz, $(CD_3)_2CO$, ppm): δ 157.5, 135.6, 133.2, 120.1, 113.8. HR-MS (ESI-QTOF): m/z calcd for $[M + H]^+$, 679.2340; found, 679.2327. CAS number: 51094-17-8.

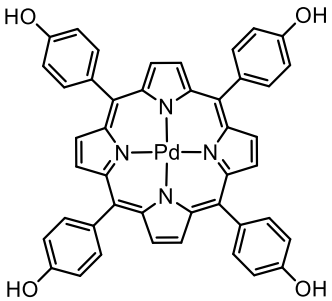

Pd (II)-5,10,15,20-tetrakis(4-hydroxyphenyl)porphyrin (25)

Palladium (II) chloride (0.26 g, 1.47 mmol) was added to a solution of **24** (0.50 g, 0.74 mmol) in benzonitrile (370 mL). The mixture was heated to reflux for 3 h. The solution was cooled to room temperature, and the solvent evaporated. The crude was purified by chromatography on silica gel eluting with acetone/petroleum ether (1:1, v:v) to give a red solid (0.48 g, yield: 83%). ^{1}H NMR (300 MHz, $(CD_3)_2CO$, ppm): δ 8.91 (s, 8H), 8.89 (s, 4H), 8.03 (d, J = 8.4 Hz, 8H), 7.30 (d, J = 8.5 Hz, 8H). ^{13}C NMR (75 MHz, $(CD_3)_2CO$, ppm): δ 157.5, 141.9, 135.1, 132.7, 130.9, 121.8, 113.8. HR-MS (ESI-QTOF): m/z calcd for M^+,

782.1155; found, 782.1154.

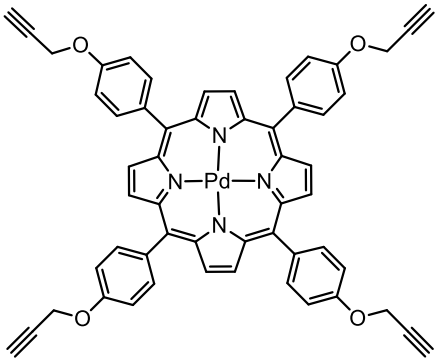

Pd (II)-5,10,15,20-tetrakis(4-propargyloxyphenyl)porphyrin (26)

25 (0.15 g, 0.20 mmol) and propargyl bromide (0.20 mL, 1.95 mmol, 80% solution in toluene) were dissolved in DMF (10 mL) in the presence of K_2CO_3 (0.27 g, 1.95 mmol). The reaction mixture was stirred at ambient temperature under an inert atmosphere for 48 h. Then water (50 mL) and CH_2Cl_2 (50 mL) were added to the reaction. Subsequently the organic layer was isolated and the aqueous layer was extracted a second time with another shot of CH_2Cl_2 (50 mL). The organic layers were combined, dried over $MgSO_4$, filtered, and the solvent was removed under reduced pressure. The crude residue was purified by chromatography on silica gel eluting with CH_2Cl_2 to afford a red solid (0.17 g, yield: 93%). ^{1}H NMR (300 MHz, $CDCl_3$, ppm): δ 8.81 (s, 8H), 8.07 (d, J = 8.6 Hz, 8H), 7.33 (d, J = 8.7 Hz, 8H), 4.96 (d, J = 2.4 Hz, 8H), 2.68 (t, J = 2.4 Hz, 4H). ^{13}C NMR (75 MHz, $CDCl_3$, ppm): δ 157.5, 141.8, 135.10, 135.07, 131.0, 121.2, 113.2, 78.7, 75.9, 56.2. HR-MS (ESI-QTOF): m/z calcd for M^+, 934.1785; found, 934.1791.

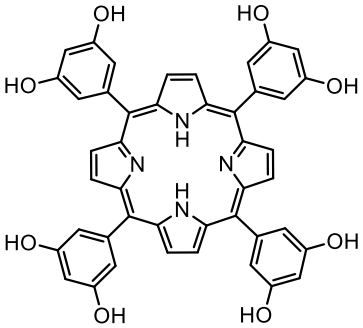

5,10,15,20-tetrakis(3,5-dihydroxyphenyl)porphyrin (27)

A solution of **4** (0.05 g, 0.06 mmol) in CH_2Cl_2 (5 mL) was stirred with cooling in an ice bath under a nitrogen atmosphere whilst boron tribromide (0.52 mL, 0.52 mmol, 1 M in CH_2Cl_2) was added slowly. The reaction was stirred at room temperature for 24 h, quenched with methanol (3 mL) and neutralized with ammonia solution till the solution turned from green to dark red colour. The mixture was evaporated till dryness, extracted with EtOAc and the organic layer was washed several times with water. The organic phase was separated,

dried over anhydrous $MgSO_4$, filtered, and concentrated. The crude product was purified by chromatography on silica gel eluting with acetone/petroleum ether (1:1, v:v) to give a purple solid (0.04 g, yield: 98%).^{1}H NMR (300 MHz, $(CD_3)_2CO$, ppm): δ 9.02 (s, 8H), 8.71 (s, 8H), 7.24 (d, J = 2.2 Hz, 8H), 6.84 (t, J = 2.2 Hz, 4H), -2.81 (s, 2H). ^{13}C NMR (75 MHz, $(CD_3)_2CO$, ppm): δ 156.8, 143.7, 120.0, 114.5, 102.3. HR-MS (ESI-QTOF): m/z calcd for $[M + H]^+$, 743.2136; found, 743.2132. CAS number: 145764-54-1.

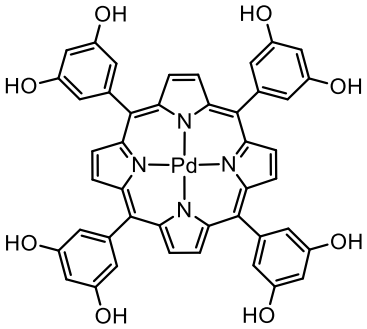

Pd (II)-5,10,15,20-tetrakis(3,5-dihydroxyphenyl)porphyrin (28)

28 was synthesized as described for **25**. Starting from **27** (0.55 g, 0.74 mmol) and palladium (II) chloride (0.26 g, 1.47 mmol). Purification by chromatography on silica gel eluting with acetone/petroleum ether (2:1, v:v) gave a red solid (0.41 mg, yield: 66%). ^{1}H NMR (300 MHz, $(CD_3)_2CO$, ppm): δ 9.00 (s, 8H), 8.73 (s, 8H), 7.20 (d, J = 2.2 Hz, 8H), 6.83 (t, J = 2.2 Hz, 4H). ^{13}C NMR (75 MHz, $(CD_3)_2CO$, ppm): δ 156.9, 143.2, 141.2, 130.9, 121.8, 114.0, 102.4. HR-MS (ESI-QTOF): m/z calcd for M^+, 846.0952; found, 846.0980.

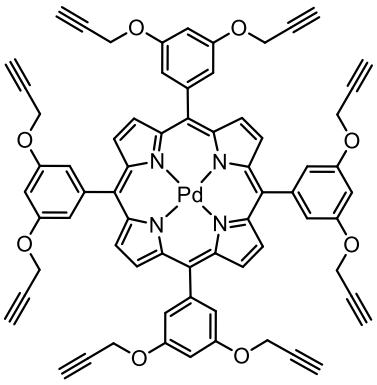

Pd (II)-5,10,15,20-tetraki*s*(3,5-dipropargyloxyphenyl)porphyrin (29)

28 (0.10 g, 0.12 mmol) and propargyl bromide (0.25 mL, 2.8 mmol, 80% solution in toluene) were dissolved in DMF (10 mL) in the presence of K_2CO_3 (0.40 g, 2.8 mmol). The reaction mixture was stirred at ambient temperature under an inert atmosphere for 48 h. Then water (50 mL) and CH_2Cl_2 (50 mL) were added to the reaction. Subsequently the organic layer was isolated and the aqueous layer was extracted a second time with another aliquot of CH_2Cl_2 (50 mL). The organic layers were combined, dried over $MgSO_4$, filtered, and the

solvent was removed under reduced pressure. The crude residue was purified by chromatography on silica gel eluting with CH_2Cl_2 to afford a red solid. (0.04 g, yield: 30%). ^{1}H NMR (300 MHz, $CDCl_3$, ppm): δ 8.92 (s, 8H), 7.48 (d, J = 2.3 Hz, 8H), 7.07 (t, J = 2.3 Hz, 4H), 4.86 (d, J = 2.4 Hz, 16H), 2.61 (d, J = 2.4 Hz, 8H). ^{13}C NMR (75 MHz, $CDCl_3$, ppm): δ 156.9, 143.6, 141.3, 131.1, 121.1, 114.9, 102.4, 78.4, 76.0, 56.2. HR-MS (ESI-QTOF): m/z calcd for M^+, 1150.2210; found, 1150.2180.

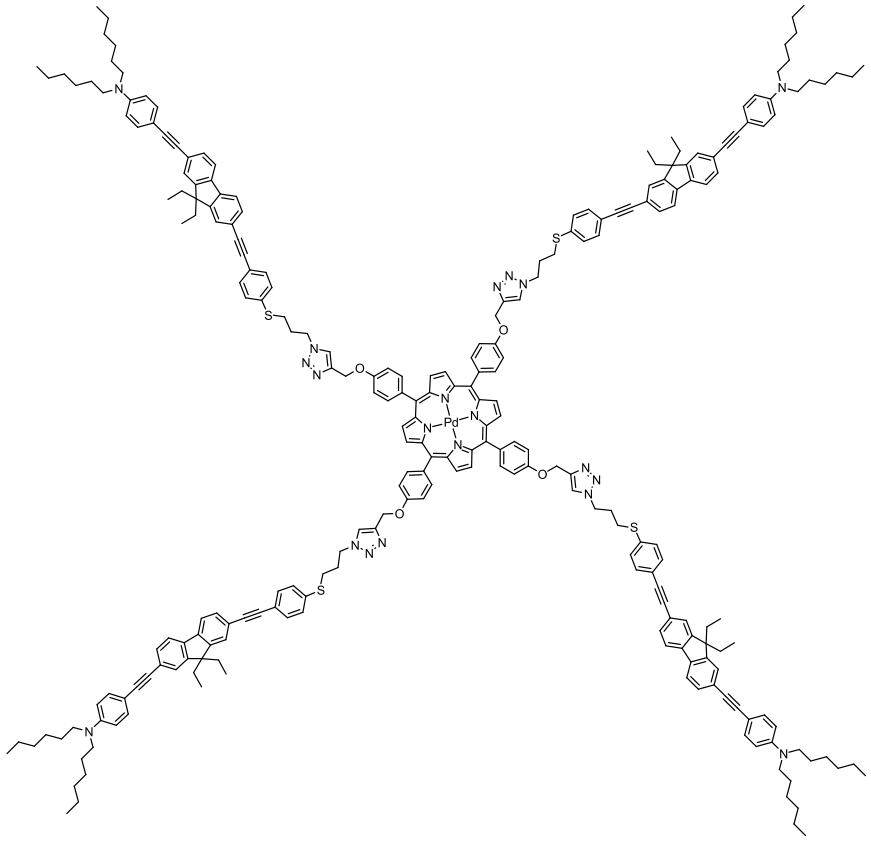

P-1

To a solution of **22** (0.11 g, 0.153 mmol) and **26** (0.024 g, 0.0254 mmol) in THF (5 mL), were added $CuSO_4$ $5H_2O$ (0.038 g, 0.152 mmol) and then sodium L-ascorbate (0.096 g, 0.483 mmol) dissolved in water (1.6 mL). The solution was heated at about 40 ℃ for 48 h. The mixture was dissolved in EtOAc and washed with brine. The organic layers were combined, dried over $MgSO_4$, filtered and the solvent was removed under reduced pressure. Purification by chromatography on silica gel eluting with $CHCl_3$/methanol (50:1, v:v) afforded **P-1** as dark orange-brown viscous oil (0.07 g, yield: 71%). ^{1}H NMR (300 MHz, $CDCl_3$, ppm): δ 8.82 (s, 8H), 8.06 (d, J = 8.5 Hz, 8H), 7.67 (s, 4H), 7.48-7.36 (m, 40H), 7.33 (d, J = 8.7 Hz, 8H), 7.29 (d, J = 8.6 Hz, 8H), 6.59 (d, J = 9.0 Hz, 8H), 5.42 (s, 8H), 4.56 (t, J = 6.6 Hz, 8H), 3.29 (t, J = 7.6 Hz, 16H), 2.98 (t, J = 6.8 Hz, 8H), 2.31 (m, 8H), 1.99 (q, 16H), 1.58 (m, 16H), 1.32 (s, 48H), 0.92 (t, J = 6.6 Hz, 24H), 0.28 (t, J = 7.3 Hz, 24H). ^{13}C NMR (75 MHz, $CDCl_3$, ppm): δ 158.1, 150.15, 150.13, 147.9, 144.3, 141.9, 141.4, 140.0, 135.8, 135.2, 134.7, 132.9, 132.3, 132.1, 131.0, 130.7, 130.4, 128.8, 125.9, 125.6, 124.0, 123.1,

121.3, 119.8, 119.7, 113.1, 111.2, 108.6, 91.5, 91.3, 89.1, 88.0, 62.3, 56.23, 56.19, 50.9, 32.7, 31.7, 29.9, 29.3, 27.2, 26.8, 22.7, 14.1, 8.5.

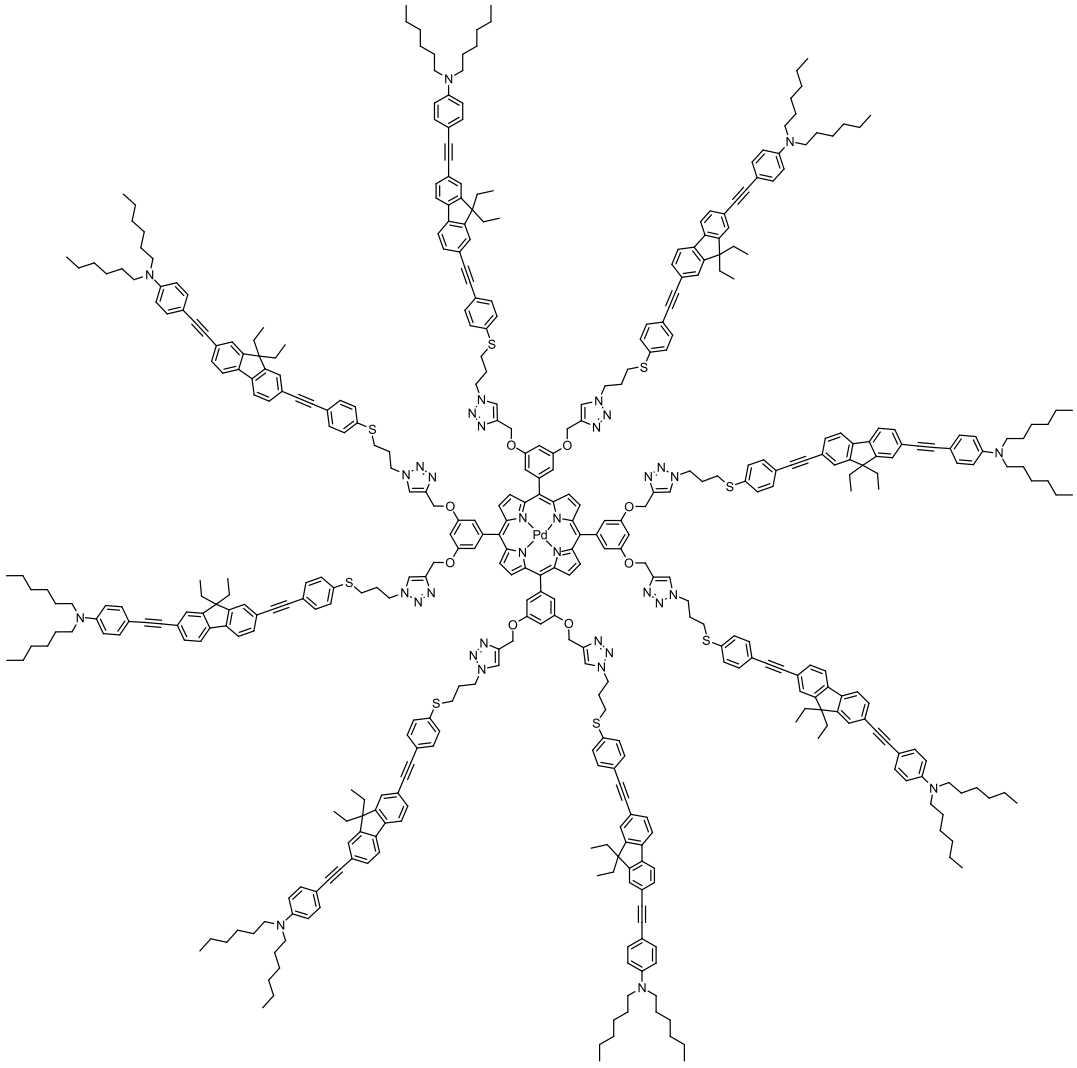

P-2

Synthesized as described for the preparation of **P-1** starting from **22** (0.20 g, 0.277 mmol) and **29** (0.027 g, 0.023 mmol) in THF (4.5 mL) with $CuSO_4$ $5H_2O$ (0.069 g, 0.277 mmol) and then sodium L-ascorbate (0.174 g, 0.874 mmol) dissolved in water (1.5 mL). Chromatography on silica gel eluting with $CHCl_3$/methanol (50:1, v:v) afforded **P-2** as dark orange-brown viscous oil (0.10 g, yield: 65%). ^{1}H NMR (300 MHz, $CDCl_3$, ppm): δ 8.92 (s, 8H), 7.62 (s, 8H), 7.58-7.34 (m, 88H), 7.20 (d, J = 8.2 Hz, 16H), 7.10 (s, 4H), 6.60 (d, J = 8.8 Hz, 16H), 5.33 (s, 16H), 4.46 (t, J = 5.9 Hz, 16H), 3.30 (t, J = 7.4 Hz, 32H), 2.89 (t, J = 6.4 Hz, 16H), 2.23 (m, 16H), 1.99 (q, 32H), 1.59 (m, 32H), 1.33 (s, 96H), 0.91 (t, J = 6.5 Hz, 48H), 0.30 (t, J = 7.1 Hz, 48H). ^{13}C NMR (75 MHz, $CDCl_3$, ppm): δ 157.7, 150.2, 147.9, 143.9, 143.7, 141.4, 140.1, 135.8, 132.9, 132.3, 132.0, 131.2, 130.7, 130.4, 128.7, 125.9, 125.6, 123.9, 123.3, 123.2, 121.4, 121.2, 119.9, 119.7, 114.9, 111.2, 108.7, 91.5, 91.2, 89.1, 88.1, 62.3, 56.2, 50.9, 48.6, 32.7, 31.7, 29.9, 29.2, 27.2, 26.8, 22.7, 14.1, 8.5. FTMS (ESI): m/z calcd for [M +

H]$^+$, 6919.6245; found, 6919.6563.

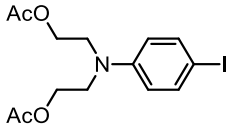

4-iodo-*N*,*N*-diethoxyacetylaniline[84] (31)

A mixture of 4-iodo-*N*,*N*-dihydroxyethylaniline (**30**) (6.76 g, 22 mmol), triethylamine (6.65 g, 66 mmol) and THF (20 mL) was added to a solution of acetyl chloride (4.65 mL, 66 mmol) in THF (20 mL). The mixture was stirred at 35 ℃ for 20 h. Then, 20 mL of water was added dropwise to the mixture slowly. After removal of THF by rotary evaporation, the mixture was extracted with CH_2Cl_2. The organic layer was dried over $MgSO_4$ and concentrated. Purification by chromatography on silica gel eluting with EtOAc/petroleum ether (2:5, v:v) afforded **31** as colourless oil (6.9 g, yield: 80%). ^{1}H NMR (300 MHz, $CDCl_3$, ppm): δ 7.45 (d, J = 9.1 Hz, 2H), 6.53 (d, J = 9.1 Hz, 2H), 4.18 (t, J = 6.3 Hz, 4H), 3.55 (t, J = 6.3 Hz, 4H), 2.02 (s, 6H).

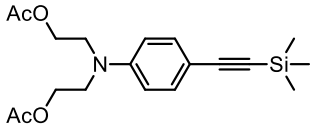

4-trimethylsilylethynyl-*N*,*N*-diethoxyacetylaniline[84] (32)

31 (3.8 g, 9.7 mmol) was dissolved in a trimethylamine/THF mixture (20 mL/20 mL). The solution was degassed by bubbling argon for 20 min. Trimethylsilylacetylene (3.6 g, 5.1 mL, 36 mmol), $(Ph_3P)_2PdCl_2$ (0.24 g, 0.34 mmol) and copper iodide (0.12 g, 0.63 mmol) were added and the reaction was stirred overnight at 55 ℃. After cooling down to room temperature, the solution was filtered and concentrated. The compound was directly used for the next step without further purification. (3.0 g, yield: 85%). ^{1}H NMR (300 MHz, $CDCl_3$, ppm): δ 7.31 (d, J = 9.0 Hz, 2H), 6.63 (d, J = 9.0 Hz, 2H), 4.20 (t, J = 6.2 Hz, 4H), 3.59 (t, J = 6.2 Hz, 4H), 2.01 (s, 6H), 0.20 (s, 9H).

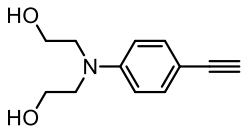

4-ethynyl-*N*,*N*-dihydroxyethylaniline (33)

A solution of **32** (3.0 g, 8.3 mmol) was treated by K_2CO_3 (5.0 g, 36.0 mmol). The mixture was stirred for 2 h at room temperature. Then the mixture was dried over $MgSO_4$ and concentrated. Purification by chromatography on silica gel eluting with methanol/CH_2Cl_2 (1:9, v:v) afforded **33** as a pale yellow solid (1.53 g, yield: 90%). ^{1}H NMR (300 MHz, $CDCl_3$,

ppm): δ 7.35 (d, J = 9.0 Hz, 2H), 6.61 (d, J = 9.0 Hz, 2H), 3.86 (t, J = 4.9 Hz, 4H), 3.59 (t, J = 4.9 Hz, 4H), 2.96 (s, 1H), 2.91 (s, 2H). ^{13}C NMR (75 MHz, $CDCl_3$, ppm): δ 147.9, 133.4, 112.0, 109.5, 84.4, 75.1, 60.7, 55.0.

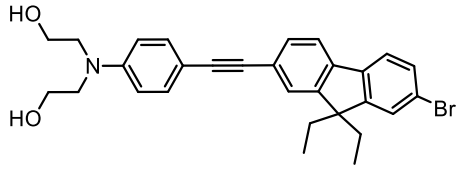

4-(2-(2–bromo-9,9–diethylfluoren-7-yl)ethynyl)-*N*,*N*-dihydroxyethylbenzenamine (34)

34 was prepared according to the procedure described for **14** using 2-bromo-9,9-diethyl-7-iodofluorene (**13**) (0.81 g, 1.89 mmol) and **33** (0.32 g, 1.58 mmol), colorless oil (0.58 g, yield: 73%).^{1}H NMR (300 MHz, $CDCl_3$, ppm): δ 7.60 (d, J = 7.9 Hz, 1H), 7.52 (d, J = 8.5 Hz, 1H), 7.46-7.37 (m, 6H), 6.65 (d, J = 8.9 Hz, 2H), 3.87 (t, J = 4.7 Hz, 4H), 3.61 (t, J = 4.9 Hz, 4H), 2.78 (s, 2H), 1.98 (m, 4H), 0.28 (t, J = 7.3 Hz, 6H). ^{13}C NMR (75 MHz, $CDCl_3$, ppm): δ 152.3, 149.5, 147.6, 140.02, 140.00, 132.8, 130.4, 130.1, 126.2, 125.7, 122.7, 121.2, 121.1, 119.6, 112.0, 110.5, 90.6, 88.4, 60.5, 56.5, 55.2, 32.6, 8.4.

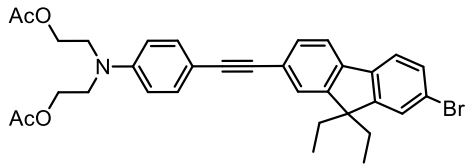

4-(2-(2–bromo-9,9–diethylfluoren-7-yl)ethynyl)-*N*,*N*-diethoxyacetylbenzenamine (35)

A mixture of **34** (0.18 g, 0.36 mmol), triethylamine (0.14 g, 1.43 mmol) and THF (2 mL) was added to a solution of acetyl chloride (0.11 g, 1.43 mmol) in THF (2 mL). The mixture was stirred at 35 ℃ for 20 h. Then the mixture was concentrated under vacuum. Purification by chromatography on silica gel eluting with EtOAc/petroleum ether (2:5, v:v) afforded **35** as a yellowish oil (0.2 g, yield: 95%). ^{1}H NMR (300 MHz, $CDCl_3$, ppm): δ 7.57 (d, J = 8.2 Hz, 1H), 7.49 (d, J = 8.7 Hz, 1H), 7.47-7.38 (m, 6H), 6.71 (d, J = 8.9 Hz, 2H), 4.22 (t, J = 6.1 Hz, 4H), 3.62 (t, J = 6.2 Hz, 4H), 2.02 (s, 6H), 1.99 (m, 4H), 0.29 (s, 6H). ^{13}C NMR (75 MHz, $CDCl_3$, ppm): δ 170.8, 152.3, 149.5, 147.1, 140.0, 139.9, 133.0, 130.5, 130.1, 126.2, 125.7, 122.8, 121.3, 121.2, 119.7, 111.7, 110.9, 90.7, 88.5, 61.2, 60.3, 56.4, 49.4, 32.6, 20.9, 20.8, 14.2, 8.4.

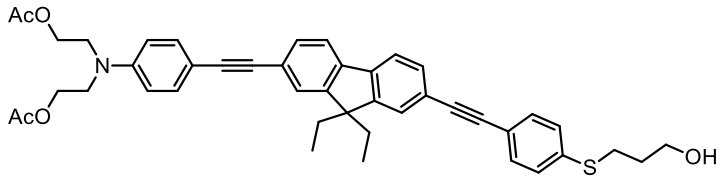

3-((4-((7-((4-(diethoxyacetylamino)phenyl)ethynyl)-9,9-diethylfluoren-2-yl)ethynyl)phenyl)thio)propan-1-ol (36)

36 was prepared according to the procedure described for **20** using **35** (0.66 g, 1.13 mmol) and **19** (0.65 g, 3.38 mmol), light yellow oil was obtained (0.67 g, yield: 85%).[1]H NMR (300 MHz, $CDCl_3$, ppm): δ 7.60 (dd, 2H), 7.48-7.39 (m, 8H), 7.27 (d, *J* = 8.4 Hz, 2H), 6.71 (d, *J* = 9.0 Hz, 2H), 4.22 (t, *J* = 6.1 Hz, 4H), 3.73 (t, *J* = 6.0 Hz, 2H), 3.61 (t, *J* = 6.1 Hz, 4H), 3.04 (t, *J* = 7.1 Hz, 2H), 2.01 (s, 6H), 1.98 (m, 4H), 1.88 (m, 2H), 0.29 (t, *J* = 7.3 Hz, 6H).

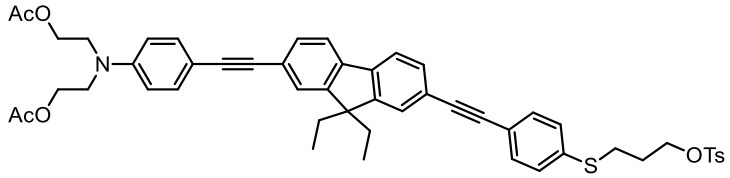

3-((4-((7-((4-(diethoxyacetylamino)phenyl)ethynyl)-9,9-diethylfluoren-2-yl)ethynyl)phenyl)thio)propyl(4-methylbenzenesulfonate) (37)

37 was prepared according to the procedure described for **21** using **36** (0.20 g, 0.29 mmol), light yellow oil was obtained (0.20 g, yield: 82%).[1]H NMR (300 MHz, $CDCl_3$, ppm): δ 7.75 (d, *J* = 8.3 Hz, 2H), 7.62 (dd, 2H), 7.50-7.39 (m, 8H), 7.33 (d, *J* = 8.0 Hz, 2H), 7.21 (d, *J* = 8.4 Hz, 2H), 6.72 (d, *J* = 9.0 Hz, 2H), 4.24 (t, *J* = 6.1 Hz, 4H), 4.14 (t, *J* = 5.9 Hz, 2H), 3.64 (t, *J* = 6.2 Hz, 4H), 2.94 (t, *J* = 7.0 Hz, 2H), 2.43 (s, 3H), 2.03 (s, 6H), 2.02 (m, 4H), 1.95 (m, 2H), 0.30 (t, *J* = 7.3 Hz, 6H).

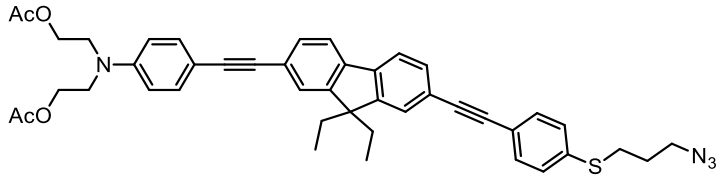

4-((7-((4-((3-azidopropyl)thio)phenyl)ethynyl)-9,9-diethylfluoren-2-yl)ethynyl)-*N*,*N*-diethoxyacetylbenzenamine (38)

38 was prepared according to the procedure described for **22** using **37** (0.20 g, 0.23 mmol), light yellow oil was obtained (0.14 g, yield: 85%). [1]H NMR (300 MHz, $CDCl_3$, ppm): 7.62 (dd, 2H), 7.50-7.44 (m, 6H), 7.39 (d, *J* = 8.9 Hz, 2H), 7.29 (d, *J* = 8.4 Hz, 2H), 6.72 (d, *J* = 9.0 Hz, 2H), 4.24 (t, *J* = 6.2 Hz, 4H), 3.63 (t, *J* = 6.2 Hz, 4H), 3.44 (t, *J* = 6.4 Hz, 2H), 3.02 (t, *J* = 7.0 Hz, 2H), 2.03 (s, 6H), 2.02 (m, 4H), 1.90 (m, 2H), 0.30 (t, *J* = 7.3 Hz, 6H).

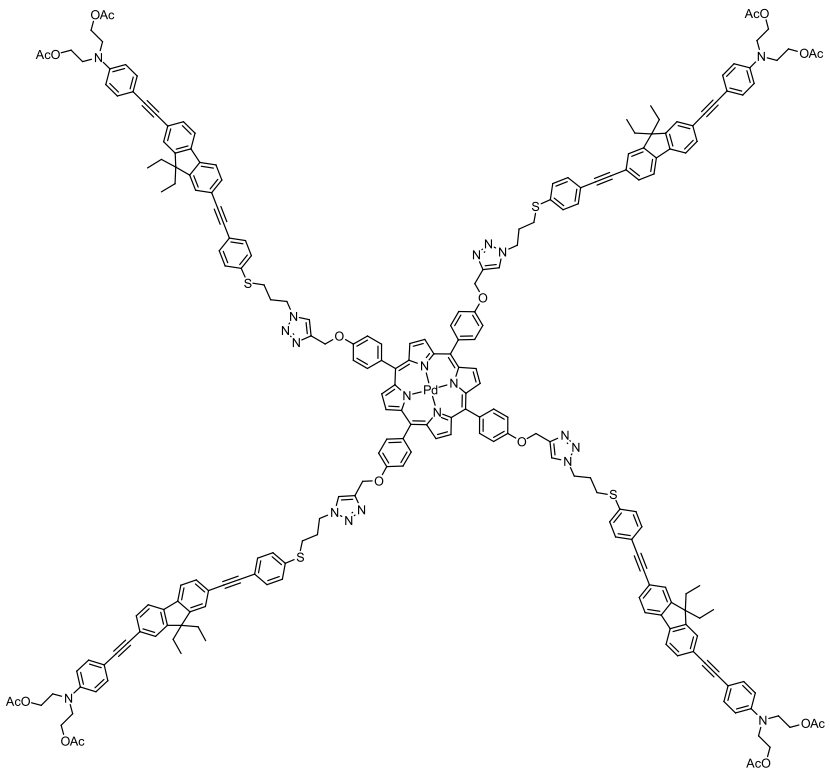

P-1-OAc

Synthesized as described for the preparation of **P-1** starting from **26** (0.032 g, 0.035 mmol) and **38** (0.15 g, 0.207 mmol) in THF (6 mL) with $CuSO_4$ $5H_2O$ (0.052 g, 0.207 mmol) and then sodium L-ascorbate (0.082 g, 0.621 mmol) dissolved in water (2 mL). Chromatography on silica gel eluting with $CHCl_3$/methanol (50:1, v:v) afforded **P-1-OAc** as dark orange-brown viscous oil (0.13 g, yield: 78%). ^{1}H NMR (300 MHz, $CDCl_3$, ppm): δ 8.82 (s, 8H), 8.03 (d, J = 8.4 Hz, 8H), 7.60 (s, 4H), 7.47-7.38 (m, 40H), 7.30-7.24 (m,14H), 6.72 (d, J = 9.0 Hz, 8H), 5.37 (s, 8H), 4.49 (t, J = 6.5 Hz, 8H), 4.24 (t, J = 6.1 Hz, 16H), 3.63 (t, J = 6.1 Hz, 16H), 2.93 (t, J = 6.8 Hz, 8H), 2.25 (m, 8H), 2.03 (s, 24H), 1.95 (m, 16H), 0.24 (t, J = 7.2 Hz, 24H).

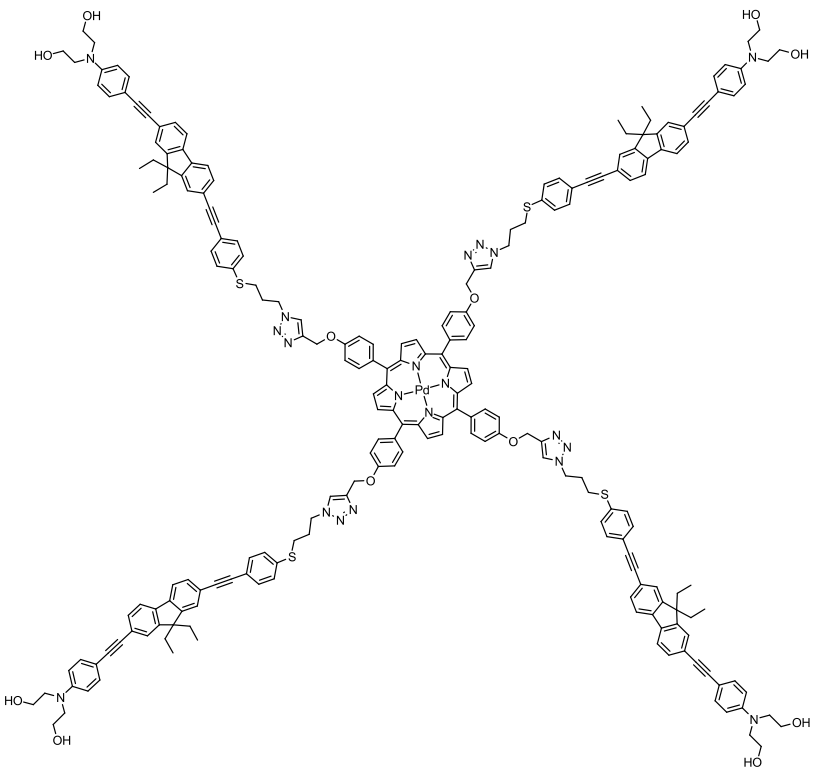

P-1-OH

P-1-OAc (0.13 g, 0.034 mmol) was dissolved in a mixture of methanol and CH_2Cl_2 (2 mL/2 mL). A solution of sodium methoxide (0.34 mL, 1 M in methanol, 0.34 mmol) was added and stirred at room temperature for overnight. Then the mixture was washed with water and concentrated. Chromatography on silica gel eluting with $CHCl_3$/methanol (10:1, v:v) afforded **P-1-OAc** as orange-brown viscous oil (0.11 g, yield: 90%). ^{1}H NMR (300 MHz, $CDCl_3$, ppm): δ 8.74 (s, 8H), 7.98 (d, J = 8.3 Hz, 8H), 7.66 (s, 8H), 7.40-7.16 (m, 54H), 6.59 (d, J = 8.8 Hz, 8H), 5.33 (s, 8H), 4.49 (t, J = 6.3 Hz, 8H), 3.75 (t, J = 4.8 Hz, 16H), 3.52 (t, J = 4.7 Hz, 16H), 2.90 (t, J = 6.7 Hz, 8H), 2.23 (m, 8H), 1.83 (s, 16H), 0.09 (m, 24H).

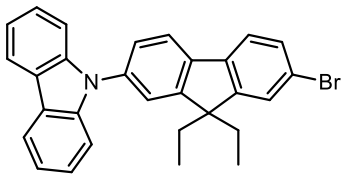

9-(7-bromo-9,9-diethylfluoren-2-yl)-9*H*-carbazole (40)

Under argon, carbazole (**39**) (0.74 g, 4.44 mmol), copper iodide (0.06 g, 0.38 mmol), 1,10-phenanthroline (0.14 g, 0.74 mmol) and K_2CO_3 (1.42 g, 7.40 mmol) were added to a solution of **13** (1.58 g, 3.70 mmol) in dry DMF (16 mL). The mixture was heated to 120 ℃ for 40 h. After removing the solvents, the resulting crude oil was purified by column chromatography on silica using EtOAc/petroleum ether (1:20, v:v) as eluent to afford a white foamy solid (1.0 g, yield: 58%). ^{1}H NMR (300 MHz, $CDCl_3$, ppm): δ 8.17 (d, J = 7.7 Hz, 2H),

7.88 (d, *J* = 7.9 Hz, 1H), 7.63 (d, *J* = 8.5 Hz, 1H), 7.54-7.48 (m, 4H), 7.42-7.40 (m, 4H), 7.32-7.26 (m, 2H), 2.07 (q, *J* = 7.4 Hz, 4H), 0.45 (t, *J* = 7.4 Hz, 6H). ^{13}C NMR (75 MHz, $CDCl_3$, ppm): δ 152.5, 151.5, 141.0, 139.8, 136.9, 130.3, 126.4, 126.1, 126.0, 123.4, 121.9, 121.5, 121.2, 120.9, 120.4, 119.9, 109.7, 56.8, 32.7, 8.6. HR-MS (ESI-QTOF): m/z calcd for $[M + H]^+$, 466.1165; found, 466.1173.

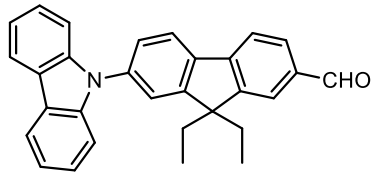

7-(9*H*-carbazol-9-yl)-9,9-diethylfluorene-2-carbaldehyde (41)

A solution of **40** (1.0 g, 2.14 mmol) in anhydrous THF (9 mL) was cooled to -78 ℃ using an acetone dry-ice bath. A solution of n-butyllithium in hexanes (2.5 M, 1.24 mL, 3.1 mmol) was added dropwise at-78 ℃. After 30 min, a solution of dry DMF (0.33 mL) in anhydrous THF (2 mL) was added at -78 ℃. The temperature was allowed to rise to 0 ℃ after 1 h by removing the dry-ice acetone bath. The flask was placed in an ice bath and the solution carefully treated with dilute hydrochloric acid (0.5 mL of concentrated HCl mixed with 4 mL of water). After dilution with toluene (10 mL), the organic phase was washed with water, aqueous sodium bicarbonate, and saturated sodium chloride solution, dried over anhydrous Na_2SO_4, filtered, and concentrated. After removing the solvents, the resulting crude oil was purified by column chromatography on silica using EtOAc/petroleum ether (1:20, v:v) as eluent to afford a yellowish oil (0.62 g, 70%). ^{1}H NMR (300 MHz, $CDCl_3$, ppm): δ 10.1 (s, 1H), 8.16 (d, *J* = 7.7 Hz, 2H), 7.99 (d, *J* = 7.9 Hz, 1H), 7.90 (s, 3H), 7.60-7.55 (m, 2H), 7.42-7.40 (m, 4H), 7.33-7.26 (m, 2H), 2.20-2.00 (m, 4H), 0.43 (t, *J* = 7.4 Hz, 6H). ^{13}C NMR (75 MHz, $CDCl_3$, ppm): δ 192.2, 153.3, 151.0, 147.1, 140.9, 139.1, 138.1, 135.6, 130.7, 126.2, 126.0, 123.5, 123.3, 122.1, 121.9, 120.4, 120.1, 109.7, 56.7, 32.6, 8.6. HR-MS (ESI-QTOF): m/z calcd for $[M + H]^+$, 416.2009; found, 416.2006.

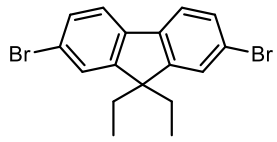

2,7-dibromo-9,9-diethylfluorene (43)

Same as for **13** starting from 2,7-dibromofluorene (**42**) (0.44 g, 1.35 mmol). White solid (0.49 g, yield: 95%). ^{1}H NMR (300 MHz, $CDCl_3$, ppm): δ 7.49 (m, 6H), 2.00 (q, *J* = 7.4 Hz, 4H), 0.31 (t, *J* = 7.3 Hz, 6H). ^{13}C NMR (75 MHz, $CDCl_3$, ppm): δ 151.7, 139.4, 130.2, 126.2, 121.5, 121.1, 56.7, 32.6, 8.4. HR-MS (EI-QTOF): m/z calcd for $[M]^+$, 377.9613; found, 377.9617. CAS number: 197969-58-7.

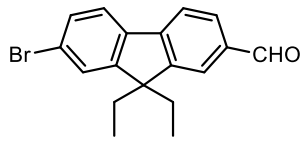

7-bromo-9,9-diethylfluorene-2-carbaldehyde[208] (44)

A solution of **43** (1 g, 2.63 mmol) in anhydrous THF (8 mL) was cooled to −78 ℃ under argon using an acetone dry-ice bath. n-BuLi (1.64 mL, 2.62 mmol., 1.6 M in hexanes) was added dropwise over 20 min. Dry DMF (0.3 mL) was added slowly to the reaction solution after 1 h at −78 ℃. After stirring for 2 h at −78 ℃, the mixture was brought back to room temperature and the reaction was quenched by carefully adding HCl (2 N). The solution was extracted with CH_2Cl_2. The organic layer was dried over Na_2SO_4, filtred, and concentrated. The crude product was purified by chromatography on silica gel eluting with EtOAc/petroleum ether (1:20, v:v) to afford a white solid (0.8 g, yield: 92%).^{1}H NMR (300 MHz, $CDCl_3$, ppm): δ 10.02 (s, 1H), 7.82 (m, 2H), 7.78 (d, J = 8.2, 1H), 7.62 (d, J = 8.6, 1H), 7.48 (m, 2H), 2.03 (m, 4H), 0.26 (t, J = 7.3 Hz, 6H). ^{13}C NMR (75 MHz, $CDCl_3$, ppm): δ 192.1, 153.4, 150.3, 146.7, 138.9, 135.6, 130.6, 130.5, 126.5, 123.2, 123.1, 122.2, 120.0, 56.6, 32.5, 8.4. HR-MS (ESI-QTOF): m/z calcd for $[M + H]^+$, 329.0528; found, 329.0536.

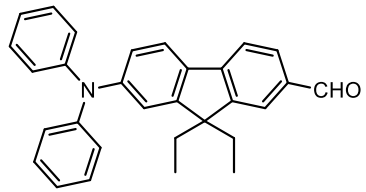

7-(diphenylamino)-9,9-diethylfluorene-2-carbaldehyde[262] (46)

44 (1.7 g, 5.14 mmol), diphenylamine (**45**) (1.3 g, 7.7 mmol) and Cs_2CO_3 (2.51 g, 7.7 mmol) were mixed in toluene (24 mL) under argon. Then $Pd(OAc)_2$ (0.06 g, 0.27 mmol) and P(tBu)$_3$ (130 μL, 0.54 mmol.) were added in the mixture. The final solution was heated at 120 ℃ for 24 h. After cooling back to room temperature, the reaction mixture was washed with water, 1 M HCl, and water again, dried over Na_2SO_4 and concentrated. The crude product was purified by chromatography on silica gel eluting with EtOAc/petroleum ether (1:20, v:v) giving **46** as yellow solid (1.82 g, yield: 85%).^{1}H NMR (300 MHz, $CDCl_3$, ppm): δ 9.99 (s, 1H), 7.78 (m, 2H), 7.70 (d, J = 8.3, 1H), 7.60 (d, J = 8.2, 1H), 7.24 (m, 4H), 7.11 (m, 8H), 1.97 (m, 4H), 0.31 (t, J = 7.3, 6H). ^{13}C NMR (75 MHz, $CDCl_3$, ppm): δ 192.2, 152.9, 150.5, 148.9, 147.9, 147.6, 134.5, 134.3, 130.8, 129.3, 124.4, 123.1, 122.93, 122.91, 121.6, 119.1, 118.2, 56.1, 32.4, 8.5. HR-MS (ESI-QTOF): m/z calcd for $[M + H]^+$, 418.2165; found, 418.2154.

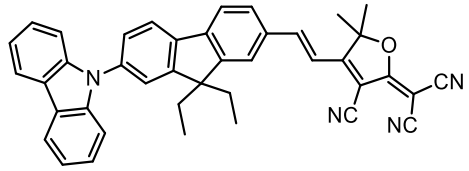

(E)-2-(4-(2-(7-(9*H*-carbazol-9-yl)-9,9-diethylfluoren-2-yl)vinyl)-3-cyano-5,5-dimethylfuran-2(5H)-ylidene)malononitrile (a1)

Under argon, **41** (0.2 g, 0.48 mmol) and 2-(3-cyano-4,5,5-trimethylfuran-2(5*H*)-ylidene)-malononitrile (**47**) (0.1 g, 0.53 mmol) were dissolved in anhydrous ethanol (4 mL). 1 drop of piperidine was added and the solution was stirred at 80 ℃ overnight. After cooling the reaction mixture, the precipitated solid was filtered, washed with cold ethanol and dried to give compound **a1** as a red solid (0.23 g, yield: 80%). ^{1}H NMR (500 MHz, $(CD_3)_2SO$, ppm): δ 8.13 (d, J = 7.6 Hz, 2H), 8.07 (d, J = 7.9 Hz, 1H), 7.96-7.84 (m, 4H), 7.62 (s, 1H), 7.49 (d, J = 7.0 Hz, 1H), 7.33 (t, 2H), 7.25-7.14 (m, 5H), 2.03-2.01 (m, 4H), 1.69 (s, 6H), 0.20 (t, J = 6.75 Hz, 6H). ^{13}C NMR (125 MHz, $(CD_3)_2SO$, ppm): δ 177.7, 175.8, 153.1, 151.3, 148.5, 145.1, 140.7, 139.7, 137.4, 134.2, 130.3, 126.8, 124.3, 123.2, 123.0, 122.2, 121.4, 121.1, 120.6, 115.3, 113.2, 112.4, 111.5, 110.0, 99.8, 99.1, 56.8, 54.6, 32.0, 25.7, 9.0. HR-MS (ESI-QTOF): m/z calcd for $[M + Na]^+$, 619.2468; found, 619.2469.

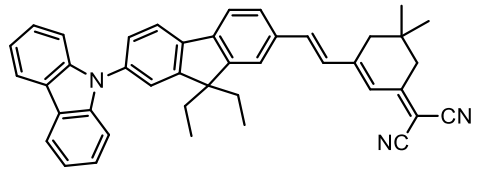

(*E*)-2-(3-(2-(7-(9*H*-carbazol-9-yl)-9,9-diethylfluoren-2-yl)vinyl)-5,5-dimethylcyclohex-2-en-1-ylidene)malononitrile (a2)

Under argon, **41** (0.2 g, 0.48 mmol) and 2-(3,5,5-trimethylcyclohex-2-enylidene)-malononitrile (**51**) (0.1 g, 0.53 mmol) were dissolved in dry acetonitrile (4 mL). 1 drop of piperidine was added and the solution was stirred at 80 ℃ overnight. After cooling the reaction mixture, the solid was filtered, washed with acetonitrile and dried to give **a2** as orange crystals (0.17 g, yield: 61%). ^{1}H NMR (500 MHz, $(CD_3)_2SO$, ppm): δ 8.12 (d, J = 7.7 Hz, 2H), 7.99 (d, J = 7.9 Hz, 1H), 7.83 (d, J = 7.9 Hz, 1H), 7.78 (s, 1H), 7.58-7.56 (m, 2H), 7.45 (d, J = 8.0 Hz, 1H), 7.41 (d, J = 16.0 Hz, 1H), 7.32-7.26 (m, 3H), 7.23 (d, J = 8.0 Hz, 2H), 7.16 (t, 2H), 6.78 (s, 1H), 2.49 (s, 2H), 2.44 (s, 2H), 2.02-1.95 (m, 4H), 0.89 (s, 6H), 0.20 (t, J = 7.2 Hz, 6H). ^{13}C NMR (125 MHz, $(CD_3)_2SO$, ppm): δ 170.8, 156.6, 152.5, 151.0, 142.3, 140.8, 140.2, 138.7, 136.7, 135.9, 129.6, 128.7, 126.8, 126.3, 123.2, 123.0, 122.3, 122.2, 122.1, 121.1, 120.5, 114.4, 113.6, 110.0, 76.4, 56.6, 42.8, 38.6, 32.2, 32.1, 27.9, 9.0. HR-MS (ESI-QTOF): m/z calcd for $[M + H]^+$, 584.3060; found, 584.3067.

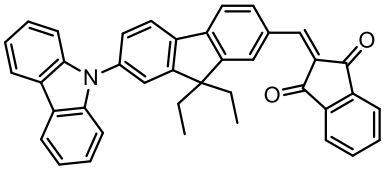

2-((7-(9*H*-carbazol-9-yl)-9,9-diethylfluoren-2-yl)methylene)-1*H*-indene-1,3(2*H*)-dione (a3)

Same procedure as for **a1** starting from **41** (0.2 g, 0.48 mmol) and indane-1,3-dione (0.07g, 0.48 mmol), stirring at 80 ℃ for 3 h. After cooling the reaction mixture, the solid was filtered, washed with acetonitrile and dried to give an orange powder (0.12 g, yield: 48%). ^{1}H NMR (500 MHz, $(CD_3)_2SO$, ppm): δ 8.70 (s, 1H), 8.43 (d, J = 7.8 Hz, 1H), 8.13-8.10 (m, 3H), 8.01 (d, J = 7.9 Hz, 1H), 7.90-7.80 (m, 5H), 7.65 (s, 1H), 7.52 (d, J = 7.9 Hz, 1H), 7.33-7.30 (t, 2H), 7.27 (d, J = 8.0 Hz, 2H), 7.17 (t, 2H), 2.05-2.00 (m, 4H), 0.26 (t, J = 7.2 Hz, 6H). ^{13}C NMR (125 MHz, $(CD_3)_2SO$, ppm): δ 190.1, 189.3, 153.6, 150.6, 146.5, 145.9, 142.5, 140.6, 139.9, 139.5, 137.7, 136.4, 136.2, 134.9, 132.6, 128.9, 126.8, 126.5, 123.6, 123.4, 123.3, 122.2, 121.1, 120.9, 120.6, 110.0, 56.7, 32.0, 9.0. HR-MS (ESI-QTOF): m/z calcd for $[M + H]^+$, 544.2271; found, 544.2287.

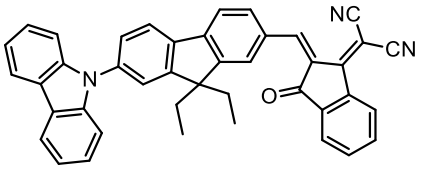

(*Z*)-2-(2-((7-(9*H*-carbazol-9-yl)-9,9-diethylfluoren-2-yl)methylene)-3-oxo-2,3-dihydro-*1H*-inden-1-ylidene)malononitrile (a4)

To a solution of 1,1-dicyanomethylene-3-indanone (**53**) (0.1 g, 0.48 mmol) in absolute ethanol (5 mL), stirred under argon at 60 ℃, **41** (0.2 g, 0.48 mmol) was added portionwise. Stirring and heating was maintained for 3 h. The reaction mixture was then cooled to 0 ℃, and the resulting precipitate was filtered, thoroughly washed with cold ethanol and dried under vacuum to give a dark red solid (0.23 g, yield: 80%). HR-MS (ESI-QTOF): m/z calcd for $[M + Na]^+$, 614.2203; found, 614.2207. It seems not stable in solution.

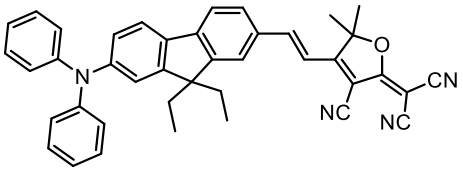

(*E*)-2-(3-cyano-4-(2-(7-(diphenylamino)-9,9-diethylfluoren-2-yl)vinyl)-5,5-dimethylfuran-2(5*H*)-ylidene)malononitrile (a5)

Prepared following the same procedure than for **a1** using **46** (0.2 g, 0.48 mmol) and 2-(3-cyano-4,5,5-trimethylfuran-2(5*H*)-ylidene)malononitrile (**47**) (0.1 g, 0.53 mmol). **a5** was

obtained after filtration as violet crystalline solid (0.25 g, 85%). ^{1}H NMR (500 MHz, $(CD_3)_2SO$, ppm): δ 7.86 (t, 2H), 7.75 (d, J = 7.5Hz, 1H), 7.70-7.66 (m, 2H), 7.18-7.10 (m, 5H), 6.93-6.89 (m, 7H), 6.81 (d, J = 7.8 Hz, 1H), 1.90-1.85 (m, 2H), 1.76-1.72 (m, 2H), 1.66 (s, 6H), 0.13 (t, J = 6.8 Hz, 6H). ^{13}C NMR (125 MHz, $(CD_3)_2SO$, ppm): δ 177.7, 175.8, 152.6, 150.9, 148.8, 148.7, 147.6, 145.9, 135.0, 133.1, 130.6, 130.0, 124.4, 124.0, 123.7, 123.1, 122.6, 120.3, 118.3, 114.5, 113.3, 112.5, 111.5, 99.7, 98.4, 56.2, 54.2, 32.0, 25.7, 8.9. HR-MS (ESI-QTOF): m/z calcd for $[M + Na]^+$, 621.2625; found, 621.2628.

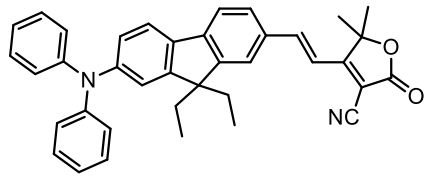

(*E*)-4-(2-(7-(diphenylamino)-9,9-diethylfluoren-2-yl)vinyl)-5,5-dimethyl-2-oxo-2,5-dihydrofuran-3-carbonitrile (a6)

a6 was prepared according to the procedure described for **a2** using **46** (0.2 g, 0.48 mmol) and 4,5,5-trimethyl-2-oxo-2,5-dihydro-3-furancarbonitrile (**52**) (0.07 g, 0.48 mmol), red solid (0.17 g, yield: 64%). ^{1}H NMR (500 MHz, $(CD_3)_2SO$, ppm): δ 7.80 (s, 1H), 7.76 (d, J = 16.3 Hz, 1H), 7.67 (s, 2H), 7.66 (d, J = 8.2 Hz, 1H), 7.18 (t, 4H), 7.12 (d, J = 16.3 Hz, 1H), 6.91-6.88 (m, 7H), 6.81 (d, J = 8.1 Hz, 1H), 1.91-1.83 (m, 2H), 1.78-1.71 (m, 2H), 1.53 (s, 6H), 0.12 (t, J = 7.2 Hz, 6H). ^{13}C NMR (125 MHz, $(CD_3)_2SO$, ppm): δ 177.6, 166.9, 152.3, 150.8, 148.3, 147.6, 146.6, 144.9, 135.3, 133.1, 130.0, 129.8, 124.2, 123.6, 123.4, 123.3, 122.4, 120.2, 118.6, 114.8, 113.5, 96.6, 88.2, 56.2, 32.1, 25.6, 8.9. HR-MS (ESI-QTOF): m/z calcd for $[M + Na]^+$, 573.2512; found, 573.2526.

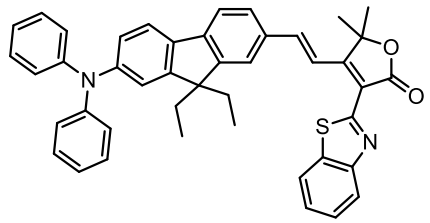

(*E*)-3-(benzo[d]thiazol-2-yl)-4-(2-(7-(diphenylamino)-9,9-diethylfluoren-2-yl)vinyl)-5,5-dimethylfuran-2(5*H*)-one (a7)

a7 was prepared following the procedure described for **a2** from **46** (0.2 g, 0.48 mmol) and 3-(2-benzothiazolyl)-4,5,5-trimethyl-Δ^3-butenolide (**49**) (0.13 g, 0.48 mmol). Obtained after filtration as a red solid (0.30 g, yield: 95%). ^{1}H NMR (500 MHz, $(CD_3)_2SO$, ppm): δ 8.74 (d, J = 17.1 Hz, 1H), 8.06 (d, J = 7.9 Hz, 1H), 7.99 (d, J = 8.1 Hz, 1H), 7.72-7.68 (q, 3H), 7.66 (d, J = 3.3 Hz, 1H), 7.63 (d, J = 5.1 Hz, 1H), 7.49 (t, J = 7.5 Hz, 1H), 7.37 (t, J = 7.4 Hz, 1H), 7.17 (t, J = 7.8 Hz, 4H), 6.95 (s, 1H), 6.91-6.88 (t, 6H), 6.83 (d, J = 8.0 Hz, 1H), 1.89-1.82 (m, 2H), 1.80-1.73 (m, 2H), 1.68 (s, 6H), 0.20 (t, J = 7.2 Hz, 6H). ^{13}C NMR (125 MHz, $(CD_3)_2SO$, ppm): δ 170.0, 165.9, 158.6, 152.9, 152.3, 150.6, 148.1, 147.7, 144.1, 143.9, 135.6, 134.7,

134.6, 130.0, 128.5, 127.2, 126.2, 124.1, 123.7, 123.5, 123.1, 122.9, 122.7, 122.1, 120.4, 119.0, 118.1, 115.7, 86.1, 56.0, 32.2, 27.2, 9.0. HR-MS (ESI-QTOF): m/z calcd for $[M + Na]^+$, 681.2546; found, 681.2546.

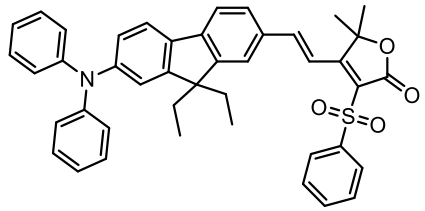

(*E*)-4-(2-(7-(diphenylamino)-9,9-diethylfluoren-2-yl)vinyl)-5,5-dimethyl-3-(phenylsulfonyl)furan-2(5*H*)-one (a8)

a8 was prepared according to the procedure described **a2** from **46** (0.2 g, 0.48 mmol) and 3-(benzenesulfonyl)-4,5,5-trimethyl-2(5*H*) furanone (**50**) (0.13 g, 0.48 mmol). Obtained after filtration as a red solid (0.25 g, yield: 77%). ^{1}H NMR (500 MHz, $(CD_3)_2SO$, ppm): δ 8.02 (d, J = 16.8 Hz, 1H), 7.90 (d, J = 7.3 Hz, 2H), 7.73 (d, J = 7.9 Hz, 1H), 7.69 (d, J = 8.2 Hz, 1H), 7.66 (d, J = 8.4 Hz, 2H), 7.62-7.59 (m, 2H), 7.52 (t, J = 7.8 Hz, 2H), 7.18 (t, J = 7.9 Hz, 4H), 6.93 (s, 1H), 6.92-6.87 (m, 6H), 6.82 (d, J = 8.1 Hz, 1H), 1.86-1.79 (m, 2H), 1.79-1.71 (m, 2H), 1.58 (s, 6H), 0.16 (t, J = 7.3 Hz, 6H). ^{13}C NMR (125 MHz, $(CD_3)_2SO$, ppm): δ 172.3, 164.7, 152.3, 150.6, 148.3, 147.6, 147.0, 144.8, 140.0, 135.3, 134.8, 133.8, 130.0, 129.9, 128.3, 124.2, 124.1, 123.6, 123.4, 122.3, 121.5, 120.4, 118.7, 114.1, 86.1, 56.1, 32.1, 27.0, 8.9. HR-MS (ESI-QTOF): m/z calcd for $[M + Na]^+$, 688.2492; found, 688.2495.

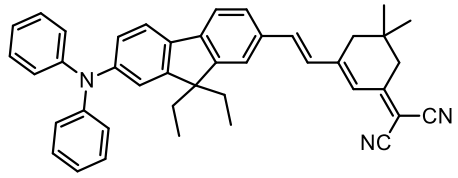

(*E*)-2-(3-(2-(7-(diphenylamino)-9,9-diethylfluoren-2-yl)vinyl)-5,5-dimethylcyclohex-2-en-1-ylidene)malononitrile (a9)

a9 was prepared according to the procedure described for **a2** using **46** (0.2 g, 0.48 mmol) and 2-(3,5,5-trimethylcyclohex-2-enylidene)malononitrile (**51**) (0.1 g, 0.53 mmol). Obtained after filtration as a red crystalline solid (0.13 g, yield: 46%). ^{1}H NMR (500 MHz, $(CD_3)_2SO$, ppm): δ 7.66 (s, 1H), 7.60 (d, J = 8.2 Hz, 1H), 7.60 (d, J = 7.8 Hz, 1H), 7.48 (d, J = 7.8 Hz, 1H), 7.34 (d, J = 16.0 Hz, 1H), 7.23 (d, J = 16.1 Hz, 1H), 7.16 (t, J = 7.8 Hz, 4H), 6.90 (s, 1H), 6.90-6.87 (t,6H), 6.80 (d, J = 8.2 Hz, 1H), 6.74 (s, 1H), 2.47 (s, 2H), 2.42 (s, 2H), 1.86-1.79 (m, 2H), 1.76-1.69 (m, 2H), 0.12 (t, J = 7.2 Hz, 6H). ^{13}C NMR (125 MHz, $(CD_3)_2SO$, ppm): δ 170.7, 156.8, 152.0, 150.6, 147.7, 142.9, 139.0, 135.9, 134.8, 130.0, 129.0, 128.7, 124.0, 123.6, 123.4, 122.7, 122.1, 121.9, 120.1, 119.1, 114.5, 113.7, 76.0, 56.0, 42.8, 38.6, 32.2, 27.9, 8.9. HR-MS (ESI-QTOF): m/z calcd for $[M + H]^+$, 586.3217; found, 586.3204.

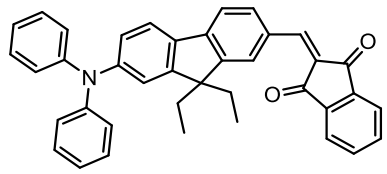

2-((7-(diphenylamino)-9,9-diethylfluoren-2-yl)methylene)-1*H*-indene-1,3(2*H*)-dione (a10)

a10 was prepared according to the procedure described for **a3** using **46** (0.2 g, 0.48 mmol) and indane-1,3-dione (**48**) (0.07 g, 0.48 mmol). Filtration afforded a red crystalline solid (0.20 g, yield: 76%). ^{1}H NMR (500 MHz, $CDCl_3$, ppm): δ 8.57 (s, 1H), 8.26 (d, J = 8.0 Hz, 1H), 7.91-7.87 (m, 2H), 7.86 (s, 1H), 7.70-7.66 (s, 2H), 7.61 (d, J = 8.0 Hz, 1H), 7.52 (d, J = 8.2 Hz, 1H), 7.18-7.14 (m, 4H), 7.03 (m, 4H), 6.98 (s, 1H), 6.95-6.92 (m, 3H), 2.02-1.95 (m, 2H), 1.85-1.78 (m, 2H), 0.30 (t, J = 7.3 Hz, 6H). ^{13}C NMR (125 MHz, $CDCl_3$, ppm): δ 190.8, 189.5, 153.4, 150.3, 149.1, 147.9, 147.6, 147.3, 142.6, 140.0, 135.2, 135.1, 134.9, 134.7, 131.4, 129.3, 128.6, 127.3, 124.6, 123.2, 123.2, 122.7, 121.7, 119.1, 118.0, 56.2, 32.5, 8.6. HR-MS (ESI-QTOF): m/z calcd for $[M + Na]^+$, 568.2247; found, 568.2263.

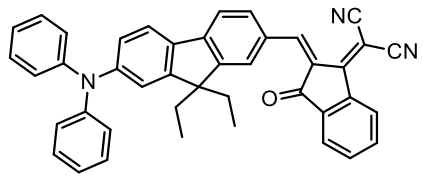

(*Z*)-2-(2-((7-(diphenylamino)-9,9-diethylfluoren-2-yl)methylene)-3-oxo-2,3-dihydro-1*H*-inden-1-ylidene)malononitrile (a11)

a11 was obtained with the same procedure as described for **a4** using **46** (0.2 g, 0.48 mmol) and 1,1-dicyanomethylene-3-indanone (**53**) (0.1 g, 0.48 mmol). Usual work-up gave a violet crystalline solid (0.28 g, yield: 98%). ^{1}H NMR (500 MHz, $CDCl_3$, ppm): δ 8.60 (d, J = 7.7 Hz, 1H), 8.56 (s, 1H), 8.27 (s, 1H), 8.03 (d, J = 8.1 Hz, 1H), 7.84 (d, J = 6.6 Hz, 1H), 7.70-7.63 (m, 2H), 7.59 (d, J = 8.0 Hz, 1H), 7.52 (d, J = 8.2 Hz, 1H), 7.19 (t, J = 7.9 Hz, 4H), 7.04 (d, J = 7.6 Hz, 4H), 6.97-6.91 (m, 4H), 2.00-1.92 (m, 2H), 1.84-1.77 (m, 2H), 0.31 (t, J = 7.3 Hz, 6H). ^{13}C NMR (125 MHz, $CDCl_3$, ppm): δ 186.6, 162.6, 153.6, 150.1, 149.4, 148.7, 148.0, 147.5, 139.6, 137.5, 135.5, 135.2, 134.7, 134.3, 130.7, 129.4, 128.7, 127.8, 125.2, 124.7, 124.2, 123.4, 122.5, 122.0, 118.9, 117.7, 114.5, 114.2, 70.9, 56.2, 32.4, 8.6. HR-MS (ESI-QTOF): m/z calcd for $[M + Na]^+$, 616.2359; found, 616.2379.

2. Preparation of Nanoparticles

Average particle sizes and sizes distribution of the nanoparticles were carried out through Dynamic Light Scattering measurements employing a Zetasizer Nano ZS Particle Sizer and Zeta Potential Analyzer (Zetasizer Nanao ZS). The surface morphologies of nanoparticles

were studied with scanning electron microscopy (SEM) (Zeiss SUPRA 55VP, Germany) and transmission electron microscopy (TOPCON EM-002B). We would like to thank Frédéric CHAPUT (LC ENS, Lyon) for TEM imaging and Frédéric LEROUGE (LC ENS, Lyon) for SEM imaging.

2.1. Preparation of Suspension (AIE)

10^{-3} mol L^{-1} stock solutions of compound in acetone were prepared ahead. Suspension can be prepared directly in the quartz fluorescence cells. For a given water fraction (f_w), as shown in **Table 6-1**, the correct amount of H_2O (V_{water}) was first mixed with the required amount of acetone ($V_{acetone}$) in the cell to give so that the final volume after injection was 2500 μL. 125 μL of stock solution was then quickly injected into the mixture solvent (one shot). The mixture was subsequently shaken several times by hand giving the final suspension with a concentration of 5×10^{-5} mol L^{-1} of compound.

Table 6-1. The corresponding volume of H_2O (V_{water}), acetone ($V_{acetone}$) and stock solutions (V_{stock}) used for preparing the suspension with different water fraction.

f_w	0%	10%	20%	30%	40%	50%	60%	70%	80%	90%
V_{water} (μL)	0	250	500	750	1000	1250	1500	1750	2000	2250
$V_{acetone}$ (μL)	2375	2125	1875	1625	1375	1125	875	625	375	125
V_{stock} (μL)	125	125	125	125	125	125	125	125	125	125

The prepared suspensions were used directly for optical measurements (absorption, fluorescence, two-photon absorption, DLS and SEM). The fluorescence quantum yields of the suspensions were measured using rubrene in methanol (Φ = 27%) as standard.

2.2. Preparation of F127/Nanoaggregates

The same weight of Pluronic F127 and **dye** were dissolved in acetone, and then the solution was quickly injected (one shot) into water under stirring (500 rpm). In a typical experiment, 1 mL of acetone solution containing 0.3 mg of Pluronic F127 and 0.3 mg of **dye** was injected in 10 mL of water. The mixture was then stirred at room temperature overnight to evaporate acetone. The suspension was filtered through a 0.2 μm syringe filter to obtain F127/aggregate suspension. In the case of compound **a9**, the size of the prepared nanoaggregates was determined to be 85 nm by DLS and SEM.

2.2.1. Preparation of Co-assembled F127/Aggregates

For co-loaded F127-nanoaggregate, two dyes (donor and acceptor) were used, with varying weight percent of acceptor. In a typical experiment, 0.5 mL of acetone solution containing

Pluronic F127 (0.14 mg), **a3** (0.14 mg) and **a5** (or **a12**) (with a mass percentage from 0.2% to 4% or 10% of that of **a3**) was injected into water (5 mL) under stirring (500 rpm). The mixture was then stirred at room temperature overnight to evaporate the acetone solvent. The suspension was filtered through a 0.2 μm syringe filter to obtain F127/aggregate suspension. The size of the obtained nanoaggregates was determined by DLS and SEM.

2.2.2. Specificity of the Preparation of F127/Aggregates for *in vivo* imaging

The nanoaggregates suspensions were prepared according to the above protocols and concentrated. Then the sodium chloride, specifically used for preparing physiological serum, was dissolved in the concentrated suspension before injection into mice for imaging. In a typical experiment, 50 mL of the prepared suspension (**a9**-aggregate-F127 or **a3**-1.2%**a5**-NPs) was concentrated to a final volume of 2.5-5 mL ($0.5–1\times10^{-3}$ mol L^{-1}) by evaporating the water at room temperature under stirring. The correct quantity of sodium chloride was dissolved in the concentrated suspension to prepare saline solution (0.90% of NaCl: 9.0 g per litre). The saline suspension was filtered through a 0.2 μm syringe filter before injection. DLS measurement revealed no difference in size after adding sodium chloride.

2.3. Preparation of micelle/silica-encapsulated nanoparticles

2.3.1. Loading Optimization

In a 5 mL round-bottom flask, Pluronic F127 (200 mg) was dissolved in 2-3 mL of dichloromethane. A predetermined amount *m* of dye was added that gave a dye to pluronic F127 weight fraction between 0.05 and 0.30 wt%. The solution was subsequently stirred at room temperature for 40 min to obtain a homogeneous solution. Dichloromethane was then evaporated with a gentle flow of argon to give a film. 0.85 N hydrochloric acid (3.12 mL) was added and the mixture was stirred until a stable and optically transparent solution was obtained. TEOS (360 μL) was then added to the solution and the stirring continued for 105 min. DEDMS (30 μL) was finally added to terminate the particle growth. The final suspension was kept stirring at room temperature for 24 h. The final suspension was kept stirring at room temperature for 24 h. The solution was dialyzed for two days against distilled water to remove hydrochloride as well as unreacted low-molecular weight components, using a membrane bag with a 14,000 cut-off molecular weight. The suspension was then filtered through a 0.2 μm syringe filter to remove large aggregates. The final volume is 3.6 mL.

2.3.2. Estimation of the Encapsulation Efficiency:

The quantity of dye encapsulated into the F127-SiO_2 NPs was estimated by measuring the absorption spectra after dissolution of the dye in DMF with reference to a standard in DMF. The encapsulation efficiency is defined as the ratio of the amount of the dye loaded in the nanoparticles to the total amount of the dye in the feed mixture.

$$\text{Encapsulation efficiency (\%)} = (\text{Abs}_{\text{solution A}} / \text{Abs}_{\text{solution B}}) \times 100 \qquad (6\text{-}1)$$

Solution A: 0.1 mL of the above solution was added to DMF (2.5 mL) in which complete dissolution of the dye occurred.

Solution B: The same amount *m* of dye was dissolved in DMF (3.6 mL). 0.1 mL of this solution was added to 2.5 mL DMF to give the same dilution as above.

2.3.3. dye@F127-SiO2 NPs

Samples for optical measurements and animal imaging experiments were obtained using the same protocol as above using Pluronic F127 (200 mg) and corresponding dye (0.3 mg, 0.15 w/w%). For *in vivo* imaging experiments, the correct quantity of sodium chloride, specifically used for preparing physiological serum, was added directly into the prepared suspension to prepare saline suspension (0.90% of NaCl: 9.0 g per litre). In the case of **a10**@F127-SiO2 NPs, 9 mg of sodium chloride was dissolved in 1 mL of the prepared nanoparticles suspension. The obtained suspension was filtered through a 0.2 µm syringe filter before injection into mice for imaging. DLS measurement revealed no difference in nanoparticle size after adding sodium chloride.

3. Spectroscopy

3.1. General Information

Absorption spectra (UV-Vis) were recorded on a dual beam JASCO 670 spectrometer. Fluorescence spectra were performed on a Horiba Jobin-Yvon Fluorolog-3® spectrofluorimeter equipped with a red-sensitive Hamamatsu R928 photomultiplier tube. Spectra were reference corrected for both the excitation source light intensity variation (lamp and grating) and the emission spectral response (detector and grating). The fluorescence decays are collected using Horiba Jobin Yvon TCSPC Lifetime system with FluoroHub single-photon counting controller module. The decays were analyzed by 'least-squares'. The quality of the exponential fits was evaluated by the goodness of fit (χ^2).

3.2. Fluorescence Quantum Yields Measurement in Solution

Fluorescence quantum yields (Φ_f) are measured in diluted solutions by a comparative method involving the use of standard reference. The standard reference showing similar absorption as that of sample is chosen to ensure that both the reference and the sample can be excited at the same wavelength (λ_{exc}). A list of fluorescence reference can be found in the literature reported by Boens *et al*.[303]

A diluted solution of reference in the appropriate solvent and a diluted solution of sample are prepared, so that absorbance at λ_{exc} and for any wavelength higher than λ_{exc} is below 0.1 in order to minimize re-absorption effects. Absorbance at the excitation wavelength (λ_{exc}) is

measured for both the reference and the sample (A_{ref} and A_S). Fluorescence spectra of both reference and sample are recorded exciting at λ_{exc} and using the same instrument configuration (excitation and emission slits, integration time and emission step). The integrated area under the fluorescence emission spectrum is determined (F_{ref} and F_S). This is repeated for at least five solutions with increasing or decreasing concentrations for reference and sample.

By plotting *F vs A*, straight lines with slopes S_S and S_{ref} are obtained for reference and sample. The fluorescence quantum yield of sample relative to the reference is given by equation:

$$\Phi = \Phi_{ref} \times \frac{S_S}{S_{ref}} \times \left(\frac{n_S}{n_{ref}} \right)^2 \qquad (6\text{-}2)$$

where *n* the refractive index of the solvents and *S* is the slope previously measured. Superscript *ref* and *s* correspond to the reference and the sample respectively.

3.3. Fluorescence Quantum Yields Measurement in Solid

The absolute fluorescence quantum yield (Φ) values of the solid or the nanoaggregate suspension are determined using an integrating sphere collecting all the emission (2π steradians covered with spectralon®) according to Porres *et al.*[304] and de Mello *et al.*[305] The sphere was corrected for both excitation and emission with standard. The principle is illustrated in the **Figure 6-1** below.

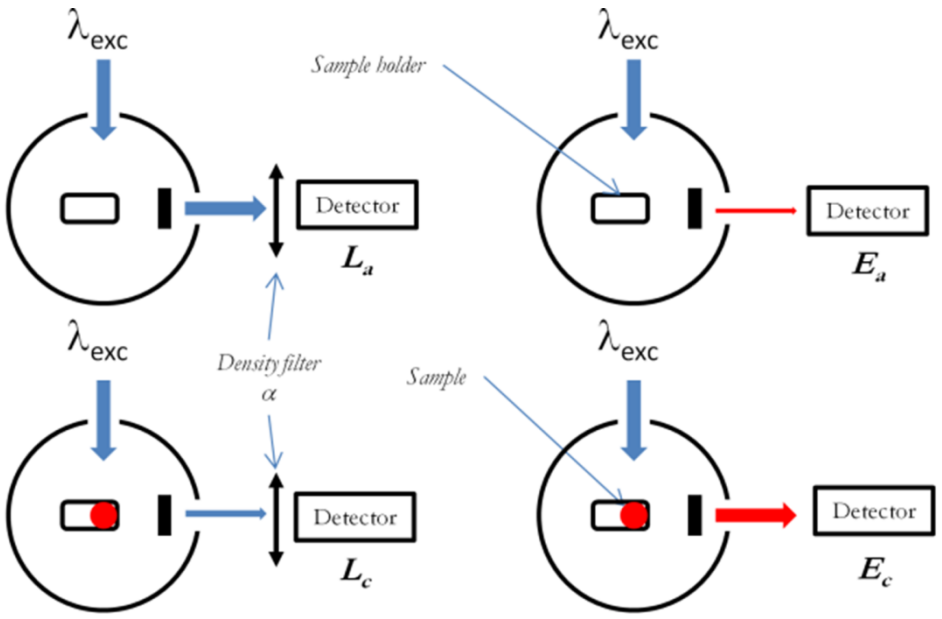

Figure 6-1. Principle of absolute quantum yield determination with an integrated sphere.[304]

For each sample, 4 measurements were made giving four integrated intensities *Ea*, *Ec*, *La* and *Lc* (**Figure 6-1**), which are needed for the determination of quantum yield (Φ) with the equation:

$$\Phi = \frac{E_c - E_a}{\alpha(L_a - L_c)} \tag{6-3}$$

$$\alpha = \frac{L_a - L_c}{L_a} \tag{6-4}$$

- *Ea* is the integrated fluorescence measured with the sphere empty without any sample (background).

- *Ec* is the integrated fluorescence as a result of direct excitation of the sample.

- *La* is the integrated excitation profile with the empty sphere.

- *Lc* is the integrated excitation profile when the sample is in the sphere in the excitation beam.

- α is the absorbance of the sample which is obtained by measuring the integrated excitation bands, *i.e*, the emission signal measured across the excitation wavelength.

All spectra are recorded using the same instrument configuration (excitation and emission monochromatic bandpass or slits opening, integration time). It is however necessary to use a density filter (ND = 0.5%) in order to reduce the intensity without changing the excitation profile when recording *La* and *Lc* to avoid saturation in the detection.

3.4. Two-Photon Absorption Measurement in Solution

Two-photon absorption spectra were obtained by two-photon excited fluorescence measurements using a femtosecond Ti:Sapphire laser in the range 730–960 nm (80 MHz, 140 fs) as the light source. The excitation beam (5 mm diameter) is focalized with a lens (focal length 10 cm) at the middle of the fluorescence cell (10 mm). The fluorescence signal, collected at 90 ° from the excitation beam, was focused into an optical fiber (diameter 600 μm) connected to an Ocean Optics S2000 spectrometer. The incident beam intensity was adjusted to 50 mW in order to ensure an intensity-square dependence of the fluorescence over the entire spectral range of excitation. Detector integration time was fixed to 1 s. Calibration of the spectra was performed by comparison with published 700-900 nm *Coumarin 307*, *Coumarin 510*, *Coumarin 540* and *Fluorescein* two-photon absorption spectra.[23, 306] Measurements were performed for **P-1** and **P-2** in chloroform (2×10^{-5} mol.L^{-1}), dipolar fluorophores in chloroform (1×10^{-4} mol.L^{-1}), nanoaggregate suspensions (5×10^{-5} mol.L^{-1}), co-assembled nanoparticles (5×10^{-5} mol.L^{-1}) and micelle/silica-encapsulated nanoparticles (1.0×10^{-4}–1.5×10^{-4} mol.L^{-1}). Two-photon cross sections σ are given by equation:

$$\sigma = \sigma_{ref} \frac{\Phi_{ref}}{\Phi_s} \frac{c_{ref}}{c_s} \frac{n_{ref}}{n_s} \frac{F_s}{F_{ref}} \tag{6-5}$$

where c is the concentration of the solution, n is the refractive index of the solution, F is the TPEF integral intensities of the solution emitted at the exciting wavelength, and Φ is the fluorescence quantum yield. Superscript *Ref* and *S* stand for reference and sample respectively.

3.5. Multi-Photon Absorption Measurement in Solid

Multi-photon absorption spectra of the compounds in solid state (powder) were measured by the multi-photon-induced fluorescence (MPIF) method for the wavelength range of 1160-1600 nm. A square glass tube (*Vitrocom 8100*, inner cross section is 1 mm x 1mm) filled with powder of the compound is used as sample for the measurements. The square tube was fixed near the focal point of the laser beam (with a 150 nm lens) with a handmade holder to fit the cell holder for 12 mm square standard cell (Thorlab CVH100). The emission in the orthogonal direction was corrected with a lens equipped to CVH100 (with a long-cut filter) and was detected by an Ocean Optics USB-2000FLG spectrometer. The peak intensity of the fluorescence spectrum under the irradiation of the fs pulses of a constant power (5 mW) is recorded and used for plotting the excitation spectrum. The spectra were corrected for a constant excitation "*intensity*" (*i.e.*, corrected with the laser pulse width and the focal length at each wavelength, see below).

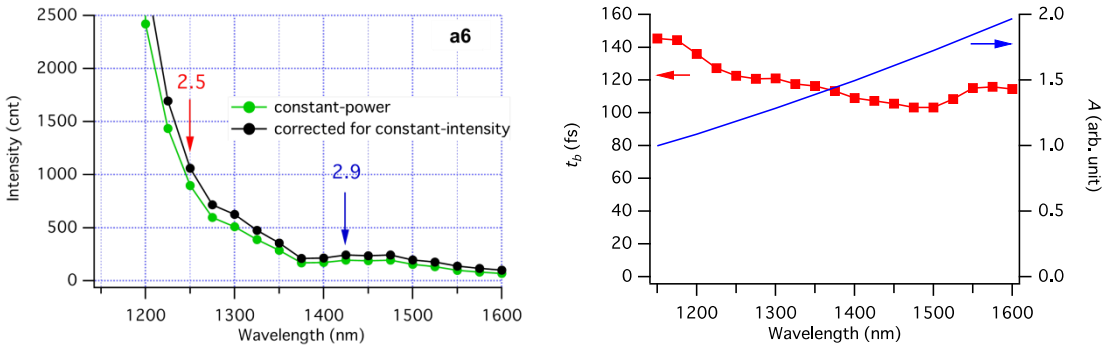

Figure 6-2. Left: comparison of the constant-power (raw data, green) and constant-intensity (corrected, black) spectra. Right: wavelength dependence of the laser pulse width t_p and irradiation area A.

Spectral correction: Because of experimental easiness, we measured at a constant excitation power. However, pulse width of the laser and the irradiation diameter (because of the focus length change) varied depending on the wavelength and may cause the change of the excitation intensity:

$$I = \left(P_{ave} / f\right) / \left(t_p A\right) \tag{6-6}$$

where P_{ave} is average excitation power, f is repetition rate of the pulse, t_p is the pulse width, and A is irradiation area defined by the focal length. The excitation spectra are corrected for t_p and A (because P_{ave} and f are constant), *i.e.*, the original spectra (by a constant excitation power) were divided by t_pA. The constant-power and constant-intensity spectra have no significant difference because the wavelength changes of t_p and A compensated each other (see **Figure 6-2**).

3.6. Phosphorescence Measurement

The sample for the phosphorescence measurement was degassed in a specific designed cuvette, which can be connected to a dual-manifold Schlenk line. The solution was freeze-pump-thaw degassed three times using the designed cuvette prior to the measurement.

The quenching effect of 2PA chromophores (**SS**, **NS**, **NN** and **PH**) on the phosphorescence of palladium porphyrin (**Pd-por-1** and **Pd-por-2**) complexes was studied by the titration of the chromophore into the DMF solution of palladium porphyrin complex. The titration cuvette for the experiment consisted of a cuvette (~3 mL) with a soft stopper, in which two stainless syringe needles were inserted to provide inlet and outlet ports for argon. The inlet needle was immersed in the solution to allow effective bubbling. A solution of palladium porphyrin (2 ml, $OD_{525\ nm}$ = 0.1) in dry DMF was placed inside the cuvette, which was positioned inside a cuvette holder in fluorometer. The solution was degassed by argon until the phosphorescence intensity reached a plateau. The first plateau corresponded to the phosphorescence intensity (I_0) of solution without adding 2PA dye. Phosphorescence spectrum was recorded upon excitation at 525 nm for both **Pd-por-1** and **Pd-por-2**. Then an aliquot of a solution of 2PA dye in dichloromethane (2×10^{-2} mol L^{-1}) was added using a syringe, and argon bubbling was resumed until the phosphorescence intensity reached the next plateau (I). The quenching effect of 2PA chromophores on the phosphorescence of palladium porphyrin complexes was expressed by the ratio of I_0 to I as a function of the concentration of 2PA chromophores.

3.7. Stability Measurements

3.7.1. Fluorescence Stability

The fluorescence stability of **a10**@F127-SiO2 NPs in 1x DPBS was monitored by a fluorometer. Prior to the measurement, a suspension of nanoparticles was prepared in a cuvette. Then the fluorescence intensity of the sample was measured every day for two weeks using the same instrument configuration (excitation and emission slits, integration time and emission step). The fluorescence intensity was further expressed by I/I_0, where I_0 is the fluorescence intensity at maximum wavelength of fresh **a10**@F127-SiO2 NPs suspension and I is that of nanoparticles measured on each day.

3.7.2. Photostability

Photostability of the sample was monitored by recording the fluorescence intensity over time (60 min) under continuous excitation. The photostability was expressed by the ratio of the fluorescence intensity after excitation for a time interval to its initial value as a function of the exposure time.

4. In vivo Imaging

4.1. Cytotoxicity Assays in Cells

Cell culture protocol: HepG2 cells were cultured in Dulbecco's modified Eagle's medium (DMEM) (Invitrogen Corp.) supplemented with 10 % (v/v) fetal bovine serum (Invitrogen Corp.), 50 $U.mL^{-1}$ penicillin, and 50 $\mu g.mL^{-1}$ streptomycin (Invitrogen Corp.) in a humidified incubator containing 5 % CO_2 in air at 37 ℃.

Viability tests: 10.10^3 HepG2 cells were seeded in 100µL of supplemented DMEM in a clear 96 well plate (Corning Costar). After 24h incubation, the medium was removed. Cells were washed with PBS and medium was replaced by an appropriate volume of DMEM (Invitrogen Corp.). A desired volume of stock solutions of **a10**-F127-SiO_2 NPs (40mM in PBS) was added to create a range of concentrations between 0µM and 4mM in 150µL final volume. Cells were then incubated for 24h. The supernatant was subsequently removed and cells were washed with PBS. 100µL of DMEM and 20µL of the MTS reagent (CellTiter 96R AQueous NonRadioactive Cell Proliferation Assay, Promega) were added. Cells were incubated for another 4h period and the absorbance at 490nm was measured with a microplate reader (Multiscan GO Microplate Spectrophotometer, Thermo Scientific). The percentage of viable cells was calculated by dividing the absorbance at a given concentration by the absorbance at 0µM. The given results are the average of 2 independent experiments performed in triplicate.

4.2. *In vivo* Two-Photon Microscopy

Animal model: In accordance with the policy of Clinatec (permit number: B38-185 10 003) and the French legislation, experiments were done in compliance with the European Parliament and the Council Directive of September 22, 2010 (2010/63/EU) on the protection of animals used for scientific purposes. The research involving animals was authorized by the Direction Départementale des Services Vétérinaires de l'Isère – Ministère de l'Agriculture et de la Pêche, and the Ministère de l'Enseignement Supérieur et de la Recherche, France permit number: 2015051914157522_v1 (PI: Boudewijn van der Sanden, PhD, permit number 38 09 40 for animal experiences). All efforts were made to minimize the number of mice used and their suffering during the experimental procedure. Nude mice were housed in ventilated cages

with food and water *ad libitum* in a 12 h light/dark cycle at 22 ± 1 ℃. Nude mice were used directly for two-photon experiments of samples **a9**-aggregate-F127 and **a3**-1.2%**a5**-NPs. For preparing mice bearing tumour for two-photon experiments of **a10**-F127-SiO_2 NPs, human glioma cells (U87MG GFP+, ATCC cell line, Teddington Middlesex, UK) were injected subcutaneously at a concentration of 10^8 cells/ml in the left and right ear of nude mice (BALB/c, Charles River, Écully, France). The total volume of injection is 20 µL: 10 µL cell suspension and 10 µL matrigel® (with growth factors, BD Bioscience, Europe, Erembodegem, Belgium). Mice were used for two-photon experiments of **a10**-F127-SiO_2 NPs at approximately 2–3 weeks after glioma cell injection.

Two-photon microscopy was performed using a Trimscope II (LaVision BioTec, Bielefeld, Germany) equipped with a 16x water-immersion objective (NA 0.8, Nikon, France) and Imspector 2015 software. The excitation wavelengths of the pulsed infrared laser (Insight DeepSea, Spectra-Physics, Evry, France) were 1000 nm for **a9**-aggregate-F127, 900 nm for **a3**-1.2%**a5**-NPs, 1000 nm for **a10**-F127-SiO_2 NPs and 750 nm for the blue nanoparticles. The fluorescence emissions of GFP+ glioma cells and the nanoparticles were epi-collected simultaneously by photomultiplier tubes using the following emission filters: 630/20 (Semrock, USA) for the red nanoparticles, 492/SP (Semrock, USA) for the blue nanoparticles and 542/50 for GFP+ cells.

Image processing was performed with NIH ImageJ software. Vasculature and tumour segmentation were performed using supervised classification with Ilastik software. A 3D model of segmented objects was generated using ImageJ 3D viewer. Texture projection and 3D rendering were performed with Blender (GNU General Public License, Blender Foundation). See legends of figures for details.

Chapter 7. Bibliography

1. Joseph, R. L.; Lakowicz, R., Principles of fluorescence spectroscopy. *Kluwer Academic/Plenum Publishers, New York*: **1999**.

2. Valeur, B.; Berberan-Santos, M. N., Molecular fluorescence: Principles and applications. *John Wiley & Sons*: **2012**.

3. Lakowicz, J. R., Principles of fluorescence spectroscopy. *Springer Science & Business Media*: **2013**.

4. Kobayashi, H.; Ogawa, M.; Alford, R.; Choyke, P. L.; Urano, Y. New strategies for fluorescent probe design in medical diagnostic imaging. *Chemical Reviews* **2009,** *110* (5), 2620-2640.

5. Frangioni, J. *In vivo* near-infrared fluorescence imaging. *Current Opinion in Chemical Biology* **2003,** *7* (5), 626-634.

6. Weissleder, R.; Ntziachristos, V. Shedding light onto live molecular targets. *Nature Medicine* **2003,** *9* (1), 123-128.

7. Licha, K.; Olbrich, C. Optical imaging in drug discovery and diagnostic applications. *Advanced Drug Delivery Reviews* **2005,** *57* (8), 1087-1108.

8. Sevick-Muraca, E. M.; Houston, J. P.; Gurfinkel, M. Fluorescence-enhanced, near infrared diagnostic imaging with contrast agents. *Current Opinion in Chemical Biology* **2002,** *6* (5), 642-650.

9. Graves, E.; Weissleder, R.; Ntziachristos, V. Fluorescence molecular imaging of small animal tumor models. *Current Molecular Medicine* **2004,** *4* (4), 419-430.

10. Ntziachristos, V.; Bremer, C.; Weissleder, R. Fluorescence imaging with near-infrared light: New technological advances that enable *in vivo* molecular imaging. *European Radiology* **2003,** *13* (1), 195-208.

11. Maiman, T. H. Stimulated optical radiation in ruby. *Nature* **1960,** *187*, 493-494.

12. He, G. S.; Tan, L.-S.; Zheng, Q.; Prasad, P. N. Multiphoton absorbing materials: Molecular designs, characterizations, and applications. *Chemical Reviews* **2008,** *108* (4), 1245-1330.

13. Göppert‐Mayer, M. Über elementarakte mit zwei quantensprüngen. *Annalen der Physik* **1931,** *401* (3), 273-294.

14. Kaiser, W.; Garrett, C. Two-photon excitation in CaF_2: Eu^{2+}. *Physical Review Letters* **1961,** *7* (6), 229-231.

15. Ning, Z.; Chen, Z.; Zhang, Q.; Yan, Y.; Qian, S.; Cao, Y.; Tian, H. Aggregation-induced emission (AIE)-active starburst triarylamine fluorophores as potential non-doped red emitters for organic light-emitting diodes and Cl_2 gas chemodosimeter. *Advanced Functional Materials* **2007,** *17* (18), 3799-3807.

16. Pawlicki, M.; Collins, H. A.; Denning, R. G.; Anderson, H. L. Two-photon absorption and the design of two-photon dyes. *Angewandte Chemie International Edition* **2009,** *48* (18), 3244-3266.

17. Sumalekshmy, S.; Fahrni, C. J. Metal-ion-responsive fluorescent probes for two-photon excitation microscopy. *Chemistry of Materials* **2010,** *23* (3), 483-500.

18. Singh, S.; Bradley, L. Three-photon absorption in napthalene crystals by laser excitation. *Physical Review Letters* **1964,** *12* (22), 612-614.

19. Gryczynski, I.; Szmacinski, H.; Lakowicz, J. R. On the possibility of calcium imaging using Indo-1 with three-photon excitation. *Photochemistry and Photobiology* **1995,** *62* (4), 804-808.

20. Rentzepis, P.; Mitschele, C.; Saxman, A. Mesurement of ultrashort laser pulses by three-photon fluorescence. *Applied Physics Letters* **1970,** *17* (3), 122-125.

21. Bhawalkar, J. D.; He, G. S.; Prasad, P. N. Nonlinear multiphoton processes in organic and polymeric materials. *Reports on Progress in Physics* **1996,** *59* (9), 1041-1070.

22. Lin, T.-C.; Chung, S.-J.; Kim, K.-S.; Wang, X.; He, G. S.; Swiatkiewicz, J.; Pudavar, H. E.; Prasad, P. N., Organics and polymers with high two-photon activities and their applications. In *Polymers for Photonics Applications II*, Springer: **2003**; pp 157-193.

23. Xu, C.; Webb, W. W. Measurement of two-photon excitation cross sections of molecular fluorophores with data from 690 to 1050 nm. *Journal of the Optical Society of America B* **1996,** *13* (3), 481-491.

24. Albota, M. A.; Xu, C.; Webb, W. W. Two-photon fluorescence excitation cross sections of biomolecular probes from 690 to 960 nm. *Applied Optics* **1998,** *37* (31), 7352-7356.

25. Sheik-Bahae, M.; Said, A. A.; Wei, T.-H.; Hagan, D. J.; Van Stryland, E. W. Sensitive measurement of optical nonlinearities using a single beam. *IEEE Journal of Quantum Electronics* **1990,** *26* (4), 760-769.

26. Geethakrishnan, T.; Palanisamy, P. Z-scan determination of the third-order optical nonlinearity of a triphenylmethane dye using 633 nm He–Ne laser. *Optics Communications* **2007,** *270* (2), 424-428.

27. Li, D.; Zhang, Q.; Wang, P.; Wu, J.; Kan, Y.; Tian, Y.; Zhou, H.; Yang, J.; Tao, X.; Jiang, M. Studies of the isomerization and photophysical properties of a novel 2, 2': 6', 2"-terpyridine-based ligand and its complexes. *Dalton Transactions* **2011,** *40* (32), 8170-8178.

28. Minsky, M., Microscopy apparatus. Google Patents: **1961**.

29. Denk, W.; Strickler, J. H.; Webb, W. W. Two-photon laser scanning fluorescence microscopy. *Science* **1990,** *248* (4951), 73-76.

30. So, P. T.; Dong, C. Y.; Masters, B. R.; Berland, K. M. Two-photon excitation fluorescence microscopy. *Annual Review of Biomedical Engineering* **2000,** *2* (1), 399-429.

31. Zipfel, W. R.; Williams, R. M.; Webb, W. W. Nonlinear magic: Multiphoton microscopy in the biosciences. *Nature Biotechnology* **2003,** *21* (11), 1369-1377.

32. Andrade, C. D.; Yanez, C. O.; Rodriguez, L.; Belfield, K. D. A series of fluorene-based two-photon absorbing molecules: Synthesis, linear and nonlinear characterization, and bioimaging. *The Journal of Organic Chemistry* **2010,** *75* (12), 3975-3982.

33. Xu, C.; Zipfel, W.; Shear, J. B.; Williams, R. M.; Webb, W. W. Multiphoton fluorescence excitation: New spectral windows for biological nonlinear microscopy. *Proceedings of the National Academy of Sciences* **1996,** *93* (20), 10763-10768.

34. Cahalan, M. D.; Parker, I.; Wei, S. H.; Miller, M. J. Two-photon tissue imaging: Seeing the immune system in a fresh light. *Nature Reviews Immunology* **2002,** *2* (11), 872-880.

35. Diaspro, A. Confocal and two-photon microscopy: Foundations, applications and advances. *Confocal and Two-Photon Microscopy: Foundations, Applications and Advances, by Alberto Diaspro (Editor), pp. 576. ISBN 0-471-40920-0. Wiley-VCH, November 2001.* **2001**, 576.

36. Diaspro, A.; Bianchini, P.; Vicidomini, G.; Faretta, M.; Ramoino, P.; Usai, C. Multi-photon excitation microscopy. *Biomed Eng Online* **2006,** *5*, 36.

37. Helmchen, F.; Denk, W. Deep tissue two-photon microscopy. *Nature Methods* **2005,** *2* (12), 932-940.

38. Piston, D. W. Imaging living cells and tissues by two-photon excitation microscopy. *Trends in Cell Biology* **1999,** *9* (2), 66-69.

39. Rubart, M. Two-photon microscopy of cells and tissue. *Circulation Research* **2004,** *95* (12), 1154-1166.

40. Schenke-Layland, K.; Riemann, I.; Damour, O.; Stock, U. A.; König, K. Two-photon microscopes and *in vivo* multiphoton tomographs—powerful diagnostic tools for tissue engineering and drug delivery. *Advanced Drug Delivery Reviews* **2006,** *58* (7), 878-896.

41. Stosiek, C.; Garaschuk, O.; Holthoff, K.; Konnerth, A. *In vivo* two-photon calcium imaging of neuronal networks. *Proceedings of the National Academy of Sciences* **2003,** *100* (12), 7319-7324.

42. Svoboda, K.; Yasuda, R. Principles of two-photon excitation microscopy and its applications to neuroscience. *Neuron* **2006,** *50* (6), 823-839.

43. Peticolas, W. L.; Goldsborough, J. P.; Rieckhoff, K. Double photon excitation in organic crystals. *Physical Review Letters* **1963,** *10* (2), 43.

44. Luo, S.; Zhang, E.; Su, Y.; Cheng, T.; Shi, C. A review of NIR dyes in cancer targeting and imaging. *Biomaterials* **2011,** *32* (29), 7127-7138.

45. Ni, Y.; Wu, J. Far-red and near infrared BODIPY dyes: Synthesis and applications for fluorescent pH probes and bio-imaging. *Organic & Biomolecular Chemistry* **2014,** *12* (23), 3774-3791.

46. Lu, H.; Mack, J.; Yang, Y.; Shen, Z. Structural modification strategies for the rational design of red/NIR region BODIPYs. *Chemical Society Reviews* **2014,** *43* (13), 4778-4823.

47. Ftouni, H.; Bolze, F.; Nicoud, J.-F. Water-soluble diketopyrrolopyrrole derivatives for two-photon excited fluorescence microscopy. *Dyes and Pigments* **2013,** *97* (1), 77-83.

48. Ftouni, H.; Bolze, F.; de Rocquigny, H.; Nicoud, J.-F. Functionalized two-photon absorbing diketopyrrolopyrrole-based fluorophores for living cells fluorescent microscopy. *Bioconjugate chemistry* **2013,** *24* (6), 942-950.

49. Grzybowski, M.; Hugues, V.; Blanchard-Desce, M.; Gryko, D. T. Two-photon-induced fluorescence in new π-expanded diketopyrrolopyrroles. *Chemistry–A European Journal* **2014,** *20* (39), 12493-12501.

50. Christian, N. A.; Benencia, F.; Milone, M. C.; Li, G.; Frail, P. R.; Therien, M. J.; Coukos, G.; Hammer, D. A. *In vivo* dendritic cell tracking using fluorescence lifetime imaging and near-infrared-emissive polymersomes. *Molecular Imaging and Biology* **2009,** *11* (3), 167-177.

51. Gioux, S.; Choi, H. S.; Frangioni, J. V. Image-guided surgery using invisible near-infrared light: Fundamentals of clinical translation. *Molecular Imaging* **2010,** *9* (5), 237-255.

52. Hutteman, M.; Mieog, J. S. D.; van der Vorst, J. R.; Liefers, G. J.; Putter, H.; Löwik, C. W.; Frangioni, J. V.; van de Velde, C. J.; Vahrmeijer, A. L. Randomized, double-blind comparison of indocyanine green with or without albumin premixing for near-infrared fluorescence imaging of sentinel lymph nodes in breast cancer patients. *Breast cancer research and treatment* **2011,** *127* (1), 163-170.

53. Jaffer, F. A.; Calfon, M. A.; Rosenthal, A.; Mallas, G.; Razansky, R. N.; Mauskapf, A.; Weissleder, R.; Libby, P.; Ntziachristos, V. Two-dimensional intravascular near-infrared fluorescence molecular imaging of inflammation in atherosclerosis and stent-induced vascular injury. *Journal of the American College of Cardiology* **2011,** *57* (25), 2516-2526.

54. Oh, Y.; Quan, Y. H.; Choi, Y.; Kim, C. K.; Kim, H.; Kim, H. K.; Kim, B.-M. Intraoperative combined color and fluorescent images–based sentinel node mapping in the porcine lung: Comparison of indocyanine green with or without albumin premixing. *The Journal of Thoracic and Cardiovascular Surgery* **2013,** *146* (6), 1509-1515.

55. Piao, D.; Pogue, B. W. Rapid near-infrared diffuse tomography for hemodynamic imaging using a low-coherence wideband light source. *Journal of Biomedical Optics* **2007,** *12* (1), 014016.

56. Piao, D.; Xie, H.; Zhang, W.; Krasinski, J. S.; Zhang, G.; Dehghani, H.; Pogue, B. W. Endoscopic, rapid near-infrared optical tomography. *Optics Letters* **2006,** *31* (19), 2876-2878.

57. Rasmussen, J. C.; Tan, I.-C.; Marshall, M. V.; Fife, C. E.; Sevick-Muraca, E. M. Lymphatic imaging in humans with near-infrared fluorescence. *Current Opinion in Biotechnology* **2009,** *20* (1), 74-82.

58. Tearney, G. J.; Waxman, S.; Shishkov, M.; Vakoc, B. J.; Suter, M. J.; Freilich, M. I.; Desjardins, A. E.; Oh, W.-Y.; Bartlett, L. A.; Rosenberg, M. Three-dimensional coronary artery microscopy by intracoronary optical frequency domain imaging. *JACC: Cardiovascular imaging* **2008,** *1* (6), 752-761.

59. Troyan, S. L.; Kianzad, V.; Gibbs-Strauss, S. L.; Gioux, S.; Matsui, A.; Oketokoun, R.; Ngo, L.; Khamene, A.; Azar, F.; Frangioni, J. V. The FLARE™ intraoperative near-infrared fluorescence imaging system: A first-in-human clinical trial in breast cancer sentinel lymph node mapping. *Annals of Surgical Oncology* **2009,** *16* (10), 2943-2952.

60. van der Vorst, J. R.; Hutteman, M.; Gaarenstroom, K. N.; Peters, A. A.; Mieog, J. S. D.; Schaafsma, B. E.; Kuppen, P. J.; Frangioni, J. V.; van de Velde, C. J.; Vahrmeijer, A. L. Optimization of near-infrared fluorescent sentinel lymph node mapping in cervical cancer patients. *International journal of gynecological cancer: official journal of the International Gynecological Cancer Society* **2011,** *21* (8), 1472.

61. Waxman, S.; Dixon, S. R.; L'Allier, P.; Moses, J. W.; Petersen, J. L.; Cutlip, D.; Tardif, J.-C.; Nesto, R. W.; Muller, J. E.; Hendricks, M. J. *In vivo* validation of a catheter-based near-infrared spectroscopy system for detection of lipid core coronary plaques: Initial results of the SPECTACL study. *JACC: Cardiovascular imaging* **2009,** *2* (7), 858-868.

62. Gorka, A. P.; Nani, R. R.; Schnermann Cyanine polyene reactivity: Scope and biomedical applications. *Organic & Biomolecular Chemistry* **2015,** *13*, 7584-7598.

63. Lei, T.; Fernandez-Fernandez, A.; Tang, Y.; Carvajal, D.; Manchanda, R.; Kazmi, S. Z.; McGoron, A. A comparative study of IR-820 and indocyanine green (ICG). *Journal of Nuclear Medicine* **2010,** *51* (supplement 2), 225-225.

64. Prajapati, S. I.; Martinez, C. O.; Bahadur, A. N.; Wu, I. Q.; Zheng, W.; Lechleiter, J. D.; McManus, L. M.; Chisholm, G. B.; Michalek, J. E.; Shireman, P. K. Near-infrared imaging of injured tissue in living subjects using IR-820. *Molecular Imaging* **2009,** *8* (1), 45-54.

65. Prajapati, S. I.; Martinez, C. O.; Abraham, J.; Mccleish, A. T.; Michalek, J. E.; McManus, L. M.; Rubin, B. P.; Shireman, P. K.; Keller, C. Crimson carrier, a long-acting contrast agent for *in vivo* near-infrared imaging of injured and diseased muscle. *Muscle & nerve* **2010,** *42* (2), 245-251.

66. Berezin, M. Y.; Zhan, C.; Lee, H.; Joo, C.; Akers, W. J.; Yazdanfar, S.; Achilefu, S. Two-photon optical properties of near-infrared dyes at 1.55 μm excitation. *The Journal of Physical Chemistry B* **2011,** *115* (39), 11530-11535.

67. Hu, H.; Przhonska, O. V.; Terenziani, F.; Painelli, A.; Fishman, D.; Ensley, T. R.; Reichert, M.; Webster, S.; Bricks, J. L.; Kachkovski, A. D. Two-photon absorption spectra of a near-infrared 2-azaazulene polymethine dye: Solvation and ground-state symmetry breaking. *Physical Chemistry Chemical Physics* **2013,** *15* (20), 7666-7678.

68. Padilha, L. A.; Webster, S.; Przhonska, O. V.; Hu, H.; Peceli, D.; Ensley, T. R.; Bondar, M. V.; Gerasov, A. O.; Kovtun, Y. P.; Shandura, M. P. Efficient two-photon absorbing acceptor-π-acceptor polymethine dyes. *The Journal of Physical Chemistry A* **2010,** *114* (23), 6493-6501.

69. Ahn, H.-Y.; Yao, S.; Wang, X.; Belfield, K. D. Near-infrared-emitting squaraine dyes with high 2PA cross-sections for multiphoton fluorescence imaging. *ACS Applied Materials & Interfaces* **2012,** *4* (6), 2847-2854.

70. Loudet, A.; Burgess, K. BODIPY dyes and their derivatives: Syntheses and spectroscopic properties. *Chemical Reviews* **2007,** *107* (11), 4891-4932.

71. Ulrich, G.; Ziessel, R.; Harriman, A. The chemistry of fluorescent bodipy dyes: Versatility unsurpassed. *Angewandte Chemie International Edition* **2008,** *47* (7), 1184-1201.

72. Zhang, X.; Xiao, Y.; Qi, J.; Qu, J.; Kim, B.; Yue, X.; Belfield, K. D. Long-wavelength, photostable, two-photon excitable BODIPY fluorophores readily modifiable for molecular probes. *The Journal of Organic Chemistry* **2013,** *78* (18), 9153-9160.

73. Patonay, G.; Salon, J.; Sowell, J.; Strekowski, L. Noncovalent labeling of biomolecules with red and near-infrared dyes. *Molecules* **2004,** *9* (3), 40-49.

74. Chung, S.-J.; Zheng, S.; Odani, T.; Beverina, L.; Fu, J.; Padilha, L. A.; Biesso, A.; Hales, J. M.; Zhan, X.; Schmidt, K. Extended squaraine dyes with large two-photon absorption cross-sections. *Journal of the American Chemical Society* **2006,** *128* (45), 14444-14445.

75. Odom, S. A.; Webster, S.; Padilha, L. A.; Peceli, D.; Hu, H.; Nootz, G.; Chung, S.-J.; Ohira, S.; Matichak, J. D.; Przhonska, O. V. Synthesis and two-photon spectrum of a bis(porphyrin)-substituted squaraine. *Journal of the American Chemical Society* **2009,** *131* (22), 7510-7511.

76. Przhonska, O. V.; Webster, S.; Padilha, L. A.; Hu, H.; Kachkovski, A. D.; Hagan, D. J.; Van Stryland, E. W., Two-photon absorption in near-IR conjugated molecules: Design strategy and structure-property relations. In *Advanced Fluorescence Reporters in Chemistry and Biology I*, Springer: 2010; pp 105-147.

77. Iqbal, A.; Cassar, L. 1, 4-Diketopyrrolo [3, 4-c] pyrrole pigments. *Patent EP* **1982,** *98808*.

78. Kaur, M.; Choi, D. H. Diketopyrrolopyrrole: Brilliant red pigment dye-based fluorescent probes and their applications. *Chemical Society Reviews* **2015,** *44* (1), 58-77.

79. Ftouni, H.; Bolze, F. d. r.; de Rocquigny, H.; Nicoud, J.-F. o. Functionalized two-photon absorbing diketopyrrolopyrrole-based fluorophores for living cells fluorescent microscopy. *Bioconjugate chemistry* **2013,** *24* (6), 942-950.

80. Adjili, S.; Favier, A.; Fargier, G.; Thomas, A.; Massin, J.; Monier, K.; Favard, C.; Vanbelle, C.; Bruneau, S.; Peyrieras, N.; Andraud, C.; Muriaux, D.; Charreyre, M. T. Biocompatible photoresistant far-red emitting, fluorescent polymer probes, with near-infrared two-photon absorption, for living cell and zebrafish embryo imaging. *Biomaterials* **2015,** *46*, 70-81.

81. Massin, J.; Charaf-Eddin, A.; Appaix, F.; Bretonnière, Y.; Jacquemin, D.; van der Sanden, B.; Monnereau, C.; Andraud, C. A water soluble probe with near infrared two-photon absorption and polarity-induced fluorescence for cerebral vascular imaging. *Chemical Science* **2013,** *4* (7), 2833.

82. Redon, S.; Massin, J.; Pouvreau, S.; De Meulenaere, E.; Clays, K.; Queneau, Y.; Andraud, C.; Girard-Egrot, A.; Bretonniere, Y.; Chambert, S. Red emitting neutral fluorescent glycoconjugates for membrane optical imaging. *Bioconjugate Chemistry* **2014,** *25* (4), 773-87.

83. Massin, J.; Dayoub, W.; Mulatier, J.-C.; Aronica, C.; Bretonniere, Y.; Andraud, C. Near-infrared solid-state emitters based on isophorone: Synthesis, crystal structure and spectroscopic properties. *Chemistry of Materials* **2010,** *23* (3), 862-873.

84. Mettra, B.; Appaix, F.; Olesiak-Banska, J.; Le Bahers, T.; Leung, A.; Matczyszyn, K.; Samoc, M.; van der Sanden, B.; Monnereau, C.; Andraud, C. A fluorescent polymer probe with high selectivity

towards vascular endothelial cells for and beyond non-invasive two-photon intravital imaging of brain vasculature. *ACS Applied Materials & Interfaces* **2016,** *8* (27), 17047-17059.

85. Chen, G.; Roy, I.; Yang, C.; Prasad, P. N. Nanochemistry and nanomedicine for nanoparticle-based diagnostics and therapy. *Chemical Reviews* **2016,** *116* (5), 2826-85.

86. Sinha, R.; Kim, G. J.; Nie, S.; Shin, D. M. Nanotechnology in cancer therapeutics: Bioconjugated nanoparticles for drug delivery. *Molecular Cancer Therapeutics* **2006,** *5* (8), 1909-1917.

87. Bertrand, N.; Wu, J.; Xu, X.; Kamaly, N.; Farokhzad, O. C. Cancer nanotechnology: The impact of passive and active targeting in the era of modern cancer biology. *Advanced Drug Delivery Reviews* **2014,** *66*, 2-25.

88. Maeda, H. Macromolecular therapeutics in cancer treatment: The EPR effect and beyond. *Journal of Controlled Release* **2012,** *164* (2), 138-144.

89. Choi, H. S.; Ipe, B. I.; Misra, P.; Lee, J. H.; Bawendi, M. G.; Frangioni, J. V. Tissue- and organ-selective biodistribution of NIR fluorescent quantum dots. *Nano Letters* **2009,** *9* (6), 2354-2359.

90. Hardman, R. A toxicologic review of quantum dots: Toxicity depends on physicochemical and environmental factors. *Environmental Health Perspectives* **2006**, 165-172.

91. Jaiswal, J. K.; Simon, S. M. Potentials and pitfalls of fluorescent quantum dots for biological imaging. *Trends in Cell Biology* **2004,** *14* (9), 497-504.

92. Lovrić, J.; Cho, S. J.; Winnik, F. M.; Maysinger, D. Unmodified cadmium telluride quantum dots induce reactive oxygen species formation leading to multiple organelle damage and cell death. *Chemistry & Biology* **2005,** *12* (11), 1227-1234.

93. Quan, L.; Liu, S.; Sun, T.; Guan, X.; Lin, W.; Xie, Z.; Huang, Y.; Wang, Y.; Jing, X. Near-infrared emitting fluorescent BODIPY nanovesicles for *in vivo* molecular imaging and drug delivery. *ACS Applied Materials & Interfaces* **2014,** *6* (18), 16166-16173.

94. Resch-Genger, U.; Grabolle, M.; Cavaliere-Jaricot, S.; Nitschke, R.; Nann, T. Quantum dots versus organic dyes as fluorescent labels. *Nature Methods* **2008,** *5* (9), 763-775.

95. van Veggel, F. C. Near-infrared quantum dots and their delicate synthesis, challenging characterization, and exciting potential applications. *Chemistry of Materials* **2013,** *26* (1), 111-122.

96. Behrendt, J. M.; Wang, Y.; Willcock, H.; Wall, L.; McCairn, M. C.; O'Reilly, R. K.; Turner, M. L. Fluorescent nanoparticles from PEGylated polyfluorenes. *Polymer Chemistry* **2013,** *4* (5), 1333-1336.

97. Fery-Forgues, S. Fluorescent organic nanocrystals and non-doped nanoparticles for biological applications. *Nanoscale* **2013,** *5* (18), 8428-8442.

98. Kandel, P. K.; Fernando, L. P.; Ackroyd, P. C.; Christensen, K. A. Incorporating functionalized polyethylene glycol lipids into reprecipitated conjugated polymer nanoparticles for bioconjugation and targeted labeling of cells. *Nanoscale* **2011,** *3* (3), 1037-1045.

99. Kumar, R.; Ohulchanskyy, T. Y.; Roy, I.; Gupta, S. K.; Borek, C.; Thompson, M. E.; Prasad, P. N. Near-infrared phosphorescent polymeric nanomicelles: Efficient optical probes for tumor imaging and detection. *ACS Applied Materials & Interfaces* **2009,** *1* (7), 1474-1481.

100. Lee, Y.; Hanif, S.; Theato, P.; Zentel, R.; Lim, J.; Char, K. Facile synthesis of fluorescent polymer nanoparticles by covalent modification–nanoprecipitation of amine-reactive ester polymers. *Macromolecular rapid communications* **2015,** *36* (11), 1089-1095.

101. Li, Y.; Liu, J.; Liu, B.; Tomczak, N. Highly emissive PEG-encapsulated conjugated polymer nanoparticles. *Nanoscale* **2012,** *4* (18), 5694-5702.

102. Liu, P.; Li, S.; Jin, Y.; Qian, L.; Gao, N.; Yao, S. Q.; Huang, F.; Xu, Q.-H.; Cao, Y. Red-emitting DPSB-based conjugated polymer nanoparticles with high two-photon brightness for cell membrane imaging. *ACS Applied Materials & Interfaces* **2015,** *7* (12), 6754-6763.

103. Reisch, A.; Klymchenko, A. S. Fluorescent polymer nanoparticles based on dyes: Seeking brighter tools for bioimaging. *Small* **2016,** *12* (15), 1968-1992.

104. Wu, C.; Bull, B.; Szymanski, C.; Christensen, K.; McNeill, J. Multicolor conjugated polymer dots for biological fluorescence imaging. *ACS nano* **2008,** *2* (11), 2415-2423.

105. Wu, C.; Hansen, S. J.; Hou, Q.; Yu, J.; Zeigler, M.; Jin, Y.; Burnham, D. R.; McNeill, J. D.; Olson, J. M.; Chiu, D. T. Design of highly emissive polymer dot bioconjugates for *in vivo* tumor targeting. *Angewandte Chemie International Edition* **2011,** *50* (15), 3430-3434.

106. Yang, Z.; Zheng, S.; Harrison, W. J.; Harder, J.; Wen, X.; Gelovani, J. G.; Qiao, A.; Li, C. Long-circulating near-infrared fluorescence core-cross-linked polymeric micelles: Synthesis, characterization, and dual nuclear/optical imaging. *Biomacromolecules* **2007,** *8* (11), 3422-3428.

107. Zhang, X.; Zhang, X.; Yang, B.; Liu, M.; Liu, W.; Chen, Y.; Wei, Y. Fabrication of aggregation induced emission dye-based fluorescent organic nanoparticles *via* emulsion polymerization and their cell imaging applications. *Polymer Chemistry* **2014,** *5* (2), 399-404.

108. Lv, Y.; Liu, P.; Ding, H.; Wu, Y.; Yan, Y.; Liu, H.; Wang, X.; Huang, F.; Zhao, Y.; Tian, Z. Conjugated polymer-based hybrid nanoparticles with two-photon excitation and near-infrared emission features for fluorescence bioimaging within the biological window. *ACS Applied Materials & Interfaces* **2015,** *7* (37), 20640-20648.

109. Mei, J.; Leung, N. L.; Kwok, R. T.; Lam, J. W.; Tang, B. Z. Aggregation-induced emission: Together we Shine, united we soar! *Chemical Reviews* **2015,** *115* (21), 11718-11940.

110. Hill, T. K.; Abdulahad, A.; Kelkar, S. S.; Marini, F. C.; Long, T. E.; Provenzale, J. M.; Mohs, A. M. Indocyanine green-ioaded nanoparticles for image-guided tumor surgery. *Bioconjugate Chemistry* **2015,** *26* (2), 294-303.

111. Hong, Y. Aggregation-induced emission—fluorophores and applications. *Methods and Applications in Fluorescence* **2016,** *4* (2), 022003.

112. Carreau, A.; Hafny-Rahbi, B. E.; Matejuk, A.; Grillon, C.; Kieda, C. Why is the partial oxygen pressure of human tissues a crucial parameter? Small molecules and hypoxia. *Journal of Cellular and Molecular Medicine* **2011,** *15* (6), 1239-1253.

113. Trayhurn, P. Hypoxia and adipose tissue function and dysfunction in obesity. *Physiological Reviews* **2013,** *93* (1), 1-21.

114. Giordano, F. J. Oxygen, oxidative stress, hypoxia, and heart failure. *The Journal of clinical investigation* **2005,** *115* (3), 500-508.

115. Semenza, G. L. Hypoxia-inducible factor 1 and cardiovascular disease. *Annual Review of Physiology* **2014,** *76*, 39-56.

116. Seidman, L. J.; Pantelis, C.; Keshavan, M. S.; Faraone, S. V.; Goldstein, J. M.; Horton, N. J.; Makris, N.; Peter, F.; Caviness, V. S.; Tsuang, M. T. A review and new report of medial temporal lobe dysfunction as a vulnerability indicator for schizophrenia: A magnetic resonance imaging morphometric family study of the parahippocampal gyrus. *Schizophrenia Bulletin* **2003,** *29* (4), 803-830.

117. Vexler, Z.; Ayus, J.; Roberts, T.; Fraser, C.; Kucharczyk, J.; Arieff, A. Hypoxic and ischemic hypoxia exacerbate brain injury associated with metabolic encephalopathy in laboratory animals. *Journal of Clinical Investigation* **1994,** *93* (1), 256.

118. Höckel, M.; Vaupel, P. Tumor hypoxia: Definitions and current clinical, biologic, and molecular aspects. *Journal of the National Cancer Institute* **2001,** *93* (4), 266-276.

119. Vaupel, P.; Kallinowski, F.; Okunieff, P. Blood flow, oxygen and nutrient supply, and metabolic microenvironment of human tumors: A review. *Cancer Research* **1989,** *49* (23), 6449-6465.

120. Semenza, G. L. Tumor metabolism: Cancer cells give and take lactate. *The Journal of clinical investigation* **2008,** *118* (12), 3835-3837.

121. Horsman, M. R.; Mortensen, L. S.; Petersen, J. B.; Busk, M.; Overgaard, J. Imaging hypoxia to improve radiotherapy outcome. *Nature Reviews Clinical Oncology* **2012,** *9* (12), 674-687.

122. Albiach, C. F.; Moreno, A. C.; Cordón, M. R.; Macías, V. M.; Babiloni, A. B.; Tortajada, I. B.; Iglesias, Á. S.; Muñoz, A. F. Contribution of hypoxia-measuring molecular imaging techniques to radiotherapy planning and treatment. *Clinical and Translational Oncology* **2010,** *12* (1), 22-26.

123. Gaertner, F. C.; Souvatzoglou, M.; Brix, G.; Beer, J. A. Imaging of hypoxia using PET and MRI. *Current Pharmaceutical Biotechnology* **2012,** *13* (4), 552-570.

124. Intes, X.; Chance, B. Non-PET functional imaging techniques: Optical. *Radiologic Clinics of North America* **2005,** *43* (1), 221-234.

125. Krause, B.; Beck, R.; Souvatzoglou, M.; Piert, M. PET and PET/CT studies of tumor tissue oxygenation. *The Quarterly Journal of Nuclear Medicine and Molecular Imaging* **2006,** *50* (1), 28-43.

126. Sasso, M. G.; Quina, F. H.; Bechara, E. J. Ruthenium (II) tris(bipyridyl) ion as a luminescent probe for oxygen uptake. *Analytical biochemistry* **1986,** *156* (1), 239-243.

127. Sinaasappel, M.; Ince, C. Calibration of Pd-porphyrin phosphorescence for oxygen concentration measurements *in vivo*. *Journal of Applied Physiology* **1996,** *81* (5), 2297-2303.

128. Vanderkooi, J. M.; Maniara, G.; Green, T. J.; Wilson, D. F. An optical method for measurement of dioxygen concentration based upon quenching of phosphorescence. *Journal of Biological Chemistry* **1987,** *262* (12), 5476-5482.

129. Rumsey, W. L.; Vanderkooi, J. M.; Wilson, D. F. Imaging of phosphorescence: A novel method for measuring oxygen distribution in perfused tissue. *Science* **1988,** *241* (4873), 1649-1651.

130. Wang, X. F.; Uchida, T.; Coleman, D. M.; Minami, S. A two-dimensional fluorescence lifetime imaging system using a gated image intensifier. *Applied Spectroscopy* **1991,** *45* (3), 360-366.

131. Lakowicz, J. R.; Berndt, K. W. Lifetime-selective fluorescence imaging using an rf phase-sensitive camera. *Review of Scientific Instruments* **1991,** *62* (7), 1727-1734.

132. Holst, G.; Kohls, O.; Klimant, I.; König, B.; Kühl, M.; Richter, T. A modular luminescence lifetime imaging system for mapping oxygen distribution in biological samples. *Sensors and Actuators B: Chemical* **1998,** *51* (1), 163-170.

133. Castellano, F. N.; Lakowicz, J. R. A water-soluble luminescence oxygen sensor. *Photochemistry and Photobiology* **1998,** *67* (2), 179-183.

134. Klimant, I.; Belser, P.; Wolfbeis, O. S. Novel metal—organic ruthenium (II) diimin complexes for use as longwave excitable luminescent oxygen probes. *Talanta* **1994,** *41* (6), 985-991.

135. Jiang, J.; Gao, L.; Zhong, W.; Meng, S.; Yong, B.; Song, Y.; Wang, X.; Bai, C. Development of fiber optic fluorescence oxygen sensor in both *in vitro* and *in vivo* systems. *Respiratory Physiology & Neurobiology* **2008,** *161* (2), 160-166.

136. Ruggi, A.; van Leeuwen, F. W.; Velders, A. H. Interaction of dioxygen with the electronic excited state of Ir (III) and Ru (II) complexes: Principles and biomedical applications. *Coordination Chemistry Reviews* **2011,** *255* (21), 2542-2554.

137. Xu, W.; Kneas, K. A.; Demas, J.; DeGraff, B. Oxygen sensors based on luminescence quenching of metal complexes: Osmium complexes suitable for laser diode excitation. *Analytical Chemistry* **1996,** *68* (15), 2605-2609.

138. Bambot, S. B.; Rao, G.; Romauld, M.; Carter, G. M.; Sipior, J.; Terpetchnig, E.; Lakowicz, J. R. Sensing oxygen through skin using a red diode laser and fluorescence lifetimes. *Biosensors and Bioelectronics* **1995,** *10* (6), 643-652.

139. You, Y.; Nam, W. Photofunctional triplet excited states of cyclometalated Ir (III) complexes: Beyond electroluminescence. *Chemical Society Reviews* **2012,** *41* (21), 7061-7084.

140. Zhao, Q.; Yu, M.; Shi, L.; Liu, S.; Li, C.; Shi, M.; Zhou, Z.; Huang, C.; Li, F. Cationic iridium (III) complexes with tunable emission color as phosphorescent dyes for live cell imaging. *Organometallics* **2010,** *29* (5), 1085-1091.

141. Tobita, S.; Yoshihara, T. Intracellular and *in vivo* oxygen sensing using phosphorescent iridium (III) complexes. *Current Opinion in Chemical Biology* **2016,** *33*, 39-45.

142. You, Y. Phosphorescence bioimaging using cyclometalated Ir (III) complexes. *Current Opinion in Chemical Biology* **2013,** *17* (4), 699-707.

143. Zhang, S.; Hosaka, M.; Yoshihara, T.; Negishi, K.; Iida, Y.; Tobita, S.; Takeuchi, T. Phosphorescent light-emitting iridium complexes serve as a hypoxia-sensing probe for tumor imaging in living animals. *Cancer Research* **2010,** *70* (11), 4490-4498.

144. Yoshihara, T.; Yamaguchi, Y.; Hosaka, M.; Takeuchi, T.; Tobita, S. Ratiometric molecular sensor for monitoring oxygen levels in living cells. *Angewandte Chemie International Edition* **2012,** *51* (17), 4148-4151.

145. Yoshihara, T.; Hosaka, M.; Terata, M.; Ichikawa, K.; Murayama, S.; Tanaka, A.; Mori, M.; Itabashi, H.; Takeuchi, T.; Tobita, S. Intracellular and *in vivo* oxygen sensing using phosphorescent Ir (III) complexes with a modified acetylacetonato ligand. *Analytical Chemistry* **2015,** *87* (5), 2710-2717.

146. Hirakawa, Y.; Yoshihara, T.; Kamiya, M.; Mimura, I.; Fujikura, D.; Masuda, T.; Kikuchi, R.; Takahashi, I.; Urano, Y.; Tobita, S. Quantitating intracellular oxygen tension *in vivo* by phosphorescence lifetime measurement. *Scientific Reports* **2015,** *5*, 17838.

147. Zeng, Y.; Zhang, S.; Jia, M.; Liu, Y.; Shang, J.; Guo, Y.; Xu, J.; Wu, D. Hypoxia-sensitive bis(2-(2'-benzothienyl)pyridinato-*N*, $C^{3'}$)iridium[poly(*n*-butyl cyanoacrylate]/chitosan nanoparticles and their phosphorescence tumor imaging *in vitro* and *in vivo*. *Nanoscale* **2013,** *5* (24), 12633-12644.

148. Zheng, X.; Tang, H.; Xie, C.; Zhang, J.; Wu, W.; Jiang, X. Tracking cancer metastasis *in vivo* by using an iridium-based hypoxia-activated optical oxygen nanosensor. *Angewandte Chemie International Edition* **2015,** *127* (28), 8212-8217.

149. Zheng, X.; Wang, X.; Mao, H.; Wu, W.; Liu, B.; Jiang, X. Hypoxia-specific ultrasensitive detection of tumours and cancer cells *in vivo*. *Nature Communications* **2015,** *6*.

150. Koren, K.; Dmitriev, R. I.; Borisov, S. M.; Papkovsky, D. B.; Klimant, I. Complexes of Ir^{III}-octaethylporphyrin with peptides as probes for sensing cellular O_2. *Chembiochem* **2012,** *13* (8), 1184-1190.

151. Sun, L.; Li, G.; Chen, X.; Chen, Y.; Jin, C.; Ji, L.; Chao, H. Azo-based Iridium (III) complexes as multicolor phosphorescent probes to detect hypoxia in 3D multicellular tumor spheroids. *Scientific reports* **2015,** *5*, 14837.

152. Sun, L.; Chen, Y.; Kuang, S.; Li, G.; Guan, R.; Liu, J.; Ji, L.; Chao, H. Iridium (III) anthraquinone complexes as two-photonphosphorescence probes for mitochondria imaging and tracking under hypoxia. *Chemistry-A European Journal* **2016,** *22*, 8955-8965.

153. Amao, Y.; Asai, K.; Okura, I. Oxygen sensing based on lifetime of photoexcited triplet state of platinum porphyrin-polystyrene film using time-resolved spectroscopy. *Journal of Porphyrins and Phthalocyanines* **2000,** *4* (3), 292-299.

154. Feng, Y.; Cheng, J.; Zhou, L.; Zhou, X.; Xiang, H. Ratiometric optical oxygen sensing: A review in respect of material design. *Analyst* **2012,** *137* (21), 4885-4901.

155. Papkovsky, D. B.; Dmitriev, R. I. Biological detection by optical oxygen sensing. *Chemical Society Reviews* **2013,** *42* (22), 8700-8732.

156. Wilson, D. F.; Gomi, S.; Pastuszko, A.; Greenberg, J. H. Microvascular damage in the cortex of cat brain from middle cerebral artery occlusion and reperfusion. *Journal of Applied Physiology* **1993,** *74* (2), 580-589.

157. Torres Filho, I.; Intaglietta, M. Microvessel PO_2 measurements by phosphorescence decay method. *American Journal of Physiology-Heart and Circulatory Physiology* **1993,** *265* (4), H1434-H1438.

158. Wilson, D. F.; Pastuszko, A.; DiGiacomo, J. E.; Pawlowski, M.; Schneiderman, R.; Delivoria-Papadopoulos, M. Effect of hyperventilation on oxygenation of the brain cortex of newborn piglets. *Journal of Applied Physiology* **1991,** *70* (6), 2691-2696.

159. Borisov, S. M.; Zenkl, G.; Klimant, I. Phosphorescent platinum (II) and palladium (II) complexes with azatetrabenzoporphyrins—new red laser diode-compatible indicators for optical oxygen sensing. *ACS Applied Materials & Interfaces* **2010,** *2* (2), 366-374.

160. Finikova, O. S.; Aleshchenkov, S. E.; Briñas, R. P.; Cheprakov, A. V.; Carroll, P. J.; Vinogradov, S. A. Synthesis of symmetrical tetraaryltetranaphtho[2, 3]porphyrins. *The Journal of Organic Chemistry* **2005,** *70* (12), 4617-4628.

161. Finikova, O. S.; Cheprakov, A. V.; Beletskaya, I. P.; Carroll, P. J.; Vinogradov, S. A. Novel versatile synthesis of substituted tetrabenzoporphyrins. *The Journal of Organic Chemistry* **2004,** *69* (2), 522-535.

162. Finikova, O. S.; Cheprakov, A. V.; Carroll, P. J.; Vinogradov, S. A. Novel route to functionalized tetraaryltetra[2, 3]naphthaloporphyrins *via* oxidative aromatization. *The Journal of Organic Chemistry* **2003,** *68* (19), 7517-7520.

163. Niedermair, F.; Borisov, S. M.; Zenkl, G.; Hofmann, O. T.; Weber, H. r.; Saf, R.; Klimant, I. Tunable phosphorescent NIR oxygen indicators based on mixed benzo- and naphthoporphyrin complexes. *Inorganic Chemistry* **2010,** *49* (20), 9333-9342.

164. Sommer, J. R.; Farley, R. T.; Graham, K. R.; Yang, Y.; Reynolds, J. R.; Xue, J.; Schanze, K. S. Efficient near-infrared polymer and organic light-emitting diodes based on electrophosphorescence from (tetraphenyltetranaphtho[2, 3]porphyrin) platinum (II). *ACS Applied Materials & Interfaces* **2009,** *1* (2), 274-278.

165. Sommer, J. R.; Shelton, A. H.; Parthasarathy, A.; Ghiviriga, I.; Reynolds, J. R.; Schanze, K. S. Photophysical properties of near-infrared phosphorescent π-extended platinum porphyrins. *Chemistry of Materials* **2011,** *23* (24), 5296-5304.

166. Samaroo, D.; Soll, C. E.; Todaro, L. J.; Drain, C. M. Efficient microwave-assisted synthesis of amine-substituted tetrakis(pentafluorophenyl) porphyrin. *Organic Letters* **2006,** *8* (22), 4985-4988.

167. Dmitriev, R. I.; Kondrashina, A. V.; Koren, K.; Klimant, I.; Zhdanov, A. V.; Pakan, J. M.; McDermott, K. W.; Papkovsky, D. B. Small molecule phosphorescent probes for O_2 imaging in 3D tissue models. *Biomaterials Science* **2014,** *2* (6), 853-866.

168. Pollak, K. W.; Leon, J. W.; Fréchet, J. M.; Maskus, M.; Abruña, H. D. Effects of dendrimer generation on site isolation of core moieties: Electrochemical and fluorescence quenching studies with metalloporphyrin core dendrimers. *Chemistry of Materials* **1998,** *10* (1), 30-38.

169. Vinogradov, S. A.; Lo, L. W.; Wilson, D. F. Dendritic polyglutamic porphyrins: Probing porphyrin protection by oxygen-dependent quenching of phosphorescence. *Chemistry–A European Journal* **1999,** *5* (4), 1338-1347.

170. Dunphy, I.; Vinogradov, S. A.; Wilson, D. F. Oxyphor R2 and G2: Phosphors for measuring oxygen by oxygen-dependent quenching of phosphorescence. *Analytical biochemistry* **2002,** *310* (2), 191-198.

171. Rozhkov, V.; Wilson, D.; Vinogradov, S. Phosphorescent Pd porphyrin-dendrimers: Tuning core accessibility by varying the hydrophobicity of the dendritic matrix. *Macromolecules* **2002,** *35* (6), 1991-1993.

172. Esipova, T. V.; Karagodov, A.; Miller, J.; Wilson, D. F.; Busch, T. M.; Vinogradov, S. A. Two new "protected" oxyphors for biological oximetry: Properties and application in tumor imaging. *Analytical Chemistry* **2011,** *83* (22), 8756-8765.

173. Lebedev, A. Y.; Cheprakov, A. V.; Sakadzic, S.; Boas, D. A.; Wilson, D. F.; Vinogradov, S. A. Dendritic phosphorescent probes for oxygen imaging in biological systems. *ACS Applied Materials & Interfaces* **2009,** *1* (6), 1292-1304.

174. Thompson, J. K.; Peterson, M. R.; Freeman, R. D. Single-neuron activity and tissue oxygenation in the cerebral cortex. *Science* **2003,** *299* (5609), 1070-1072.

175. Wilson, D. F.; Lee, W. M.; Makonnen, S.; Apreleva, S.; Vinogradov, S. A., Oxygen pressures in the interstitial space of skeletal muscle and tumors *in vivo*. In *Oxygen Transport to Tissue XXIX*, Springer: **2008**; pp 53-62.

176. Pirow, R.; Bäumer, C.; Paul, R. Crater landscape: Two-dimensional oxygen gradients in the circulatory system of the microcrustacean Daphnia magna. *Journal of Experimental Biology* **2004,** *207* (25), 4393-4405.

177. Poole, D. C.; Behnke, B. J.; Mcdonough, P.; Mcallister, R. M.; Wilson, D. F. Measurement of muscle microvascular oxygen pressures: Compartmentalization of phosphorescent probe. *Microcirculation* **2004,** *11* (4), 317-326.

178. Dmitriev, R. I.; Zhdanov, A. V.; Nolan, Y. M.; Papkovsky, D. B. Imaging of neurosphere oxygenation with phosphorescent probes. *Biomaterials* **2013,** *34* (37), 9307-9317.

179. Fercher, A.; Borisov, S. M.; Zhdanov, A. V.; Klimant, I.; Papkovsky, D. B. Intracellular O_2 sensing probe based on cell-penetrating phosphorescent nanoparticles. *ACS nano* **2011,** *5* (7), 5499-5508.

180. Kondrashina, A. V.; Dmitriev, R. I.; Borisov, S. M.; Klimant, I.; O'Brien, I.; Nolan, Y. M.; Zhdanov, A. V.; Papkovsky, D. B. A phosphorescent nanoparticle-based probe for sensing and imaging of (intra) cellular oxygen in multiple detection modalities. *Advanced Functional Materials* **2012,** *22* (23), 4931-4939.

181. Wu, C.; Bull, B.; Christensen, K.; McNeill, J. Ratiometric single-nanoparticle oxygen sensors for biological imaging. *Angewandte Chemie International Edition* **2009,** *48* (15), 2741-2745.

182. Xiang, H.; Zhou, L.; Feng, Y.; Cheng, J.; Wu, D.; Zhou, X. Tunable fluorescent/phosphorescent platinum (II) porphyrin–fluorene copolymers for ratiometric dual emissive oxygen sensing. *Inorganic Chemistry* **2012,** *51* (9), 5208-5212.

183. Zhao, Z.; He, B.; Tang, B. Z. Aggregation-induced emission of siloles. *Chemical Science* **2015,** *6* (10), 5347-5365.

184. Wang, X. D.; Stolwijk, J. A.; Lang, T.; Sperber, M.; Meier, R. J.; Wegener, J.; Wolfbeis, O. S. Ultra-small, highly stable, and sensitive dual nanosensors for imaging intracellular oxygen and pH in cytosol. *Journal of the American Chemical Society* **2012,** *134* (41), 17011-17014.

185. Drobizhev, M.; Karotki, A.; Kruk, M.; Rebane, A. Resonance enhancement of two-photon absorption in porphyrins. *Chemical Physics Letters* **2002,** *355* (1), 175-182.

186. Kruk, M.; Karotki, A.; Drobizhev, M.; Kuzmitsky, V.; Gael, V.; Rebane, A. Two-photon absorption of tetraphenylporphin free base. *Journal of Luminescence* **2003,** *105* (1), 45-55.

187. Mik, E. G.; van Leeuwen, T. G.; Raat, N. J.; Ince, C. Quantitative determination of localized tissue oxygen concentration *in vivo* by two-photon excitation phosphorescence lifetime measurements. *Journal of Applied Physiology* **2004,** *97* (5), 1962-1969.

188. Esipova, T. V.; Vinogradov, S. A. Synthesis of phosphorescent asymmetrically π-extended porphyrins for two-photon applications. *The Journal of Organic Chemistry* **2014,** *79* (18), 8812-8825.

189. Dichtel, W. R.; Serin, J. M.; Edder, C.; Fréchet, J. M.; Matuszewski, M.; Tan, L.-S.; Ohulchanskyy, T. Y.; Prasad, P. N. Singlet oxygen generation *via* two-photon excited FRET. *Journal of the American Chemical Society* **2004,** *126* (17), 5380-5381.

190. Oar, M. A.; Serin, J. M.; Dichtel, W. R.; Fréchet, J. M.; Ohulchanskyy, T. Y.; Prasad, P. N. Photosensitization of singlet oxygen *via* two-photon-excited fluorescence resonance energy transfer in a water-soluble dendrimer. *Chemistry of Materials* **2005,** *17* (9), 2267-2275.

191. Briñas, R. P.; Troxler, T.; Hochstrasser, R. M.; Vinogradov, S. A. Phosphorescent oxygen sensor with dendritic protection and two-photon absorbing antenna. *Journal of the American Chemical Society* **2005,** *127* (33), 11851-11862.

192. Finikova, O. S.; Lebedev, A. Y.; Aprelev, A.; Troxler, T.; Gao, F.; Garnacho, C.; Muro, S.; Hochstrasser, R. M.; Vinogradov, S. A. Oxygen microscopy by two-photon-excited phosphorescence. *Chemphyschem* **2008,** *9* (12), 1673-1679.

193. Finikova, O. S.; Troxler, T.; Senes, A.; DeGrado, W. F.; Hochstrasser, R. M.; Vinogradov, S. A. Energy and electron transfer in enhanced two-photon-absorbing systems with triplet cores. *The Journal of Physical Chemistry A* **2007,** *111* (30), 6977-6990.

194. Roussakis, E.; Spencer, J. A.; Lin, C. P.; Vinogradov, S. A. Two-photon antenna-core oxygen probe with enhanced performance. *Analytical Chemistry* **2014,** *86* (12), 5937-5945.

195. Sakadžić, S.; Roussakis, E.; Yaseen, M. A.; Mandeville, E. T.; Srinivasan, V. J.; Arai, K.; Ruvinskaya, S.; Devor, A.; Lo, E. H.; Vinogradov, S. A. Two-photon high-resolution measurement of partial pressure of oxygen in cerebral vasculature and tissue. *Nature Methods* **2010,** *7* (9), 755-759.

196. Spencer, J. A.; Ferraro, F.; Roussakis, E.; Klein, A.; Wu, J.; Runnels, J. M.; Zaher, W.; Mortensen, L. J.; Alt, C.; Turcotte, R.; Yusuf, R.; Cote, D.; Vinogradov, S. A.; Scadden, D. T.; Lin, C. P. Direct measurement of local oxygen concentration in the bone marrow of live animals. *Nature* **2014,** *508* (7495), 269-73.

197. Lecoq, J.; Parpaleix, A.; Roussakis, E.; Ducros, M.; Houssen, Y. G.; Vinogradov, S. A.; Charpak, S. Simultaneous two-photon imaging of oxygen and blood flow in deep cerebral vessels. *Nature Medicine* **2011,** *17* (7), 893-898.

198. Parpaleix, A.; Houssen, Y. G.; Charpak, S. Imaging local neuronal activity by monitoring PO_2 transients in capillaries. *Nature Medicine* **2013,** *19* (2), 241-246.

199. Rostovtsev, V. V.; Green, L. G.; Fokin, V. V.; Sharpless, K. B. A stepwise huisgen cycloaddition process: Copper (I)-catalyzed regioselective “ligation” of azides and terminal alkynes. *Angewandte Chemie* **2002,** *114* (14), 2708-2711.

200. Tornøe, C. W.; Christensen, C.; Meldal, M. Peptidotriazoles on solid phase: [1, 2, 3]-triazoles by regiospecific copper (I)-catalyzed 1, 3-dipolar cycloadditions of terminal alkynes to azides. *The Journal of organic chemistry* **2002,** *67* (9), 3057-3064.

201. Eastwood, D.; Gouterman, M. Porphyrins: Xviii. Luminescence of (Co), (Ni), Pd, Pt complexes. *Journal of Molecular Spectroscopy* **1970,** *35* (3), 359-375.

202. Antipas, A.; Gouterman, M. Porphyrins. 44. Electronic states of cobalt, nickel, rhodium, and palladium complexes. *Journal of the American Chemical Society* **1983,** *105* (15), 4896-4901.

203. Weinkauf, J. R.; Cooper, S. W.; Schweiger, A.; Wamser, C. C. Substituent and solvent effects on the hyperporphyrin spectra of diprotonated tetraphenylporphyrins. *The Journal of Physical Chemistry A* **2003,** *107* (18), 3486-3496.

204. Şen, P.; Hirel, C.; Andraud, C.; Aronica, C.; Bretonnière, Y.; Mohammed, A.; Ågren, H.; Minaev, B.; Minaeva, V.; Baryshnikov, G.; Lee, H.-H.; Duboisset, J.; Lindgren, M. Fluorescence and FTIR spectra analysis of *trans*-A_2B_2-substituted di- and tetra-phenyl porphyrins. *Materials* **2010,** *3* (8), 4446-4475.

205. Yao, S.; Belfield, K. D. Synthesis of two-photon absorbing unsymmetrical branched chromophores through direct tris(bromomethylation) of fluorene. *The Journal of Organic Chemistry* **2005,** *70* (13), 5126-5132.

206. Chen, C.-Y.; Tian, Y.; Cheng, Y.-J.; Young, A. C.; Ka, J.-W.; Jen, A. K.-Y. Two-photon absorbing block copolymer as a nanocarrier for porphyrin: Energy transfer and singlet oxygen generation in micellar aqueous solution. *Journal of the American Chemical Society* **2007,** *129* (23), 7220-7221.

207. Mikroyannidis, J. A.; Fenenko, L.; Adachi, C. Synthesis and photophysical characteristics of 2, 7-fluorenevinylene-based trimers and their electroluminescence. *The Journal of Physical Chemistry B* **2006,** *110* (41), 20317-20326.

208. Kannan, R.; He, G. S.; Yuan, L.; Xu, F.; Prasad, P. N.; Dombroskie, A. G.; Reinhardt, B. A.; Baur, J. W.; Vaia, R. A.; Tan, L.-S. Diphenylaminofluorene-based two-photon-absorbing chromophores with various π-electron acceptors. *Chemistry of Materials* **2001,** *13* (5), 1896-1904.

209. Mongin, O.; Porrès, L.; Charlot, M.; Katan, C.; Blanchard-Desce, M. Synthesis, fluorescence, and two-photon absorption of a series of elongated rodlike and banana-shaped quadrupolar fluorophores: A comprehensive study of structure–property relationships. *Chemistry–A European Journal* **2007,** *13* (5), 1481-1498.

210. Gallavardin, T.; Armagnat, C.; Maury, O.; Baldeck, P. L.; Lindgren, M.; Monnereau, C.; Andraud, C. An improved singlet oxygen sensitizer with two-photon absorption and emission in the biological transparency window as a result of ground state symmetry-breaking. *Chemical Communications* **2012,** *48* (11), 1689-1691.

211. Marder, S. R.; Torruellas, W. E.; Blanchard-Desce, M.; Ricci, V.; Stegeman, G. I.; Gilmour, S.; Bredas, J.-L.; Li, J.; Bublitz, G. U.; Boxer, S. G. Large molecular third-order optical nonlinearities in polarized carotenoids. *Science* **1997,** *276* (5316), 1233-1236.

212. Wang, Z.; Yan, L.; Zhang, L.; Chen, Y.; Li, H.; Zhang, J.; Zhang, Y.; Li, X.; Xu, B.; Fu, X.; Sun, Z.; Tian, W. Ultra bright red AIE dots for cytoplasm and nuclear imaging. *Polymer Chemistry* **2014,** *5* (24), 7013-7020.

213. Finikova, O. S.; Chen, P.; Ou, Z.; Kadish, K. M.; Vinogradov, S. A. Dynamic quenching of porphyrin triplet states by two-photon absorbing dyes: Towards two-photon-enhanced oxygen nanosensors. *Journal of Photochemistry and Photobiology A: Chemistry* **2008,** *198* (1), 75-84.

214. Hecht, S.; Vladimirov, N.; Frechet, J. M. Encapsulation of functional moieties within branched star polymers: Effect of chain length and solvent on site isolation. *Journal of the American Chemical Society* **2001,** *123* (1), 18-25.

215. Rietveld, I. B.; Kim, E.; Vinogradov, S. A. Dendrimers with tetrabenzoporphyrin cores: Near infrared phosphors for *in vivo* oxygen imaging. *Tetrahedron* **2003,** *59* (22), 3821-3831.

216. Das, R.; Mukhopadhyay, B. Use of 'click chemistry' for the synthesis of carbohydrate-porphyrin dendrimers and their multivalent approach toward lectin sensing. *Tetrahedron Letters* **2016,** *57* (16), 1775-1781.

217. Fathalla, M.; Li, S.-C.; Diebold, U.; Alb, A.; Jayawickramarajah, J. Water-soluble nanorods self-assembled *via* pristine C_{60} and porphyrin moieties. *Chemical Communications* **2009,** (28), 4209-4211.

218. Fathalla, M.; Neuberger, A.; Li, S.-C.; Schmehl, R.; Diebold, U.; Jayawickramarajah, J. Straightforward self-assembly of porphyrin nanowires in water: Harnessing adamantane/β-cyclodextrin interactions. *Journal of the American Chemical Society* **2010,** *132* (29), 9966-9967.

219. Kushwaha, D.; Tiwari, V. K. Click chemistry inspired synthesis of glycoporphyrin dendrimers. *The Journal of Organic Chemistry* **2013,** *78* (16), 8184-8190.

220. Leonardi, M. J.; Topka, M. R.; Dinolfo, P. H. Efficient förster resonance energy transfer in 1,2,3-triazole linked BODIPY-Zn(II) meso-tetraphenylporphyrin donor–acceptor arrays. *Inorganic Chemistry* **2012,** *51* (24), 13114-13122.

221. Liu, Y.; Ke, C.-F.; Zhang, H.-Y.; Cui, J.; Ding, F. Complexation-induced transition of nanorod to network aggregates: Alternate porphyrin and cyclodextrin arrays. *Journal of the American Chemical Society* **2008,** *130* (2), 600-605.

222. Wu, K.; Guo, J.; Wang, C. Dispersible and discrete metalloporphyrin-based CMP nanoparticles enabling colorimetric detection and quantitation of gaseous SO_2. *Chemical Communications* **2013,** *50* (6), 695-697.

223. Tidwell, T. T. Sulfur trioxide–pyridine. *e-EROS Encyclopedia of Reagents for Organic Synthesis* **2001**, DOI: 10.1002/047084289X.rs139m.

224. Ding, D.; Li, K.; Liu, B.; Tang, B. Z. Bioprobes based on AIE fluorogens. *Accounts of Chemical Research* **2013,** *46* (11), 2441-2453.

225. Hu, R.; Leung, N. L.; Tang, B. Z. AIE macromolecules: Syntheses, structures and functionalities. *Chemical Society Reviews* **2014,** *43* (13), 4494-562.

226. Birks, J. B. Photophysics of aromatic molecules. **1970**.

227. Ding, D.; Li, K.; Qin, W.; Zhan, R.; Hu, Y.; Liu, J.; Tang, B. Z.; Liu, B. Conjugated polymer amplified far-red/near-infrared fluorescence from nanoparticles with aggregation-induced emission characteristics for targeted *in vivo* imaging. *Advanced Health Materials* **2013,** *2* (3), 500-7.

228. Zhao, Z.; Geng, J.; Chang, Z.; Chen, S.; Deng, C.; Jiang, T.; Qin, W.; Lam, J. W. Y.; Kwok, H. S.; Qiu, H.; Liu, B.; Tang, B. Z. A tetraphenylethene-based red luminophor for an efficient non-doped electroluminescence device and cellular imaging. *Journal of Materials Chemistry* **2012,** *22* (22), 11018.

229. Luo, J.; Xie, Z.; Lam, J. W.; Cheng, L.; Chen, H.; Qiu, C.; Kwok, H. S.; Zhan, X.; Liu, Y.; Zhu, D. Aggregation-induced emission of 1-methyl-1, 2, 3, 4, 5-pentaphenylsilole. *Chemical Communications* **2001,** (18), 1740-1741.

230. Hong, Y.; Lam, J. W.; Tang, B. Z. Aggregation-induced emission: Phenomenon, mechanism and applications. *Chemical Communications* **2009,** (29), 4332-4353.

231. Hong, Y.; Lam, J. W.; Tang, B. Z. Aggregation-induced emission. *Chemical Society Reviews* **2011,** *40* (11), 5361-5388.

232. Mei, J.; Hong, Y.; Lam, J. W.; Qin, A.; Tang, Y.; Tang, B. Z. Aggregation-induced emission: The whole is more brilliant than the parts. *Advanced Materials* **2014,** *26* (31), 5429-79.

233. Li, K.; Yamamoto, M.; Chan, S. J.; Chiam, M. Y.; Qin, W.; Wong, P. T.; Yim, E. K.; Tang, B. Z.; Liu, B. Organic nanoparticles with aggregation-induced emission for tracking bone marrow stromal cells in the rat ischemic stroke model. *Chemical Communications* **2014,** *50* (96), 15136-9.

234. Shao, A.; Xie, Y.; Zhu, S.; Guo, Z.; Zhu, S.; Guo, J.; Shi, P.; James, T. D.; Tian, H.; Zhu, W. H. Far-red and near-IR AIE-active fluorescent organic nanoprobes with enhanced tumor-targeting efficacy: Shape-specific effects. *Angewandte Chemie International Edition* **2015,** *54* (25), 7275-80.

235. Zhang, J.; Chen, R.; Zhu, Z.; Adachi, C.; Zhang, X.; Lee, C. S. Highly stable near-infrared fluorescent organic nanoparticles with a large stokes shift for noninvasive long-term cellular imaging. *ACS Applied Materials & Interfaces* **2015,** *7* (47), 26266-74.

236. Liang, J.; Tang, B. Z.; Liu, B. Specific light-up bioprobes based on AIEgen conjugates. *Chemical Society Reviews* **2015,** *44* (10), 2798-811.

237. Yan, L.; Zhang, Y.; Xu, B.; Tian, W. Fluorescent nanoparticles based on AIE fluorogens for bioimaging. *Nanoscale* **2016,** *8* (5), 2471-87.

238. Yuan, Y.; Feng, G.; Qin, W.; Tang, B. Z.; Liu, B. Targeted and image-guided photodynamic cancer therapy based on organic nanoparticles with aggregation-induced emission characteristics. *Chemical Communications* **2014,** *50* (63), 8757-60.

239. Zhao, Q.; Li, K.; Chen, S.; Qin, A.; Ding, D.; Zhang, S.; Liu, Y.; Liu, B.; Sun, J. Z.; Tang, B. Z. Aggregation-induced red-NIR emission organic nanoparticles as effective and photostable fluorescent probes for bioimaging. *Journal of Materials Chemistry* **2012,** *22* (30), 15128.

240. Li, K.; Qin, W.; Ding, D.; Tomczak, N.; Geng, J.; Liu, R.; Liu, J.; Zhang, X.; Liu, H.; Liu, B.; Tang, B. Z. Photostable fluorescent organic dots with aggregation-induced emission (AIE dots) for noninvasive long-term cell tracing. *Scientific Reports* **2013,** *3*, 1150.

241. Li, K.; Zhu, Z.; Cai, P.; Liu, R.; Tomczak, N.; Ding, D.; Liu, J.; Qin, W.; Zhao, Z.; Hu, Y.; Chen, X.; Tang, B. Z.; Liu, B. Organic dots with aggregation-induced emission (AIE dots) characteristics for dual-color cell tracing. *Chemistry of Materials* **2013,** *25* (21), 4181-4187.

242. Geng, J.; Li, K.; Qin, W.; Ma, L.; Gurzadyan, G. G.; Tang, B. Z.; Liu, B. Eccentric loading of fluorogen with aggregation-induced emission in PLGA matrix increases nanoparticle fluorescence quantum yield for targeted cellular imaging. *Small* **2013,** *9* (11), 2012-2019.

243. Ding, D.; Mao, D.; Li, K.; Wang, X.; Qin, W.; Liu, R.; Chiam, D. S.; Tomczak, N.; Yang, Z.; Tang, B. Z. Precise and long-term tracking of adipose-derived stem cells and their regenerative capacity *via* superb bright and stable organic nanodots. *ACS nano* **2014,** *8* (12), 12620-12631.

244. Geng, J.; Zhu, Z.; Qin, W.; Ma, L.; Hu, Y.; Gurzadyan, G. G.; Tang, B. Z.; Liu, B. Near-infrared fluorescence amplified organic nanoparticles with aggregation-induced emission characteristics for *in vivo* imaging. *Nanoscale* **2014,** *6* (2), 939-945.

245. Qian, J.; Zhu, Z.; Qin, A.; Qin, W.; Chu, L.; Cai, F.; Zhang, H.; Wu, Q.; Hu, R.; Tang, B. Z.; He, S. High-order non-linear optical effects in organic luminogens with aggregation-induced emission. *Advanced Materials* **2015,** *27* (14), 2332-2339.

246. Wang, D.; Qian, J.; Qin, W.; Qin, A.; Tang, B. Z.; He, S. Biocompatible and photostable AIE dots with red emission for *in vivo* two-photon bioimaging. *Scientific Reports* **2014,** *4*, 4279.

247. Qin, W.; Ding, D.; Liu, J.; Yuan, W. Z.; Hu, Y.; Liu, B.; Tang, B. Z. Biocompatible nanoparticles with aggregation-induced emission characteristics as far-red/near-infrared fluorescent bioprobes for *in vitro* and *in vivo* imaging applications. *Advanced Functional Materials* **2012,** *22* (4), 771-779.

248. Geng, J.; Li, K.; Qin, W.; Tang, B. Z.; Liu, B. Red-emissive chemiluminescent nanoparticles with aggregation-induced emission characteristics for *in vivo* hydrogen peroxide imaging. *Particle & Particle Systems Characterization* **2014,** *31* (12), 1238-1243.

249. Jiang, T.; Qu, Y.; Li, B.; Gao, Y.; Hua, J. Tetraphenylethene end-capped [1,2,5]thiadiazolo[3,4-c]pyridine with aggregation-induced emission and large two-photon absorption cross-sections. *RSC Advances* **2015,** *5* (2), 1500-1506.

250. Hang, Y.; Yang, L.; Qu, Y.; Hua, J. A new diketopyrrolopyrrole-based near-infrared (NIR) fluorescent biosensor for BSA detection and AIE-assisted bioimaging. *Tetrahedron Letters* **2014,** *55* (51), 6998-7001.

251. Gao, Y.; Feng, G.; Jiang, T.; Goh, C.; Ng, L.; Liu, B.; Li, B.; Yang, L.; Hua, J.; Tian, H. Biocompatible nanoparticles based on diketo-pyrrolo-pyrrole (DPP) with aggregation-induced red/NIR emission for *in vivo* two-photon fluorescence imaging. *Advanced Functional Materials* **2015,** *25* (19), 2857-2866.

252. Wang, X.; Morales, A. R.; Urakami, T.; Zhang, L.; Bondar, M. V.; Komatsu, M.; Belfield, K. D. Folate receptor-targeted aggregation-enhanced near-IR emitting silica nanoprobe for one-photon *in vivo* and two-photon *ex vivo* fluorescence bioimaging. *Bioconjugate Chemistry* **2011,** *22* (7), 1438-1450.

253. Massin, J.; Dayoub, W.; Mulatier, J.-C.; Aronica, C.; Bretonnière, Y.; Andraud, C. Near-infrared solid-state emitters based on isophorone: Synthesis, crystal structure and spectroscopic properties. *Chemistry of Materials* **2011,** *23* (3), 862-873.

254. Ipuy, M. Développement de nouveaux chromophores basés sur le groupement tricyanofurane pour différentes applications en biologie. Lyon, École normale supérieure, **2014**.

255. Ipuy, M.; Liao, Y.-Y.; Jeanneau, E.; Baldeck, P. L.; Bretonnière, Y.; Andraud, C. Solid state red biphotonic excited emission from small dipolar fluorophores. *Journal of Materials Chemistry C* **2016,** *4* (4), 766-779.

256. Singh, A.; Lim, C.-K.; Lee, Y.-D.; Maeng, J.-h.; Lee, S.; Koh, J.; Kim, S. Tuning solid-state fluorescence to the near-infrared: A combinatorial approach to discovering molecular nanoprobes for biomedical imaging. *ACS Applied Materials & Interfaces* **2013,** *5* (18), 8881-8888.

257. Wang, L.; Shen, Y.; Zhu, Q.; Xu, W.; Yang, M.; Zhou, H.; Wu, J.; Tian, Y. Systematic study and imaging application of aggregation-induced emission of ester-isophorone derivatives. *The Journal of Physical Chemistry C* **2014,** *118* (16), 8531-8540.

258. Ho, C.-L.; Wong, W.-Y.; Yao, B.; Xie, Z.; Wang, L.; Lin, Z. Synthesis, characterization, photophysics and electrophosphorescent applications of phosphorescent platinum cyclometalated complexes with 9-arylcarbazole moieties. *Journal of Organometallic Chemistry* **2009,** *694* (17), 2735-2749.

259. Weber, G.; Farris, F. J. Synthesis and spectral properties of a hydrophobic fluorescent probe: 6-propionyl-2-(dimethylamino)naphthalene. *Biochemistry* **1979,** *18* (14), 3075-3078.

260. Kucherak, O. A.; Didier, P.; Mély, Y.; Klymchenko, A. S. Fluorene analogues of Prodan with superior fluorescence brightness and solvatochromism. *The Journal of Physical Chemistry Letters* **2010,** *1* (3), 616-620.

261. Stewart, D. J.; Dalton, M. J.; Swiger, R. N.; Fore, J. L.; Walker, M. A.; Cooper, T. M.; Haley, J. E.; Tan, L.-S. Symmetry- and solvent-dependent photophysics of fluorenes containing donor and acceptor groups. *The Journal of Physical Chemistry A* **2014,** *118* (28), 5228-5237.

262. Morales, A. R.; Frazer, A.; Woodward, A. W.; Ahn-White, H.-Y.; Fonari, A.; Tongwa, P.; Timofeeva, T.; Belfield, K. D. Design, synthesis, and structural and spectroscopic studies of push–pull two-photon absorbing chromophores with acceptor groups of varying strength. *The Journal of Organic Chemistry* **2013,** *78* (3), 1014-1025.

263. Zheng, Z.; Yu, Z.; Yang, M.; Jin, F.; Zhang, Q.; Zhou, H.; Wu, J.; Tian, Y. Substituent group variations directing the molecular packing, electronic structure, and aggregation-induced emission property of isophorone derivatives. *The Journal of Organic Chemistry* **2013,** *78* (7), 3222-3234.

264. Chan, C. Y.; Zhao, Z.; Lam, J. W.; Liu, J.; Chen, S.; Lu, P.; Mahtab, F.; Chen, X.; Sung, H. H.; Kwok, H. S. Efficient light emitters in the solid state: Synthesis, aggregation-induced emission, electroluminescence, and sensory properties of luminogens with benzene cores and multiple triarylvinyl peripherals. *Advanced Functional Materials* **2012,** *22* (2), 378-389.

265. Flammer, J.; Konieczka, K.; Flammer, A. J. The primary vascular dysregulation syndrome: Implications for eye diseases. *The EPMA Journal* **2013,** *4* (1), 14.

266. Ormseth, M. J.; Oeser, A. M.; Cunningham, A.; Bian, A.; Shintani, A.; Solus, J.; Tanner, S. B.; Stein, C. M. Reversing vascular dysfunction in rheumatoid arthritis: Improved augmentation index but not endothelial function with peroxisome proliferator–activated receptor γ agonist therapy. *Arthritis & Rheumatology* **2014,** *66* (9), 2331-2338.

267. Rahman, M.; Xie, D.; Feldman, H. I.; Go, A. S.; He, J.; Kusek, J. W.; Lash, J.; Miller III, E. R.; Ojo, A.; Pan, Q.; Seliger, S. L.; Steigerwalt, S.; Townsend, R. R. Association between chronic kidney disease progression and cardiovascular disease: Results from the CRIC study. *American Journal of Nephrology* **2014,** *40* (5), 399-407.

268. Goel, S.; Duda, D. G.; Xu, L.; Munn, L. L.; Boucher, Y.; Fukumura, D.; Jain, R. K. Normalization of the vasculature for treatment of cancer and other diseases. *Physiological Reviews* **2011,** *91* (3), 1071-1121.

269. Ameer-Beg, S.; Barber, P. R.; Hodgkiss, R. J.; Locke, R. J.; Newman, R. G.; Tozer, G. M.; Vojnovic, B.; Wilson, J. Application of multiphoton steady state and lifetime imaging to mapping of tumor vascular architecture *in vivo*. *Proceedings of SPIE - The International Society for Optical Engineering* **2002,** *4620* (Multiphoton Microscopy in the Biomedical Sciences II), 85-95.

270. Han, Z.; Fu, A.; Wang, H.; Diaz, R.; Geng, L.; Onishko, H.; Hallahan, D. E. Noninvasive assessment of cancer response to therapy. *Nature Medicine* **2008,** *14*, 343-349.

271. Proulx, S. T.; Luciani, P.; Alitalo, A.; Mumprecht, V.; Christiansen, A. J.; Huggenberger, R.; Leroux, J.-C.; Detmar, M. Non-invasive dynamic near-infrared imaging and quantification of vascular leakage *in vivo*. *Angiogenesis* **2013,** *16* (3), 525-540.

272. Hilderbrand, S. A.; Weissleder, R. Near-infrared fluorescence: Application to *in vivo* molecular imaging. *Current Opinion in Chemical Biology* **2010,** *14* (1), 71-79.

273. Quek, C.-H.; Leong, K. W. Near-infrared fluorescent nanoprobes for *in vivo* optical imaging. *Nanomaterials* **2012,** *2* (2), 92-112.

274. Sevick-Muraca, E. M. Translation of near-infrared fluorescence imaging technologies: Emerging clinical applications. *Annual Reviews of Medicine* **2012,** *63*, 217-231.

275. Kobat, D.; Horton, N. G.; Xu, C. *In vivo* two-photon microscopy to 1.6-mm depth in mouse cortex. *Journal of Biomedical Optics* **2011,** *16* (10), 106014.

276. Koga, S.; Oshima, Y.; Honkura, N.; Iimura, T.; Kameda, K.; Sato, K.; Yoshida, M.; Yamamoto, Y.; Watanabe, Y.; Hikita, A.; Imamura, T. *In vivo* subcellular imaging of tumors in mouse models using a fluorophore-conjugated anti-carcinoembryonic antigen antibody in two-photon excitation microscopy. *Cancer Science* **2014,** *105* (10), 1299-1306.

277. Peron, S.; Chen, T.-W.; Svoboda, K. Comprehensive imaging of cortical networks. *Current Opinion in Neurobiology* **2015,** *32*, 115-123.

278. Sarder, P.; Yazdanfar, S.; Akers, W. J.; Tang, R.; Sudlow, G. P.; Egbulefu, C.; Achilefu, S. All-near-infrared multiphoton microscopy interrogates intact tissues at deeper imaging depths than conventional single- and two-photon near-infrared excitation microscopes. *Journal of Biomedical Optics* **2013,** *18* (10), 106012.

279. Wang, Y.; Hu, R.; Xi, W.; Cai, F.; Wang, S.; Zhu, Z.; Bai, R.; Qian, J. Red emissive AIE nanodots with high two-photon absorption efficiency at 1040 nm for deep-tissue *in-vivo* imaging *Biomedical Optics Express* **2015,** *6* (10), 3783-3794.

280. Yang, P.-P.; Yang, Y.; Gao, Y.-J.; Wang, Y.; Zhang, J.-C.; Lin, Y.-X.; Dai, L.; Li, J.; Wang, L.; Wan, H. Unprecedentedly high tissue penetration capability of co-assembled nanosystems for two-photon fluorescence imaging *in vivo*. *Advanced Optical Materials* **2015,** *3* (5), 646-651.

281. Guo, Z.; Park, S.; Yoon, J.; Shin, I. Recent progress in the development of near-infrared fluorescent probes for bioimaging applications. *Chemical Society Reviews* **2014,** *43* (1), 16-29.

282. Zhao, Z.; Chen, B.; Geng, J.; Chang, Z.; Aparicio-Ixta, L.; Nie, H.; Goh, C. C.; Ng, L. G.; Qin, A.; Ramos-Ortiz, G.; Liu, B.; Tang, B. Z. Red emissive biocompatible nanoparticles from tetraphenylethene-decorated BODIPY luminogens for two-photon excited fluorescence cellular imaging and mouse brain blood vascular visualization. *Particle & Particle Systems Characterization* **2014,** *31* (4), 481-491.

283. Zhu, M.-Q.; Zhang, G.-F.; Li, C.; Aldred, M. P.; Chang, E.; Drezek, R. A.; Li, A. D. Q. Reversible two-photon photoswitching and two-photon imaging of immunofunctionalized nanoparticles targeted to cancer cells. *Journal of the American Chemical Society* **2011,** *133* (2), 365-372.

284. Lu, H.; Zhao, X.; Tian, W.; Wang, Q.; Shi, J. Pluronic F127–folic acid encapsulated nanoparticles with aggregation-induced emission characteristics for targeted cellular imaging. *RSC Advances* **2014,** *4* (35), 18460-18466.

285. Lakowicz, J. R.; Masters, B. R. Principles of fluorescence spectroscopy. *Journal of Biomedical Optics* **2008,** *13* (2), 9901.

286. Torchilin, V. P. Structure and design of polymeric surfactant-based drug delivery systems. *Journal of Controlled Release* **2001,** *73* (2), 137-172.

287. Kabanov, A. V.; Lemieux, P.; Vinogradov, S.; Alakhov, V. Pluronic® block copolymers: Novel functional molecules for gene therapy. *Advanced Drug Delivery Reviews* **2002,** *54* (2), 223-233.

288. Maurin, M.; Stéphan, O.; Vial, J.-C.; Marder, S. R.; van der Sanden, B. Deep *in-vivo* two-photon imaging of blood vessels with a new dye encapsulated in pluronic nanomicelles. *Journal of Biomedical Optics* **2011,** *16* (3), 036001.

289. Maurin, M.; Vurth, L.; Vial, J.-C.; Baldeck, P. L.; Marder, S. R.; van der Sanden, B.; Stéphan, O. Fluorescent Pluronic nanodots for *in vivo* two-photon imaging. *Nanotechnology* **2009,** *20*, 235102.

290. Rapoport, N. Stabilization and activation of Pluronic micelles for tumor-targeted drug delivery. *Colloids and Surfaces B: Biointerfaces* **1999,** *16* (1-4), 93-111.

291. Huo, Q.; Liu, J.; Wang, L.-Q.; Jiang, Y.; Lambert, T. N.; Fang, E. A new class of silica cross-linked micellar core−shell nanoparticles. *Journal of the American Chemical Society* **2006,** *128* (19), 6447-6453.

292. Zanarini, S.; Rampazzo, E.; Bonacchi, S.; Juris, R.; Marcaccio, M.; Montalti, M.; Paolucci, F.; Prodi, L. Iridium doped silica−PEG nanoparticles: Enabling electrochemiluminescence of neutral complexes in aqueous media. *Journal of the American Chemical Society* **2009,** *131* (40), 4208–14209.

293. Huo, Q.; Liu, J.; Wang, L.-Q.; Jiang, Y.; Lambert, T. N.; Fang, E. A new class of silica cross-linked micellar core-shell nanoparticles. *Journal of the American Chemical Society* **2006,** *128* (19), 6447-6453.

294. Genovese, D.; Bonacchi, S.; Juris, R.; Montalti, M.; Prodi, L.; Rampazzo, E.; Zaccheroni, N. Prevention of self-quenching in fluorescent silica nanoparticles by efficient energy transfer. *Angewandte Chemie International Edition* **2013,** *52*, 5965-5968.

295. Rampazzo, E.; Bonacchi, S.; Genovese, D.; Juris, R.; Montalti, M.; Paterlini, V.; Zaccheroni, N.; Dumas-Verdes, C. c.; Clavier, G.; Méallet-Renault, R.; Prodi, L. Pluronic-silica (PluS) nanoparticles doped with multiple dyes featuring complete energy transfer. *The Journal of Physical Chemistry C* **2014,** *118* (17), 9261-9267.

296. Rampazzo, E.; Bonacchi, S.; Juris, R.; Montalti, M.; Genovese, D.; Zaccheroni, N.; Prodi, L.; Rambaldi, D. C.; Zattoni, A.; Reschiglian, P. Energy transfer from silica core-surfactant shell nanoparticles to hosted molecular fluorophores. *The Journal of Physical Chemistry B* **2010,** *114* (45), 14605–14613.

297. Rampazzo, E.; Boschi, F.; Bonacchi, S.; Juris, R.; Montalti, M.; Zaccheroni, N.; Prodi, L.; Calderan, L.; Rossi, B.; Becchi, S.; Sbarbati, A. Multicolor core/shell silica nanoparticles for *in vivo* and *ex vivo* imaging. *Nanoscale* **2012,** *4*, 824-830.

298. Geng, J.; Goh, C. C.; Tomczak, N.; Liu, J.; Liu, R.; Ma, L.; Ng, L. G.; Gurzadyan, G. G.; Liu, B. Micelle/silica co-protected conjugated polymer nanoparticles for two-photon excited brain vascular imaging. *Chemistry of Materials* **2014,** *26* (5), 1874-1880.

299. Geng, J.; Goh, C. C.; Qin, W.; Liu, R.; Tomczak, N.; Ng, L. G.; Tang, B. Z.; Liu, B. Silica shelled and block copolymer encapsulated red-emissive AIE nanoparticles with 50% quantum yield for two-photon excited vascular imaging. *Chemical Communications* **2015,** *51*, 13416-13419.

300. D'Aléo, A.; Felouat, A.; Heresanu, V.; Ranguis, A.; Chaudanson, D.; Karapetyan, A.; Giorgi, M.; Fages, F. Two-photon excited fluorescence of BF_2 complexes of curcumin analogues: Toward NIR-to-NIR fluorescent organic nanoparticles. *Journal of Materials Chemistry C* **2014,** *2* (26), 5208-5215.

301. Baronzio, G.; Parmar, G.; Baronzio, M.; Kiselevky, M. Tumor interstitial fluid: Proteomic determination as a possible source of biomarkers. *Cancer Genomics and Proteomics* **2014,** *11* (5), 225-237.

302. Yuan, Y.; Feng, G.; Qin, W.; Tang, B. Z.; Liu, B. Targeted and image-guided photodynamic cancer therapy based on organic nanoparticles with aggregation-induced emission characteristics. *Chemical Communications* **2014,** *50* (63), 8757-8760.

303. Boens, N.; Qin, W.; Basarić, N.; Hofkens, J.; Ameloot, M.; Pouget, J.; Lefèvre, J.-P.; Valeur, B.; Gratton, E.; vandeVen, M.; Silva, N. D. J.; Engelborghs, Y.; Willaert, K.; Sillen, A.; Visser, A. J. W. G.; van Hoek, A.; Lakowicz, J. R.; Malak, H.; Gryczynski, I.; Szabo, A. G.; Krajcarski, D. T.; Tamai, N.; Miura, A. Fluorescence lifetime standards for time and frequency domain fluorescence spectroscopy. *Analytical Chemistry* **2007,** *79* (5), 2137-2149.

304. Porres, L.; Holland, A.; Pålsson, L.-O.; Monkman, A. P.; Kemp, C.; Beeby, A. Absolute measurements of photoluminescence quantum yields of solutions using an integrating sphere. *Journal of Fluorescence* **2006,** *16* (2), 267-273.

305. de Mello, J. C.; Wittmann, H. F.; Friend, R. H. An improved experimental determination of external photoluminescence quantum efficiency. *Advanced Materials* **1997,** *9* (3), 230-232.

306. Makarov, N. S.; Drobizhev, M.; Rebane, A. Two-photon absorption standards in the 550-1600 nm excitation wavelength range. *Optics Express* **2008,** *16* (6), 4029-4047.

Annexes

X-ray crystallography

Single crystals of compounds **SS**, **PH**, **a2**, **a5**, **a6**, **a9**, **a10** and **a11** were slowly prepared by a slow evaporation method from chloroform/ethanol mixture solvent at room temperature and were characterized crystallographically.

Data collection: Processing of the data was performed by the Kappa CCD analysis softwares. The lattice constants were refined by least-square refinement. No absorption correction was applied to the data sets.

Structure solution and refinement: Each system was attributed according to the observed systematic extinctions and the structures have been solved in the appropriate space group. The structure was solved by direct methods using the SIR97 program combined to Fourier difference syntheses and refined against F using reflections with [$I/\sigma(I) > 2$] with the CRYSTALS program. All atomic displacements parameters for non-hydrogen atoms have been refined with anisotropic terms. After anisotropic refinement, all the hydrogen atoms are found with a Fourier Difference. The following tables summarize the crystallographic data and refinement details for all compounds.

Computational methodology

The ground states for each molecule were calculated using the density functional theory level with the B3LYP functional employing a 6-31G* basis set. No symmetry or internal coordinate constraints were applied during optimization. The absorption energies were investigated by time-dependent density functional theory (TD-DFT). All calculations were performed by the use of the Gaussian 03 suite of programs.

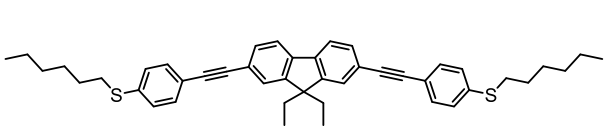

SS

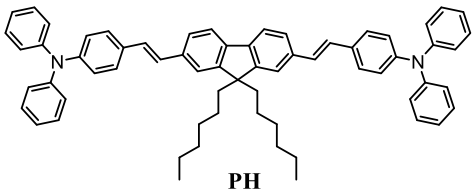

PH

compound	**SS**	**PH**
empirical formula	$C_{45}H_{50}S_2$	$C_{65}H_{64}N_2$
formula weight	654.97	873.18
crystal system	Monoclinic	Triclinic
space group	$P2_1/n$	$P\bar{1}$
a [Å]	18.5324(13)	11.0704(9)
b [Å]	7.4286(5)	14.3596(11)
c [Å]	7.4286(5)	17.1745(10)
α[°]	90	79.770(6)
β[°]	102.721(7)	87.148(6)
γ[°]	90	69.427(8)
V [Å^3]	3712.0(5)	2515.2(3)
Z	4	2
T [K]	100	100
D_{calcd}[g cm^{-3}]	1.172	1.153
μ [mm^{-1}]	1.511	0.496
θrange [°]	3.229-67.030	3.872-67.219
total no. data	27659	35024
no.unique data	6582	8884
no. params refined	428	606
R_1	0.0402	0.0884
wR_2	0.1022	0.2748
GOF	1.018	1.069

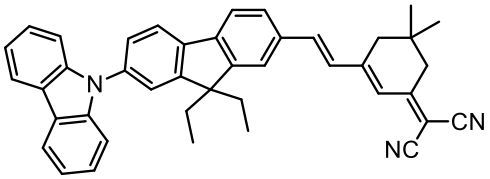

a2

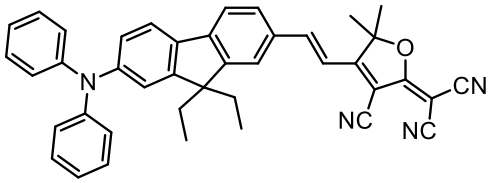

a5

compound	**a2**	**a5**
empirical formula	$C_{42}H_{37}N_3$	$C_{41}H_{34}N_4O$
formula weight	583.74	598.72
crystal system	Triclinic	Monoclinic
space group	$P\bar{1}$	$P2_1/c$
a [Å]	12.3044(8)	21.349(5)
b [Å]	15.2659(8)	8.947(5)
c [Å]	17.4894(7)	16.907(5)
α[°]	84.120(4)	90.000(5)
β[°]	83.698(4)	96.017(5)
γ[°]	81.451(5)	90.000(5)
V [Å^3]	3216.6(3)	3212(2)
Z	4	4
T [K]	100	100
D_{calcd}[g cm^{-3}]	1.205	1.238
μ [mm^{-1}]	0.537	0.584
θrange [°]	2.939-67.139	3.5117-67.0729
total no. data	42836	20949
no.unique data	11243	5647
no. params refined	821	421
R_1	0.0748	0.1229
wR_2	0.2010	0.2846
GOF	1.126	1.165

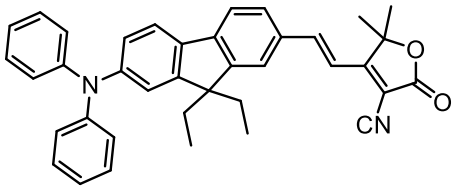

a8

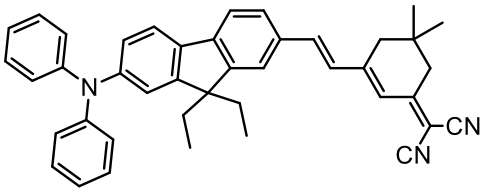

a9

compound	**a6**	**a9**
empirical formula	$C_{38}H_{34}N_2O_2$	$C_{42}H_{39}N_3$
formula weight	550.67	585.76
crystal system	Monoclinic	Triclinic
space group	C2/c	$P\bar{1}$
a [Å]	22.8539(12)	8.3595(7)
b [Å]	8.9180(5)	13.3051(10)
c [Å]	30.1636(18)	15.4894(11)
α[°]	90	81.173(6)
β[°]	106.339(6)	89.665(7)
γ[°]	90	79.887(7)
V [Å^3]	5899.4(6)	1675.5(2)
Z	8	2
T [K]	100	100
D_{calcd}[g cm^{-3}]	1.240	1.161
μ [mm^{-1}]	0.596	0.516
θrange [°]	4.031-67.135	3.415-67.224
total no. data	45192	23298
no.unique data	5238	5904
no. params refined	384	410
R_1	0.0491	0.0560
wR_2	0.1259	0.1462
GOF	1.034	1.046

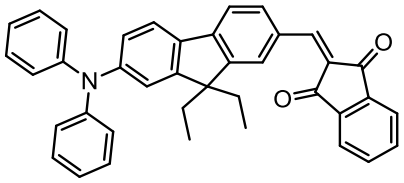

a10

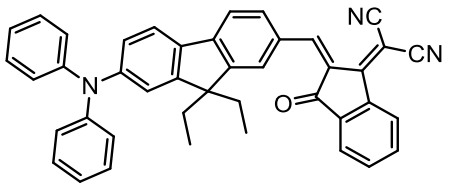

a11

compound	**a10**	**a11**
empirical formula	$C_{39}H_{31}NO_2$	$C_{42}H_{31}N_3O$
formula weight	545.65	593.70
crystal system	Triclinic	Monoclinic
space group	$P\bar{1}$	$P2_1/n$
a [Å]	8.4123(5)	10.111(5)
b [Å]	10.5424(5)	31.580(5)
c [Å]	17.0126(7)	10.120(5)
α[°]	77.818(4)	90.000(5)
β[°]	85.519(4)	105.028(5)
γ[°]	72.940(5)	90.000(5)
V [Å^3]	1409.70(13)	3121(2)
Z	2	4
T [K]	100	150.01(10)
D_{calcd}[g cm^{-3}]	1.285	1.264
μ [mm^{-1}]	0.611	0.592
θrange [°]	4.475-67.108	4.2041-66.9208
total no. data	54931	29996
no.unique data	4987	5523
no. params refined	382	418
R_1	0.0465	0.0418
wR_2	0.1225	0.1096
GOF	1.043	1.041